

Mapping the local and brain-wide network  
effects by optogenetic activation with an MRI-  
guided robotic arm

Dissertation

zur Erlangung des Grades eines  
Doktors der Naturwissenschaften

der Mathematisch-Naturwissenschaftlichen Fakultät  
und  
der Medizinischen Fakultät  
der Eberhard-Karls-Universität Tübingen

vorgelegt

von

Yi Chen  
aus Hangzhou, China

November-2019

Tag der mündlichen Prüfung: .....17, June, 2020.....

Dekan der Math.-Nat. Fakultät: Prof. Dr. W. Rosenstiel

Dekan der Medizinischen Fakultät: Prof. Dr. I. B. Autenrieth

1. Berichterstatter: Dr. Xin Yu

2. Berichterstatter: Prof. Dr. Cornelius Schwarz

Prüfungskommission: Dr. Xin Yu

Prof. Dr. Cornelius Schwarz

Prof. Dr. Jens Anders

Prof. Dr. Klaus Scheffler

**Erklärung / Declaration:**

Ich erkläre, dass ich die zur Promotion eingereichte Arbeit mit dem Titel:

„Mapping the local and brain-wide network effects by optogenetic activation with an MRI-guided robotic arm“

selbständig verfasst, nur die angegebenen Quellen und Hilfsmittel benutzt und wörtlich oder inhaltlich übernommene Stellen als solche gekennzeichnet habe. Ich versichere an Eides statt, dass diese Angaben wahr sind und dass ich nichts verschwiegen habe. Mir ist bekannt, dass die falsche Abgabe einer Versicherung an Eides statt mit Freiheitsstrafe bis zu drei Jahren oder mit Geldstrafe bestraft wird.

*I hereby declare that I have produced the work entitled “Mapping the local and brain-wide network effects by optogenetic activation with an MRI-guided robotic arm”, submitted for the award of a doctorate, on my own (without external help), have used only the sources and aids indicated and have marked passages included from other works, whether verbatim or in content, as such. I swear upon oath that these statements are true and that I have not concealed anything. I am aware that making a false declaration under oath is punishable by a term of imprisonment of up to three years or by a fine.*

Tübingen, den .....

Datum / Date

.....

Unterschrift /Signature

# Table of Contents

<b>Acknowledgements</b> .....	2
<b>Abstract</b> .....	3
<b>Abstract in German (Zusammenfassung)</b> .....	5
<b>Introduction</b> .....	7
<b>Scope of this thesis</b> .....	10
<b>Summary of publications</b> .....	12
Patent 1: Positioning system for an imaging device.....	12
Manuscript 1: MRI-guided robotic arm drives optogenetic fMRI with concurrent Ca <sup>2+</sup> recording.....	13
Manuscript 2: Mapping the brain-wide network effects by optogenetic activation of the corpus callosum ....	14
Manuscript 3: Mapping optogenetically-driven single-vessel fMRI with concurrent neuronal calcium recordings in the rat hippocampus.....	15
<b>Discussion</b> .....	17
<b>Conclusion</b> .....	21
<b>References</b> .....	22
<b>Statement of contributions</b> .....	25
<b>Appended patent/manuscripts</b> .....	26

## Acknowledgements

This work would not have been possible without the outstanding support of the Chinese Scholarship Council and several people.

I would like to express my sincere gratitude to my supervisor, Dr. Xin Yu, for the dedicated support, continuous supervising and guiding during the PhD and related research. I appreciate this environment and projects as a unique chance to make my foray into Neuroscience from an Electrical Engineering background. Meanwhile, thank him for his direct comments on the multiple facets of the PhD training (logic, writing, presentation, communication,...), this guidance reshaped my thinking path and behavior. His ambition and standards in doing research will remain as a guiding model for me.

I would like to thank the rest of my advisory board members: Prof. Schwarz, and Prof. Anders, not only for their insightful comments and encouragement in the previous advisory board meetings, but also for the questions which incited me to deepen my understanding for projects from various perspectives.

I am deeply grateful to Mr. S. Yu for the first prototype of the manual robotic arm and the Fine Mechanic and Electronics Workshop at MPI for Biological Cybernetics for robotic arm automation. All robotic aspects described here took their form from the close interaction with Mr. J. Boldt. This has been the most important prerequisite for the project.

I thank my lab mates for working together, for the discussions, for the friendship and all the fun. My sincere thanks also goes to the people who provide indispensable support to conduct this research, Dr. R. Pohmann, Mrs. H. Schulz, Dr. J. Engelmann, Dr. N. Avdievitch, Mrs. T. Schröder, Mr. M. Vintiloiu, and Mr. T. Hertel for technical support, Dr. P. Douay, Mrs. R. König, Dr. E. Weiler, Ms. S. Fischer, Mrs. M. Pitscheider and Mr. T. Cavlina for animal support.

The most fundamental spiritual support was from my beloved ones and friends. I would like to thank my parents and sister for their unconditional love, understanding, encouraging and the pressure-free world they created for me. Thank you, my dear friends, for badminton, bicycling, scuba diving and traveling, for all the moments we spent together, the shared happiness/sadness,... They shaped my decisions and showed me how to be a better person.

## Abstract

The optogenetically driven manipulation of circuit-specific activity has been very successful to enable functional causality studies in animals, but its global effect on the brain is rarely reported. Optical fiber-mediated optogenetic activation and neuronal  $\text{Ca}^{2+}$  recording in combination with fMRI provide a multi-modal fMRI platform with cross-scale brain dynamic mapping schemes, which can elucidate network activity upon circuit-specific optogenetic activation. However, despite highly promising prospects in animal brain research, there are still methodological and conceptual deficiencies, e.g., off-target effects and antidromic activity effects, which remain challenging for the current state of the art. To overcome these difficulties, this thesis describes two technical advances applied at the multi-modal fMRI platform, bridging the methodological and conceptual gap in optogenetics, brain function and animal behavior.

First, an MRI-guided robotic arm (MgRA) is developed to increase the target accuracy for optogenetic manipulation or microinjection at the multi-modal fMRI platform, merging fMRI with concurrent deep brain optogenetics in rats. The 4-degrees-of-freedom MgRA allows high precision (50  $\mu\text{m}$  per step) and sufficient mobility range (10 mm in the ventral-dorsal, rostral-caudal and medial-lateral directions) to manipulate fiber optic or injection needles into the brain in real time and provide high flexibility for multi-site targeting along the trajectory, which shows a clear advantage over the standard stereotaxic-based implantation strategy.

Second, the multi-modal fMRI platform provides a specific calcium amplitude-based correlation analysis to study corpus callosum (CC)-mediated brain-wide network dynamics with taking antidromic activity effect into consideration. Since the callosal fibers are reciprocally projecting to two hemispheres, bilateral ortho-vs. antidromically evoked neural activity is difficult to disentangle. Here we not only detected strong antidromic activity, but also detailed temporal dynamics through CC-mediated orthodromic inhibitory activity. The calcium amplitude-based correlation map was created to reveal the brain-wide inhibitory effects from the CC-specific optogenetic stimulation.

Last, this multi-modal fMRI platform was used to acquire the optogenetically driven neuronal  $\text{Ca}^{2+}$  with single-vessel BOLD and cerebral-blood-volume weighted signal from individual venules and arterioles, respectively, in the hippocampus. We characterized distinct spatiotemporal patterns of hippocampal hemodynamic responses that were correlated to the

optogenetically evoked  $\text{Ca}^{2+}$  events and further demonstrated the significantly reduced neurovascular coupling (NVC) efficiency upon spreading depression-like  $\text{Ca}^{2+}$  events. These results provide a direct measure of the NVC function at varied hippocampal states in animal models.

Overall, the technical advances described in this thesis demonstrate the powerful multi-modal fMRI platform to map, analyze and characterize the dynamic brain function across multiple scales and underscore the caution to interpret circuit-specific regulatory mechanisms underlying behavioral or functional outcomes with optogenetic tools.

## **Abstract in German (Zusammenfassung)**

Die optogenetisch gesteuerte Manipulation der kreissspezifischen Aktivität war sehr erfolgreich, um funktionale Kausalitätsstudien an Tieren zu ermöglichen, aber ihre globale Wirkung auf das Gehirn wird selten berichtet. Die faservermittelte optische Aktivierung und die neuronale  $\text{Ca}^{2+}$ -Aufzeichnung in Kombination mit fMRI bilden eine multimodale fMRI-Plattform mit skalenübergreifenden hirndynamischen Mapping-Schemata, die die Netzwerkaktivität bei schaltungsspezifischer optogenetischer Aktivierung verdeutlichen können. Trotz vielversprechender Perspektiven in der tierischen Hirnforschung gibt es jedoch immer noch methodische und konzeptionelle Defizite, z.B. Off-Target-Effekte und antidromische Aktivitätseffekte, die nach wie vor eine Herausforderung für den aktuellen Stand der Technik darstellen. Um diese Schwierigkeiten zu überwinden, beschreibt diese Arbeit zwei technische Fortschritte, die auf der multimodalen fMRI-Plattform angewendet werden und die methodische und konzeptionelle Lücke in der Optogenetik, der Gehirnfunktion und dem Verhalten der Tiere schließen.

Zunächst wird ein MRT-geführter Roboterarm (MgRA) entwickelt, um die Zielgenauigkeit für die optogenetische Manipulation oder Mikroinjektion auf der multimodalen fMRI-Plattform zu erhöhen, indem fMRI mit gleichzeitiger Tiefenhirnoptik bei Ratten kombiniert wird. Das MgRA mit 4 Freiheitsgraden ermöglicht eine hohe Präzision ( $50\ \mu\text{m}$  pro Schritt) und einen ausreichenden Mobilitätsbereich (10 mm in ventral-dorsaler, rostral-caudaler und medial-lateraler Richtung), um Lichtwellenleiter- oder Injektionsnadeln in Echtzeit in das Gehirn zu manipulieren und eine hohe Flexibilität für Multi-Site-Targeting entlang der Trajektorie zu bieten, was einen klaren Vorteil gegenüber der standardmäßigen stereotaxischen Implantationsstrategie zeigt.

Zweitens bietet die multimodale fMRI-Plattform eine spezifische amplitudenbasierte Korrelationsanalyse zur Untersuchung der Corpus Callosum (CC)-vermittelten hirnweiten Netzwerkdyamik unter Berücksichtigung des antidromischen Aktivitätseffekts. Da die Kallosofasern wechselseitig in zwei Hemisphären vorstehen, ist es schwierig, die bilaterale ortho-vs. antidromisch evozierte neuronale Aktivität zu entwirren. Hier konnten wir nicht nur eine starke antidromatische Aktivität feststellen, sondern auch eine detaillierte zeitliche Dynamik durch CC-vermittelte orthodromische inhibitorische Aktivität. Die



amplitudenbasierte Korrelationskarte wurde erstellt, um die hirnweiten hemmenden Effekte der CC-spezifischen optischen Stimulation aufzuzeigen.

Schließlich wurde mit dieser multimodalen fMRI-Plattform das optogenetisch gesteuerte neuronale  $\text{Ca}^{2+}$  mit Single-Vessel BOLD und cerebral-blood-volume-gewichtetem Signal von einzelnen Venolen bzw. Arteriolen im Hippocampus erfasst. Wir charakterisierten unterschiedliche räumlich-zeitliche Muster von hippocampalen hämodynamischen Reaktionen, die mit den optisch evozierten  $\text{Ca}^{2+}$ -Ereignissen korreliert waren, und zeigten weiterhin die signifikant reduzierte Effizienz der neurovaskulären Kopplung (NVC) bei der Ausbreitung depressionsartiger  $\text{Ca}^{2+}$ -Ereignisse. Diese Ergebnisse liefern ein direktes Maß für die NVC-Funktion bei verschiedenen Hippocampus-Zuständen in Tiermodellen.

Insgesamt zeigen die in dieser Arbeit beschriebenen technischen Fortschritte die leistungsstarke multimodale fMRI-Plattform zur Abbildung, Analyse und Charakterisierung der dynamischen Gehirnfunktion über mehrere Skalen hinweg und unterstreichen die Vorsicht bei der Interpretation schaltkreisspezifischer Regulationsmechanismen, die verhaltens- oder funktionellen Ergebnissen mit optogenetischen Werkzeugen zugrunde liegen.

## Introduction

The genetic expression of channelrhodopsin (ChR2) has been extensively applied to target specific cell types to ensure the activation of neuronal ensembles of interest [1-5]. Optogenetic tools have revolutionized the strategy to perturb or manipulate the behavior of animals [6-9]. Interpreting the linkage of the brain function to specific behavioral readout relies on the assumed circuit-specific neural activity manipulated (*on* or *off*) through *in vivo* optogenetic activation [10-12]. However, there is a lack of systematic mapping of the brain-wide network activity modulations, which may relay and critically effect the proposed link between function and behavior. Progress in this direction crucially depends on the combined application of methods to explore large scale brain dynamics as well [13-15].

For this purpose, wide-field camera imaging [16, 17] and multi-photon mesoscopes (millimeter-sized field of view) [18, 19] can be used to explore large areas of the surface in the mammalian brain, and other approaches like electrophysiology [20, 21] and multi-fiber photometry remain point-specific [15]. One useful and widely used imaging modality to investigate whole brain activity is functional magnetic resonance imaging (fMRI), which has been successfully combined with optogenetics [20, 22-26] and is advantaged by subcortical region visualization and non-invasiveness. Optical-fibers, given their non-magnetic properties, can be used in combination with fMRI for stimulation or recording without electromagnetic interference with the radio frequency transmission and magnetic gradient switching of the MR scanner. The addition of concurrent GCaMP-mediated cell-specific calcium recordings through optical fibers to the fMRI platform provides a multi-modal cross-scale brain dynamic mapping scheme, which can elucidate network activity upon circuit-specific optogenetic activation at the specific target level as well as across large brain regions [27-29].

It can be well said that the multi-modal fMRI platform has transformed into one of the most promising avenues of neuro-imaging investigation to bridge the gap between cellular specific optogenetics and animal behavior. However, important methodological advances and conceptual steps are still needed to further unfold its invaluable potential to decipher the brain function/dysfunction in animal studies, eventually providing essential knowledge to help to understand the human brain organization and function/dysfunction, as introduced below.

### **Whole brain function mediated by corpus callosum with multi-modal fMRI**

Here, we take the corpus callosum (CC) as an example which can be manipulated to produce both, local and global changes in the brain activity, and which, therefore, benefits from the use of combined optogenetics, fiber-mediated calcium recording and whole brain fMRI. The CC is a structure in the brain containing the major neural fiber bundles connecting the two brain hemispheres and also plays a critical role to mediate the interhemispheric cortico-cortical connections [30-32]. Despite the highly-correlated structural anomalies of the CC with a wide range of disorders, e.g., schizophrenia [33, 34], autism [35, 36], epilepsy [37, 38] and mental retardation [39, 40], the CC-mediated neural mechanisms are primarily studied in loss-of-function models, such as split-brain/callosotomy or partial callosal lesions [31, 41, 42]. To directly investigate the functional roles of callosal projections on regulating the interhemispheric excitatory-inhibitory balance, both *in vitro* and *in vivo* studies have applied micro-stimulation on one hemisphere or directly on the callosal fiber bundles [43-46], or performed bilateral motor or sensory tasks in both human [47-50] and animal models [50-54]. Since the callosal fibers are reciprocally projecting to two hemispheres, distinguishing ortho- vs. antidromically evoked neural activity remains challenging. With optogenetic tools, the callosal projection neurons can be specifically (primarily) labeled with ChR2 from one hemisphere, enabling unidirectional modulation of the callosal activity [55, 56]. The optogenetically driven callosal activity, has been particularly helpful to disentangle interhemispheric inhibitory effects, e.g., in the auditory cortex [57], prefrontal cortex [58] or hindlimb somatosensory cortex [59]. Beyond studying the target-specific excitatory-inhibitory regulation, we expand the view to investigate the CC-mediated inhibition by using the multi-modal fMRI platform to additionally characterize the global neural network activity upon optogenetic callosal activation.

### **Single-vessel fMRI in hippocampus with multi-modal fMRI**

As described above, the multi modal fMRI platform provides the whole brain mapping scheme. Moreover, with the development of high-resolution fMRI methods, it is possible to map the BOLD and cerebral blood volume (CBV) fMRI signals from individual arteriole and venule voxels from deep cortical layers, e.g., hippocampus. Previous *in vivo* hippocampal functional imaging studies removed the cortex above the hippocampus or applied micro-lens/micro-prism through the cortical tissue [60-63]. Not only has the 3D location of the hippocampus in the brain restricted its accessibility to the conventional optical imaging methods, but also the mesoscale hippocampal vasculature has been seldom specified for

hemodynamic mapping with fMRI. The balanced Steady-State-Free-Precession (bSSFP) method permits the acquisition of the fMRI signal from individual cortical penetrating arterioles and venules [29], thereby expands the line-scanning based method for real-time single-vessel fMRI mapping [22, 64, 65]. This high temporospatial resolution vessel-specific fMRI mapping method allowed to directly measure the mesoscale hemodynamic responses to specify the properties of neurovascular coupling (NVC) across hippocampal vasculature beyond the penetration depth of conventional optical imaging methods. By implementing the simultaneous single-vessel fMRI and optical fiber  $\text{Ca}^{2+}$  recordings with optogenetic activation, distinct hemodynamic spatiotemporal patterns across the sub-centimeter hippocampal vasculature could be directly characterized based on the concurrent neuronal  $\text{Ca}^{2+}$  signals.

### **Development of an MRI-guided robotic arm**

Although the increased cellular specificity of genetic labeling reassures the advantageous usage of optical fiber stimulation/recording to manipulate/track neural activity, it remains challenging to precisely target the regions in animal brains, e.g., CC, whose thickness is only several hundreds micrometers [66, 67]. The procedure of fiber optic implantation in rodent studies has been commonly performed with conventional stereotaxic devices [22-24, 27, 68-70], while the brain atlas [66, 71] is used to calculate the coordinates of nuclei. The main challenge when targeting deep brain structures is the potential error that appears between the actual and the calculated coordinates due to the variability in bregma location, skull thickness/angles, and potential shift of brain structures within the cranium after dura removal [72-74]. This potential error is particularly problematic when targeting some functional nuclei or neuronal fiber tracts of the rat brain that are less than 2-300  $\mu\text{m}$  in one of their dimensions, such as the central thalamic nuclei [24] or corpus callosal fibers [66, 67]. This problem can introduce a high variability when trying to target deeper brain nuclei, e.g. the lateral hypothalamus, since longer trajectories are subjected to larger errors [70]. The multi-modal fMRI platform, therefore, provides the advantage of taking the high spatial resolution anatomical images as feedback to evaluate the exact location of the optical fiber tip, making it possible to use MRI-guided robotic arm (MgRA) to real-time assist optical fiber intervention and even monitor the collateral tissue damage during fiber insertion.

Another drawback of the conventional stereotaxic device-based insertion strategy is the little flexibility after the fiber tips are fixed in the brain for fMRI mapping before the animals are

transferred into the scanner [23, 27-29]. The precise coordinates of a certain functional brain nucleus can vary between different animals, and incorrect positioning may result in largely altered functional activation and behavioral outcomes. This systematic error, which is intrinsic to the blind optical fiber placement with a stereotaxic device, can potentially conceal important discoveries and lead to inappropriate conclusions in causality analysis, especially for “hypothesis free” brain studies. Using MgRA assisted fiber-optic insertion in combination with real-time fMRI, more precise fiber optic placement can be achieved and a step-wise optogenetic activation scheme is enabled that allows multi-site targeting along a fiber insertion trajectory during the fMRI study. This strategy can not only improve the precision, but also provide a thorough view to examine the subtle differences in the whole brain activation patterns when targeting the sub-regions of the functional nuclei of interest.

To the best of our knowledge, there is currently no MRI-compatible robotic control system to assist fiber optic insertion in small bore high field MRI scanners (>9.4 T) for optogenetic fMRI studies. There is clearly a scientific need to develop a MRI-compatible, automatically controlled, real-time guided system to provide feasible targeting accuracy, high temporal and spatial resolution to guide the fiber intervention and monitor the collateral tissue damage during fiber insertion in order to investigate the effectiveness, safety and feasibility of deep brain nuclei targeting for translational applications, e.g. DBS or an implantable pump/needle for direct drug delivery.

## **Scope of this thesis**

The work described in this thesis aims at creating new approaches for widespread optogenetic fMRI studies with/without simultaneous cell-specific calcium recordings e.g., for CC and hippocampus, which address important shortcomings of the current state of the art, i.e., fiber optic off-target effect and antidromic activity effects. The overarching goal is to present the powerful multi-modal fMRI platform to map, analyze and characterize the dynamic brain function across multiple scales and underscore the caution to interpret circuit-specific regulatory mechanisms underlying behavioral or functional outcomes with optogenetic tools.

Specifically, two methodological advances are introduced in this thesis. First, an MRI-guided robotic arm is presented, which provides high precision to maneuver the real-time optical fiber implantation into the brain. This tool improves the multi-modal platform merging concurrent fMRI with optogenetics, fiber optic-mediated optical imaging and microinjection,

showing a clear advantage over the standard stereotaxic-based fiber implantation. Second, in contrast to the conventional general linear model (GLM) for fMRI analysis, by extracting the event-dependent calcium peak amplitudes at varied conditions as a regressor, a calcium amplitude-based correlation analysis is presented, for the first time, not only reveals the brain-wide inhibitory effects from the CC-specific optogenetic stimulation, but also demonstrate varying NVC efficiency across the hippocampal vasculature at single-vessel level for optogenetically evoked neuronal  $\text{Ca}^{2+}$  and the spreading depression-like  $\text{Ca}^{2+}$  (SDL- $\text{Ca}^{2+}$ ) events.

This thesis comprises one European patent, two 1<sup>st</sup>-author and one coauthor manuscripts. A workflow leading to this thesis is shown in Fig. 1. The first patent (*P1*) describes the system

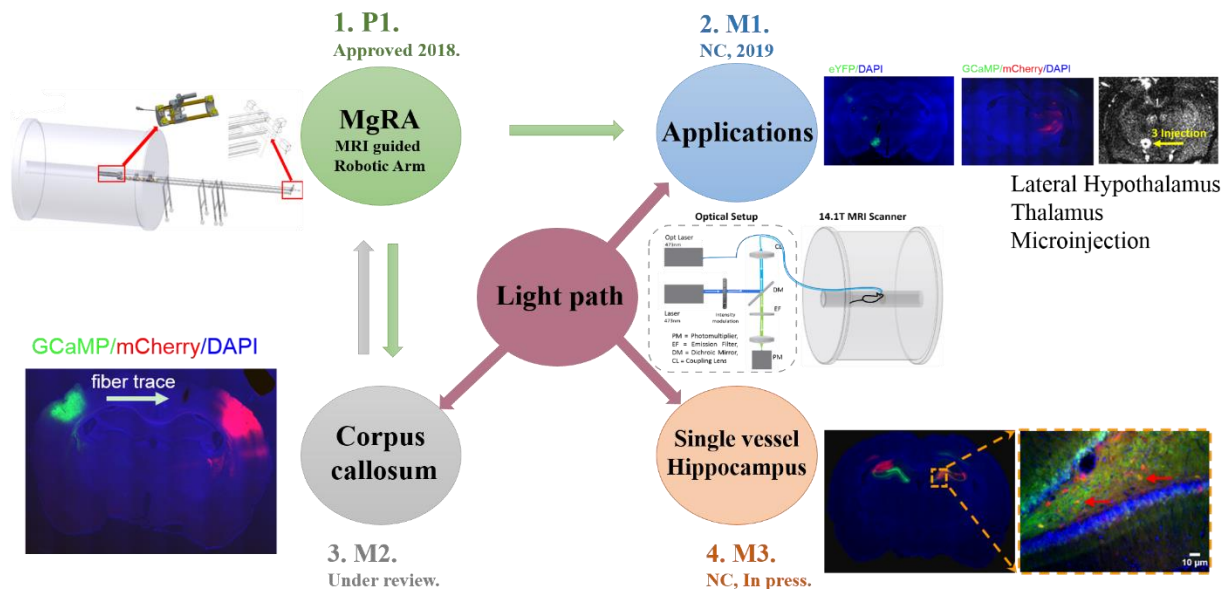


Fig.1. PhD projects work flow and composition of the thesis. The calcium recording lightpath was used in M1, M2 and M3.

units, drive mechanism, mechanical design and components details of the MRI-guided robotic arm positioning system working in the small bore high field MRI scanner (14.1 T) for positioning an inserting elements in the rat brain. The first manuscript (*M1*) not only presents *ex vivo* precision evaluation of MgRA, but also a series of *in vivo* high precision brain interventional applications for optogenetics and microinjection in the context of multi-modal neuroimaging using MgRA. The second manuscript (*M2*) benefits from the MgRA to target the CC and, by integrating calcium amplitude-based correlation analysis, it demonstrates the combined application of both methodological advances to study the information integration in the thalamocortical system and between both brain hemispheres through the callosal fibers in rats. The third manuscript (*M3*) further shows the powerfulness of the multi-modal fMRI

platform with high temporospatial resolution to specify the multi-scale neurovascular coupling in the hippocampus by correlating simultaneous single-vessel hippocampal fMRI with  $\text{Ca}^{2+}$  signals with optogenetic stimulation at various hippocampal states.

## **Summary of publications**

### ***Patent 1: Positioning system for an imaging device.***

Brain intervention, e.g., deep brain stimulation, could be directly used as a therapeutic strategy to treat patients with severe brain diseases, e.g. epilepsy, Parkinson disease, depression or brain tumors. Animal brain studies aim to better understand the complexity of the brain. However, how to precisely target the specific functional nuclei and reduce the collateral tissue damage remains challenging. Brain MRI is widely used to help localize targets or investigate the outcomes of a surgical procedure. Therefore, in this study, an MRI-compatible positioning system, i.e., MRI-guided robotic arm, was developed to provide feasible targeting accuracy, high temporal and spatial resolution by using MRI anatomical images as feedback to guide the brain implantation of electrodes/optical fibers/injection needles.

This European patent describes the system units, drive mechanism, mechanical design and components details for the MgRA system in the 14 T MRI scanner. As shown in the Fig.1 and 5, this system consists of a positioning module (the back part of the MgRA), the head of the MgRA and a custom-designed user interface. The positioning module accommodates 4 stepper motors to fulfill 4-degree of freedom movement of the insertion element mounted on the driving pieces in the head of the MgRA, which includes the driving pieces, cameras and a customized rat holder (Fig. 4 and 7). The movements include three dimensions like conventional stereotactic devices, as well as pitch and yaw (manually). The mobility range of the MgRA (10 mm in the ventral-dorsal, rostral-caudal and medial-lateral directions) is sufficient to reach any brain structure in small animal brains. The step-size, i.e. spatial resolution, for ventral-dorsal movement achieved by an Archimedean spiral mechanism is 50  $\mu\text{m}$ , which is sufficient to target nearly all the functional nuclei in the rat brain (Fig. 3). The coupling of the actuators from the positioning module to the matching toothed pulley in the head of the MgRA was achieved by a synchronous belt drive in a form-fit manner (Fig. 6). With MRI-compatible cameras, the user can watch the element insertion in real time outside of the brain parenchyma, while the robot is executing a maneuver. If any movement needs to

be modified, the user can start, stop, change, or resume the fiber movement at any time from the user-interface. The MRI-compatible arm, including the head part and aluminum holder, were placed inside the MRI scanner room, while digital components including stepper motors, the motor controller and motor power supply, were placed outside the scanner room (Fig. 8). Most of the components inside the MRI scanner room are constructed from fully MRI-compatible materials like plastic, carbon fiber, and a minimal amount of nonferrous metals like brass and anodized aluminum to avoid eddy currents and deterioration of magnetic field homogeneity.

Overall, this positioning system provides feasible targeting accuracy and high temporal and spatial resolution to guide the element insertion, e.g., electrodes/fiber optic/injection needle, while reducing the position error significantly in the animal brain and monitor the collateral tissue damage, with direct image feedback from the build-in camera and radio frequency surface coil, for outside and inside the brain parenchyma, respectively. The compatibility with the 14.1 T high magnetic field and compact head part design make this positioning system applicable to 8 cm bores for future animal brain intervention studies, while ascribing it a potential to be translated to the clinical practice, e.g. deep brain stimulation, an implantable pump/needle for direct drug delivery, in multiple brain targeting tasks.

***Manuscript 1: MRI-guided robotic arm drives optogenetic fMRI with concurrent  $Ca^{2+}$  recording.***

The cell-type specific genetic labeling ensures the optogenetic activation on neuronal ensembles of interest assuming that the optical fiber is precisely located at the functional nuclei. However, the conventional stereotaxic device-driven fiber optic implantation scheme shows insufficient accuracy and little flexibility after the fiber tips are fixed in the brain for fMRI mapping. The MgRA could not only fulfill the role of accurately placing the fiber tip at the desired coordinates to identify the ideal targets for light delivery (Fig. 1), but it can also move the stimulating fiber and run opto-fMRI at different locations in one single study (Fig. 2), especially useful for “hypothesis-free” brain activity mapping studies.

This work demonstrates a series of high precision brain interventional applications in the context of multi-modal neuroimaging using the MgRA system in ultra high-field MRI (14.1 T scanner). First, optogenetic activation of the lateral hypothalamus can be directly driven by the MgRA system to produce highly reliable activation patterns not only at the LH region



close to the tip of the optical fiber, but also in the lateral preoptic area (LPO), medial preoptic area (MPA), medial preoptic nucleus, lateral part (MPOL) and strial part of the preoptic area (StA). These widespread changes in BOLD activity were reliably detected in 5 different rats with similar spatial patterns, which was analyzed by co-registering the brain atlas to individual rat functional maps (Fig. 3). Second, the MgRA guided the fiber tip to deliver the optogenetic activation at multiple sites along the insertion trajectory to target the ventral posteromedial nucleus (VPM) with a step-size of 700  $\mu\text{m}$  (Fig. 4). Evoked calcium and BOLD signals from the somatosensory cortex ipsilateral to the targeted thalamic nucleus increased in a stepwise manner as the optical fiber was moved closer to the VPM region, while, after the fiber bypassed the VPM region, BOLD and calcium signal decreased accordingly. Last, the MgRA was applied for real-time microinjection to specific deep brain nuclei, as demonstrated with a Mn-enhanced MRI method, demonstrating its microinjection capabilities for contrast agent or drug delivery with high precision inside the MRI scanner. Besides the multiple stops along a single injection trajectory (corpus callosum and central lateral thalamic nucleus), the MgRA can be used to drive multi-trial microinjection to target different nuclei, e.g. to the lateral hypothalamic nucleus, CC and CL in the same rat (Fig. 5).

In summary, the real-time MRI-guided robotic arm positioning system is verified and practiced for the optical fiber brain intervention in animals using the high field MRI scanner (>14 T). The MgRA represents a clear advantage over the conventional stereotaxic device-based fiber implantation and opens a broad avenue to investigate the circuit-specific functional brain mapping with the multi-modal fMRI platform merging fMRI with concurrent optogenetics, optical fiber-mediated calcium signal recording and microinjection.

### ***Manuscript 2: Mapping the brain-wide network effects by optogenetic activation of the corpus callosum***

Recently, the optogenetically driven manipulation of corpus callosum-specific activity enabled to directly investigate the functional roles of callosal projections on regulating the interhemispheric excitatory-inhibitory balance in animals. However, its global effect on the brain is rarely reported. With precise optical fiber targeting guided by MgRA, the multi-modal fMRI platform provides a cross-scale brain dynamic mapping scheme to elucidate global neuronal network upon corpus callosum activation.

This study investigated the CC-mediated interhemispheric inhibition on the brain-wide network dynamics in three consecutive steps. First, we identified the antidromic vs. orthodromic effect of CC-specific optogenetic stimulation. Unilateral optogenetic stimulation of the callosal fibers connecting the barrel cortex (BC) to the contralateral hemisphere revealed robust antidromic activation in the ipsilateral BC (Fig. 1). In the orthodromic direction (i.e. projection to the contralateral BC), both fMRI and neuronal calcium signals indicated strong depression of calcium signals upon stimulation with 40 Hz light pulses (Fig. 2). Second, we specified the temporal characteristics of this presumptive CC-mediated inhibition of the thalamocortical activation to the BC (Fig. 3). The optogenetic CC light pulses were paired with electrical pulses delivered to the whisker pad (contralateral to the stimulated callosal area) at varying intervals from 0 ms to 200 ms in a randomized stimulation scheme. Significant inhibitory effects at 50 ms and 100 ms interval were detected by both fMRI and neural calcium recordings, but little difference was observed in the antidromically evoked fMRI signal in the ipsilateral BC. Thirdly, to further examine the brain-wide activity modulation upon paired optogenetic and whisker stimulation, the concurrent evoked-calcium signals in the contralateral BC, detected in real time at varied conditions, were used to correlate with the whole-brain fMRI signal using a calcium amplitude modulation-based correlation analysis method (Fig. 4). Besides the contralateral BC, the homologous ventral part of the ipsilateral BC, the motor cortex and posterior thalamus from the same side of the contralateral BC were highlighted in the correlation maps, showing amplitudes modulated by CC-mediated inhibition at varied time intervals.

Overall, this study not only specifies the optogenetically driven CC-mediated regulation of the local excitation/inhibition balance in the local barrel cortex but also depicts the power of the multi-modal fMRI to characterize the brain-wide network activity associated with circuit-specific optogenetic activations *in vivo*. It highlights a vital aspect of the brain-wide activity for circuit-specific causality studies with optogenetic tools.

### ***Manuscript 3: Mapping optogenetically-driven single-vessel fMRI with concurrent neuronal calcium recordings in the rat hippocampus***

The hemodynamic responses linked to specific neural activity remains to be elucidated at the single-vessel level across hippocampal vasculature at the sub-centimeter spatial scale, which hindered to better decipher the hippocampal malfunction in diseased animal models. Here, we used the multi-modal fMRI platform to investigate the detailed, spatiotemporally resolved

NVC events in rat hippocampus at two different states, which are based on the concurrent neuronal  $\text{Ca}^{2+}$  signals, e.g., the optogenetically evoked or the SDL- $\text{Ca}^{2+}$  events.

First, by co-expressing ChR2 and the genetically encoded  $\text{Ca}^{2+}$  sensor, GCaMP6f, in the rat hippocampus using AAV vectors, BOLD fMRI signals could be detected from the activated hippocampus voxels, and the concurrent  $\text{Ca}^{2+}$  signals from nearby neurons upon optogenetic stimulation (Fig. 1). The in-plane resolution was increased to 100  $\mu\text{m}$  and 130  $\mu\text{m}$  for the BOLD and CBV-weighted fMRI, respectively, by performing the bSSFP-based single-vessel fMRI on the slice chosen to be 500  $\mu\text{m}$  away from the optical fiber along the caudal-ventral axis (Fig. 2). Second, in contrast to the normal trains of  $\text{Ca}^{2+}$  transients evoked by the light pulses (Fig. 3C), we also observed the large-scale hippocampal  $\text{Ca}^{2+}$  transient, i.e., the spreading depression-like (SDL)  $\text{Ca}^{2+}$  transient, at inter-stimulus intervals following the optogenetic stimulation with 3 or 5 Hz light pulses at 8s stimulation-on duration, which coincided with spreading positive BOLD and negative CBV-weighted signals during inter-stimulus intervals in the hippocampus (Fig. 3D). In addition, the simultaneous LFP and fiber optic  $\text{Ca}^{2+}$  recordings also detected epileptic events as a train of strong LFP deflections and concurrent  $\text{Ca}^{2+}$  transients. These epileptic events were often accompanied by the large amplitude SDL- $\text{Ca}^{2+}$  event in the hippocampus. Third, in contrast to the conventional general linear model that fits the fMRI signal with the ideal time course, we applied a  $\text{Ca}^{2+}$  amplitude modulated model to calculate the GLM beta coefficients, as the efficiency estimates of the NVC (eNVC) to the optogenetically evoked and SDL- $\text{Ca}^{2+}$  events. Mean vessel-specific eNVC beta values of optogenetically evoked  $\text{Ca}^{2+}$  events were significantly higher than those of SDL- $\text{Ca}^{2+}$  events (Fig. 4G). Despite the fact that SDL- $\text{Ca}^{2+}$  + events were elicited in the hippocampal structure close to the optogenetic stimulation site, their eNVC beta values were found to be similar and evenly distributed across the hippocampal vasculature, whereas the eNVC beta values of optogenetically evoked  $\text{Ca}^{2+}$  events showed a distance-dependent distribution (Fig. 4).

In summary, by implementing the simultaneous optogenetic single-vessel fMRI and optical fiber  $\text{Ca}^{2+}$  recordings, distinct hemodynamic spatiotemporal patterns across the sub-centimeter hippocampal vasculature could be directly characterized based on the concurrent neuronal  $\text{Ca}^{2+}$  signals. The multi modal fMRI platform not only provides a unique cross-scale mapping scheme to study the neurovascular activity in the hippocampus in both normal and

pathological conditions, but also sheds light on the future pathological hippocampal NVC studies in disease animal models with stroke, epilepsy, and Alzheimer's disease.

## **Discussion**

This thesis provided two methodological innovations, whose novelty will be described first and followed by highlighting the conceptual impact of their application for the multi modal fMRI platform, which has been used broadly as neuroscientific tools for the neuroimaging and has become an especially fruitful road to understand the network-scale functional organization of the animal brain.

### **MRI-guided robotic arm to improve targeting precision for multi modal fMRI platform**

First, an MRI-guided robotic arm which is implemented compatibly on the multi-modal fMRI platform is presented (*PI/MI*). Compared to the conventional stereotaxic device-based implantation strategy, the major advance of MgRA is that it allows high precision and flexibility for optical fiber insertion along one or multiple trajectories in the same rats, as well as monitoring the collateral tissue damage during optical fiber insertion. Besides fulfilling the role of accurately placing the fiber tip at the desired coordinates, the MgRA provides a flexible platform to identify, *de novo*, the ideal targets for deep brain stimulation in pre-clinical studies. This could be easily investigated with the MgRA by moving the stimulating fiber and running opto-fMRI at different locations in one single study, particularly for “hypothesis-free” brain activity mapping studies. This application will be critical to optimize and specify the ideal subcortical targets aiming at controlling pathological tremor or searching for more reliable treatment for depression in animal models [75-77]. Importantly, potential collateral damage to the choroid plexus or other blood vessels, which are certain effects inherent in the insertion of an optical fiber into the brain, could be well monitored by real-time imaging and avoided by changing the trajectory of the fiber. This is a particularly relevant feature of the MgRA, as it contributes to the maintenance of the integrity of the surrounding tissue to a certain level, which is beyond the capabilities of the standard implantation techniques with stereotactic devices.

Numerous efforts have been made to develop robotic positioning systems inside the MRI scanner for translational application from animals to the clinical practice, e.g. deep brain stimulation (DBS) or brain tumor ablation [69-75]. In contrast to the growing access to

robotic manipulation strategies inside large-bore MRI scanners (e.g. 1.5 T or 3 T human scanner), there are only a handful of works that have implemented remote controlling systems inside high field MRI scanners with smaller bore (>7 T, <12 cm gradient bore size). Examples include an MR image-guided mini-DBS system for BOLD activation during subthalamic nucleus DBS in nonhuman primates in a 3 T scanner [75], an angle positioning system to increase the image signal intensity of fibrous microstructure in a 9.4 T 12 cm-bore scanner [76], an integrated system, driven by piezoelectric actuators, for auto-tuning of a multichannel transceiver array at 7 T [77] or MRI-compatible systems for focused ultrasound experiments in rodents in 3 T scanners [78, 79].

To the best of our knowledge, the MgRA described in this study is the first automatic prototype to assist fiber optic insertion in small bore high field MRI scanners for optogenetic studies. Besides the mechanical design of MgRA (*PI*), a series of *in vivo* applications in *MI* including deep brain targeting, multi-site targeting and microinjection compatibility demonstrates the power of this novel approach. In another step, this approach was applied to guide the optical fiber to activate the corpus callosum, whose thickness is only ~200  $\mu\text{m}$  (*M2*), which further confirms the role of it as the key component for a multi-modal fMRI platform.

### **Whole brain mapping and $\text{Ca}^{2+}$ amplitude-based correlation mediated by CC inhibition**

Second, a generic approach by correlating calcium amplitude from designed experiment conditions with whole brain BOLD signal for identifying brain-wide network effects of CC-mediated inhibition was presented. The core advance of this methodology combining multi-modal platform is that it allows to reveal the functional connectivity which results from activating optogenetically (and unidirectionally) callosal fibers without being confounded by the antidromic activity. The observation of strong antidromic propagation by callosal optogenetic stimulation and related synaptic spread of activity presents a caveat for circuit specific *in vivo* optogenetic studies. In particular, when projection terminals from neurons labelled with ChR-2 that are located at specific functional nuclei are targeted, possible spreading network activity from the antidromically activated brain sites needs to be considered. In our experiments BOLD signals were detected upon stimulation with 5 Hz light pulses in both the motor cortex and the posterior thalamus projected from the antidromically activated BC, indicating a wide-spread optogenetic activation pattern in the brain-wide network (which was unintended for the experimental purpose). Therefore, it is mandatory to

consider brain-wide activation patterns, even in case of application of highly circuit-specific optogenetic activation schemes.

Besides the antidromically evoked network activation pattern, the orthodromic CC-mediated inhibition generates a brain-wide activity pattern of its own. The whole brain fMRI with concurrent calcium recording, allows to access brain-wide network effects of CC-mediated inhibition. The correlation map highlighted three brain regions: First, the ventral part of ipsilateral BC, second, the contralateral MC and third, the contralateral PO. These findings point at a potential participation of the callosal inputs in the regulation of a wider network of reciprocal thalamo-cortical network, which mediates BC signals from the other hemisphere for whisking related processing [78-83]. Indeed, when studying circuit specific optogenetics induced behavior, global regime is of special importance because the animal behavior originates from neuronal activity often distributed and coordinated across multiple brain areas, i.e., associated with brain-wide networks. Common approaches like electrophysiological approaches [21, 84] and the multi-fiber photometry [85] so far offer either preselect limited brain sites or primarily investigate the surface of the brain, e. g. wide-field camera imaging [16, 17] and multi-photo mesoscopes [18, 19]. Therefore, new methodologies like the multi-modal platform could be used to comprehensively explore large scale brain dynamics, which are crucial to avoid leading to incomplete causal conclusions and concealing important discoveries of parallel pathways, as well as feed-forward/feed-back loops. The procedures described in this manuscript provide the possibility to identify the global functional connectivity by correlating cell-specific calcium signals in local areas (mediated by designed stimulation conditions) with the BOLD signal from each voxel within the brain.

Overall, the results obtained with the calcium amplitude-based method for global connectivity graph from calcium and fMRI, underline the importance of comprehensively understanding potential pathways while making inferences about the association of optogenetic stimulation and behavior.

### **Single vessel mapping and $\text{Ca}^{2+}$ amplitude-based correlation in hippocampus**

In addition, this thesis also demonstrating the hippocampal vascular hemodynamic mapping using the single-vessel fMRI with simultaneous cell-specific calcium signals in the hippocampus to specify the hippocampal neurovascular coupling NVC events driven by

optogenetic stimulation. Despite extensive imaging studies on hippocampal neural activity, the actual information flow from neuronal activity to the hippocampal neurovascular system, the modulation of which provides the vast majority of fMRI signals, has seldom been taken into account in investigations attempting to relate behavior to the function or dysfunction of this structure [60, 86-88]. One major barrier is the ability to access large-scale hippocampal vascular dynamics in vivo with minimally invasive procedures, preserving the NVC function. This work is trying to solve three critical features for the existing neuroimaging methods: large FOV, high resolution to detect the vessel-specific hemodynamic signal with sufficient SNR, and accessibility to deep brain nuclei. By improving the spatial resolution of fMRI image, the fMRI signals from individual penetrating vessels through the hippocampus were detected beyond the penetration depth of the conventional optical methods.

In addition, using GCaMP6f, the optogenetically evoked hippocampal neuronal calcium with similar temporal dynamics to cortical calcium transients were detected, as well the robust SDL-Ca<sup>2+</sup> events during the inter-stimulus intervals in the hippocampus (Fig. 3). These SDL-Ca<sup>2+</sup> events were recently reported to follow the trains of interictal spikes during the optogenetically-induced seizure [89] in the mouse cortex. The epileptic events observed in the cortex are usually accompanied by the cortical spreading depression [89-91], which is typically studied with fMRI by direct KCl topical treatment or focal ischemia in animal brains [92, 93]. In the hippocampus, we detected the robust SDL-Ca<sup>2+</sup> events independent of the epileptic activity in the inter-stimulus intervals when 3-5 Hz optogenetic light pulses were used (Fig. 3D), which have dominated the random incidence of the epileptic events using similar stimulation paradigm in the hippocampus. Combining with the fMRI platform, coupled to the SDL-Ca<sup>2+</sup> events, we detected the correlated BOLD signal increase and CBV-weighted signal decrease (due to vasodilation), but no clear sign of vasoconstriction-based fMRI signal change was detected. Interestingly, although no clear vasoconstriction-based fMRI signal was detected following the SDL-Ca<sup>2+</sup> event, significantly reduced NVC efficiency was detected when comparing to the optogenetically evoked Ca<sup>2+</sup> transients (Fig. 5). Consistent with the impaired NVC during cortical SD [90, 94], we provide a multi-modal fMRI platform to directly measure the altered NVC efficiency directly linked to the concurrent SDL- Ca<sup>2+</sup> + events in the hippocampus.

Overall, the multi-modal fMRI platform used to acquire the concurrent neuronal Ca<sup>2+</sup> and single-vessel fMRI signal in the hippocampus allows for detecting the hemodynamic fMRI

responses from individual vessels through the sub-centimeter hippocampal vasculature. In particular, the large-scale vascular hemodynamic responses can be represented based on the estimated NVC efficiency at different hippocampal states.

## **Conclusion**

In sum, this thesis presents two new approaches for studying animal brain activity based on the multi-modal fMRI platform. The methodological developments and results provided in this thesis overcome some of the methodological and conceptual gaps in the current state of the art and constitute significant steps for unfolding the potential of the multi-modal fMRI platform to decipher brain network function/dysfunction and bridge the scales at cellular, neural circuit, and eventually the whole brain network level. The multi-modal fMRI platform thus opens a new avenue to investigate animal brain function in health as well as diseases by providing additional and complementary information across the whole brain.



## References

1. Nagel, G., et al., *Channelrhodopsin-1: a light-gated proton channel in green algae*. Science, 2002. **296**(5577): p. 2395-8.
2. Nagel, G., et al., *Channelrhodopsin-2, a directly light-gated cation-selective membrane channel*. Proc Natl Acad Sci U S A, 2003. **100**(24): p. 13940-5.
3. Boyden, E.S., et al., *Millisecond-timescale, genetically targeted optical control of neural activity*. Nat Neurosci, 2005. **8**(9): p. 1263-8.
4. Zhang, F., et al., *Channelrhodopsin-2 and optical control of excitable cells*. Nat Methods, 2006. **3**(10): p. 785-92.
5. Li, X., et al., *Fast noninvasive activation and inhibition of neural and network activity by vertebrate rhodopsin and green algae channelrhodopsin*. Proc Natl Acad Sci U S A, 2005. **102**(49): p. 17816-21.
6. Adamantidis, A.R., et al., *Neural substrates of awakening probed with optogenetic control of hypocretin neurons*. Nature, 2007. **450**(7168): p. 420-4.
7. Lima, S.Q. and G. Miesenbock, *Remote control of behavior through genetically targeted photostimulation of neurons*. Cell, 2005. **121**(1): p. 141-52.
8. Nagel, G., et al., *Light activation of channelrhodopsin-2 in excitable cells of Caenorhabditis elegans triggers rapid behavioral responses*. Curr Biol, 2005. **15**(24): p. 2279-84.
9. Tsai, H.C., et al., *Phasic firing in dopaminergic neurons is sufficient for behavioral conditioning*. Science, 2009. **324**(5930): p. 1080-4.
10. Carter, M.E., et al., *Tuning arousal with optogenetic modulation of locus coeruleus neurons*. Nat Neurosci, 2010. **13**(12): p. 1526-33.
11. Tye, K.M. and K. Deisseroth, *Optogenetic investigation of neural circuits underlying brain disease in animal models*. Nat Rev Neurosci, 2012. **13**(4): p. 251-66.
12. Kim, C.K., A. Adhikari, and K. Deisseroth, *Integration of optogenetics with complementary methodologies in systems neuroscience*. Nat Rev Neurosci, 2017. **18**(4): p. 222-235.
13. Bernal-Casas, D., et al., *Studying Brain Circuit Function with Dynamic Causal Modeling for Optogenetic fMRI*. Neuron, 2017. **93**(3): p. 522-532 e5.
14. Inoue, K.I., M. Takada, and M. Matsumoto, *Neuronal and behavioural modulations by pathway-selective optogenetic stimulation of the primate oculomotor system*. Nat Commun, 2015. **6**: p. 8378.
15. Sych, Y., et al., *High-density multi-fiber photometry for studying large-scale brain circuit dynamics*. Nat Methods, 2019. **16**(6): p. 553-560.
16. Chen, T.W., et al., *A Map of Anticipatory Activity in Mouse Motor Cortex*. Neuron, 2017. **94**(4): p. 866-+.
17. Gilad, A., et al., *Behavioral Strategy Determines Frontal or Posterior Location of Short-Term Memory in Neocortex*. Neuron, 2018. **99**(4): p. 814-+.
18. Stirman, J.N., et al., *Wide field-of-view, multi-region, two-photon imaging of neuronal activity in the mammalian brain*. Nature Biotechnology, 2016. **34**(8): p. 857-+.
19. Sofroniew, N.J., et al., *A large field of view two-photon mesoscope with subcellular resolution for in vivo imaging*. Elife, 2016. **5**.
20. Albers, F., et al., *Line scanning fMRI reveals earlier onset of optogenetically evoked BOLD response in rat somatosensory cortex as compared to sensory stimulation*. Neuroimage, 2018. **164**: p. 144-154.
21. Jun, J.J., et al., *Fully integrated silicon probes for high-density recording of neural activity*. Nature, 2017. **551**(7679): p. 232-+.
22. Yu, X., et al., *Sensory and optogenetically driven single-vessel fMRI*. Nat Methods, 2016. **13**(4): p. 337-40.
23. Lee, J.H., et al., *Global and local fMRI signals driven by neurons defined optogenetically by type and wiring*. Nature, 2010. **465**(7299): p. 788-92.
24. Liu, J., et al., *Frequency-selective control of cortical and subcortical networks by central thalamus*. Elife, 2015. **4**: p. e09215.
25. Ryali, S., et al., *Combining optogenetic stimulation and fMRI to validate a multivariate dynamical systems model for estimating causal brain interactions*. Neuroimage, 2016. **132**: p. 398-405.
26. Grandjean, J., et al., *A brain-wide functional map of the serotonergic responses to acute stress and fluoxetine*. Nat Commun, 2019. **10**(1): p. 350.
27. Schulz, K., et al., *Simultaneous BOLD fMRI and fiber-optic calcium recording in rat neocortex*. Nat Methods, 2012. **9**(6): p. 597-602.
28. Wang, M., et al., *Brain-state dependent astrocytic Ca(2+) signals are coupled to both positive and negative BOLD-fMRI signals*. Proc Natl Acad Sci U S A, 2018. **115**(7): p. E1647-E1656.
29. He, Y., et al., *Ultra-Slow Single-Vessel BOLD and CBV-Based fMRI Spatiotemporal Dynamics and Their Correlation with Neuronal Intracellular Calcium Signals*. Neuron, 2018. **97**(4): p. 925-939 e5.
30. Sperry, R.W., *Cerebral Organization and Behavior: The split brain behaves in many respects like two separate brains, providing new research possibilities*. Science, 1961. **133**(3466): p. 1749-57.
31. Gazzaniga, M.S., *Forty-five years of split-brain research and still going strong*. Nat Rev Neurosci, 2005. **6**(8): p. 653-9.

32. Karolis, V.R., M. Corbetta, and M. Thiebaut de Schotten, *The architecture of functional lateralisation and its relationship to callosal connectivity in the human brain*. Nat Commun, 2019. **10**(1): p. 1417.
33. Innocenti, G.M., F. Ansermet, and J. Parnas, *Schizophrenia, neurodevelopment and corpus callosum*. Mol Psychiatry, 2003. **8**(3): p. 261-74.
34. Pomarol-Clotet, E., et al., *Medial prefrontal cortex pathology in schizophrenia as revealed by convergent findings from multimodal imaging*. Mol Psychiatry, 2010. **15**(8): p. 823-30.
35. Egaas, B., E. Courchesne, and O. Saitoh, *Reduced size of corpus callosum in autism*. Arch Neurol, 1995. **52**(8): p. 794-801.
36. Anderson, J.S., et al., *Decreased interhemispheric functional connectivity in autism*. Cereb Cortex, 2011. **21**(5): p. 1134-46.
37. Spencer, S.S., et al., *Corpus callosotomy for epilepsy. I. Seizure effects*. Neurology, 1988. **38**(1): p. 19-24.
38. van Eijsden, P., et al., *In vivo diffusion tensor imaging and ex vivo histologic characterization of white matter pathology in a post-status epilepticus model of temporal lobe epilepsy*. Epilepsia, 2011. **52**(4): p. 841-5.
39. Schaefer, G.B. and J.B. Bodensteiner, *Developmental anomalies of the brain in mental retardation*. International Review of Psychiatry, 1999. **11**(1): p. 47-55.
40. van Schooneveld, M.M., et al., *Hemispherectomy: a basis for mental development in children with epilepsy*. Epileptic Disord, 2011. **13**(1): p. 47-55.
41. Gazzaniga, M.S., *Cerebral specialization and interhemispheric communication: does the corpus callosum enable the human condition?* Brain, 2000. **123** ( Pt 7): p. 1293-326.
42. Schulte, T. and E.M. Muller-Oehring, *Contribution of callosal connections to the interhemispheric integration of visuomotor and cognitive processes*. Neuropsychol Rev, 2010. **20**(2): p. 174-90.
43. Hoffmeyer, H.W., et al., *Nonlinear neurovascular coupling in rat sensory cortex by activation of transcallosal fibers*. J Cereb Blood Flow Metab, 2007. **27**(3): p. 575-87.
44. Kawaguchi, Y., *Receptor subtypes involved in callosally-induced postsynaptic potentials in rat frontal agranular cortex in vitro*. Exp Brain Res, 1992. **88**(1): p. 33-40.
45. Kumar, S.S. and J.R. Huguenard, *Properties of excitatory synaptic connections mediated by the corpus callosum in the developing rat neocortex*. J Neurophysiol, 2001. **86**(6): p. 2973-85.
46. Karayannis, T., I. Huerta-Ocampo, and M. Capogna, *GABAergic and pyramidal neurons of deep cortical layers directly receive and differently integrate callosal input*. Cereb Cortex, 2007. **17**(5): p. 1213-26.
47. Ni, Z., et al., *Two phases of interhemispheric inhibition between motor related cortical areas and the primary motor cortex in human*. Cereb Cortex, 2009. **19**(7): p. 1654-65.
48. Schnitzler, A., K.R. Kessler, and R. Benecke, *Transcallosally mediated inhibition of interneurons within human primary motor cortex*. Exp Brain Res, 1996. **112**(3): p. 381-91.
49. Bocci, T., et al., *Transcallosal inhibition dampens neural responses to high contrast stimuli in human visual cortex*. Neuroscience, 2011. **187**: p. 43-51.
50. Ogawa, S., et al., *An approach to probe some neural systems interaction by functional MRI at neural time scale down to milliseconds*. Proc Natl Acad Sci U S A, 2000. **97**(20): p. 11026-31.
51. Shuler, M.G., D.J. Krupa, and M.A. Nicolelis, *Bilateral integration of whisker information in the primary somatosensory cortex of rats*. J Neurosci, 2001. **21**(14): p. 5251-61.
52. Wiest, M.C., N. Bentley, and M.A. Nicolelis, *Heterogeneous integration of bilateral whisker signals by neurons in primary somatosensory cortex of awake rats*. J Neurophysiol, 2005. **93**(5): p. 2966-73.
53. Berwick, J., et al., *Integration of neural responses originating from different regions of the cortical somatosensory map*. Brain Res, 2004. **1030**(2): p. 284-93.
54. Nemoto, M., et al., *Diversity of neural-hemodynamic relationships associated with differences in cortical processing during bilateral somatosensory activation in rats*. Neuroimage, 2012. **59**(4): p. 3325-38.
55. Iordanova, B., et al., *Optogenetic investigation of the variable neurovascular coupling along the interhemispheric circuits*. J Cereb Blood Flow Metab, 2018. **38**(4): p. 627-640.
56. Petreanu, L., et al., *Channelrhodopsin-2-assisted circuit mapping of long-range callosal projections*. Nat Neurosci, 2007. **10**(5): p. 663-8.
57. Rock, C. and A.J. Apicella, *Callosal projections drive neuronal-specific responses in the mouse auditory cortex*. J Neurosci, 2015. **35**(17): p. 6703-13.
58. Lee, A.T., et al., *Pyramidal neurons in prefrontal cortex receive subtype-specific forms of excitation and inhibition*. Neuron, 2014. **81**(1): p. 61-8.
59. Palmer, L.M., et al., *The cellular basis of GABA(B)-mediated interhemispheric inhibition*. Science, 2012. **335**(6071): p. 989-93.
60. Dombeck, D.A., et al., *Functional imaging of hippocampal place cells at cellular resolution during virtual navigation*. Nat Neurosci, 2010. **13**(11): p. 1433-40.
61. Low, R.J., Y. Gu, and D.W. Tank, *Cellular resolution optical access to brain regions in fissures: imaging medial prefrontal cortex and grid cells in entorhinal cortex*. Proc Natl Acad Sci U S A, 2014. **111**(52): p. 18739-44.
62. Attardo, A., J.E. Fitzgerald, and M.J. Schnitzer, *Impermanence of dendritic spines in live adult CA1 hippocampus*. Nature, 2015. **523**(7562): p. 592-6.
63. Kondo, M., et al., *Two-photon calcium imaging of the medial prefrontal cortex and hippocampus without cortical invasion*. Elife, 2017. **6**.

64. Yu, X., et al., *Deciphering laminar-specific neural inputs with line-scanning fMRI*. Nat Methods, 2014. **11**(1): p. 55-8.
65. Silva, A.C. and A.P. Koretsky, *Laminar specificity of functional MRI onset times during somatosensory stimulation in rat*. Proc Natl Acad Sci U S A, 2002. **99**(23): p. 15182-7.
66. Paxinos, G., Watson, C., Calabrese, E., Badaea, A. & Johnson, G.A., *MRI / DTI atlas of the rat Brain*. (Elsevier, Academic Press, London ; San Diego; 2015).
67. Yu, X., et al., *Thalamocortical inputs show post-critical-period plasticity*. Neuron, 2012. **74**(4): p. 731-42.
68. Ferenczi, E.A., et al., *Prefrontal cortical regulation of brainwide circuit dynamics and reward-related behavior*. Science, 2016. **351**(6268): p. aac9698.
69. Marshall, J.D., et al., *Cell-Type-Specific Optical Recording of Membrane Voltage Dynamics in Freely Moving Mice*. Cell, 2016. **167**(6): p. 1650-1662 e15.
70. Resendez, S.L., et al., *Visualization of cortical, subcortical and deep brain neural circuit dynamics during naturalistic mammalian behavior with head-mounted microscopes and chronically implanted lenses*. Nat Protoc, 2016. **11**(3): p. 566-97.
71. Paxinos, G.W., C., *The rat brain in stereotaxic coordinates, Edn. 6th*. (Academic Press/Elsevier, Amsterdam ; Boston ;; 2007).
72. Miyagi, Y., F. Shima, and T. Sasaki, *Brain shift: an error factor during implantation of deep brain stimulation electrodes*. J Neurosurg, 2007. **107**(5): p. 989-97.
73. Kramer, D.R., et al., *The effect of intraventricular trajectory on brain shift in deep brain stimulation*. Stereotact Funct Neurosurg, 2012. **90**(1): p. 20-4.
74. Pallavaram, S., et al., *Effect of brain shift on the creation of functional atlases for deep brain stimulation surgery*. Int J Comput Assist Radiol Surg, 2010. **5**(3): p. 221-8.
75. Gradinaru, V., et al., *Optical Deconstruction of Parkinsonian Neural Circuitry*. Science, 2009. **324**(5925): p. 354-359.
76. Plaha, P., S. Khan, and S.S. Gill, *Bilateral stimulation of the caudal zona incerta nucleus for tremor control*. Journal of Neurology Neurosurgery and Psychiatry, 2008. **79**(5): p. 504-513.
77. Ondo, W.G., et al., *Subthalamic deep brain stimulation in patients with a previous pallidotomy*. Movement Disorders, 2006. **21**(8): p. 1252-1254.
78. Gambino, F., et al., *Sensory-evoked LTP driven by dendritic plateau potentials in vivo*. Nature, 2014. **515**(7525): p. 116+.
79. Feldmeyer, D., et al., *Barrel cortex function*. Progress in Neurobiology, 2013. **103**: p. 3-27.
80. Groh, A., et al., *Convergence of Cortical and Sensory Driver Inputs on Single Thalamocortical Cells*. Cerebral Cortex, 2014. **24**(12): p. 3167-3179.
81. Mease, R.A., M. Metz, and A. Groh, *Cortical Sensory Responses Are Enhanced by the Higher-Order Thalamus*. Cell Reports, 2016. **14**(2): p. 208-215.
82. Sumser, A., et al., *Organization and somatotopy of corticothalamic projections from L5B in mouse barrel cortex*. Proceedings of the National Academy of Sciences of the United States of America, 2017. **114**(33): p. 8853-8858.
83. Petreanu, L., et al., *The subcellular organization of neocortical excitatory connections*. Nature, 2009. **457**(7233): p. 1142-U100.
84. Scanziani, M. and M. Hausser, *Electrophysiology in the age of light*. Nature, 2009. **461**(7266): p. 930-939.
85. Sych, Y., et al., *High-density multi-fiber photometry for studying large-scale brain circuit dynamics*. Nature Methods, 2019. **16**(6): p. 553+.
86. Lovett-Barron, M., et al., *Dendritic inhibition in the hippocampus supports fear learning*. Science, 2014. **343**(6173): p. 857-63.
87. Sheffield, M.E. and D.A. Dombeck, *Calcium transient prevalence across the dendritic arbour predicts place field properties*. Nature, 2015. **517**(7533): p. 200-4.
88. Danielson, N.B., et al., *Sublayer-Specific Coding Dynamics during Spatial Navigation and Learning in Hippocampal Area CA1*. Neuron, 2016. **91**(3): p. 652-65.
89. Khoshkhoo, S., D. Vogt, and V.S. Sohal, *Dynamic, Cell-Type-Specific Roles for GABAergic Interneurons in a Mouse Model of Optogenetically Inducible Seizures*. Neuron, 2017. **93**(2): p. 291-298.
90. Ayata, C. and M. Lauritzen, *Spreading Depression, Spreading Depolarizations, and the Cerebral Vasculature*. Physiol Rev, 2015. **95**(3): p. 953-93.
91. Fabricius, M., et al., *Association of seizures with cortical spreading depression and peri-infarct depolarisations in the acutely injured human brain*. Clin Neurophysiol, 2008. **119**(9): p. 1973-84.
92. Shatillo, A., et al., *Involvement of NMDA receptor subtypes in cortical spreading depression in rats assessed by fMRI*. Neuropharmacology, 2015. **93**: p. 164-70.
93. Kao, Y.C., et al., *Dynamic perfusion and diffusion MRI of cortical spreading depolarization in photothrombotic ischemia*. Neurobiol Dis, 2014. **71**: p. 131-9.
94. Dreier, J.P., *The role of spreading depression, spreading depolarization and spreading ischemia in neurological disease*. Nat Med, 2011. **17**(4): p. 439-47.

## Statement of contributions

### P1:

**Chen, Y.;** Yu, X.; Yu, S.. (2018) Positioning system for an imaging device. EP3315064.

X.Y. designed and supervised the research. **Y.C.** drawn the first mechanical design of the robotic arm with stepper motors based on the first manual prototype built up by Mr. S. Yu. Fine Mechanic and Electronic Workshop at MPI for Biological Cybernetics for robotic arm automation. **Y.C.** tested the stepper motors-driven positioning system, analyzed data and drafted description of the system for patent application.

### M1:

**Chen, Y.,** Pais-Roldán, P., Chen, X., Frosz, M., Yu, X.. MRI-guided robotic arm drives optogenetic fMRI with concurrent Ca<sup>2+</sup> recording. Nature Communications 10, 2536 (2019).

X.Y. designed and supervised the research. **Y.C.,** X.Y., P.P.-R., and X.C. performed animal experiments. **Y.C.,** X.Y., and P.P.-R. acquired data. **Y.C.** analyzed data. X.C. and M.H.F. provided key technical support. X.Y. and **Y.C.** wrote the manuscript.

### M2:

**Chen, Y.,** Sobczak, F., Pais-Roldán P., Schwarz C., Koretsky P. A., Yu X.. Mapping the brain-wide network effects by optogenetic activation of the corpus callosum. Submitted.

X.Y. designed and supervised the research, **Y.C.** and X.Y. performed animal experiments, **Y.C.** acquired data, **Y.C.** analyzed data, A.K., C.S., F.S. and P.P-R. provided conceptual and technical support, X.Y., **Y.C.,** A.K. and C.S. wrote the manuscript.

### M3:

Chen X, Sobczak F., **Chen Y.,** Jiang Y., Qian C., Lu Z., Ayata C., Logothetis N., Yu X.. Mapping optogenetically-driven single-vessel fMRI with concurrent neuronal calcium recordings in the rat hippocampus. Nature Communications 10, 5239 (2019).

X.Y., N.K. and X.C. designed the research; X.C. and X.Y. performed animal experiments; X.C., Y.J. and F.S. performed data analysis; **Y. C.,** C.Q., C.A. and Z.L. provided technical support; X.Y., N.K., C.A. and X.C. wrote the paper.

## **Appended patent/manuscripts**

# HANNKE BITTNER & PARTNER

PATENTANWÄLTE RECHTSANWÄLTE

Prüfeninger Straße 1

93049 Regensburg

Max-Planck-Gesellschaft  
zur Förderung der Wissenschaften e.V.  
Hofgartenstr. 8  
80539 München

October 27, 2016  
GAI01-042-EPPT  
HA/vo

---

## Positioning system for an imaging device

---

### Description

The invention relates to a positioning system for an imaging device, in particular a MR imaging device, to position an insertion element on or in the body of a subject, in particular an animal, wherein the imaging device comprises a bore, in which the subject is received, wherein the positioning system comprises a robot, which can be at least partially arranged in  
5 the bore of the imaging device and comprises a holding element to hold the insertion element.

Brain intervention techniques are primarily used to treat patients with severe brain diseases, e.g. epilepsy, Parkinson disease, clinical depression or brain tumors. Deep brain stimulation  
10 is a key model to show how brain intervention could be directly used as a therapeutic strategy to treat patients. How to precisely target the specific functional nuclei of the diseased human brain and reduce the collateral tissue damage is a key challenge of the brain interventional clinical practice. The human brain MRI is usually used to help localize the target, as well as monitor the surgical procedure.

15 Magnetic resonance imaging (MRI), or Nuclear magnetic resonance imaging (NMRI), is an imaging technique to visualize the structure and function of tissue. This imaging technique provides detailed images of the tissue in any plane and a greater contrast between the different soft tissues compared to computer tomography (CT). Thus, it is especially favorable in  
20 neurological (brain), musculoskeletal, cardiovascular, and oncological (cancer) imaging. MRI utilizes a powerful magnetic field to align the nuclear magnetization of hydrogen atoms in the tissue. This alignment is then systematically altered by radiofrequency fields (RF). The hy-

drogen nuclei produce a rotating magnetic field detectable by the scanner. Such a signal can be manipulated by additional magnetic fields to build up information to construct an image of the body. By now Functional Magnetic Resonance Imaging (fMRI) has come to dominate the field of brain mapping. fMRI directly detects the hemodynamic signal from vessels, such as the blood-oxygen-level dependent (BOLD) contrast. Hereby the neural activity in the brain is mapped by imaging the change in blood flow/volume (hemodynamic response) related to energy consumption by brain cells.

The use of the high magnetic fields in the MRI-system makes the design of MRI-compatible robots difficult, since most of the components commonly used in robotics are unsuitable in close proximity of the MRI-device. In such a range ferromagnetic materials are exposed to very high magnetic interaction. Thus, strong forces may act on individual parts. Further, heating may occur in conductive materials by electromagnetic induction. Additionally, the use of electricity may cause interference-effects in the RF coils of the imager which can create image artifacts.

There are a few existing MRI-compatible or based devices that help better perform the procedure. However, the MRI-guided strategy is usually used as an assisting or verification procedure. The main surgical procedure remains to be done by neurosurgeons. There is long way to evolve from manual procedure to full automation. Besides technical limits, the safety and human brain complexity are the main limiting factors.

In contrast to the human brain/body intervention, there is less safety concern for animal brain surgeries. Moreover, animal brain studies are aimed to better understand the complexity of the brain. Recently, genetically encoded proteins make it possible to mediate and monitor the brain function from the molecular level to networks with cell specificity under multi-modal neuroimaging platform. Specific brain cells can be activated and the activity signal can be monitored inside the MRI-scanner with fiber optic-mediated signal detection strategies. However, it remains challenging to precisely target the brain cells in specific brain nuclei of animal brains (only a few hundred micron size). The common way is to use the animal brain atlas (e.g. Paxinos rat brain atlas) to find the 3D coordinates based on a control point (zero point), which is defined by the bregma (the anatomical point on the skull at which the coronal suture is intersected perpendicularly by the sagittal suture). The physical position of the bregma point on the skull varies largely across animals with over a few hundred micron, which contributes to the key variation for most of the animal brain nuclei surgical procedures.

The above mentioned animal brain studies are conducted on small animals like rodents e.g. rats. Typical MR scanners used for human subjects (with bore size >60cm) are however unsuitable for imaging small animal models, since it has been found to be difficult to achieve a reasonable spatial resolution at an acceptable signal-to-noise ratio with such scanners. Thus, special "small-bore" animal high magnetic field MRI-scanners are typically used.

So far, no MRI-compatible, automatic robotic control, real-time guiding system exists, which further may be applied in special "small-bore" animal-MRI-scanners. However, there are clearly scientific needs for such a device. Especially during the new era of Human Brain Project and BRAIN INITIATIVE from the European Union and the USA, there will be tremendous opportunities to carry on animal experiments under the precise brain targeting scheme to study brain function from molecules to networks.

Object of the invention is therefore to provide a positioning system for an imaging device that overcomes the above-mentioned disadvantages.

The problem is addressed by a positioning system for an imaging device, in particular a MR imaging device to position an insertion element on or in the body of a subject, in particular an animal, wherein the imaging device comprises a bore, in which the subject is received, wherein the positioning system comprises a robot, which can be at least partially arranged in the bore of the imaging device and comprises a holding element to hold the insertion element; wherein the robot further comprises at least one actuator acting on the holding element such that an end portion of the insertion element is movable, wherein said at least one actuator is arranged with a distance  $D$  from the bore to minimize magnetic and/or electromagnetic interferences between the imaging device and the at least one actuator and said first actuator is coupled to the holding element in a form-fit- and/or a force-fit-manner.

Due to the arrangement of the at least one actuator at a distance  $D$  from the imaging device or the bore respectively magnetic and/or electromagnetic interferences are minimized. Such interferences or influences may be the magnetic field or the stray magnetic field of an MRI-device influencing the at least one actuator. Such an influence may be a force on ferromagnetic components of the actuator. Typically, the magnetic fields used in such imaging devices are in the range of several Tesla. Magnetic fields of such a strength impede the functionality or would even destroy conventional actuators. Further, due to the acting forces in the magnetic field the ferromagnetic parts may be accelerated towards the imaging device, which leads to a potential risk of injuries for the subject and or personal operating the device. Fur-



ther, such interferences could also be influences on the imaging device, in particular the RF coils of the imager. Electromagnetic interferences originating from the actuators could for example create image artifacts. Due to the positioning of the actuators at a distance  $D$ , it is possible to use conventional actuators. There is no need for costly special (MRI-) compatible actuators. Due to the form-fit- and/or a force-fit-coupling between the holding element and the actuator, a straightforward and inexpensive solution for the transmission of the force between actuator and holding element is presented. The subjects are preferably small animals like rodents, e.g. rats. However it is also possible to apply the positioning system on other animals like monkeys or even on humans.

Advantageously the imaging device is a fMRI-device comprising an MRI-scanner, using a magnetic field preferably in the range of 3 T to 21 T, more preferably in the range of 7 T to 14 T, and a bore diameter of preferably in the range of 50 cm to 6 cm, more preferably 12cm. Preferably the insertion element can be a fiber-optic for optogenetic stimulation and fluorescent recording from endogenous/exogenous biosensors of metabolites of the subject brain, an electrode for recording electrophysiological or electrochemical signal, and an implantable pump/needle for direct drug delivery to treat tumor or other diseases.

Obviously the distance  $D$  depends on the magnetic field the imaging device uses. In the case of small animals, typically a magnetic field in the range of 7 T to 14 T is preferred. For a magnetic field of 14 T (without active shielding) the distance  $D$  is 4.7 meters. For conventional MRI-scanners, e.g. 9.4 T or 11.7 T, the distance  $D$  is shortened to less than 1.5 meters since the active shielding. Generally, the distance  $D$  is measured from the center of the bore.

Preferably the at least one actuator is a step motor such as a brushless DC electric motor. A full rotation of such an electric motor is divided into a number of equal steps, wherein the motor-position may be controlled and held. Such stepper motors may be permanent magnet step-, hybrid synchronous step- or variable reluctance step-motors. However, the use of any other type of actuator is equally conceivable. In particular the use of a piezo driven motor may be conceivable. By the use of a piezo-motor the distance  $D$  may be further decreased, since a piezo-motor is less susceptible to magnetic interferences.

Advantageously the bore has a longitudinal expansion along an X-axis and further expands along a Z-axis and a Y-axis, wherein said X-axis, Y-axis and Z-axis are orthogonal to each other. Preferably at least the end portion of the insertion element has a longitudinal extension

along an A-axis, wherein the axis A and the Z-axis form an angle  $\alpha$ , which is in the range between  $0^\circ$  and  $\pm 90^\circ$ , preferably in the range between  $0^\circ$  and  $\pm 45^\circ$ .

5 According to a preferred embodiment the robot comprises a head part, a first and a second drive mechanism. Preferably a first actuator acts on the holding element via the first drive mechanism such that the end portion of the insertion element is linearly movable along the A-axis. It is further preferred that a second actuator acts on the holding element via the second drive mechanism such that the end portion of the insertion element can be pivoted about a pivot axis B, wherein by said pivoting-motion the angle  $\alpha$ , is adjusted. By said linear motion  
10 the end portion of the insertion element, for example the tip of a fiber, may therefore be inserted into the brain tissue through a hole in the skull of the subject. The pivoting-motion offers a convenient tool to insert the insertion element at a specific angle, whereby a specific adjustment to the target element is possible. Further a particular trajectory of the insertion path is executable.

15

According to a preferred embodiment, the first drive mechanism comprises a first pulley, which is connected to the first actuator by a first belt. Preferably the first drive mechanism further comprises a shaft, which is received in a central hub portion of the first pulley and connects the first pulley and a converting element, on which the holding element is mounted.  
20 Preferably the converting element converts a rotational motion of the first pulley into a linear motion of the holding element along the A-axis. Preferably the holding element, the first pulley, the shaft and the converting element are components of the head part.

Thus, according to this preferred embodiment the coupling of the first actuator to the holding  
25 element in a form-fit- and/or a force-fit-manner is achieved by a belt drive. Advantageously the first belt is looped over the first pulley and a pulley connected to the first actuator. Hereby, different embodiments known in the state of the art are conceivable for example a normal belt drive or a crossed belt. Conceivable belts are flat belts, V-belts, multi groove belts or the like. Further, the first belt may be connected to the first pulley in a force-fit-manner. Preferably the connection between the first belt and the first pulley is in a form-fit-manner. Such belts  
30 are called trimming-, toothed-, notch-, cog-, synchronous- or positive-transfer-belts. These belts have teeth that fit into a matching toothed pulley. When correctly tensioned, they have no slippage, and run at constant speed. By using the first drive mechanism according to this embodiment, a high precision and accuracy can be achieved at very low costs. The step size  
35 of the first actuator can be transferred to the converting element through the belt in an effi-

cient manner. Further the drive mechanism can be easily adjusted to the space available in the scanner room, by altering the belt length.

5 According to a further embodiment, the converting element comprises a disc-like element with a first surface on which a first guiding element is arranged. Preferably the holding element comprises at least one, preferably at least three second guiding element(s), which engage(s) the first guiding element.

10 Advantageously the first guiding element has a continuous course, which originates in, or in the proximity of a center of the disc-like element, wherein the continuous course evolves in form of a spiral to an edge of the disc-like element. Preferably the spiral is described by a polar equation of  $r = a \cdot \theta$ , wherein  $r$  is the radial distance,  $\theta$  is the polar angle and  $a$  is a constant  $>0$ . Such a spiral is called an Archimedean spiral. The Archimedean spiral has the property that any ray from the origin intersects successive turnings of the spiral in points with  
15 a constant separation distance (equal to  $2\pi a$  if  $\theta$  is measured in radians).

The first and the second guiding element are preferably designed as a projection. Thus, the first guiding element could be continuous projection on the first surface of the disc-like element. The second guiding element(s) could be (a) projection(s) or (a) pin(s), which engage(s)  
20 and (is) are guided by the first guiding element in form of a spiral. The projection could be formed on the holding element. It is also conceivable that the second guiding element(s) is (are) (a) pin(s) which (is) are arranged in (a) bore(s) of the holding element. The projection fits preferably in the space between two points of the projecting spiral without play. Hereby an accurate guiding is ensured. It is also conceivable that the first guiding element is a slit, a  
25 groove or the like, arranged on the first surface of the disc-like element. The second guiding element in form of a projection may then engage in such a structure preferably without play.

A rotation of the disc-like element and the Archimedean spiral respectively drives the holding element due to the engagement of the second guiding element(s) along the A-axis. Due to  
30 different parameters, e.g. said separation distance, of the Archimedean spiral and precision of the step motors, different precision can be achieved. Preferably one round of the actuator (step-motor) causes one rotation round of the Archimedean spiral. In a preferred embodiment one round of the Archimedean spiral displaces the holding element by 2mm and the smallest step-size of the holding element along the A-axis is 10  $\mu\text{m}$ . Thus, it is possible to  
35 accurately and precisely target the deep brain nuclei with a simple and inexpensive mechanism.

According to a further preferred embodiment the second drive mechanism comprises a second pulley, which is connected to the second actuator by a second belt. The second drive mechanism preferably comprises further a cup-like element, which is rigidly connected to the second pulley. Advantageously the cup-like element comprises a receiving element, which extends along the A-axis and receives the holding element. Preferably the cup-like element engages the holding element such that a rotational motion of the cup-like element causes a pivoting-motion of the holding element around the B-axis. Preferably the second pulley and the cup-like element are a component of the head part of the robot.

10 It is further advantageous that the receiving element allows the motion of the holding element along the A-axis. The receiving element is preferably designed as a slit or a groove in which the holding element is received and guided. It is also conceivable that the receiving element is designed as a projection on the cup-like element which extends along the A-axis. Accordingly the holding element would comprise a structure like a groove in which the projection  
15 engages. Thus, according to this preferred embodiment the coupling of the second actuator to the holding element in a form-fit- and/or a force-fit-manner is achieved by a belt drive. Advantageously the second belt is looped over the second pulley and a pulley connected to the second actuator. Hereby, different embodiments known in the art are conceivable, for example a normal belt drive or a crossed belt. Conceivable belts are flat belts. V-belts, multi  
20 groove belts or the like. Further, the second belt may be connected to the first pulley in a force-fit-manner. Preferably the connection between the second belt and the second pulley is in a form-fit-manner. Such belts are called trimming-, toothed-, notch-, cog-, synchronous- or positive-transfer-belts. These belts have teeth that fit into a matching toothed pulley. When correctly tensioned, they have no slippage, and run at constant speed. By using the second  
25 drive mechanism according to this embodiment, a high precision and accuracy can be achieved at very low costs. The step size of the second actuator can be transferred to the converting element through the belt in an efficient manner. Further, the drive mechanism can be easily adjusted to the space available in the scanner room by altering the belt length.

30 Preferably the shaft projects through the center of the second pulley. However, there is no connection between the shaft and the second pulley, which would transmit rotational motion between the second pulley and the shaft or vice versa. The minimal friction forces between the shaft and the second pulley are negligible. Thus, the rotational motions of the first pulley and the second pulley are effectively decoupled from each other. It is further favorable that  
35 the pivoting-motion of second pulley and the cup like element is blocked by the second actuator when the first actuator drives the holding element via the first drive mechanism. In this

way the angle  $\alpha$  is unchanged and the motion of the holding element is guided by the receiving element.

5 By using belt drives in the first and second drive mechanisms, not only the problem of the undesired interferences is addressed, also the physical limitation of in-bore access and the limited workspace in the bore (12cm for small animal MRI's) can be advantageously addressed, since the head part of the robot can be designed relatively small.

10 In a further preferred embodiment, the head part of the robot is connected to a holding rod via a connection element. Preferably the robot further comprises a third actuator which acts on the holding rod via a third drive mechanism, such that the head part of the robot can be moved along the Y-axis. It is further preferred that the robot comprises a fourth actuator, which acts on the holding rod via a fourth drive mechanism, such that the head part of the robot can be moved along the X-axis. The displacement of the head part of the robot along  
15 the X- and Y-axis allows a positioning of the insertion element over the inserting point, e.g. a hole in the skull of the subject.

According to a preferred embodiment the third drive mechanism comprises a third pulley, which is connected to the third actuator by a third belt. Preferably the third pulley is rigidly  
20 connected to a threaded spindle on which a nut is arranged. Advantageously, the nut is connected to the holding rod of the robot. It is preferred that the threaded spindle is arranged perpendicularly to the holding rod. Preferably a rotation of the third pulley causes a rotation of the threaded spindle and a movement of the nut and the holding rod along the Y-axis. It is further conceivable that the third drive mechanism comprises further threaded spindles with  
25 accompanied nuts. These spindles may advantageously be arranged along the length of the holding rod at equal distances. Each spindle is driven by a belt which is connected to a pulley arranged on a spindle closer to the third actuator. In this way a chain-like drive is obtained.

Thus, according to this preferred embodiment the coupling of the third actuator to the holding  
30 element, a form-fit- and/or a force-fit-manner is achieved by a belt drive. Advantageously the third belt is looped over the third pulley and a pulley connected to the third actuator. Hereby, different embodiments known in the art are conceivable for example a normal belt drive or a crossed belt. Conceivable belts are flat belts, V-belts, multi groove belts or the like. Further, the third belt may be connected to the third pulley in a force-fit-manner. Preferably the con-  
35 nection between the third belt and the third pulley is in a form-fit-manner. Such belts are called trimming-, toothed-, notch-, cog-, synchronous- or positive-transfer-belts. These belts

have teeth that fit into a matching toothed pulley. When correctly tensioned, they have no slippage, and run at constant speed. By using the third drive mechanism according to this embodiment, a high precision and accuracy can be achieved at very low costs. The step size of the third actuator can be transferred to the converting element through the belt in an efficient manner. Further, the drive mechanism can be easily adjusted to the space available in the scanner room by altering the belt length.

According to a preferred embodiment, the third drive mechanism acts additionally on a first translation stage. Advantageously, the first actuator, the pulley connected to the first actuator, the second actuator, the pulley connected to the second actuator and the holding are mounted on the first translation stage. Preferably said translation along the Y-axis, driven by the third pulley and the third belt, of the one or more nuts, connected to the holding rod, is accompanied by a translation of the first translation stage along the Y-axis. It is preferred that the translation distance of the first translation stage and the one or more nuts, connected to the holding rod are the same, to ensure an accurate displacement without bending the holding rod or causing tension in the holding rod. The third drive mechanism advantageously further comprises a gear, a threaded spindle or the like, which is driven by the third actuator, and is also arranged at a distance  $D$  from the bore.

According to a further preferred embodiment, the fourth drive mechanism acts on a second translation stage. Advantageously, on second translation stage the first translation stage and the third actuator are arranged. Preferably, a translation of the second translation stage along the X-axis results in a translation of the first translation stage, its elements mounted on it and the third actuator as a whole along the X-axis. The fourth drive mechanism advantageously further comprises a gear, a threaded spindle or the like, which is driven by the fourth actuator and which is also arranged at a distance  $D$  from the bore.

In addition, it is advantageous that the positioning system comprises a platform, on which the robot (5) is arranged. Preferably the subject is suspended and/or held at a head part of the platform, which can be arranged in the bore of the imaging device. Preferably the first, second, third and fourth actuators are arranged at the foot part of the platform (40). Preferably the threaded spindle(s) is (are) arranged on (a) holder(s) connected to the platform.

Advantageously, the robot and the platform mainly consist of MRI-compatible materials. Preferably such materials are nonmagnetic, dielectric materials, plastics, rubbers, or ceramics. It is also preferable that the components of the robot may consist of minimal amounts of

brass or anodized aluminum to avoid deterioration of magnetic field homogeneity. The holding rod preferably is constructed from carbon fiber. The advantage of the carbon fiber is its very light weight, which allows the use of conventional step motors with relative small set sizes. Although the conductivity of carbon fiber could get a certain eddy current during the MR imaging because of the MR gradient shift, it is negligible for the animal fMRI studies. For human safety issue, however, it may be better to replace all carbon fiber material to fiber-glass-based material.

According to a preferred embodiment the positioning system comprises at least one, preferably at least two MRI-compatible camera(s), which is (are) mounted on the head part of the platform.

Preferably the positioning system further comprises a navigation unit, which advantageously comprises a control unit. Preferably the control unit controls the motion of the first, second, third and fourth actuator. It is advantageous that the navigation unit further comprises an image processing unit which processes real time images of the imaging device and/or the at least one camera in the bore.

The object is also addressed by a method to position an insertion element using a positioning system according to any one of the preceding embodiments in a MR imaging device:

- a. Lowering the insertion element by the robot to a first position on the subject or close to the subject;
- b. Acquiring a 3D-MRI image and process the image via the image processing unit to identify the location of subject, as well as the position of insertion element;
- c. Calculation of the coordinates of the target point and the insertion element and calculation of an optimized movement trajectory for the insertion element by the control unit;
- d. Monitoring movement trajectory by real-time MRI image via the image processing unit.

Advantageously, the navigation unit allows an operator to visualize the (MRI-) image from the imaging device. A target and an entry point for the insertion element is defined by a brain atlas and a 3D MRI-image by a control algorithm of the control unit. Preferably, two cameras are positioned to obtain visual guidance of the insertion, e.g. a brain intervention. Preferably camera-based visual signals are presented by the navigation unit. Thus, the operator can

monitor the real time situation inside the scanner. Alternatively the operator could also manually adjust the target and an entry point.

The method may be particularly adjusted to automatically control a fiber/electrode (insertion element) insertion into the brain of a small animal. Preferably the following steps may be performed before step a)

- Applying a craniotomy on the animal skull;
- Fixing the animal on the head part of the platform with RF coil attached on the animal head;
- 10 - Covering the skull with a circular transparent agarose gel with 1 cm diameter and 2mm thickness;
- Positioning the head part of the robot above the animal skull;
- Setting at least two MRI-compatible cameras ( $\geq 2$ ) to directly visualize the craniotomy and fiber/electrode tip;
- 15 - Placing the head part of the platform and the head part of the robot in the bore of the MRI-scanner.

Step a) is adjusted such that the fiber/electrode is lowered for 1 mm to insert into the agarose gel.

20

Step b) is adjusted such that a 3D MRI image is acquired to identify the location of animal brain, as well as the position of the fiber/electrode tip in the agarose gel.

Step c) is adjusted such that the coordinates of the interested brain nuclei and the fiber/electrode tip will be calculated from the 3D MRI images and that the optimized movement trajectory of the fiber/electrode is calculated.

25

Step c) is adjusted such that the real-time MRI image can monitor the location of the fiber after the insertion into the animal brain.

30

Further, the MRI-compatible cameras can be used to directly visualize the movement of the fiber/electrode tips outside the animal brain.

Thus, an advantageous multiple degree-of-freedom robotic controlling system to target brain nuclei or specific brain cells in the brain inside the high field (14.1 T) MRI-scanner is provided. A MRI-compatible positioning system provides feasible targeting accuracy, high temporal

35



and spatial resolution by using MRI images as feedback to guide the brain intervention. Meanwhile, a MRI-compatible camera-monitored insertion trajectory is optimized in order to investigate the effectiveness, safety and feasibility of deep brain nuclei targeting for translational application. The positioning system provides:

- 5       - A fully motor-based automatic system using the MRI images to guide the brain intervention;
- A special design for animal brain surgeries, which is also possible to be expanded to the whole animal body in vivo targeting inside the MRI-scanner;
- Compatibility with the 14 T high magnetic field of the MRI-scanners, which could also  
10       be even pushed to 17 T;
- Accommodation of the space limit of the high field MRI-scanners, The positioning system is even applicable to 8 cm bores;
- Providing a fully implementable system with build-in camera and RF surface coil to allow direct measurement of MRI images and position of electrode/fiber optic/injection  
15       needle tips;
- Providing a 50-100 micron resolution to target the region of interests;
- Providing an individual animal specificity with more precise targeting strategy than only based on the atlas.

20   The multimodal neuroimaging methodologies on animal models are crucial for better understanding brain function. The neuron-glia-vessel (NGV) network is one of the most challenging areas given the multifaceted requirements of signal acquisition from the brain. The combination of fMRI with optogenetic stimulation of genetically defined cells in animal models has enabled scientists to study the causality between the activation of specific neuronal populations and the hemodynamic signal, such as the blood-oxygen-level-dependent (BOLD) fMRI  
25   signal. Simultaneous BOLD fMRI and fiber-optic recording of fluorescent calcium signal can help clarify the cellular contributions to neurovascular coupling in different brain regions of healthy and diseased animal models. The hereby solved key challenge of the fiber optic-mediated multimodal fMRI methodologies is how to locate the fiber tip accurately and to precisely target the deep brain nuclei, mostly the requirement of precision is only several hundreds of microns.  
30

Further advantages, aims and properties of the present invention will be described by way of the appended drawings and the following description.

In the drawings:

- Fig. 1 shows the platform with the robot arranged in the imaging device according to one embodiment;
- 5 Fig. 2 shows the head part of the robot according to one embodiment;
- Fig. 2a shows the head part of the robot and its components according to one embodiment in an exploded view;
- 10 Fig. 3 shows the converting element and the holding element according to one embodiment;
- Fig. 3a shows schematically the principle of the converting element;
- 15 Fig. 4 shows the robot according to one embodiment mounted on the platform;
- Fig. 5 shows the robot according to one embodiment;
- Fig. 6 shows the robot according to one embodiment;
- 20 Fig. 7 shows the head part of the platform according to one embodiment;
- Fig. 8 shows the principle function of the positioning system according to one embodiment and an MRI-system;
- 25 Fig. 9 shows an image of a fiber position above a hole in a rat skull;
- Figs. 10 show a fiber placement of perfused rat brain in vitro;
- 30 Figs. 11 show a fiber placement of perfused rat brain in vitro with different moving distances;
- Figs. 12 show time-lapsed images of fiber optic targeting in the rat brain in vivo.
- 35 Without limiting the generality, in the following embodiments a MRI-(Magnetic resonance imaging) device is assumed as imaging device. Such an imaging device (2) is a fMRI-device

comprising an MRI-scanner, using a magnetic field preferably in the range of ca. 3 T to ca. 21 T more preferably in the range of ca. 7 T to ca. 14 T, and a bore diameter of preferably in the range of 50 cm to 6 cm, more preferably 12 cm, wherein the insertion element can be a fiber-optic for optogenetic stimulation and fluorescent recording from endogenous/exogenous biosensors of metabolites of the subject brain, an electrode for recording electrophysiological or electrochemical signal, and an implantable pump/needle for direct drug delivery to treat tumor or other diseases.

Figures 1 to 8 display a positioning system (1) for an imaging device (2), in particular a MR imaging device, to position an insertion element (3) on or in the body of a subject, in particular an animal, wherein the imaging device (2) comprises a bore (4), in which the subject is received, wherein the positioning system (1) comprises a robot (5), which can be at least partially arranged in the bore (4) of the imaging device (2) and comprises a holding element (7) to hold the insertion element (3); wherein the robot (5) further comprises at least one actuator (8, 9, 10, 11), acting on the holding element such that an end portion (3a) of the insertion element (3) is movable, wherein said at least one actuator (8, 9, 10, 11) is arranged with a distance D from the bore to minimize magnetic and/or electromagnetic interferences between the imaging device (2) and the at least one actuator (8, 9, 10, 11) and said first actuator (8, 9, 10, 11) is coupled to the holding element (3) in a form-fit- and/or a force-fit-manner.

Fig. 1 shows a MRI-scanner, typically located in a scanner room, and a platform (40), on which the robot (5) is arranged. The bore (4) of the imaging device (2) has a longitudinal expansion along an X-axis and further expands along a Z-axis and a Y-axis, wherein said X-axis, Y-axis and Z-axis are orthogonal to each other. The platform (40) has a longitudinal expansion along the X-axis of at least the distance D and a width which expands along the Y-axis. Further, the platform is mounted on a support device (48) which is equipped with several wheels and is partially arranged in the bore (4) of the imaging device (2).

The robot (5) further comprises a first (12) and a second drive mechanism (13) and a first (8) and a second actuator (9). These components are depicted in figures 2 to 6. The first actuator (8) acts on the holding element (7) via the first drive mechanism (12) such that the end portion (3a) of the insertion element (3) is linearly movable along the A-axis. The second actuator (9) acts on the holding element (7) via the second drive mechanism (13) such that the end portion (3a) of the insertion element (3) can be pivoted about a pivot axis B, wherein by said pivoting-motion the angle  $\alpha$ , is adjusted. The first (8) and the second actuator (9) are mounted at a foot part (42) of the platform (40) wherein the foot part (42) is arranged with a

distance D from the bore (4) to minimize magnetic and/or electromagnetic interferences between the imaging device (2) and the actuators (8, 9).

5 The holding element (7) comprises a body (7a) of an essentially rectangular shape which extends along the A-axis. The bores for the second guiding elements (24) in form of pins are arranged in row, placed in the center of the rectangular body (24a). On the body (7a) a gripping portion (7b) is arranged, by which the insertion element (3) is fastened. Further, the body (24a) comprises two lateral grooves (54a, 54b).

10 The figures 2 and 2a display a head part (6) of the robot (5), wherein the individual components of the head part (6) are shown in fig. 2a in an exploded view. The components of the head part (6) are the holding element (7), a first pulley (14), a second pulley (26), a shaft (16) which is rigidly connected to a converting element (18), a cup-like element (28), a connection element (33), which connects the head part (6) to a holding rod (32), and a fixing element (49).  
15

The first drive mechanism (12) comprises the first pulley (14), which is connected to the first actuator (8) by a first belt (15), the shaft (16), which is received in a central hub portion (17) of the first pulley (14) and connects the first pulley (14), and the converting element (18), on  
20 which the holding element (7) is mounted. The converting element (18) converts a rotational motion (19) of the first pulley (14) into a linear motion (20) of the holding element (7) along the A-axis. Thus, the coupling of the first actuator (8) to the holding element (7) in a form-fit-and/or a force-fit-manner is achieved by such a belt drive. The first belt (15) is looped over the first pulley (14) and a pulley (50) connected to the first actuator (8). Fig. 5 displays this  
25 connection between the first pulley (14) and the pulley (50) connected to the first actuator (8) by the first belt (15). The first belt (15) is a toothed belt having teeth (15a) that fit into matching teeth (14a) of the first pulley (14) and teeth of the pulley (50) connected to the first actuator (8). By such a design, slippage of the belt is avoided.

The shaft (16) is rigidly connected to the central hub portion (17) of the first pulley (14) and  
30 the converting element (18). The rotational motion of the first pulley (14) is therefore transmitted by the shaft (16) to the converting element (18).

The converting element (18) comprises a disc-like element (21) with a first surface (22) on which a first guiding element (23) is arranged. The disc-like element has a circular form with  
35 a center (21a) and an edge (21b). The shaft is rigidly connected to a second surface (51) opposite to the first surface (22).

The first guiding element (23) has a continuous course, which originates in, or in the proximity of the center (21a) of the disc-like element (21), wherein the continuous course evolves in form of a spiral (25) to the edge (21b) of the disc-like element (21). The spiral (25) is described by a polar equation of  $r = a \cdot \theta$ , wherein  $r$  is the radial distance,  $\theta$  is the polar angle and  $a$  is a constant  $>0$ . Such a spiral (25) is called an Archimedean spiral. The Archimedean spiral has the property that any ray from the center (21a) intersects successive turnings of the spiral (25) in points with a constant separation distance (equal to  $2\pi \cdot a$ ,  $\theta$  is measured in radians). The first guiding element (23) in the form of a spiral (25) is designed as a projection projecting from the first surface (22).

10

The holding element (7) comprises a plurality of second guiding elements (24), which engage the first guiding element (23). The second guiding elements (24) are in form of a projection or a pin which is either formed directly on the holding element (7) or rigidly arranged in bores of the holding element (7). The second guiding elements (24) in form of pins fit in the space (25a) between two opposing points of the projecting spiral (25), preferably without play. Fig. 3a displays the principle of the drive using an Archimedean spiral. The spiral (25) and the holding element (7) with three exemplary second guiding elements (24): second guiding element one (24a), second guiding element two (24b) and second guiding element three (24c) are shown in this fig. 3a. The distance between second guiding element one (24a) and second guiding element two (24b) is the same as the distance between second guiding element two (24b) and second guiding element three (24c). A rotation of the Archimedean spiral (25) will drive the holding element (7) up or down along the direction of arrow (53).

15

20

25

In this embodiment one round of the Archimedean spiral (25) displaces the holding element (7) by 2 mm and the smallest step-size of the holding element (7) along the A-axis is  $10 \mu\text{m}$ . Thus, it is possible to accurately and precisely target the deep brain nuclei with a simple and inexpensive mechanism.

30

The holding element (7) is further secured by the cup-like element (28). The cup-like element (28) is rigidly connected to the second pulley (26), encloses the disc-like element (21) and comprises a receiving element (29), which extends along the A-axis and receives the holding element (7). The disc-like element (21) is received in the inner space (28a) of the cup-like element (28) such that it may rotate freely. The holding element (7) is received in the receiving element (29) such that only the linear motion (20) along the A-axis is allowed. In this way a rotation of the holding element due to a force transmission, for example due to the friction between the disc-like element (21) and the holding element, is prevented.

35

The receiving element (29) is designed as a slit in the frontal part (28b) of the cup-like element (28). The slit comprises two opposing guiding projections (52a, 52b) on its edges, which project radially inwards and extend along the A-axis. Each of the guiding projections (52a, 52b) engages in a groove (54a, 54b) of the holding element (7), which also extends  
5 along the A-axis.

The second drive mechanism (13) comprises a second pulley (26), which is connected to the second actuator (9) by a second belt (27), and a cup-like element (28), which is rigidly connected to the second pulley (26). The cup-like element (28) comprises the receiving ele-  
10 ment (29), which extends along the A-axis and receives the holding element (7). The cup-like element (28) engages the holding element (7) such that a rotational motion (30) of the cup-like element (28) causes a pivoting-motion (31) of the holding element (7) around the B-axis. In particular the rotational motion of the second pulley (26) is transferred to the holding element (7) via the engagement of the guiding projections (52a, 52b) in the lateral grooves (54a,  
15 54b) of the holding element (7). Thus, the coupling of the second actuator (9) to the holding element (7) in a form-fit- and/or a force-fit-manner is achieved by such a belt drive. The second belt (27) is looped over the second pulley (26) and a pulley (55) connected to the second actuator (9). Fig. 5 displays this connection between the second pulley (26) and the pulley (55) connected to the second actuator (9) by the second belt (27). The second belt (27) is a  
20 toothed belt having teeth (27a) that fit into matching teeth (26a) of the second pulley (26) and teeth of the pulley (55) connected to the second actuator (9). By such a design, slippage of the belt is avoided.

Once the angle  $\alpha$  is adjusted by the pivoting-motion (31) of the holding element (7) around  
25 the B-axis, the actuator blocks any further motion. In this way an effective guidance of the linear motion (20) of the holding element (7) along the adjusted A-axis by the engagement of the guiding projections (52a, 52b) in the lateral grooves (54a, 54b) is ensured.

The shaft (16) projects through the center of the second pulley (26). However, there is no connection between the shaft (16) and the second pulley (26), which would transmit rotation-  
30 al motion between the second pulley (26) and the shaft (16) or vice versa. The minimal friction forces between the shaft (16) and the second pulley (26) are negligible (which is highly dependent on the material used, e.g. fiber glass or titanium with high rigidity is preferred). Thus, the rotational motions of the first pulley (14) and the second pulley (26) are effectively decoupled from each other. Additionally the shaft is fixed by a fixing element (49).

35

Between the first (14) and the second pulley (26) the connection element (33), which connects the head part (6) of the robot (5) to the holding rod (32), is arranged. The connection element (33) comprises a loop portion (33a) and an insertion portion (33b). The shaft (16) projects through the loop portion (33a). However, there is no connection between the shaft (16) and the loop portion (33a), which would transmit rotational motion between the second pulley (26) and the shaft (16) or vice versa. The minimal friction forces between the shaft (16) and the loop portion (33a) are negligible. The arrangement of the loop portion (33a) of the connection element (33) between the first (14) and second pulley (26) is further advantageous, since a direct contact between the pulleys (14, 26) and a transmission of rotational movement between the pulleys are avoided.

The insertion portion (33b) of the connection element (33) has a cross-like shape and is inserted in a tube-like end portion (32a) of the holding rod (32). It is also conceivable that the holding rod (32) is tubular over its full length.

The holding rod (32) extends over the distance D along the platform (40) and is supported by at least one holder (43) which is connected to the platform 40. Eventually the holding rod (32) is mounted on a first translation stage (56) at the foot part (42) of the platform (40).

The robot (5) further comprises a third actuator (10) which acts on the holding rod (32) via a third drive mechanism (34), such that the head part (6) of the robot (5) can be moved along the Y-axis. Additionally, the robot (5) comprises a fourth actuator (11) which acts on a holding rod (32) via a fourth drive mechanism (35), such that the head part (6) of the robot (5) can be moved along the X-axis. The third actuator (10) and the fourth actuator (11) are partially arranged underneath the first translation stage (56). The drive mechanisms (12, 13, 34, 35) are depicted in figures 4 to 6.

The third drive mechanism (34) comprises a third pulley (36), which is connected to the third actuator (10) by a third belt (37). The third pulley (36) is rigidly connected to a threaded spindle (38) on which a nut (39) is arranged. The nut (39) is connected to the holding rod (32) of the robot (5). Further, the threaded spindle (38) is arranged perpendicularly to the holding rod (32). Thus, a rotation of the third pulley (36) causes a rotation of the threaded spindle (38) and a movement of the nut (39) and with it the holding rod (32) along the Y-axis. Thus, the coupling of the third actuator (10) to the holding element (7) in a form-fit- and/or a force-fit-manner is achieved by such a belt drive. The third belt (37) is looped over the third pulley (36) and a pulley (not shown in the figures) connected to the third actuator (10). The third belt

(37) is a toothed belt having teeth (37a) that fit into matching teeth (36a) of the third pulley (36) and teeth of the pulley connected to the third actuator (10). By such a design, slippage of the belt is avoided. The threaded spindle (38) is mounted on the holder (43) by bearings (58).

5

It is further conceivable that the third drive mechanism (34) comprises further threaded spindles with accompanied nuts. These spindles may be arranged along the length of the holding rod (32) at equal distances. Each spindle is driven by a belt which is connected to a pulley arranged on spindle closer to the third actuator (10). In this way a chain-like drive is obtained.

10

Additionally, the third drive mechanism (34) acts on the first translation stage (56) at the foot part (42) of the platform (40). On the first translation stage (56) the holding rod (32) is mounted at the mounting element (57). Further, the first actuator (8), the pulley (50) connected to the first actuator (8), the second actuator (9) and the pulley (55) connected to the second

15

actuator (9) are mounted on the first translation stage. A translation of the first translation stage (56) along the Y-axis results therefore in a translation of said elements as a whole mounted on it along the Y-axis. A translation along the Y-axis, driven by the third pulley (36) and the third belt (37), of the one or more nuts (39), connected to the holding rod (32), is, therefore, accompanied by a translation of the first translation stage (56) along the Y-axis.

20

Obviously, the translation distance of the first translation stage (56) and the one or more nuts (39), connected to the holding rod (32) needs to be the same. Such a translation along the Y-direction allows an accurate displacement without bending the holding rod (32) or causing tension in the holding rod (32). Thus, the third drive mechanism (34) further comprise a gear, a threaded spindle or the like, which is driven by the third actuator (10), and is

25

The fourth drive mechanism (35) acts on a second translation stage (62) at the foot part (42)

of the platform (40). On second translation stage (62) the first translation stage (56) and the third actuator (10) are arranged. A translation of the second translation stage (62) along the

30

X-axis results therefore in a translation of the first translation stage (56), its elements mounted on it and the third actuator (10) as a whole along the X-axis. Thus, the fourth drive mechanism (35) can be a gear, a threaded spindle or the like, which is driven by the fourth actuator (11) and which is also arranged at the foot part of the platform (40) at a distance D from the bore (4). In figures 4-6 the third (10) and fourth actuators (11) and the first (56) and second translation stage (62) are shown.

35



Hence, upon a command, the holding rod (32) with the whole first translation stage (56) is movable back-to-forth (along the X-axis) driven by actuator (11), and for the left-to-right motion (along the Y-axis) driven by actuator (10), the holding rod moves with the first translation stage (59) only. Such a translation along the X- and Y-axis allows an accurate displacement without bending the holding rod (32).or causing tension in the holding rod (32).

The positioning system (1) comprises at least one, preferably at least two MRI-compatible camera(s) (44), which is (are) mounted on a head part (41) of the platform (44). As already mentioned, the positioning system (1) comprises a platform (40), on which the robot (5) is arranged. The platform (40) comprises a head part (41), which can be arranged in the bore (4) of the imaging device (2), wherein the subject is suspended and/or held at this head part of the platform (40). The platform (40) with the head part (41) and the robot (5) are displayed in fig. 4. The head part (41) is shown in detail in fig. 7. The head part (41) comprises a holder for the subject (59) and four mounts (60), each designed to mount MRI-compatible camera (44).

The positioning system further comprises a navigation unit (45), comprising a control unit (46), which controls the motion of the first (8), second (9), third (10) and fourth (11) actuator, an image processing unit (47), which processes real time images of the imaging device (2) and/or the at least one camera (44) in the bore (4). Fig. 8 shows the principle function of the positioning system and an MRI-system.

The MRI-system comprises a Host Workstation and MRI-Hardware which communicate with the MRI-scanner. In which the multi DOF (degrees of freedom) robot of the positioning system (1) is arranged. The Host Workstation communicates via a 1000 Base – T Ethernet with the image processing unit (47) of the navigation unit (45). In particular the MRI-images are sent in real time to the image processing unit (47). Further, the at least one camera (44) sends images to the image processing unit (47). The navigation unit (45) further comprises a brain atlas and a control unit (46). The control unit (46) communicates with the actuators (8, 9, 10, 11) via USB Serial bus. This communication comprises control commands from the control unit (46) to the actuators (8, 9, 10, 11) and a position feedback from the actuators (8, 9, 10, 11) to the control unit (46). Eventually a power supply is provided for the power supply of the actuators (8, 9, 10, 11). The power supply, the actuators (8, 9, 10, 11) and the MRI-scanner are placed in the scanner room. The Host Workstation, MRI-Hardware and the navigation unit (45) are placed in a control room.

These components may be applied for a method to position an insertion element (3) using a positioning system (1) according to any one of the preceding embodiments in a MR imaging device (2):

- a. Lowering the insertion element (3) by the robot (5) to a first position on the subject or close to the subject;
- b. Acquiring a 3D-MRI image and process the image via the image processing unit (47) to identify the location of subject, as well as the position of insertion element;
- c. Calculation of the coordinates of the target point and the insertion element (3) and calculation of an optimized movement trajectory for the insertion element (3) by the control unit (46);
- d. Monitoring movement trajectory by real-time MRI image via the image processing unit (47).

In the following, working results are presented on tests of said positioning system and method.

Fig. 9 shows an image by MRI-compatible cameras (44) of a fiber position above a hole in a rat skull. Two cameras (44) are positioned to obtain visual guidance of the brain intervention. Camera-based visual signals are presented in the navigation unit (45). Thus, an operator can monitor the real time situation inside the MRI-scanner (2). After the operator can clearly see the fiber (3) above the rat brain, and the hole in the skull (61), a laser is switched on. The light from the tip (3a) can be used as a marker of fiber tip (3a) for further 3D registration with MRI images (visual cue-based 3D registration will be solved by script with self-design algorithm). The operator could also manually adjust the probe position to target the craniotomy window above the animal skull.

Firstly, the fiber (3) will be moved to be above the hole (61) on the rat skull using the third (10) and fourth actuators (11). Secondly, the operator sets the steps and distance for the final movement, down to the brain using the first actuator (8) and the second actuator for holding the angle position (9). In parallel, the real time camera signals are displayed.

Figs.10(A-D) present a fiber (3) placement of perfused rat brain in vitro. The capability to place the fiber (3) with different depth is particularly useful to target multiple sites along the insertion path. Fig.10 A shows the targeting position in the rat brain atlas with the bregma and Interaural position: -3.48 mm and 5.52 mm, respectively. Fig.10 B shows the fiber loca-

tion in the targeted brain region, centrolateral thalamic nucleus (CL), which is illustrated in Fig.10 D.

Fig.11 shows three images with two actuator (8) steps (with a step distance of 100  $\mu\text{m}$ ) to clarify the precision of the robot (5). Three continuous MRI images with step distance 100  $\mu\text{m}$ . Because the MRI resolution is 100  $\mu\text{m}$ , it can be seen that every step of the fiber (3) moving distance is approximately 100  $\mu\text{m}$ . At each step, the fiber (3) was one line of voxel deeper. Meanwhile, this distance difference was maintained through the whole fiber insertion procedure.

10

Fig. 12 shows time-lapsed images of fiber optic targeting in the rat brain in vivo. In this application, the damage of the brain is visible during the insertion, as illustrated in Fig. 12. When the fiber tip (3a) touched the ventricle, the pushing force caused deformation of the parenchyma tissue of the ventricle border, but lead tissue bleeding. After penetrating the ventricle, the fiber (3) was further deepened to target the subcortical regions in the rat brain.

15

All the features disclosed in the application documents are claimed as being essential to the invention if, individually or in combination, they are novel over the prior art.

20

#### List of reference numerals

1	positioning system
2	imaging device
3	insertion element
25	3a end portion of the insertion element
4	bore of the imaging device
5	robot
6	head part of the robot
7	holding element
30	7a body of the holding element
	7b gripping portion holding element
8	first actuator
9	second actuator
10	third actuator
35	11 fourth actuator
	12 first drive mechanism

	13	second drive mechanism
	14	first pulley
	14a	teeth of first pulley
	15	first belt
5	15a	teeth of first belt
	16	shaft
	17	central hub portion of the first pulley
	18	converting element
	19	rotational motion of the first pulley
10	20	linear motion of the holding element along the A-axis
	21	disc-like element
	21a	center of the disc-like element
	21b	edge of the disc-like element
	22	first surface of disc-like element
15	23	first guiding element
	24	second guiding element
	24a	second guiding element one
	24b	second guiding element two
	24c	second guiding element three
20	25	spiral
	25a	space between two opposing points of the spiral
	26	second pulley
	26a	teeth of second pulley
	27	second belt
25	27a	teeth of second belt
	28	cup-like element
	28a	inner space of the cup-like element
	28b	frontal part of the cup-like element
	29	third guiding element
30	30	rotational motion of the cup-like element
	31	pivoting-motion of the holding element
	32	holding rod
	32a	tube-like end portion of the holding rod
	33	connection element
35	33a	loop portion of the connection element
	33b	insertion portion of the connection element

	34	third drive mechanism
	35	fourth drive mechanism
	36	third pulley
	36a	teeth of third pulley
5	37	third belt
	37a	teeth of third belt
	38	threaded spindle
	39	nut
	40	platform
10	41	head part of the platform
	42	foot part of the platform
	43	holder
	44	camera
	45	navigation unit
15	46	control unit
	47	image processing unit
	48	support device
	49	fixing element
	50	pulley connected to the first actuator
20	51	second surface of disc-like element
	52a, 52b	guiding projections
	53	direction
	54a, 54b	grooves
	55	pulley connected to the second actuator
25	56	first translation stage
	57	mounting element
	58	bearings
	59	holder for subject
	60	mount MRI-compatible camera
30	61	hole in the skull
	62	second translation stage
		X-axis
		Y-axis
35		Z-axis
		A-axis

B-axis

$\alpha$  angle

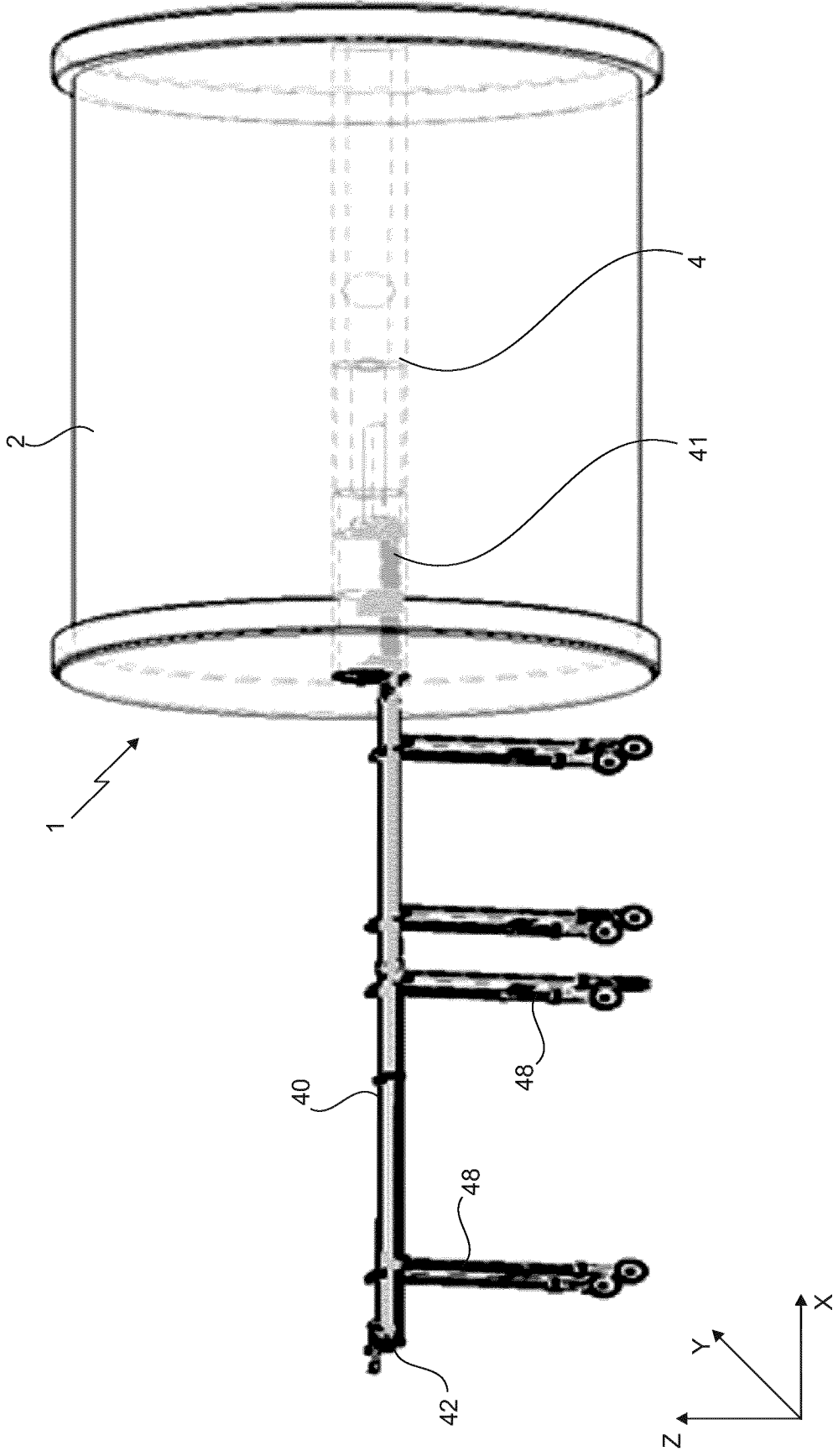


Fig. 1





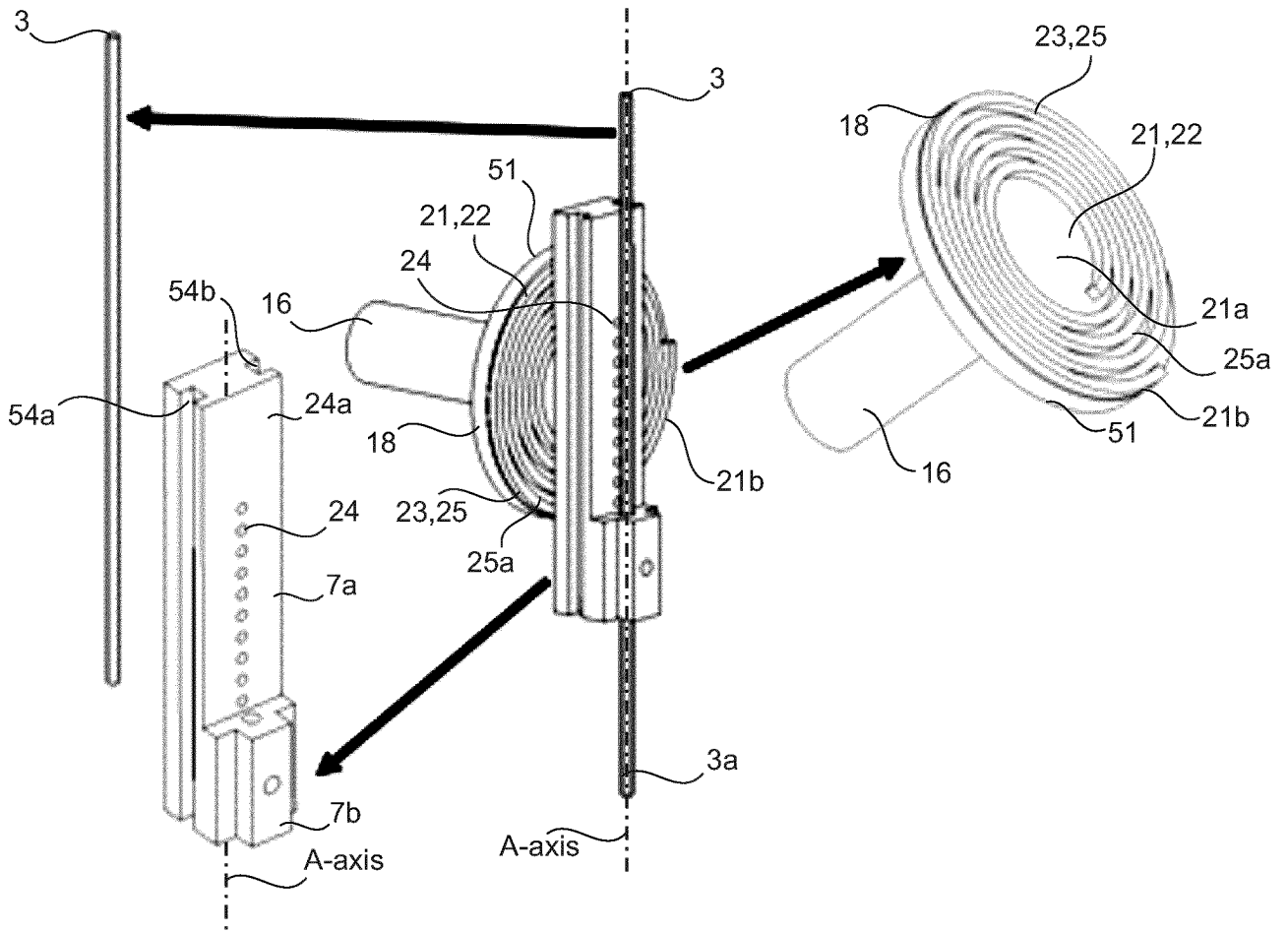


Fig. 3

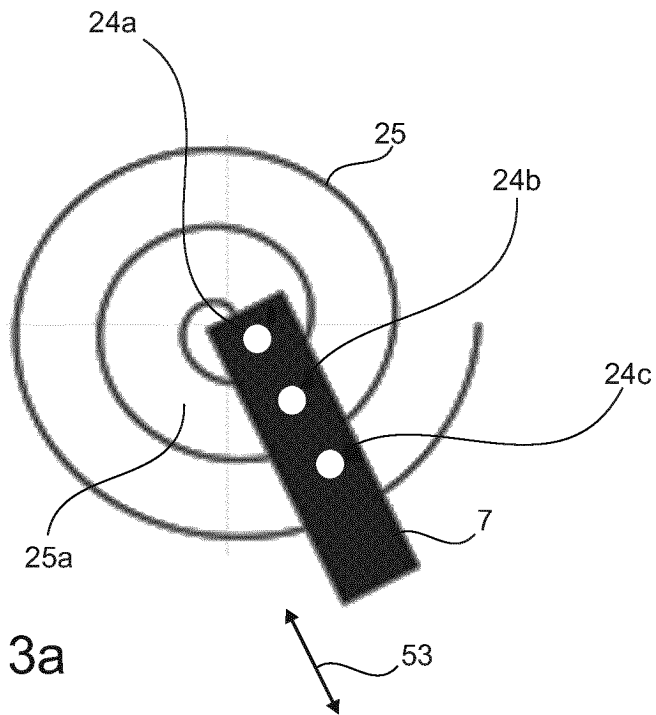


Fig. 3a



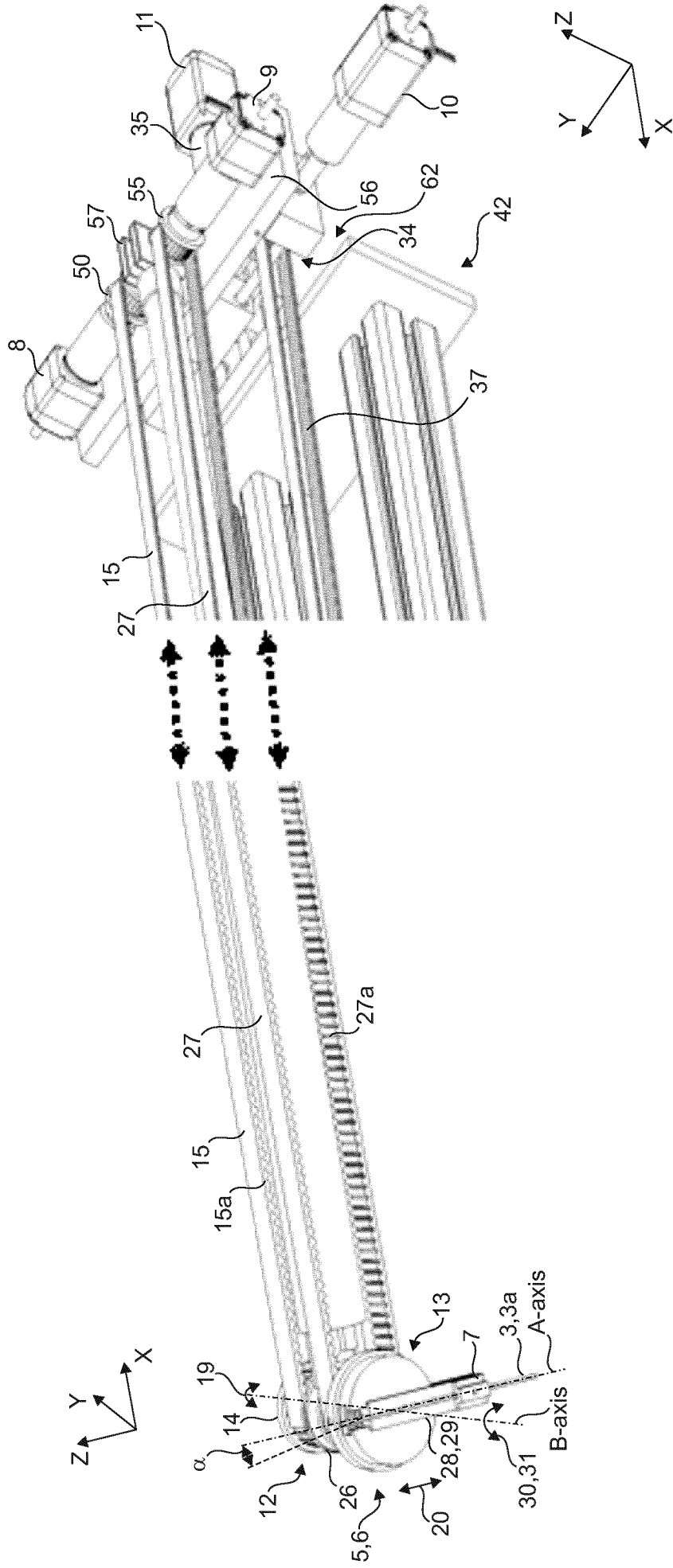


Fig. 5

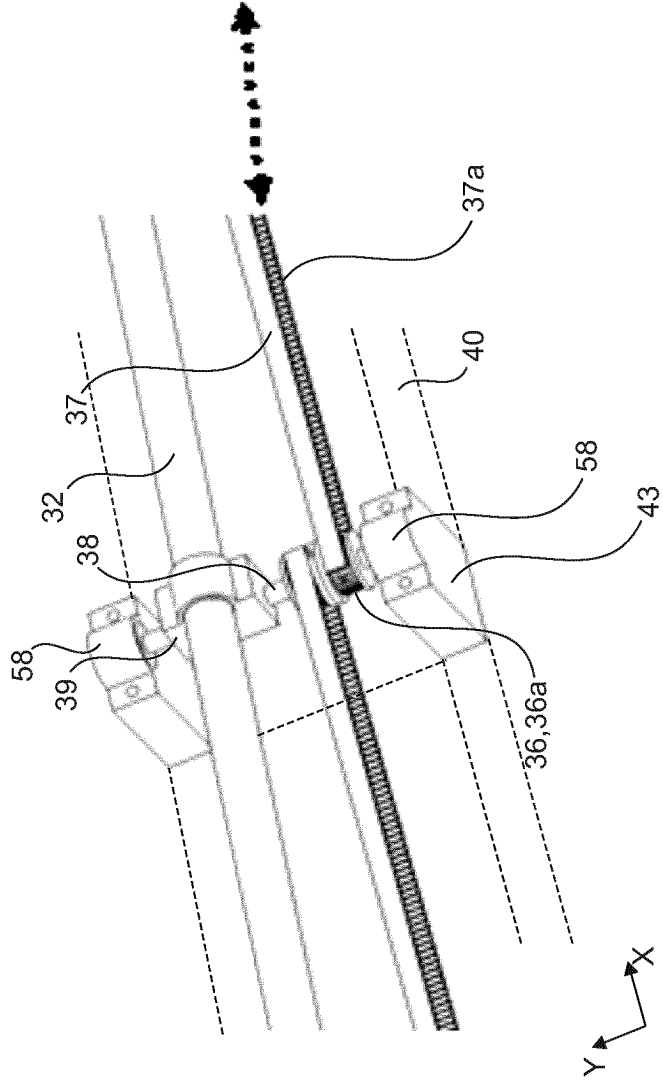
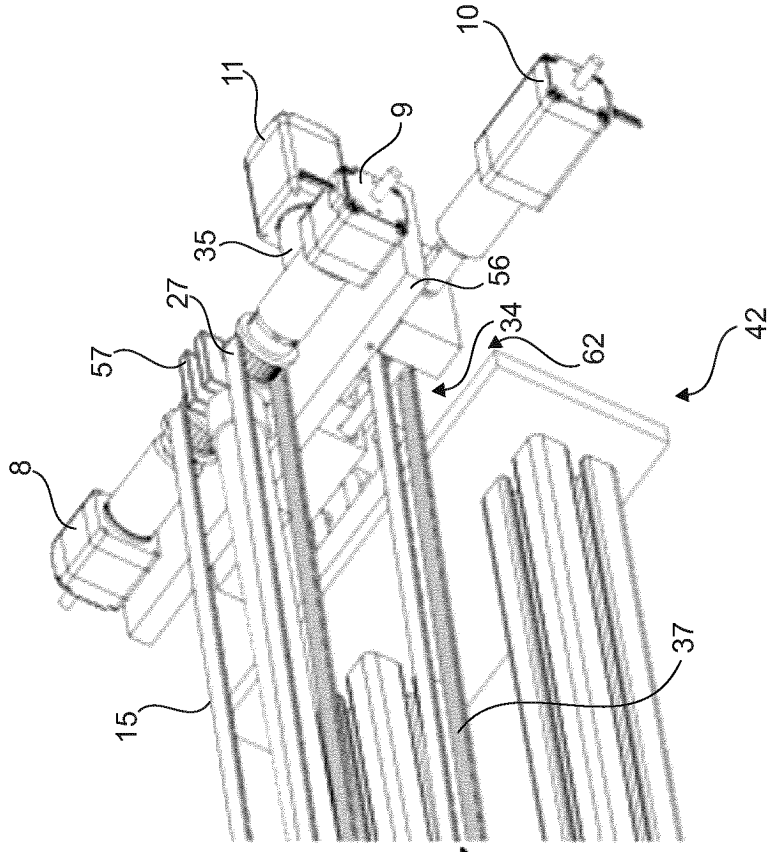


Fig. 6

7/12

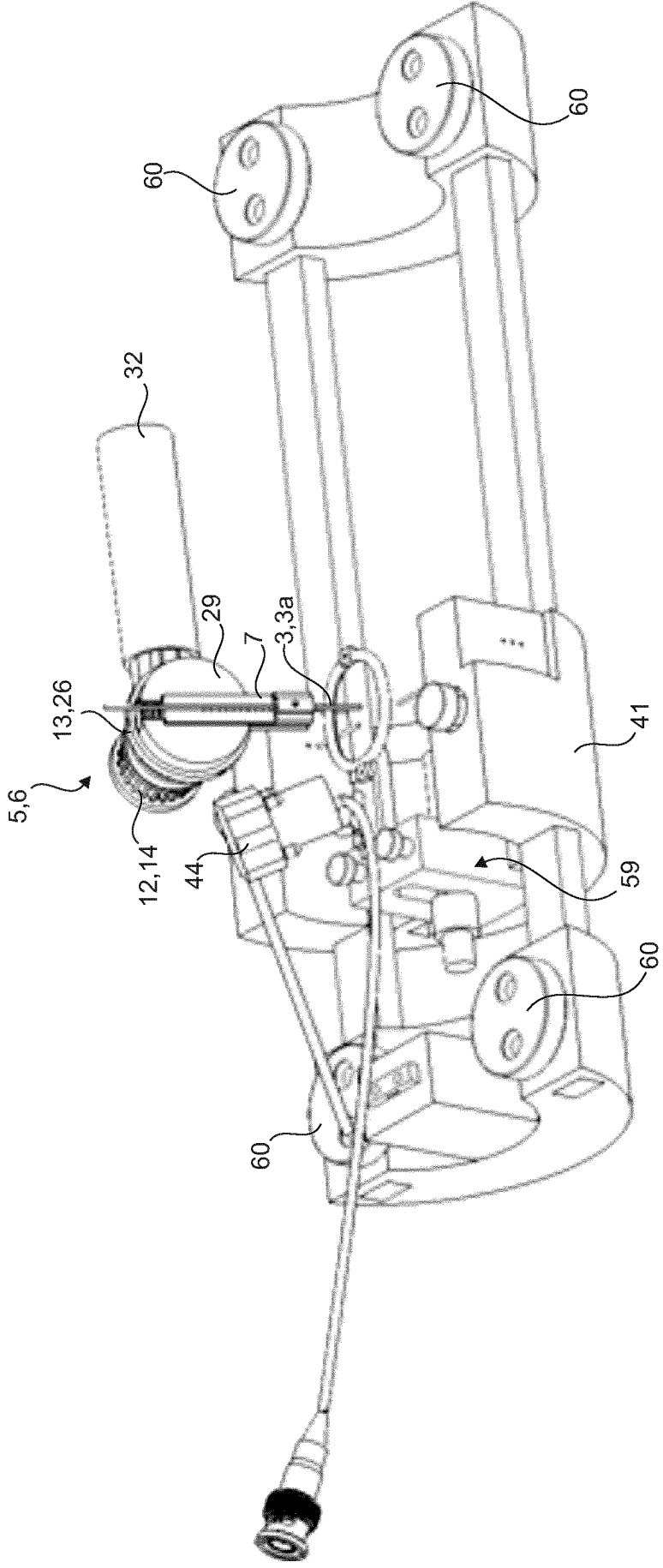


Fig. 7

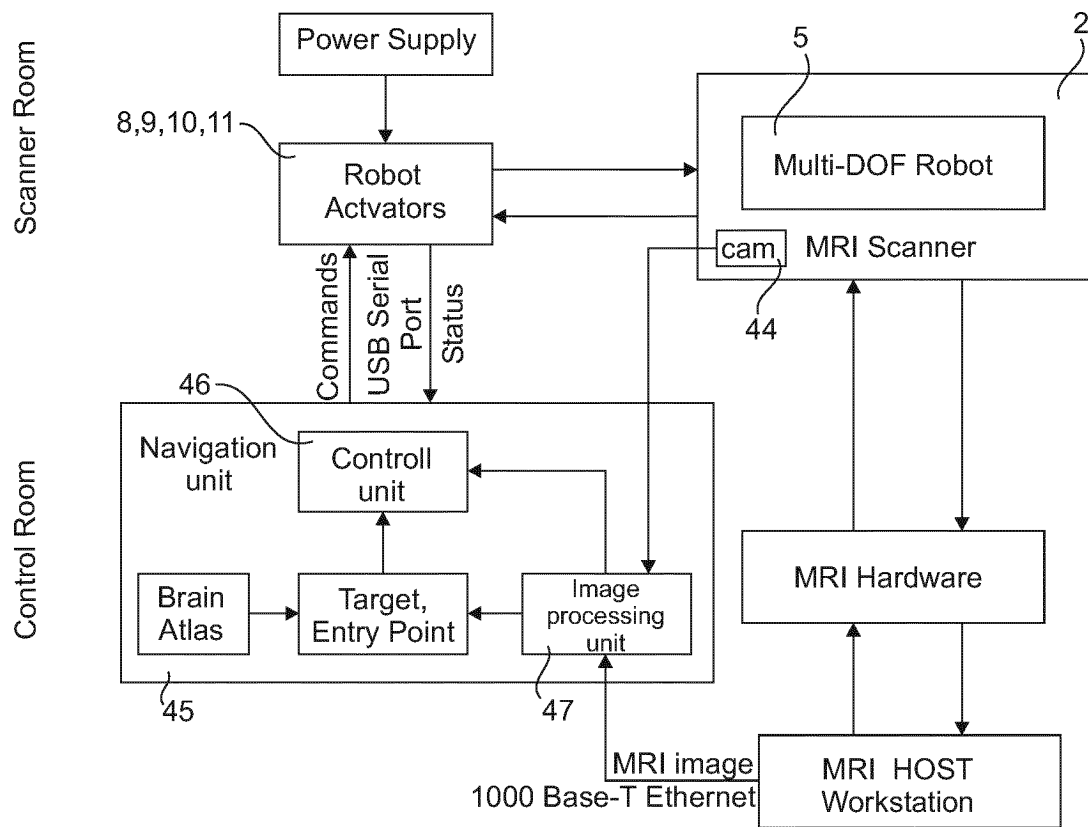


Fig. 8

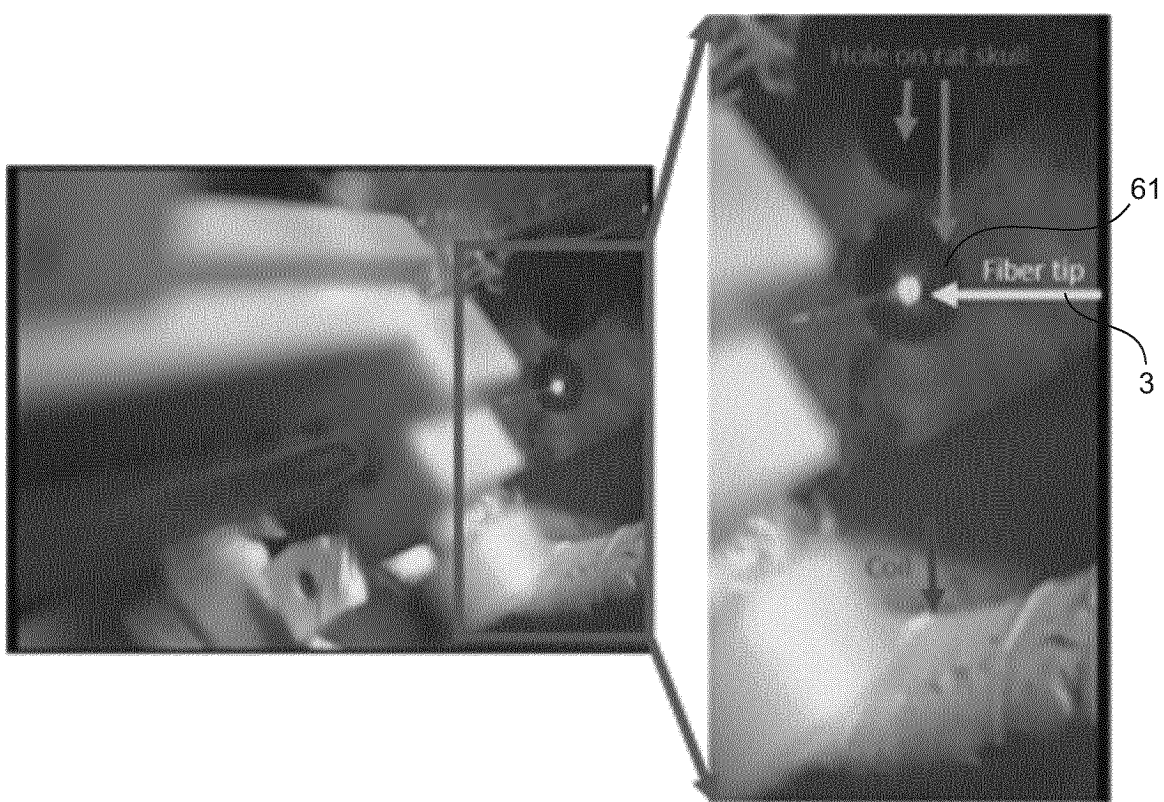


Fig. 9

10/12

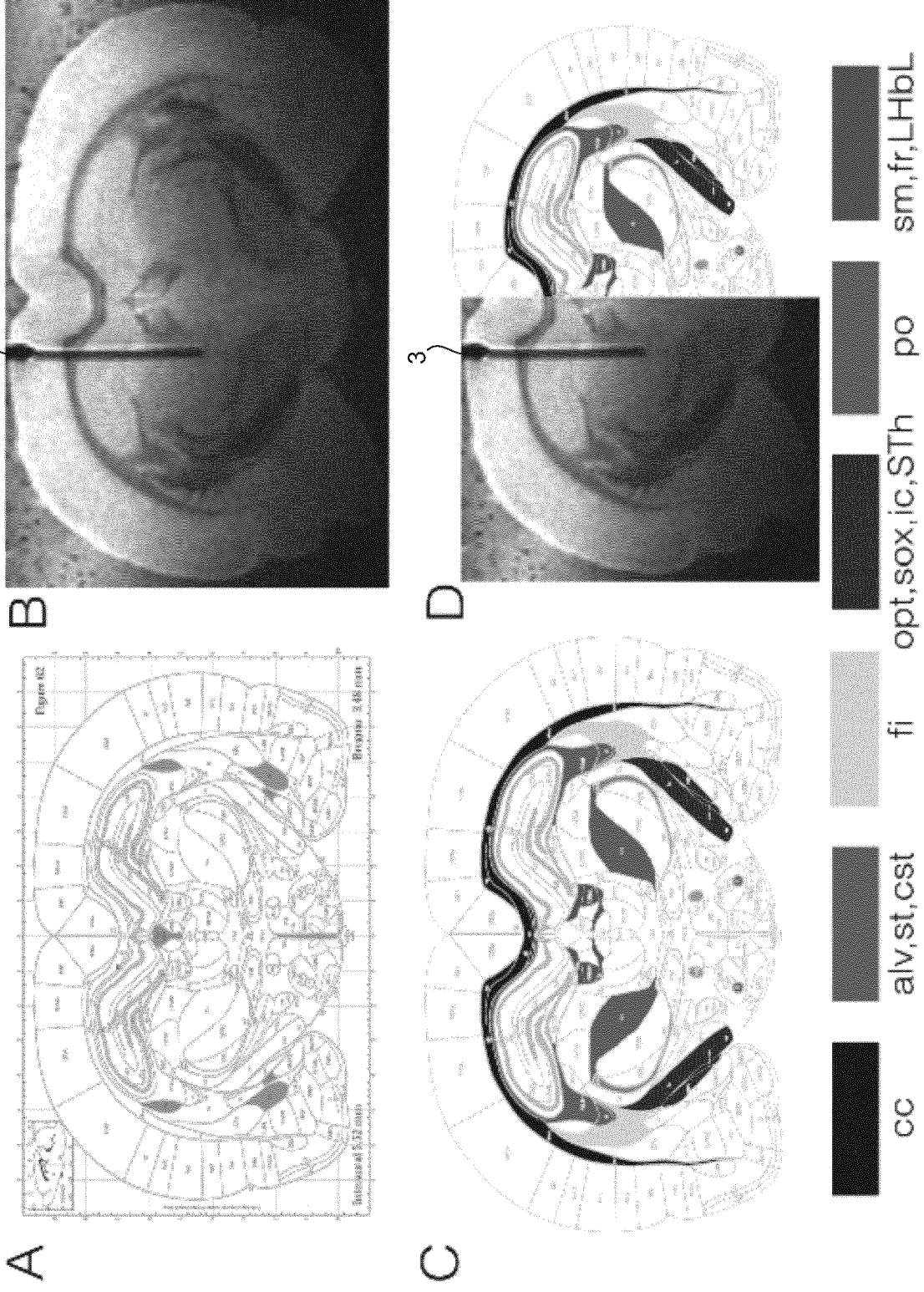


Fig. 10



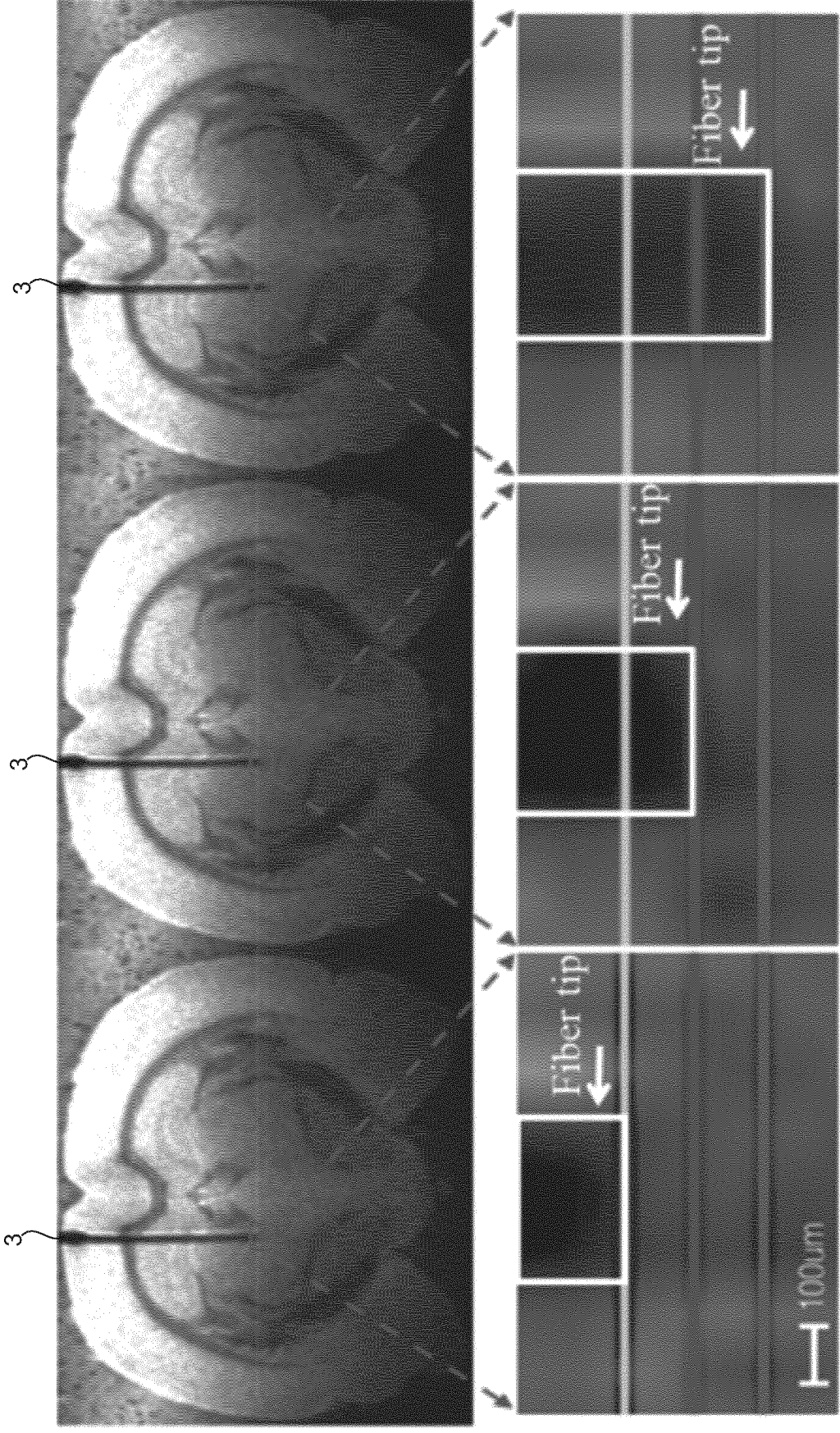


Fig. 11

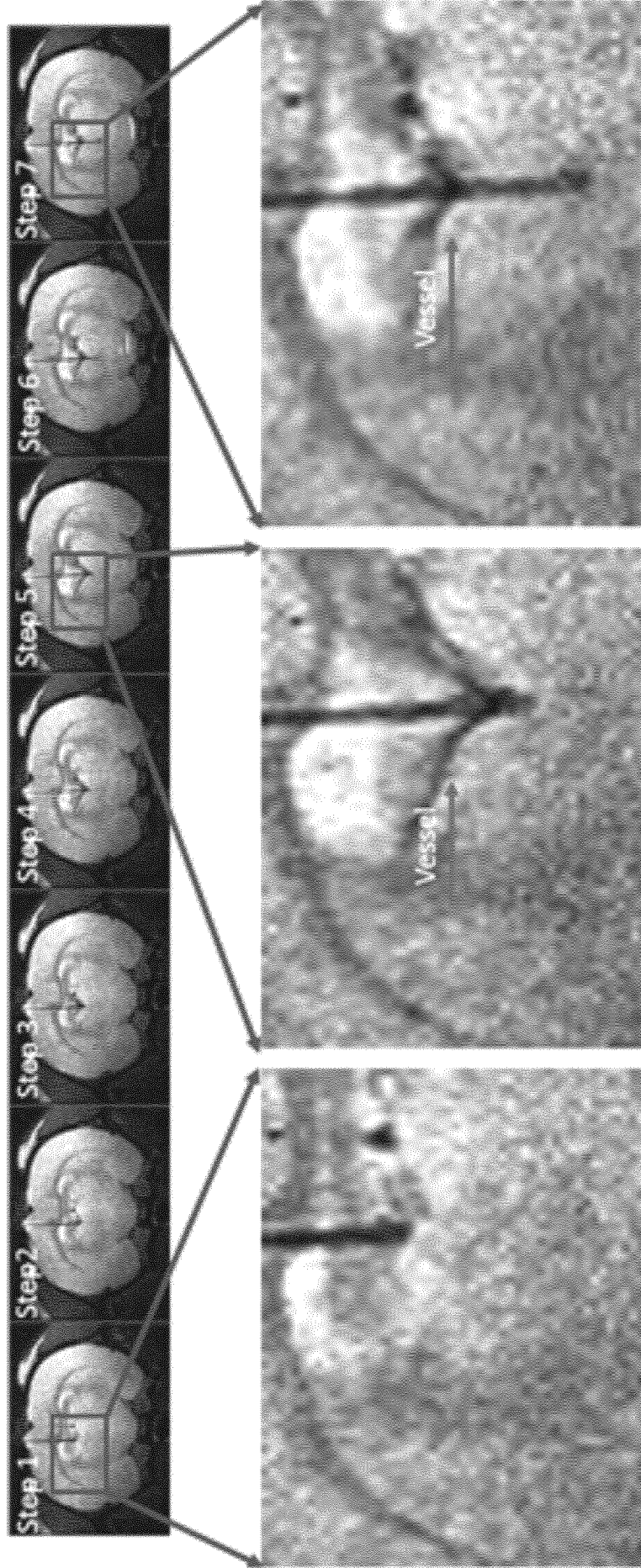




Fig. 12

ARTICLE

<https://doi.org/10.1038/s41467-019-10450-3>

OPEN

# MRI-guided robotic arm drives optogenetic fMRI with concurrent $\text{Ca}^{2+}$ recording

Yi Chen<sup>1,2</sup>, Patricia Pais-Roldan<sup>1,2</sup>, Xuming Chen<sup>1,3</sup>, Michael H. Frosz <sup>4</sup> & Xin Yu <sup>1,5</sup>

Optical fiber-mediated optogenetic activation and neuronal  $\text{Ca}^{2+}$  recording in combination with fMRI provide a multi-modal fMRI platform. Here, we developed an MRI-guided robotic arm (MgRA) as a flexible positioning system with high precision to real-time assist optical fiber brain intervention for multi-modal animal fMRI. Besides the ex vivo precision evaluation, we present the highly reliable brain activity patterns in the projected basal forebrain regions upon MgRA-driven optogenetic stimulation in the lateral hypothalamus. Also, we show the step-wise optical fiber targeting thalamic nuclei and map the region-specific functional connectivity with whole-brain fMRI accompanied by simultaneous calcium recordings to specify its circuit-specificity. The MgRA also guides the real-time microinjection to specific deep brain nuclei, which is demonstrated by an Mn-enhanced MRI method. The MgRA represents a clear advantage over the standard stereotaxic-based fiber implantation and opens a broad avenue to investigate the circuit-specific functional brain mapping with the multi-modal fMRI platform.

<sup>1</sup>Research Group of Translational Neuroimaging and Neural Control, High-Field Magnetic Resonance, Max Planck Institute for Biological Cybernetics, 72076 Tuebingen, Germany. <sup>2</sup>Graduate Training Centre of Neuroscience, University of Tuebingen, 72076 Tuebingen, Germany. <sup>3</sup>Department of Neurology, Renmin Hospital of Wuhan University, Wuhan University, 430060 Wuhan, China. <sup>4</sup>Max Planck Institute for the Science of Light, 91058 Erlangen, Germany. <sup>5</sup>Athinoula A. Martinos Center for Biomedical Imaging, Massachusetts General Hospital and Harvard Medical School, Charlestown, MA 02129, USA. Correspondence and requests for materials should be addressed to X.Y. (email: [xin.yu@tuebingen.mpg.de](mailto:xin.yu@tuebingen.mpg.de))

A multi-modal brain mapping platform for animals has been established by merging the fiber optic-mediated optogenetic activation and neuronal  $\text{Ca}^{2+}$  recording with functional magnetic resonance imaging (fMRI)<sup>1–5</sup>. Given its non-magnetic properties, the optical fiber can be used in combination with fMRI brain mapping without electromagnetic interference with the radio frequency (RF) transmission and magnetic gradient switching of the MR scanner<sup>2,3,6,7</sup>. The increased cellular specificity of genetic labeling reassures the advantageous usage of optical fiber recording/imaging to track neural spiking activity in the deep brain regions<sup>8–13</sup>. However, one emerged challenge is how to precisely target specific functional nuclei in the animal brain<sup>8,14</sup>. The procedure of fiber optic implantation in rodent studies has been commonly performed with conventional stereotaxic devices<sup>2,3,7–11,14,15</sup>, but the success rate to precisely target the deep brain nuclei remains low, especially for the functional nuclei that cover only a few hundred microns space in the animal brain, e.g., the central thalamic nuclei<sup>8</sup>. A solution to precisely target the genetically labeled neuronal tracts or subdivisions of functional nuclei could significantly improve the reproducibility of basic scientific discoveries. Here, we report an MRI-guided robotic arm (MgRA) positioning device to maneuver the real-time fiber optic implantation into the animal brain inside a high-field MR scanner (14.1 T), intended for parallel optogenetics and/or calcium imaging and fMRI studies.

The genetic expression of channelrhodopsins (ChR2) has been extensively applied to target-specific cell types in the deep brain nuclei, such as the dopaminergic neurons in the midbrain<sup>9</sup>, the orexin in the lateral hypothalamus (LH)<sup>16,17</sup> or noradrenergic neurons in the locus coeruleus<sup>18</sup>. The cell-type specific genetic labeling ensures the optogenetic activation on neuronal ensembles of interest assuming that the optical fiber is precisely located at the functional nuclei. However, the stereotaxic device-driven fiber optic implantation scheme shows little flexibility after the fiber tips are fixed in the brain for either fMRI mapping, electrophysiological recordings, or behavioral studies<sup>8,19</sup>. The precise coordinates of a certain functional brain nucleus can vary between different animals, and incorrect positioning may result in largely altered functional activation and behavioral outcomes. This systematic error, which is intrinsic to the blind optical fiber

placement, can potentially conceal important discoveries and lead to inappropriate conclusions in causality analysis. Using MgRA assisted fiber-optic insertion in combination with real-time fMRI, we can provide a step-wise optogenetic activation scheme to allow multi-site targeting through a fiber insertion trajectory during the fMRI study. This strategy can not only improve the precision, but also provide a thorough view to examine the subtle differences in the whole brain activation patterns when targeting the sub-regions of the functional nuclei of interest.

Numerous efforts have been made to develop robotic positioning systems inside the MRI scanner for translational application from animals to the clinical practice, e.g., deep brain stimulation or brain tumor ablation<sup>20–26</sup>. In contrast to the growing access to robotic manipulation strategies inside large-bore MRI scanners (e.g., 1.5 or 3 T human scanner), there are only a handful of works that have implemented remote controlling systems inside high field MRI scanners with smaller bore (>7 T, <12 cm gradient bore size), which have been applied to adjust sample orientation within the  $B_0$  field<sup>27</sup> or to tune RF coil arrays<sup>28</sup>. To the best of our knowledge, there is currently no MRI-compatible robotic control system to assist fiber optic insertion in small bore high field MRI scanners (>9.4 T) for optogenetic fMRI studies. Hence, as a proof-of-concept, we developed an MgRA to provide a flexible positioning system inside a 14.1 T MRI scanner which assists fiber optical brain intervention in animals. Besides an ex vivo precision evaluation, we present a series of in vivo studies showing the whole brain activity patterns upon optogenetic stimulation of MgRA-targeted nuclei in the LH or thalamus in a step-wise manner and with simultaneous fiber-optic calcium recordings to specify the region-specific optogenetic activation patterns. In addition, the MgRA system can be applied for region-specific deep brain microinjection. Here, we demonstrate a series of high precision brain interventional applications in the context of multi-modal neuroimaging using the MgRA system.

## Results

**Mechanical design of the MgRA with ex vivo operation.** A stepper motor-driven MgRA was designed for real-time control of the insertion of an optical fiber into animal brains inside a 14.1

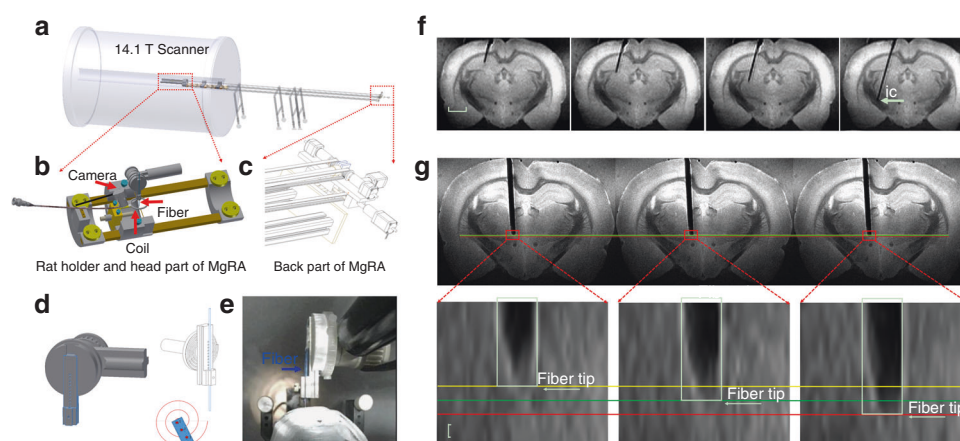


**Fig. 1** 3D view of the MgRA and its application in ex vivo studies. **a** Overview of the MgRA inside the 14.1 T MR scanner. **b** Schematic of the customized animal holder and head part of the MgRA. Both MR compatible camera and surface transceiver coil are included for monitoring the fiber optic insertion inside the MR scanner. **c** Stepper motors implemented at the back part of the MgRA to control up to four degrees-of-freedom movement. The long arm reaching 4.7 m away from the magnetic center point excludes the influence by the ultra-high magnetic field. **d** Schematic drawing of the Archimedean spiral design to transmit the dorsal-ventral movement. **e** Snapshot of the mechanically controlled fiber optic movement videotaped by the built-in camera. **f** Time-lapsed images showing the optical fiber targeting the hippocampus, thalamus, and internal capsule along the insertion trajectory. Scale bar, 2 mm. **g** Three continuous MRI anatomical images with step distance 50  $\mu\text{m}$  (the MRI in-plane resolution is  $50 \times 50 \mu\text{m}^2$ , thus it can be seen that the distance moved in each step is approximately 50  $\mu\text{m}$ ). Scale bar, 50  $\mu\text{m}$

T scanner (Fig. 1a, 3D schematic view in Supplementary Movie 1, Supplementary Fig. 1). The MgRA contains two key parts: the front part (head of the MgRA) includes the driving pieces and a customized rat holder (Fig. 1b), and the back part accommodates the stepper motors to fulfill the optical fiber movement with multi-degree of freedom (Fig. 1c). The coupling of the actuator (back part) to the matching toothed pulley in the head was achieved by a synchronous belt drive (Fig. 1c) in a form-fit manner, without slippage and run at constant speed. Insertion of the optical fiber in the dorsal-ventral direction into the rat brain is executed using an Archimedean spiral mechanism to achieve high precision and accuracy (Fig. 1d). With a built-in MRI compatible camera, the insertion of the optical fiber could be monitored outside of the scanner to verify the effectiveness, safety, and feasibility of the MgRA (Fig. 1e and Supplementary Movie 2), simultaneously tracked with anatomical MRI. The assembly of all components provides the MgRA unique features in a portable frame that can be easily located inside the MRI room substituting the conventional subject table. A more detailed description of MgRA can be found in Methods and Supplementary Figs. 11–13.

The MgRA was first evaluated in perfused brains embedded in agarose (Fig. 1f), in order to simulate the procedure of intracerebral fiber insertion in the living animal. The optical fiber was first inserted into the agarose-embedded brain preparation in a 100  $\mu\text{m}$  step-wise manner, and real-time MRI images were acquired to monitor the movement trajectory and to identify the location of the fiber tip (Supplementary Movie 3). Precision of the MgRA was determined as the smallest step in the dorsal-ventral direction that could be maneuvered based on the remote stepper motor controlling. Figure 1g shows the step-wise movement of the fiber inside the rat brain at 50  $\mu\text{m}$  per step with high-resolution MRI time-lapsed 2D images (Supplementary Movie 4). It is worth noting that fiber insertion trajectories can be optimized with special angles to target specific deep brain nuclei or fiber bundles while avoiding disturbance of neural circuits, projection pathways of interest or certain brain vessels. For instance, an angled fiber optic insertion can be implemented to target the internal capsule to preserve the ascending pathway of the thalamocortical circuits (Fig. 1f and Supplementary Fig. 2). In summary, MgRA-based fiber optic insertion in the *ex vivo* brain verifies its functionality and demonstrates the stability in terms of remote motor control.

### **In vivo MgRA-driven fiber insertion with optogenetic fMRI.**

MgRA allows the insertion of optical fibers *in vivo* inside the 14 T MRI scanner, which induces great advantages for optogenetic fMRI studies<sup>3,29,30</sup>. To locate the fiber tip prior to intracerebral insertion inside the MRI scanner, two procedures were followed. First, we implemented two MRI-compatible cameras to visually locate the fiber tip, as well as the craniotomy on the animal skull (Fig. 2a and Supplementary Movie 5). Second, a prior application of a manganese-treated agarose gel was applied over the skull and the sequential lowering of the fiber was monitored with real-time anatomical MRI to locate the fiber tip as well as the craniotomy hole on the skull to guide the fiber targeting inside the brain (Supplementary Fig. 3). A more detailed description can be found in Methods, Supplementary Fig. 3. Figure 2b shows snapshots of the fiber tip outside the brain during the MgRA-driven fiber insertion. Figure 2c demonstrates an example of the *in vivo* fiber targeting of subcortical thalamic regions. Also noteworthy is the bleeding-induced T2-weighted signal drop when the fiber was inserted through the lateral ventricle (Fig. 2c). When a fiber tip first reaches a ventricle, its pushing force causes deformation of the surrounding ependyma, which can induce minor bleeding from the choroid plexus. This observation should raise a note of

caution to target deep brain regions. The damage could be reduced by decreasing the insertion speed, which can be accomplished at approximately 20  $\mu\text{m}/\text{s}$  with the MgRA (Supplementary Movie 5 and Supplementary Fig. 4).

Fiber optic insertions with customized angles can also be applied with MgRA for the *in vivo* animal fMRI environment. Figure 2d shows the step-wise fiber tip targeting to the hippocampus and ventral posteromedial nucleus (VPM) of the thalamus by inserting the optical fiber with a 40° angle from the midline. Figure 2e demonstrates the whole brain BOLD fMRI map upon optogenetic activation of either the hippocampus or the VPM, based on the MgRA-driven step-wise fiber tip localization. Thus, the implementation of MgRA in standard opto-fMRI workflows provides flexibility to guide an optical fiber along a certain insertion trajectory, allowing to target different nuclei in a single fMRI experiment, and hence, to study whole brain responses upon deliberate region-specific stimulation.

**Whole brain fMRI with LH optogenetic activation.** The MgRA can be used to target the deep brain nuclei with much higher precision for fiber optic-mediated optogenetic activation than the conventional stereotaxic-based fiber implantation on bench. For example, the LH is a heterogeneous nucleus with highly varied cell types across a few millimeter space in the ventral brain<sup>31</sup>. The MgRA-driven fiber optic positioning provides a reliable and precise targeting scheme for the LH optogenetic activation during fMRI. Figure 3a shows ChR2 expression with the AAV viral vector AVV9.CaMKII.ChR2.eYFP into the LH and the fiber optic trace to target the LH in the histological slice, as well as the MR image showing how the fiber tip coincides with the traced site of viral injection. The whole brain activation pattern upon the LH optogenetic activation is presented in Fig. 3b, showing the blood oxygen level dependent (BOLD) signal along the ascending projection to the basal forebrain from the LH. Figure 3c shows the temporal evolution of the optogenetically evoked BOLD signals in both LH and its projected basal forebrain regions with the mean time courses acquired at different stimulation durations. Figure 3d shows the mean BOLD signal time courses from both nuclei with varied optical light pulse frequencies and pulse widths (whole brain functional patterns at varied pulse width are shown in Supplementary Fig. 5). The BOLD amplitude dependency on the light pulse parameters provides strong evidence for reliable detection of the functional projections from the LH with optogenetic fMRI. It is also noteworthy that MgRA-driven fiber optic implantation ensures highly comparable activation patterns in the LH across different animals (results from 5 individual rats, Fig. 3b), as well as the activation of areas in the basal forebrain including the lateral preoptic area (LPO), medial preoptic area (MPA), and the strial part of the preoptic area (StA) (the co-registered brain atlas to the individual rat functional map, Fig. 3b). Additionally, the evoked calcium and BOLD signals in the barrel cortex (BC) were observed in these animals upon somatosensory whisker stimulation (Supplementary Fig. 6), which indicates a stable physiological state of the animal and therefore validates the biological data acquired from these experiments. These results indicate that MgRA provides high targeting accuracy and effectiveness to target deep brain circuits and produce optogenetically-driven brain activation in a highly reliable manner.

### **Step-wise optogenetically driven fMRI and calcium recording.**

The flexibility and high precision of MgRA-driven fiber optic targeting was further verified in a series of experiments that combined optogenetic activation with concurrent fMRI and calcium fiber optic recording (Fig. 4a). This multi-modal fMRI

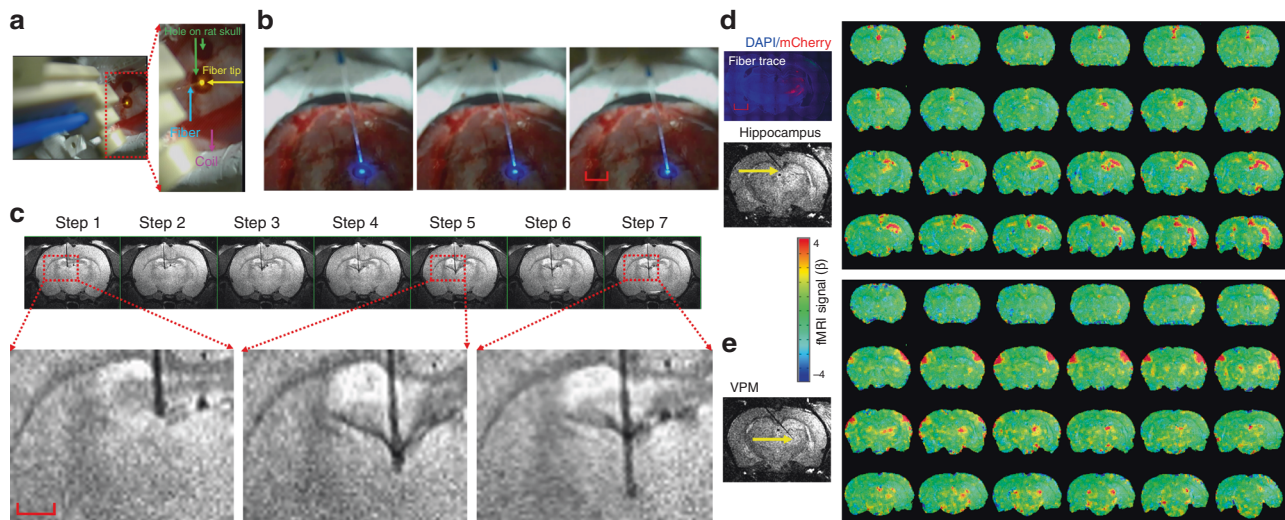


**Fig. 2** Evaluation of MgRA for in vivo studies and brain-wide opto-fMRI patterns in multiple targets. **a** Snapshot of the optical fiber (tip with 589 nm wavelength laser light, yellow arrow) positioned above the burr hole (green arrow) on the skull of an anesthetized rat with the driving piece of the head part. **b** Camera-based fiber optic movement for three steps outside the rat brain. The fiber tip delivers blue laser light (473 nm wavelength). The bright ring-structure above the rat skull is the RF surface coil. Scale bar, 2 mm. **c** Potential collateral damage from the choroid plexus when the fiber was lowered to pass through the lateral ventricles, shown as a dark signal below the hippocampus. The step size was 300  $\mu\text{m}$ . Scale bar, 1 mm. **d** Left, histological image demonstrates Chr2-mCherry expression in most of the thalamus and part of hippocampus. Red, Chr2-mCherry; blue, 4',6-Diamidino-2-phenylindole (DAPI). Right, the fiber tip targets the hippocampal area and the BOLD fMRI map shows the activated area primarily located in the ipsilateral hippocampal structure. Scale bar, 2 mm. **e** The fiber tip targets the ventral postero-medial (VPM) thalamus and map of BOLD activity was detected in bilateral vibrissal S1 cortex in response to blue light stimulation. (For both (**d**) and (**e**), 3D whole brain EPI: 400  $\mu\text{m}$  isotropic resolution, 1.5 s repetition time; stimulation block design: 8 s on 37 s off; laser pulse: 10 ms, 5 Hz, 3.7 mW/200  $\mu\text{m}$  core diameter of fiber tip)

scheme with MgRA enables real-time feedback at the level of the whole brain (via fMRI) and specifically from the fiber tip (via optical fiber) regarding the activation of the projection structures upon region-specific stimulation. Here, calcium imaging was acquired from the neurons in the BC that received afferents from the subcortical thalamic region by using the calcium reporter GCaMP6<sup>4,5,12</sup>; optogenetic stimulation was performed on the VPM thalamic nuclei, after expression of the light-sensitive protein ChR2 (Fig. 4b–d)<sup>2,3,32</sup>. The recording fiber was directly implanted to record the GCaMP6f-mediated calcium signal in the BC, while the optogenetic activation fiber was controlled by the MgRA inside the scanner with real-time anatomical and functional MRI to track the insertion trajectory. The MgRA guided the fiber tip to deliver the optogenetic activation at multiple sites along the insertion trajectory (Fig. 4e and Supplementary Movie 6). Evoked calcium and BOLD signals from the somatosensory cortex ipsilateral to the targeted thalamic nucleus increased in a stepwise manner as the optical fiber was moved closer to the VPM region, while, after the fiber bypassed the VPM region, BOLD and calcium signal decreased accordingly (Fig. 4f–i). There was a slightly different stepwise fMRI response from the contralateral somatosensory cortex as well (Fig. 4h, i), which has been previously reported with electrical stimulation<sup>33,34</sup>. To further demonstrate the reliability of MgRA, five power levels of light pulses were used to trigger increased BOLD and simultaneous calcium signals (Supplementary Fig. 7). Moreover, by altering the frequency of the light from 0.5 to 5 Hz, we could observe a fully recovered evoked calcium baseline signal at 0.5 Hz and elevated calcium signals from 1 to 3 Hz, while at 5 Hz, the overall plateau amplitude was not further increased (Supplementary Fig. 8). The BOLD signal increased with higher frequency, but not at 5 Hz, which was consistent with the calcium signal dynamics (Supplementary Fig. 8). Results from two additional rats with different or similar insertion trajectories

confirmed the reliability of the stepwise optogenetic activated fMRI and calcium signals acquired using the MgRA (Supplementary Figs. 9 and 10). These experiments further demonstrate the unique capability of the MgRA to specifically target subcortical nuclei, which, combined with cortical recordings in the projection area, allow unequivocal stimulation of the target sites.

**MgRA-driven Mn-injection into CL and LH.** The MgRA can also be used to guide the real-time microinjection with high precision inside the MRI scanner. MnCl<sub>2</sub> solution was used as the MR contrast agent and a modified MPRAGE sequence<sup>35</sup> (Mdef, ~4 min) was implemented to detect the manganese-enhanced T1-weighted MRI signal<sup>15,36–38</sup>. As shown in Fig. 5a, a hollow core optical fiber<sup>39–41</sup> was used to target the central lateral thalamic nucleus (CL) and Mn solution was delivered in two consecutive steps. The initial stop was introduced to target the corpus callosum with a small dosage of Mn delivery (Fig. 5b), illustrating the real-time guided injection to target the callosal fibers with a few hundred micron thickness. When the fiber tip as located at the CL (position was verified with a T2-weighted MR image (RARE) overlapped with the brain atlas), Mn solution was injected for three times to show dose-dependent signal changes in the T1-weighted Mdef images acquired before and after Mn injection (Fig. 5b). This result demonstrates the real-time injection capabilities of the MgRA.

Besides the multiple stops along the single trail of injection trajectory, the MgRA can be used to drive multi-trial microinjection, e.g., to the lateral hypothalamic nucleus from the same rat, inside the MRI scanner. As shown in Fig. 5c, the fiber tip was guided to target the LH. The Mdef images were acquired before and after the injection (3 times, Fig. 5d, e), showing clear effective Mn delivery to the LH. In addition, we continuously acquired the Mdef images within the first ~1 h following the injection, showing highly robust and confined Mn-enhanced signal of the

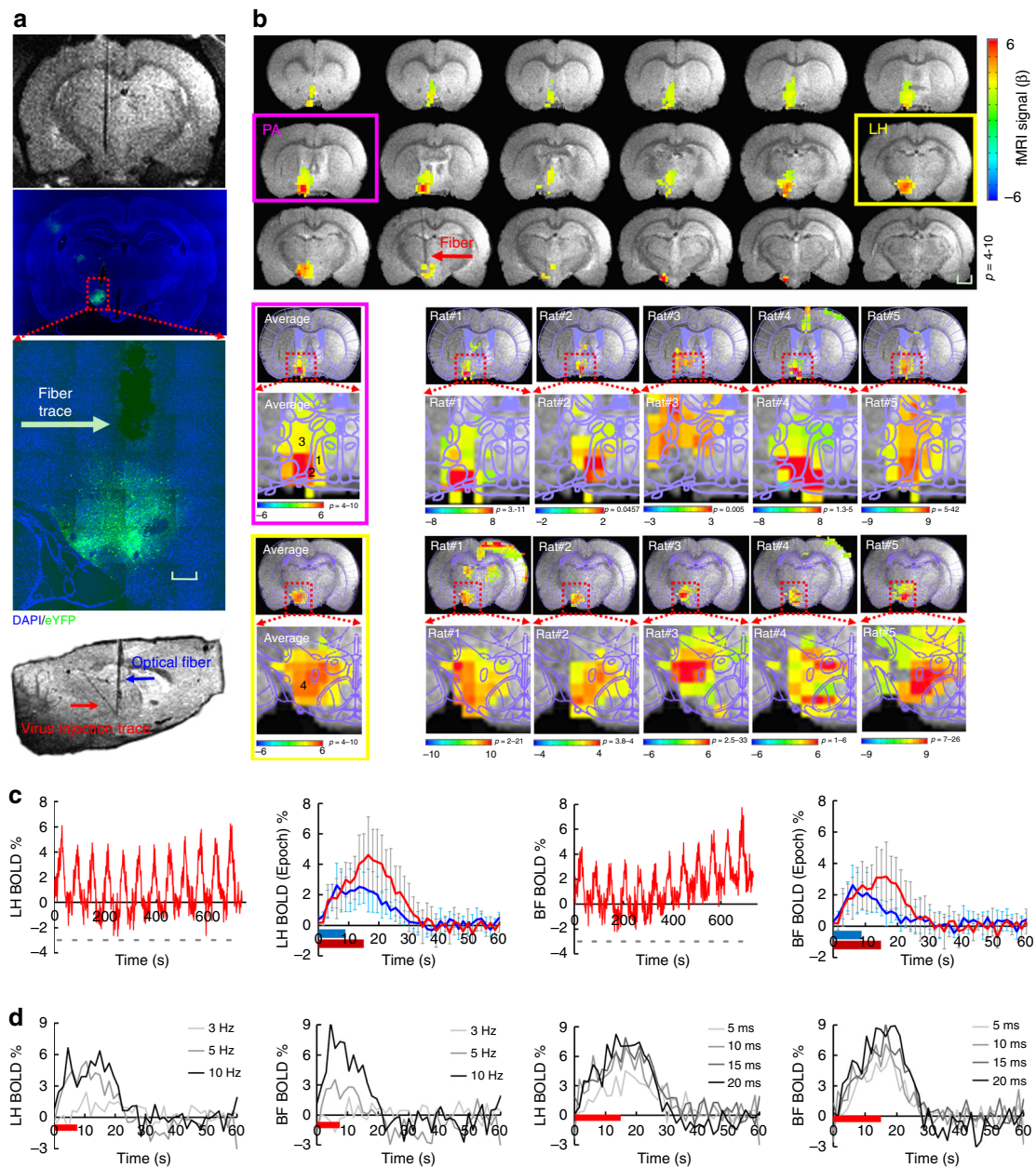


**Fig. 3** MgRA-driven fiber optic targeting of the lateral hypothalamic nuclei with optogenetic fMRI. **a** Top: representative RARE anatomical image used to clarify the optical fiber location driven by MgRA for optical stimulation in LH. Middle: representative wide-field fluorescence image illustrating robust ChR2-eYFP expression focused on LH. Fiber optic insertion trace marked with white arrow. Scale bar, 200  $\mu$ m. Bottom: sagittal RARE anatomical image showing the fiber optic trace (blue arrow) and virus injection trace (red arrow). **b** Top: average fMRI map of brain-wide activity during optogenetic stimulation of LH neurons at 5 Hz, 20 ms pulse width, 15 s duration. Middle: averaged evoked BOLD map (left) and the same map from 5 individual rats (right) zoomed in on the basal forebrain (BF) showing activation of the lateral preoptic nucleus (LPO) and medial preoptic area (MPA), overlaid with the brain atlas. Bottom: average evoked BOLD map (left) and 5 individual rats (right) in lateral hypothalamic region, overlaid with the brain atlas. GLM-based *t*-statistics in AFNI is used. Scale bar, 2 mm. **c** Average time courses of significantly modulated voxels showing fMRI signal changes within the ipsilateral LH and BF (*n* = 5 animals) upon optogenetic stimulation of block design: 15 s on/45 s off, 12 epoch, 20 ms light pulse, 5 Hz, 18.9 mW. The individual hemodynamic response shows the average BOLD signal upon different stimulation durations (8 s in blue, 15 s in red). Error bars represent mean  $\pm$  SD across 5 animals. **d** Average stimulation duration-locked time evolution for both LH and BF depicting the frequency-dependent hemodynamic responses at 3, 5, and 10 Hz with 8 s stimulus duration, as well as pulse-width-dependent hemodynamic responses at 5, 10, 15, and 20 ms with 15 s stimulus duration, from one representative rat

targeted regions with limited diffusion (Fig. 5f and Supplementary Movie 7). The MgRA-driven microinjection was reproduced in multiple animals, suggesting a highly robust performance of the MgRA to target deep brain nuclei for injection purposes, as quantified in Fig. 5g. The high spatial specificity of MgRA-driven

microinjection can be used to improve the tract-tracing studies with MEMRI<sup>15,36–38</sup>, as well as to optimize the real-time in vivo neuromodulation or molecular MRI by direct intracranial injection of drugs<sup>42–44</sup> and MRI contrast sensors for neurotransmitters<sup>45–49</sup>.

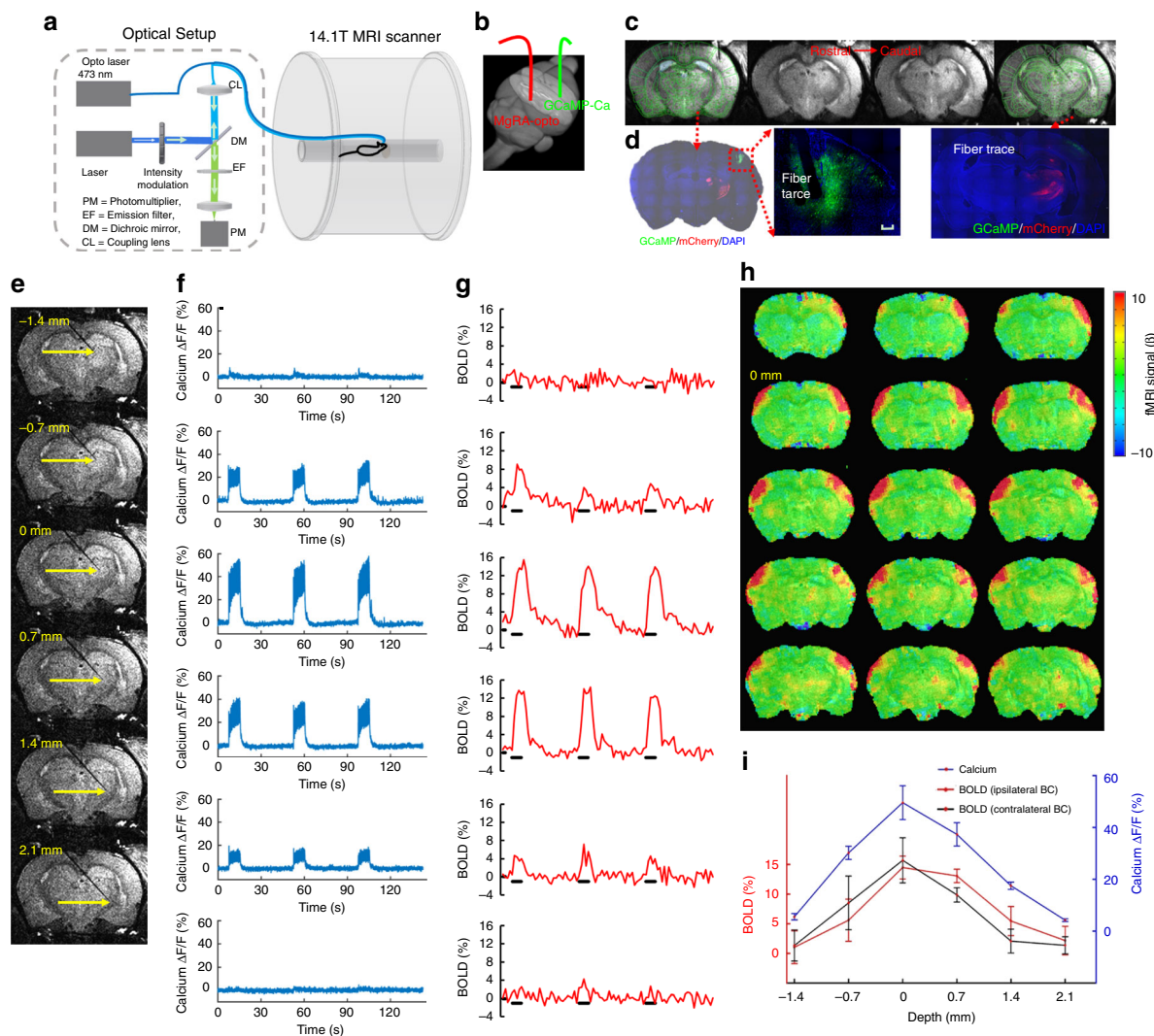


**Fig. 4** MgRA-driven stepwise optogenetic activation of the thalamic nuclei with simultaneous fMRI and neuronal  $\text{Ca}^{2+}$  recordings. **a** Schematic drawing of the experimental setup to conduct optogenetic fMRI with simultaneous fiber optic calcium recording. The optical setup was placed outside the 14.1 T scanner. Opto Laser: laser for optogenetics. **b** Schematic of the fiber optic insertion inside the rat brain (3D view) with MgRA-controlled optical fiber for optogenetic activation (red) and a second optical fiber for calcium recording (green) in the barrel cortex. **c** The anatomical MRI images confirm the location of the recording fiber and the stimulation fiber targeting the VPM thalamic region. The brain atlas is superimposed on the anatomical image (green). **d** The immunostaining images show the ChR2 expression in the thalamic region (ChR2-mCherry marked in red), as well as the GCaMP6f expression (green) in the vibrissal S1 cortical neurons (BC) with the fiber trace. Scale bar, 200  $\mu\text{m}$ . **e** Anatomical RARE MR images illustrate the fiber tip location at 6 steps, at a step-size of 700  $\mu\text{m}$ . **f** Percentage changes of the evoked calcium signal for 3 epochs upon light stimulation (3 Hz, 10 ms pulse width, 3.7 mW laser power, 8 s on 37 s off block design). **g** Simultaneous BOLD signals for 3 epochs within the ipsilateral somatosensory cortex (see (h)). **h** Evoked BOLD fMRI map when the fiber tip was positioned at 0 mm along the insertion trajectory (zero considered as the position that leads to the peak fMRI and calcium signals). **i** Average amplitudes of the ipsilateral evoked calcium and BOLD signals of both hemispheres as a function of the fiber tip locations. Error bars represent mean  $\pm$  SD

## Discussion

This work presents an MRI compatible robotic arm as the navigation technique for accurate placement of optical fibers in multi-modal fMRI studies in animals using ultra high-field MRI (14.1 T scanner). The MgRA was first developed and improved with a series of phantom tests and was posteriorly evaluated in vivo for deep brain optical fiber placement. MgRA-driven optogenetic activation at subcortical nuclei, e.g., LH and VPM, in a stepwise manner not only demonstrates the high precision of MgRA to target subcortical brain nuclei as deep as 8–9 mm from the skull surface, but also increases the reproducibility of the region-specific optogenetic activation for the whole-brain fMRI mapping in combination with the concurrent fiber optic calcium recordings. Also noted is that the mobility range of the MgRA (10 mm

in the rostral–caudal and medial–lateral directions) is sufficient to reach any brain structure in small animals for optogenetic fMRI and intracellular calcium recording. In addition, the MgRA was applied for real-time microinjection to specific deep brain nuclei, as demonstrated with an Mn-enhanced MRI method, demonstrating its microinjection capabilities for contrast agent or drug delivery with high precision inside the MRI scanner.

The main challenge when targeting deep brain structures is the potential error that appears between the actual and the calculated coordinates due to the variability in bregma location, skull thickness/angles, and potential shift of brain structures within the cranium after dura removal<sup>50–52</sup>. This potential error is particularly problematic when targeting some functional nuclei or neuronal fiber tracts of the rat brain that are less than 2–300  $\mu\text{m}$  in



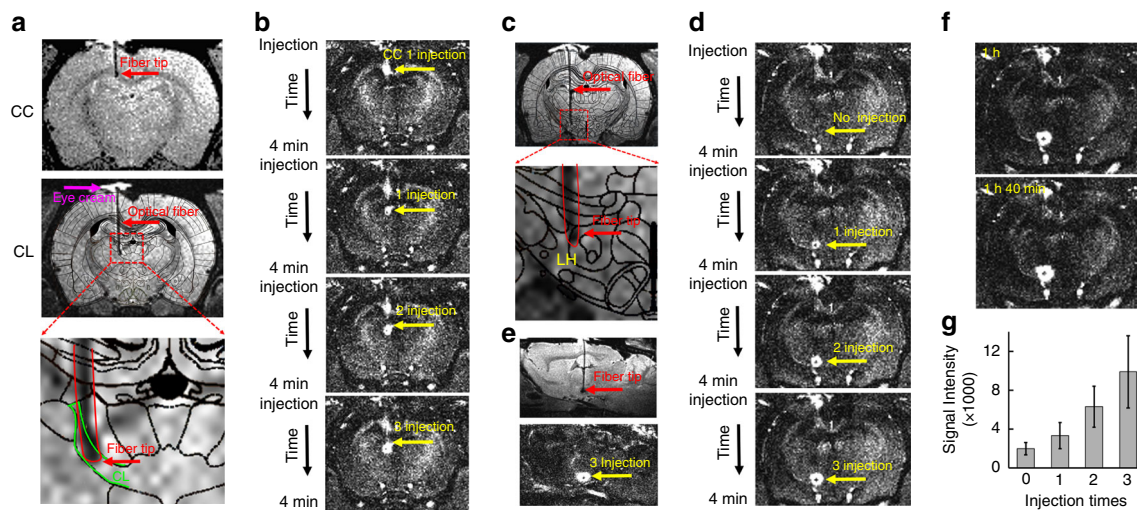


**Fig. 5** MgRA-driven Mn-injection into CL and LH. **a** Top: the representative RARE anatomical image used to clarify the optical fiber location driven by MgRA for Mn injection in CC. Middle: the atlas overlapped RARE images to illustrate the fiber tip location at the CL. Eye cream is covering the craniotomy (magenta arrow). Bottom: enlarged image of fiber location. **b** T1-weighted MPRAGE image (Mdef) showing enhanced signal from Mn injection site in the CC and CL with dose-dependency. **c** Top: the atlas overlapped RARE images to illustrate the fiber tip location at the LH, Bottom: enlarged image of fiber location. **d** T1-weighted MPRAGE image showing enhanced signal from Mn injection site in the LH with dose-dependency. **e** Sagittal view of RARE anatomical image and MPRAGE image after  $\text{MnCl}_2$  solution injection. **f** T1-weighted MPRAGE image at 1 h and 1 h 40 min after the injection. **g** The analysis of MEMRI signal at no injection, 1 injection, 2 injection, and 3 injection times, as shown in (b, d) ( $n = 5$  injection points from 3 animals). Error bars represent mean  $\pm$  SD

one of their dimensions, such as the central thalamic nuclei or corpus callosum fibers<sup>38,53</sup>. This problem can produce high variability when we try to target the deeper brain nuclei, e.g., LH, since longer trajectories are subjected to larger errors<sup>8,14</sup>. In order to optimize the positioning of the optical fiber into precise coordinates of the rat brain, we propose to avoid the atlas-based blind implantation by using a real-time feedback strategy that allows visualization of the whole brain with MRI during fiber insertion. We designed an MRI-compatible robotic arm which allows lowering the optical fiber inside the rat brain with real-time MRI scanning. By combining MRI guidance with the precise control of four stereotactic parameters (radial angle, rostral-caudal, dorsal-ventral, medial-lateral), the MgRA can fine-tune the fiber positioning to conduct highly reproducible and stepwise optogenetic fMRI studies.

The number of applications for robotic arms in animal research is considerably increased as a result of their potential combination with MRI. Examples include an MR image-guided mini-DBS system for BOLD activation during subthalamic nucleus DBS in nonhuman primates in a 3 T scanner<sup>26</sup>, an angle positioning system to increase the image signal intensity of fibrous microstructure in a 9.4 T 12 cm-bore scanner<sup>27</sup>, an integrated system, driven by piezoelectric actuators, for auto-tuning of a multichannel transceiver array at 7 T<sup>28</sup> or MRI-compatible systems for focused ultrasound experiments in rodents in 3 T scanners<sup>54,55</sup>. Here, we developed a stepper motor-controlled compacted MgRA system in a 14.1 T horizontal MRI scanner with built-in MRI compatible cameras and RF surface coils to drive fiber optic insertion for optogenetic fMRI studies with concurrent intracellular calcium recordings. To our knowledge, this is the first time to combine the multi-modal fMRI neuroimaging platform with the MRI-guided robotic controlling system for in vivo rodent brain functional mapping.

There are two key advantages that need to be highlighted from the mechanical design of the MgRA system. In high-field MRI scanners, the open space inside the magnetic bore above the animal brain is usually less than 3–4 cm, which significantly limits the kinematic design options for mechanical movement. Also, the

ultra-high field ( $>11.7$  T) also limits the commercially available motor supplies that avoid the electromagnetic interference with the MR scanning. We designed the MgRA head-probe based on an Archimedean spiral mechanism to achieve high precision and accuracy to maneuver the optical fiber insertion at less than 50  $\mu\text{m}$  step-size along the dorsal-ventral axis (Fig. 1g, Supplementary Fig. 11, and Supplementary Movie 4). This head-probe is controlled by a synchronous belt drive, which can carry up to 4 degree-of-freedom movements inside the horizontal bore of the 14.1 T MRI scanner (Supplementary Fig. 12), and only occupies 1.5–2 cm space.

To deal with the MRI compatibility, in addition to hydraulic<sup>56,57</sup> or pneumatic<sup>27,58–60</sup> actuators, other types such as ultrasonic or piezoelectric motors, which have been the favorite so far due to their non-magnetic core, short response time and small size<sup>61,62</sup>, could have been utilized. However, no commercially available piezo motors are available for the 14.1 T MRI scanner and it has been recently shown that piezo motors could induce geometric distortions in MR images even at a lower magnetic field strength<sup>63,64</sup>. Also, different MRI sequences could have effects on the behavior of ultrasonic motors<sup>65</sup>. To address the compatibility issue, remotely actuated MR-compatible manipulators were implemented using drive shafts, belts, chain drive, and linkages to transfer the motion to the distant actuated points<sup>66–68</sup>. We have applied the long robotic arm to allow us to apply the regular stepper motor to control the optical fiber insertion. As shown in the Supplementary Movies 2–5, the mechanical control of the optical fiber insertion remains highly precise and reliable in both ex vivo and in vivo tests. Our MgRA design not only provides a highly robust mechanical controlling system, but also solves the MRI compatibility issue with a reliable and economically affordable solution. We will further optimize our MgRA system by shortening the robotic arm and implementing the piezo motors with a safe distance to avoid electromagnetic interference.

Besides fulfilling the role of accurately placing the fiber tip at the desired coordinates, the MgRA provides a flexible platform (Fig. 1g) to identify, de novo, the ideal targets for deep brain

stimulation in pre-clinical studies. This could be easily investigated with the MgRA by moving the stimulating fiber and running opto-fMRI at different locations in one single study, particularly for “hypothesis-free” brain activity mapping studies. This application will be critical to optimize and specify the ideal subcortical targets aiming at controlling pathological tremor or searching for more reliable treatment for depression in animal models<sup>69–71</sup>. Importantly, certain effects inherent in the insertion of electrodes or optical fiber into the brain can be visualized and avoided using the MgRA strategy. One example is the case of the potential collateral damage to the choroid plexus (Fig. 2c) or other blood vessels, which could be well monitored by real-time imaging and avoided by changing the trajectory of the fiber. This is a particularly relevant feature of the MgRA, as it contributes to the maintenance of certain integrity of the surrounding tissue, which is beyond the capabilities of the standard implantation techniques with stereotactic devices and is crucial for potentially translational studies, as raised in a report showing MRI-guided cell transplantation into the brain<sup>72</sup>.

Several limitations pertaining to the first version of the MgRA should be considered when interpreting the results of this study and for future optimization of the MgRA in high field MRI scanner for animal imaging. Firstly, the angle/direction of the optical fiber cannot be changed once that it has been placed inside the brain parenchyma, as this would lead to excessive tissue damage and/or bleeding. Instead, in case needed, the optical fiber should be withdrawn and reinserted; thus it is crucial to improve the algorithm to calculate the trajectory based on the location of the optical fiber tip in the agarose covering the craniotomy outside of the brain parenchyma. Secondly, it is noteworthy that, because of the long arm to keep the stepper motors work properly outside of the MRI scanner, the most precise movement occurs along the ventral–dorsal direction (Fig. 1g and Supplementary Movie 4). It will be an important step forward to implement the piezo motors with a safe distance to avoid electromagnetic interference, which would allow to dramatically shorten the robotic arm and, consequently, to optimize of the precision in all the axis. Thirdly, although we acquired the 3D anatomical images of the rat brain, the major registration procedure between atlas and MRI images is still based on a 2D registration algorithm, which is applied to control the fiber tip movement along the dorsal–ventral direction. In the future development, we will provide a real-time 3D registration system to take advantage of the full motor control movement capability of the MgRA system to achieve a fully automatic performance. Lastly, the precision measurement of the MgRA can be directly evaluated based on the real-time anatomical MRI images. However, the best resolution acquired so far in our MRI scanner is  $50 \times 50 \mu\text{m}$  in-plane. The MRI spatial resolution is much lower than the mechanistic movement precision provided by the MgRA system. For future piezo-based micron-resolution motor control system, the implementation of an optical encoder inside the ultra-high magnetic field will be needed for the close-loop feedback.

In summary, the real-time MRI-guidance in a robotic controlling system is verified and practiced for the optical fiber brain intervention in animals using the high field MRI scanner ( $>14\text{ T}$ ). This MgRA positioning system serves as a key component for the future multi-modal fMRI platform merging concurrent fMRI with optogenetics, fiber optic-mediated optical imaging, micro-injection, and even electrophysiological recordings. The high flexibility and precision of MgRA to target the deep brain nuclei with neural circuit-specificity expands the brain functional mapping studies from the cellular levels, to the neural circuit levels, and eventually to the systems' levels in combination with behavioral tests in animals.

## Methods

**MgRA system.** The MgRA was manufactured by the Fine Mechanical and Electrical Workshop in the Max Planck Institute for Biological Cybernetics, Tuebingen, Germany. This system consists of a positioning module, the head of the MgRA, and a custom-designed user interface. The positioning module (back part) accommodates the stepper motors (ST4118D1804-B, Nanotec, Germany) to fulfill the optical fiber movement with multi-degree of freedom, and the head of the MgRA (front part) includes the driving pieces, cameras, and a customized rat holder (Fig. 1b). The coupling of the actuators (back part) to the matching toothed pulley in the head was achieved by a synchronous belt (Optibelt OMEGA 3M, OPTI-BELT, Germany) drive in a form-fit manner. The driving pieces with Archimedean spiral mechanism were manufactured manually or with a 3D printer (Form 2, Formlabs, Germany). The detailed design and components are shown in Fig. 1a–c, Supplementary Figs. 11–13, with a table of all components and the European patent as the following link: <https://patentscope.wipo.int/search/en/detail.jsf?docId=EP215319263&tab=PCTDESCRIPTION&maxRec=1000>. The movements include three dimensions like conventional stereotactic devices, as well as pitch and yaw (manually). With MRI-compatible cameras (RS-OV7949-1818, Conrad Electronic, Germany), the user can watch the fiber insertion in real time, while the robot is executing a maneuver. If any movement needs to be modified, the user can start, stop, change, or resume the fiber movement at any time from the user-interface. Most of the other components are constructed from fully MRI-compatible materials like plastic, carbon fiber, and a minimal amount of non-ferrous metals like brass and anodized aluminum to avoid eddy currents and deterioration of magnetic field homogeneity. The MRI-compatible arm including the head part and aluminum holder were placed inside the MRI scanner room. Digital components including stepper motors (ST4118D1804-B, Nanotec, Germany), the motor controller (SMC133-1, Nanotec, Germany) and motor power supply (NTS-24V-40A, Nanotec, Germany), were placed outside the scanner room (Supplementary Fig. 1).

**Viral injection.** The study was performed in accordance with the German Animal Welfare Act (TierSchG) and Animal Welfare Laboratory Animal Ordinance (TierSchVersV). This is in full compliance with the guidelines of the EU Directive on the protection of animals used for scientific purposes (2010/63/EU). The study was reviewed by the ethics commission (§15 TierSchG) and approved by the state authority (Regierungspräsidium, Tübingen, Baden-Württemberg, Germany). A total of 21 male Sprague–Dawley rats were used in this study.

Intracerebral viral injection was performed in 3–4-week-old male Sprague–Dawley to express the viral vectors containing the calcium-sensitive protein (GCaMP for calcium recording) or the light-sensitive protein channelrhodopsin-2 (ChR2 for optogenetics) in neurons. The construct AAV5.Syn.GCaMP6f.WPRE.SV40 (2.818e13 genome copies per milliliter) was used to express GCaMP in the BC and the constructs AAV9.CAG.hChR2(H134R)-mCherry.WPRE.SV40 (2.918e13 genome copies per milliliter) and AAV9.CaMKII.hChR2(E123A)-eYFP.WPRE.hGH (1.19e13 genome copies per milliliter) were used to express ChR2 in the thalamus and LH, respectively. Rats were anesthetized with 1.5–2% isoflurane via nose cone and placed on a stereotaxic frame, an incision was made on the scalp and the skull was exposed. Craniotomies were performed with a pneumatic drill so as to cause minimal damage to cortical tissue. For optogenetics, a volume of 0.6–1  $\mu\text{L}$  was injected using a 10  $\mu\text{L}$  syringe and 33-gauge needle. The injection rate was controlled by an infusion pump (Pump 11 Elite, Harvard Apparatus, USA). The stereotaxic coordinates of the injections were 2.5 mm posterior to Bregma, 5.0 mm lateral to the midline, 0.8–1.4 mm below the cortical surface to target the BC; 2.6–2.7 mm posterior to Bregma, 2.8 mm lateral to the midline, 5.5–6.0 mm below the cortical surface for the ventral posterior medial nucleus of thalamus (VPM); and 2.75–2.85 mm posterior to Bregma, 1.1 mm lateral to the midline, 7.5–7.9 mm below the cortical surface for LH. After injection, the needle was left in place for approximately 5 min before being slowly withdrawn. The craniotomies were sealed with the bone wax and the skin around the wound was sutured. Rats were subcutaneously injected with antibiotic and painkiller for 3 consecutive days to prevent bacterial infections and relieve postoperative pain.

**Animal preparation for fMRI.** Anesthesia was first induced in the animal with 5% isoflurane in chamber. The anesthetized rat was intubated using a tracheal tube and a mechanical ventilator (SAR-830, CWE, USA) was used to ventilate animals throughout the whole experiment. Femoral arterial and venous catheterization was performed with polyethylene tubing for blood sampling, drug administration, and constant blood pressure measurements. After the surgery, isoflurane was switched off and a bolus of the anesthetic alpha-chloralose (80 mg/kg) was infused intravenously. A mixture of Alpha-Chloralose (26.5 mg/kg/h) and pancuronium (2 mg/kg/h) was constantly infused to maintain the anesthesia/keep the animal anesthetized and reduce motion artifacts.

**Fiber optic implantation and optogenetic stimulation.** Before transferring the animal to the MRI scanner, 2 craniotomies were performed. Briefly, the animal was placed on a stereotaxic frame, the scalp was opened and two  $\sim 1.5$  mm diameter burr holes were drilled on the skull. The dura was carefully removed and an optical fiber with 200  $\mu\text{m}$  core diameter (FT200EMT, Thorlabs, Germany) was inserted

into the BC, at coordinates: 2.75–3.3 mm posterior to Bregma, 5.0 mm lateral to the midline, 1.2–1.4 mm below the cortical surface. An adhesive gel was used to secure the calcium recording fiber to the skull. The craniotomy for optogenetics (in VPM or LH) was covered by agarose gel for robotic arm-driven fiber insertion inside the MRI scanner. Toothpaste was applied within the ears to minimize MR susceptibility artifacts for the whole brain fMRI mapping. The eyes of the rats were covered to prevent stimulation of the visual system during the light-driven fMRI.

For optogenetic stimulation, square pulses of blue light (473 nm) were delivered using a laser (MBL-III, CNI, China) connected to the 200  $\mu\text{m}$  core optical fiber (FT200EMT, Thorlabs, Germany) and controlled by Master 9 (Master-9, A.M.P.I., Israel). The light intensity was tested before each experiment, and was calibrated with a power meter (PM20A, Thorlabs, Germany) to emit 0.6–40 mW from the tip of the optical fiber for LH and thalamus. The power levels used for light-driven fMRI studies did not induce pseudo-BOLD signal due to heating effects, by testing in regions of interest both with and without ChR2 expression.

**Immunohistochemistry.** To verify the phenotype of the transfected cells, opsin localization, and optical fiber placement, perfused rat brains were fixed overnight in 4% paraformaldehyde and then equilibrated in 15 and 30% sucrose in 0.1 M PBS at 4 °C. 30  $\mu\text{m}$ -thick coronal sections were cut on a cryotome (CM3050S, Leica, Germany). Free-floating sections were washed in PBS, mounted on microscope slides, and incubated with DAPI (VectaShield, Vector Laboratories, USA) for 30 min at room temperature. Wide-field fluorescent images were acquired using a microscope (Zeiss, Germany) for assessment of GCaMP expression in BC, ChR2 in LH and VPM. Digital images were minimally processed using ImageJ to enhance brightness and contrast for visualization purposes.

**Optical setup.** An OBIS laser was used as excitation light source (OBIS 488LS, Coherent, Germany) with a heat sink to enable laser operation throughout the entire specified temperature range from 10 to 40 °C. The light passed through a continuously variable neutral density filter (NDC-50C-2M-B, Thorlabs, Germany) and was reflected on a dichroic beam splitter (F48-487, AHF analysentechnik AG, Germany). The beam was collected into an AR coated achromatic lens (AC254-030-A, Thorlabs, Germany) fixed on a threaded flexure stage (HCS013, Thorlabs, Germany) mounted on an extension platform (AMA009/M, Thorlabs, Germany) of a fiber launch system (MAX350D/M, Thorlabs, Germany). The laser beam was injected into the fiber and propagated to the tip. The emitted fluorescence was collected through the fiber tip, propagated back and collimated by the achromatic lens, passed through the dichroic beam splitter and filtered by a band-pass filter (ET525/50M, Chroma, USA) and focused by an AR coated achromatic lens (AC254-030-A, Thorlabs, Germany). A silicon photomultiplier module (MiniSiM 10035, SensL, Germany) was applied to detect the emitted fluorescence. The entire optical system was enclosed in a light isolator box. The photomultiplier output was amplified (gain = 100) by a voltage amplifier (DLPVA-100-BLN-S, Femto, Germany), digitized and detected by Biopac system (MP150 System, BIOPAC Systems, USA).

**MRI image acquisition.** All images were acquired with a 14.1 T/26 cm horizontal bore magnet interfaced to an Avance III console and equipped with a 12 cm gradient set capable of providing 100 G/cm over a time of 150  $\mu\text{s}$ . A transceiver single-loop surface coil with an inner diameter of 22 mm was placed directly over the rat head to acquire anatomical and fMRI images. Magnetic field homogeneity was optimized first by global shimming for anatomical images and followed by FASTMAP shimming protocol for EPI sequence.

Anatomical images were acquired for approximate fiber location using 3D FLASH MRA sequence with the following parameters: repetition time, 20 ms; echo time, 2.82 ms; FOV: 2.28 cm  $\times$  2.28 cm  $\times$  2.28 cm, matrix = 114  $\times$  114  $\times$  114, spatial resolution = 0.2 mm  $\times$  0.2 mm  $\times$  0.2 mm. A high-resolution RARE sequence was used accurately identify the optical fiber in the coronal plane, with the following parameters: repetition time, 1200 ms; echo time, 7 ms; FOV: 1.92 cm  $\times$  1.68 cm, matrix = 128  $\times$  112, resolution = 0.15 mm  $\times$  0.15 mm, slice thickness = 0.5 mm, RARE factor = 8, averages = 16.

Higher resolution (50  $\mu\text{m}$ ) RARE sequence, specifically for Fig. 1f, g, to accurately identify the optical fiber in the coronal plane, with the following parameters: repetition time, 1500 ms; echo time, 11.0428 ms; FOV: 1.92 cm  $\times$  1.56 cm, matrix = 384  $\times$  312, resolution = 50  $\mu\text{m}$   $\times$  50  $\mu\text{m}$ , slice thickness = 0.75 mm, RARE factor = 6, averages = 6.

For Mn injections and Mn tracing studies, rats received 150 nL of 5 mM MnCl<sub>2</sub> (MnCl<sub>2</sub>, Sigma-Aldrich, Germany) solution for three times delivered by a hollow core photonic crystal fiber (diameter: ~240  $\mu\text{m}$ )<sup>39–41</sup>, manufactured by the Division of Photonic Crystal Fibre Science at Max-Planck Institute for the Science of Light, Erlangen, Germany. A magnetization prepared rapid gradient echo (MP-RAGE) sequence<sup>35</sup> was used. Eight coronal slices with FOV = 1.92  $\times$  1.92 cm, matrix 128  $\times$  128, thickness = 0.7 mm, (TR = 4000 ms, echo TR/TE = 15/1.7 ms, TI = 1000 ms, number of segments = 4, averages = 2), were used to cover the area of interest at 150  $\mu\text{m}$  in-plane resolution with total imaging time 4 min 16 s. A same field of view T2-weighted RARE sequence was used with the following parameters: repetition time, 3000 ms; echo time, 8.3333 ms; FOV: 1.92 cm  $\times$  1.92 cm, matrix = 128  $\times$  128,

resolution = 150  $\mu\text{m}$   $\times$  150  $\mu\text{m}$ , slice thickness = 0.7 mm, RARE factor = 6, averages = 4.

**Functional MRI acquisition.** Adjustments to echo spacing and symmetry, and B<sub>0</sub> compensation were set up first. Functional images were acquired with a 3D gradient-echo EPI sequence with the following parameters: echo time 12.5 ms, repetition time 1.5 s, FOV 1.92 cm  $\times$  1.92 cm  $\times$  1.92 cm, 48  $\times$  48  $\times$  48 matrix size, spatial resolution = 0.4 mm  $\times$  0.4 mm  $\times$  0.4 mm. To reach steady state 10 dummy scans were used. For anatomical reference, the RARE sequence was applied to acquire 48 coronal slices with the same geometry of the fMRI images.

For fMRI studies, needle electrodes were placed on the forepaw or whisker pads of the rats, and electric pulses (333  $\mu\text{s}$  duration at 1.5 mA repeated at 3 Hz for 4 s) were first used as stimulation to serve as positive control for the evoked BOLD signal. Once that reliable fMRI signals were observed in response to electrical stimulation, optical stimulation was performed. An optical fiber of 200  $\mu\text{m}$  core diameter (FT200EMT, Thorlabs, Germany) was connected to a 473 nm laser source (MBL-III, CNI, China) using a built-in FC/PC coupler to deliver blue light pulses at 3–10 Hz, 5–20 ms pulse width with different durations. To reach steady state 10 dummy scans were used and followed by 10 pre-stimulation scans, 5 scans during stimulation, and 25 inter-stimulation scans for 10 epochs and 5 scans during stimulation and 35 inter-stimulation scans for 12 epochs for thalamus and LH, respectively. The stimulation control was established using the BIOPAC system (MP150 System, BIOPAC Systems, USA) and Master 9 (Master-9, A.M.P.I., Israel).

**Data analysis.** For evoked fMRI analysis, EPI images were first aligned to anatomical images acquired in the same orientation with the same geometry. The anatomical MRI images were registered to a template across animals, as well as EPI datasets. The baseline signal of EPI images was normalized to 100 for statistical analysis of the multiple runs of EPI time courses. The hemodynamic response function (HRF) used the block function of the linear program 3dDeconvolve in AFNI. BLOCK (*L*, 1) is a convolution of a square wave of duration *L*, makes a peak amplitude of block response = 1, with the  $g(t) = t^4 e^{-t}/[4^4 e^{-4}]$  (peak value = 1). The HRF model is defined as follows:

$$\text{HRF}(t) = \text{int}(g(t-s), s = 0.. \text{min}(t, L))$$

In this case, each beta weight represents the peak height of the corresponding BLOCK curve for that class, i.e., the beta weight is the magnitude of the response to the entire stimulus block.

The fiber optical neuronal calcium signals were low-pass filtered at 100 Hz using zero-phase shift digital filtering. The relative percentage change of fluorescence ( $\Delta F/F$ ) was defined as  $(F - F_0)/F_0$ , where  $F_0$  is the baseline, that is to say, the average fluorescent signal in a 2 s pre-stimulation window. The amplitudes of the neuronal fluorescent signal in response to 4 s optogenetic stimulus (Fig. 4f) were calculated as the average of difference in  $\Delta F/F$  in a time window 300 ms after stimulus. Error bars in Figs. 3c, 4i, 5g, and Supplementary Fig. 10f represent standard deviation.

**Reporting summary.** Further information on research design is available in the Nature Research Reporting Summary linked to this article.

## Data availability

The raw data can be provided upon email request to the corresponding author. Excel files containing raw data and each quantitative plot included in the main figures can be found in the Source Data File. For the design of the robotic arm, detailed information can be directly downloaded through the official link of World Intellectual Property Organization (WIPO): <https://patentscope.wipo.int/search/en/detail.jsf?docId=EP215319263&tab=NATIONALBIBLIO&maxRec=1000>.

## Code availability

The Analysis of Functional NeuroImages software (AFNI, NIH, USA) and Matlab (MATLAB, MathWorks, USA) were used to process the fMRI and simultaneously acquired calcium signals, respectively. The relevant source codes can be downloaded through <https://afni.nimh.nih.gov/afni/>. The related image processing codes can be provided upon direct email request to the corresponding author.

Received: 11 August 2018 Accepted: 11 May 2019

Published online: 10 June 2019

## References

1. Yu, X.: When Photons Meet Protons: Optogenetics, Calcium Signal Detection, and fMRI in Small Animals. In: *Small Animal Imaging: Basics and Practical Guide*, pp. 773 – 791 (Eds Kiessling, F., Pichler, B.J. & Hauff, P.). (Springer, Cham, Switzerland 2017).

2. Lee, J. H. et al. Global and local fMRI signals driven by neurons defined optogenetically by type and wiring. *Nature* **465**, 788–792 (2010).
3. Yu, X. et al. Sensory and optogenetically driven single-vessel fMRI. *Nat. Methods* **13**, 337–340 (2016).
4. Wang, M., He, Y., Sejnowski, T. J. & Yu, X. Brain-state dependent astrocytic Ca(2+) signals are coupled to both positive and negative BOLD-fMRI signals. *Proc. Natl. Acad. Sci. USA* **115**, E1647–E1656 (2018).
5. He, Y. et al. Ultra-slow single-vessel BOLD and CBV-based fMRI spatiotemporal dynamics and their correlation with neuronal intracellular calcium signals. *Neuron* **97**, 925–939 (2018).
6. Logothetis, N. K., Pauls, J., Augath, M., Trinath, T. & Oeltermann, A. Neurophysiological investigation of the basis of the fMRI signal. *Nature* **412**, 150–157 (2001).
7. Schulz, K. et al. Simultaneous BOLD fMRI and fiber-optic calcium recording in rat neocortex. *Nat. Methods* **9**, 597–602 (2012).
8. Liu, J. et al. Frequency-selective control of cortical and subcortical networks by central thalamus. *eLife* **4**, e09215 (2015).
9. Ferenczi, E. A. et al. Prefrontal cortical regulation of brainwide circuit dynamics and reward-related behavior. *Science* **351**, aac9698 (2016).
10. Kim, C. K. et al. Simultaneous fast measurement of circuit dynamics at multiple sites across the mammalian brain. *Nat. Methods* **13**, 325–328 (2016).
11. Marshall, J. D. et al. Cell-type-specific optical recording of membrane voltage dynamics in freely moving mice. *Cell* **167**, 1650–1662 (2016).
12. Tian, L. et al. Imaging neural activity in worms, flies and mice with improved GCaMP calcium indicators. *Nat. Methods* **6**, 875–881 (2009).
13. Chen, T. W. et al. Ultrasensitive fluorescent proteins for imaging neuronal activity. *Nature* **499**, 295–300 (2013).
14. Resendez, S. L. et al. Visualization of cortical, subcortical and deep brain neural circuit dynamics during naturalistic mammalian behavior with head-mounted microscopes and chronically implanted lenses. *Nat. Protoc.* **11**, 566–597 (2016).
15. Yu, X., Qian, C., Chen, D. Y., Dodd, S. J. & Koretsky, A. P. Deciphering laminar-specific neural inputs with line-scanning fMRI. *Nat. Methods* **11**, 55–58 (2014).
16. Dergacheva, O., Yamanaka, A., Schwartz, A. R., Polotsky, V. Y. & Mendelowitz, D. Optogenetic identification of hypothalamic orexin neuron projections to paraventricular spinally projecting neurons. *Am. J. Physiol. Heart Circ. Physiol.* **312**, H808–H817 (2017).
17. Kosse, C., Schone, C., Bracey, E. & Burdakov, D. Orexin-driven GAD65 network of the lateral hypothalamus sets physical activity in mice. *Proc. Natl. Acad. Sci. USA* **114**, 4525–4530 (2017).
18. Carter, M. E. et al. Tuning arousal with optogenetic modulation of locus coeruleus neurons. *Nat. Neurosci.* **13**, 1526–1533 (2010).
19. Sparta, D. R. et al. Construction of implantable optical fibers for long-term optogenetic manipulation of neural circuits. *Nat. Protoc.* **7**, 12–23 (2011).
20. Li, G. et al. Robotic system for MRI-guided stereotactic neurosurgery. *IEEE Trans. Biomed. Eng.* **62**, 1077–1088 (2015).
21. MacDonell, J. et al. Robotic assisted MRI-guided interventional interstitial MR guided focused ultrasound ablation in a swine model. *Neurosurgery* **84**, 1138–1148 (2018).
22. MacDonell, J. et al. Magnetic resonance-guided interstitial high-intensity focused ultrasound for brain tumor ablation. *Neurosurg. Focus* **44**, E11 (2018).
23. Starr, P. A. et al. Subthalamic nucleus deep brain stimulator placement using high-field interventional magnetic resonance imaging and a skull-mounted aiming device: technique and application accuracy. *J. Neurosurg.* **112**, 479–490 (2010).
24. Stoianovici, D. et al. Multi-imager compatible, MR safe, remote center of motion needle-guide robot. *IEEE Trans. Biomed. Eng.* **65**, 165–177 (2018).
25. Gassert, R., Moser, R., Burdet, E. & Bleuler, H. MRI/fMRI-compatible robotic system with force feedback for interaction with human motion. *IEEE/ASME Trans. Mech.* **11**, 216–224 (2006).
26. Min, H. K. et al. Subthalamic nucleus deep brain stimulation induces motor network BOLD activation: use of a high precision MRI guided stereotactic system for nonhuman primates. *Brain Stimul.* **7**, 603–607 (2014).
27. Squires, A. et al. MAPS—a magic angle positioning system for enhanced imaging in high-field small-bore MRI. *J. Med. Robot. Res.* **1**, 1640004 (2016).
28. Keith, G. A. et al. Automated tuning of an eight-channel cardiac transceiver array at 7 Tesla using piezoelectric actuators. *Magn. Reson. Med.* **73**, 2390–2397 (2015).
29. Ryali, S. et al. Combining optogenetic stimulation and fMRI to validate a multivariate dynamical systems model for estimating causal brain interactions. *NeuroImage* **132**, 398–405 (2016).
30. Lin, P., Fang, Z., Liu, J., Lee, J. H. Optogenetic Functional MRI. *J. Vis. Exp.* **110**, e53346, (2016). <https://doi.org/10.3791/53346>.
31. Bonnavion, P., Mickelsen, L. E., Fujita, A., de Lecea, L. & Jackson, A. C. Hubs and spokes of the lateral hypothalamus: cell types, circuits and behaviour. *J. Physiol.* **594**, 6443–6462 (2016).
32. Boyden, E. S., Zhang, F., Bamberg, E., Nagel, G. & Deisseroth, K. Millisecond-timescale, genetically targeted optical control of neural activity. *Nat. Neurosci.* **8**, 1263–1268 (2005).
33. Liu, J. V. et al. fMRI in the awake marmoset: somatosensory-evoked responses, functional connectivity, and comparison with propofol anesthesia. *NeuroImage* **78**, 186–195 (2013).
34. Yen, C. C., Papoti, D. & Silva, A. C. Investigating the spatiotemporal characteristics of the deoxyhemoglobin-related and deoxyhemoglobin-unrelated functional hemodynamic response across cortical layers in awake marmosets. *NeuroImage* **164**, 121–130 (2018).
35. Mugler, J. P. 3rd & Brookeman, J. R. Three-dimensional magnetization-prepared rapid gradient-echo imaging (3D MP RAGE). *Magn. Reson. Med.* **15**, 152–157 (1990).
36. Pautler, R. G., Silva, A. C. & Koretsky, A. P. In vivo neuronal tract tracing using manganese-enhanced magnetic resonance imaging. *Magn. Reson. Med.* **40**, 740–748 (1998).
37. Pautler, R. G. & Koretsky, A. P. Tracing odor-induced activation in the olfactory bulbs of mice using manganese-enhanced magnetic resonance imaging. *NeuroImage* **16**, 441–448 (2002).
38. Yu, X. et al. Thalamocortical inputs show post-critical-period plasticity. *Neuron* **74**, 731–742 (2012).
39. Cregan, R. F. et al. Single-mode photonic band gap guidance of light in air. *Science* **285**, 1537–1539 (1999).
40. Russell, P. Photonic crystal fibers. *Science* **299**, 358–362 (2003).
41. Knight, J. C., Birks, T. A., Russell, P. S. & Atkin, D. M. All-silica single-mode optical fiber with photonic crystal cladding. *Opt. Lett.* **21**, 1547–1549 (1996).
42. Turchi, J. et al. The basal forebrain regulates global resting-state fMRI fluctuations. *Neuron* **97**, 940–952 (2018).
43. Saleem, K. S. et al. Magnetic resonance imaging of neuronal connections in the macaque monkey. *Neuron* **34**, 685–700 (2002).
44. Schmid, M. C. et al. Blindsight depends on the lateral geniculate nucleus. *Nature* **466**, 373–377 (2010).
45. Okada, S. et al. Calcium-dependent molecular fMRI using a magnetic nanosensor. *Nat. Nanotechnol.* **13**, 473–477 (2018).
46. Ghosh, S., Harvey, P., Simon, J. C. & Jasanoff, A. Probing the brain with molecular fMRI. *Curr. Opin. Neurobiol.* **50**, 201–210 (2018).
47. Hai, A., Cai, L. X., Lee, T., Lelyveld, V. S. & Jasanoff, A. Molecular fMRI of serotonin transport. *Neuron* **92**, 754–765 (2016).
48. Lee, T., Cai, L. X., Lelyveld, V. S., Hai, A. & Jasanoff, A. Molecular-level functional magnetic resonance imaging of dopaminergic signaling. *Science* **344**, 533–535 (2014).
49. Barandov, A. et al. Sensing intracellular calcium ions using a manganese-based MRI contrast agent. *Nat. Commun.* **10**, 897 (2019).
50. Miyagi, Y., Shima, F. & Sasaki, T. Brain shift: an error factor during implantation of deep brain stimulation electrodes. *J. Neurosurg.* **107**, 989–997 (2007).
51. Kramer, D. R., Halpern, C. H., Danish, S. F., Jaggi, J. L. & Baltuch, G. H. The effect of intraventricular trajectory on brain shift in deep brain stimulation. *Stereotact. Funct. Neurosurg.* **90**, 20–24 (2012).
52. Pallavaram, S. et al. Effect of brain shift on the creation of functional atlases for deep brain stimulation surgery. *Int. J. Comput. Assist. Radiol. Surg.* **5**, 221–228 (2010).
53. Paxinos, G., Watson, C., Calabrese, E., Badaea, A. & Johnson, G. A. *MRI/DTI Atlas of the Rat Brain* (Elsevier, Academic Press, London, San Diego, 2015).
54. Chopra, R., Curiel, L., Staruch, R., Morrison, L. & Hynynen, K. An MRI-compatible system for focused ultrasound experiments in small animal models. *Med. Phys.* **36**, 1867–1874 (2009).
55. Yiannakou, M., Menikou, G., Yiallouras, C., Ioannides, C. & Damianou, C. MRI guided focused ultrasound robotic system for animal experiments. *Int. J. Med. Robot.* **13**, e1804 (2017). <https://doi.org/10.1002/rcs.1804>
56. Kim, D., Kobayashi, E., Dohi, T. & Sakuma, I. A new, compact MR-compatible surgical manipulator for minimally invasive liver surgery. *Lect. Notes Comput. Sci.* **2488**, 99–106 (2002).
57. Moser, R. et al. An MR compatible robot technology. *IEEE International Conference on Robotics and Automation*, 670–675 (2003).
58. Chen, Y. et al. Robotic system for MRI-guided focal laser ablation in the prostate. *IEEE/ASME Trans. Mech.* **22**, 107–114 (2017).
59. Franco, E., Ristic, M., Rea, M. & Gedroyc, W. M. Robot-assistant for MRI-guided liver ablation: a pilot study. *Med. Phys.* **43**, 5347 (2016).
60. Yoon, H. et al. Metabolomics of breast cancer using high-resolution magic angle spinning magnetic resonance spectroscopy: correlations with 18F-FDG positron emission tomography-computed tomography, dynamic contrast-enhanced and diffusion-weighted imaging MRI. *PLoS One* **11**, e0159949 (2016).
61. Su, H. et al. Piezoelectrically actuated robotic system for MRI-guided prostate percutaneous therapy. *IEEE/ASME Trans. Mech.* **20**, 1920–1932 (2015).
62. Tsekos, N. V., Khanicheh, A., Christoforou, E. & Mavroidis, C. Magnetic resonance-compatible robotic and mechatronics systems for image-guided

- interventions and rehabilitation: a review study. *Annu. Rev. Biomed. Eng.* **9**, 351–387 (2007).
63. Shokrollahi, P., Drake, J. M. & Goldenberg, A. A. Signal-to-noise ratio evaluation of magnetic resonance images in the presence of an ultrasonic motor. *Biomed. Eng. Online* **16**, 45 (2017).
  64. Shokrollahi, P., Drake, J. M. & Goldenberg, A. A. Ultrasonic motor-induced geometric distortions in magnetic resonance images. *Med. Biol. Eng. Comput.* **56**, 61–70 (2018).
  65. Shokrollahi, P., Drake, J. M. & Goldenberg, A. A. Comparing the effects of three MRI RF sequences on ultrasonic motors. *IFMBE Proc.* **51**, 846–849 (2015).
  66. Chinzei, K., Hata, N., Jolesz, F. A. & Kikinis, R. MR compatible surgical assist robot: system integration and preliminary feasibility study. *Medical Image Computing and Computer-Assisted Intervention—MICCAI 2000*, 921–930 (2000).
  67. Tajima, F. et al. A prototype master-slave system consisting of two MR-compatible manipulators with interchangeable surgical tools—part of a unified support system for diagnosis and treatment. *IEEE International Conference on Robotics and Automation Proceedings*, Vols. 1–5, 2505–2510 (2004).
  68. Tsekos, N. V., Ozcan, A. & Christoforou, E. A prototype manipulator for magnetic resonance-guided interventions inside standard cylindrical magnetic resonance imaging scanners. *J. Biomech. Eng. Trans. ASME* **127**, 972–980 (2005).
  69. Gradinaru, V., Mogri, M., Thompson, K. R., Henderson, J. M. & Deisseroth, K. Optical deconstruction of parkinsonian neural circuitry. *Science* **324**, 354–359 (2009).
  70. Plaha, P., Khan, S. & Gill, S. S. Bilateral stimulation of the caudal zona incerta nucleus for tremor control. *J. Neurol. Neurosurg. Psychiatry* **79**, 504–513 (2008).
  71. Ondo, W. G., Silay, Y., Almaguer, M. & Jankovic, J. Subthalamic deep brain stimulation in patients with a previous pallidotomy. *Mov. Disord.* **21**, 1252–1254 (2006).
  72. Silvestrini, M. T. et al. Interventional magnetic resonance imaging-guided cell transplantation into the brain with radially branched deployment. *Mol. Ther.* **23**, 119–129 (2015).

## Acknowledgements

The authors thank Mr. S. Yu for building up the first prototype of the robotic arm and Fine Mechanic and Electronic Workshop at MPI for Biological Cybernetics for MgRA system automation. The financial support of the Max-Planck-Society, the Sino-Germany joint grant by DFG (YU215/3-1645423), and the China Scholarship Council (Ph.D. fellowship to Y. Chen) are gratefully acknowledged. We thank the collaborative support from Dr. G.A. Johnson to provide the original 3D MRI/DTI dataset for image processing and Dr. G. Paxinos for the support of brain atlas (the permission was issued by Elsevier). The authors thank Dr. N. Avdievitch, Ms. H. Schulz, Mr. F.

Sobczak, Mr. J.K. Schlüsener, and Mr. H. Huang for technical support, Dr. P. Douay, Dr. E. Weiler, Ms. S. Fischer, and Mrs. M. Pitscheider for animal support, the AFNI team for the software support, the Genetically-Encoded Neuronal Indicator and Effector (GENIE) Program and the Janelia Farm Research Campus for kindly providing viral plasmids.

## Author contributions

X.Y. designed and supervised the research. Y.C., X.Y., P.P.-R., and X.C. performed animal experiments. Y.C., X.Y., and P.P.-R. acquired data. Y.C. analyzed data. X.C. and M.H.F. provided key technical support. X.Y. and Y.C. wrote the manuscript.

## Additional information

**Supplementary Information** accompanies this paper at <https://doi.org/10.1038/s41467-019-10450-3>.

**Competing interests:** X.Y. and Y.C. are co-authors of a patent that describes the mechanical design of the MRI-guided robotic arm (EP3315064). The other authors declare no competing interests.

**Reprints and permission** information is available online at <http://npg.nature.com/reprintsandpermissions/>

**Journal peer review information:** *Nature Communications* thanks Cornelius Faber, Gregory Fischer, and other anonymous reviewer(s) for their contribution to the peer review of this work. Peer reviewer reports are available.

**Publisher's note:** Springer Nature remains neutral with regard to jurisdictional claims in published maps and institutional affiliations.



**Open Access** This article is licensed under a Creative Commons Attribution 4.0 International License, which permits use, sharing, adaptation, distribution and reproduction in any medium or format, as long as you give appropriate credit to the original author(s) and the source, provide a link to the Creative Commons license, and indicate if changes were made. The images or other third party material in this article are included in the article's Creative Commons license, unless indicated otherwise in a credit line to the material. If material is not included in the article's Creative Commons license and your intended use is not permitted by statutory regulation or exceeds the permitted use, you will need to obtain permission directly from the copyright holder. To view a copy of this license, visit <http://creativecommons.org/licenses/by/4.0/>.

© The Author(s) 2019

## Supplementary Information

**MRI-guided robotic arm drives optogenetic fMRI with concurrent Ca<sup>2+</sup> recording**

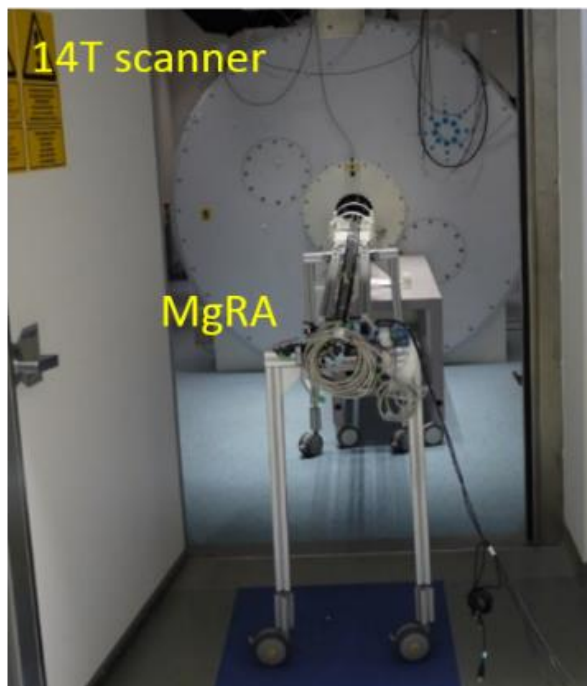
Chen et al.

## Supplementary Table (1)

**Supplementary Table 1.** List of Components of MgRA

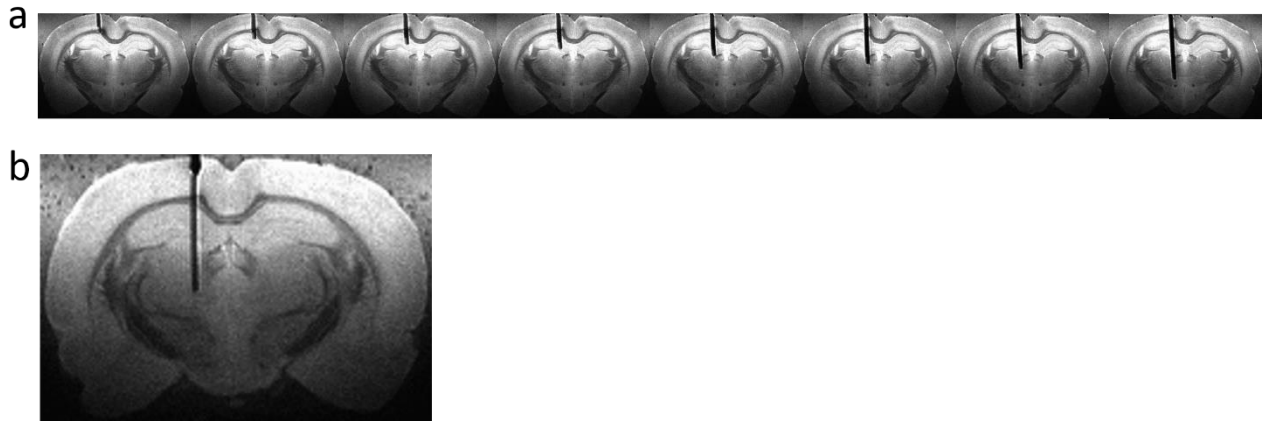
Name	Information
Archimedean spiral driving design	Custom-designed, MPI for BC Mechanic Workshop
Bearings for back/forward	JSM-2022-20, Igus, Germany
Bearings for left/right	BB-625-B180-10-GL, Igus, Germany
Belts	Optibelt OMEGA 3M, OPTIBELT, Germany
Camera	RS-OV7949-1818, Conrad Electronic, Germany
Carbon fiber tube (1)	7420182, R&G, Germany
Carbon fiber tube (2)	7420173, R&G, Germany
Charging condenser	Z-K4700/50, Nanotec, Germany
Cross table	Custom-designed, MPI for BC Mechanic Workshop
Encoder cable	ZK-NOE1-10-20000-S, Nanotec, Germany
Encoders	NOE2-05-B14, Nanotec, Germany
Gearbox	GPLE22-2S-12, Nanotec, Germany
Matching toothed pulley	Custom-designed, MPI for BC Mechanic Workshop
Motor controller	SMCI33-1, Nanotec, Germany
Platform for MgRA	Custom-designed, MPI for BC Mechanic Workshop
Power supply	NTS-24V-40A, Nanotec, Germany
Rat holder	Custom-designed, MPI for BC Mechanic Workshop
Robotic arm holder	Custom-designed, MPI for BC Mechanic Workshop
Stepper motor	ST4118D1804-B, Nanotec, Germany
USB cable for motor controller	ZK-USB, Nanotec, Germany
Cable lengthening	Custom-designed, MPI for BC Electronic Workshop
Other pieces of MgRA	Custom-designed, MPI for BC Mechanic Workshop

## Supplementary Figures (13)

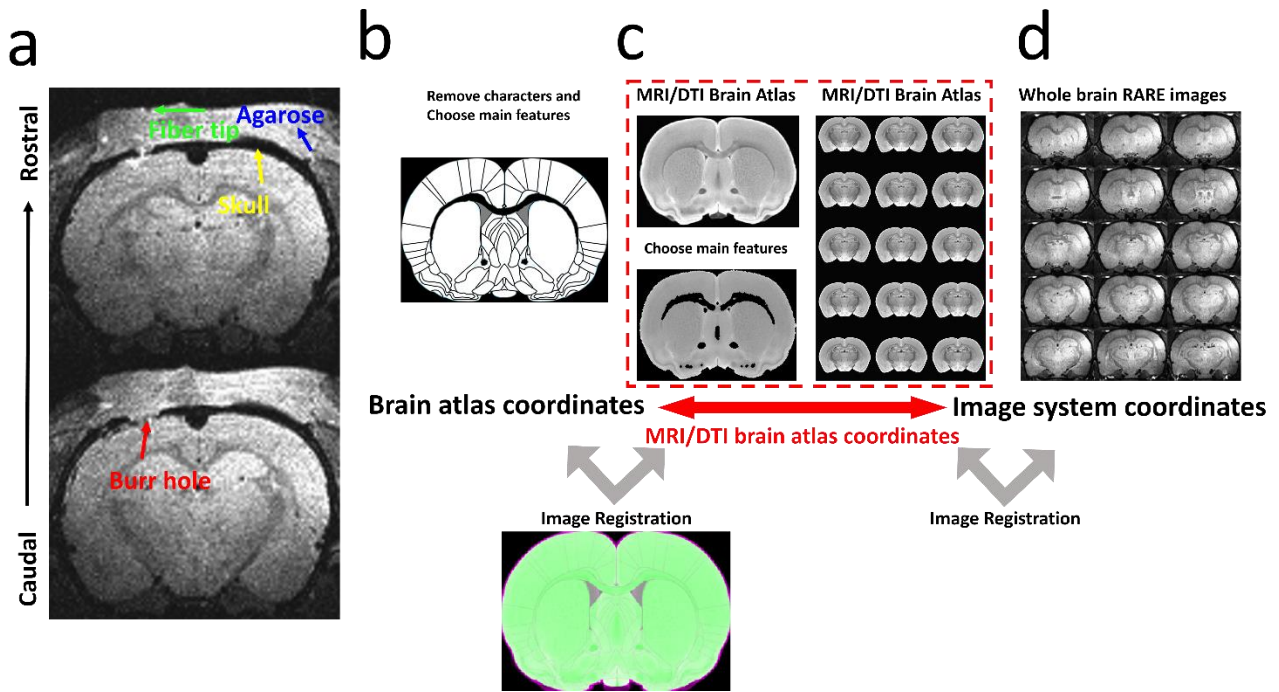


**Supplementary Figure 1.** MRI compatible MgRA mounted inside the 14T MRI scanner (picture taken from the control room).



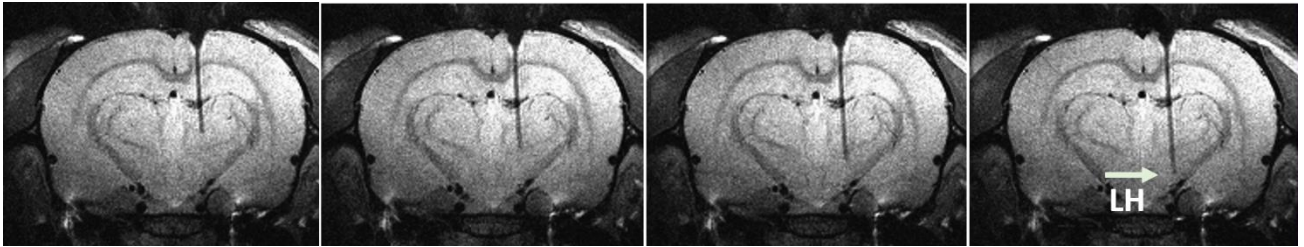


**Supplementary Figure 2.** Examples of optical fibers with different core diameters driven by MgRA for *in vitro* evaluation. **a** The T2-weighted MRI images show 8 different locations of the optical fiber (400  $\mu\text{m}$  core diameter, black stripe) along the insertion trajectory in a perfused rat brain embedded in the soft agarose with manganese. **b** Optical fiber (200  $\mu\text{m}$  core diameter, black stripe) was inserted vertically into the perfused rat brain.

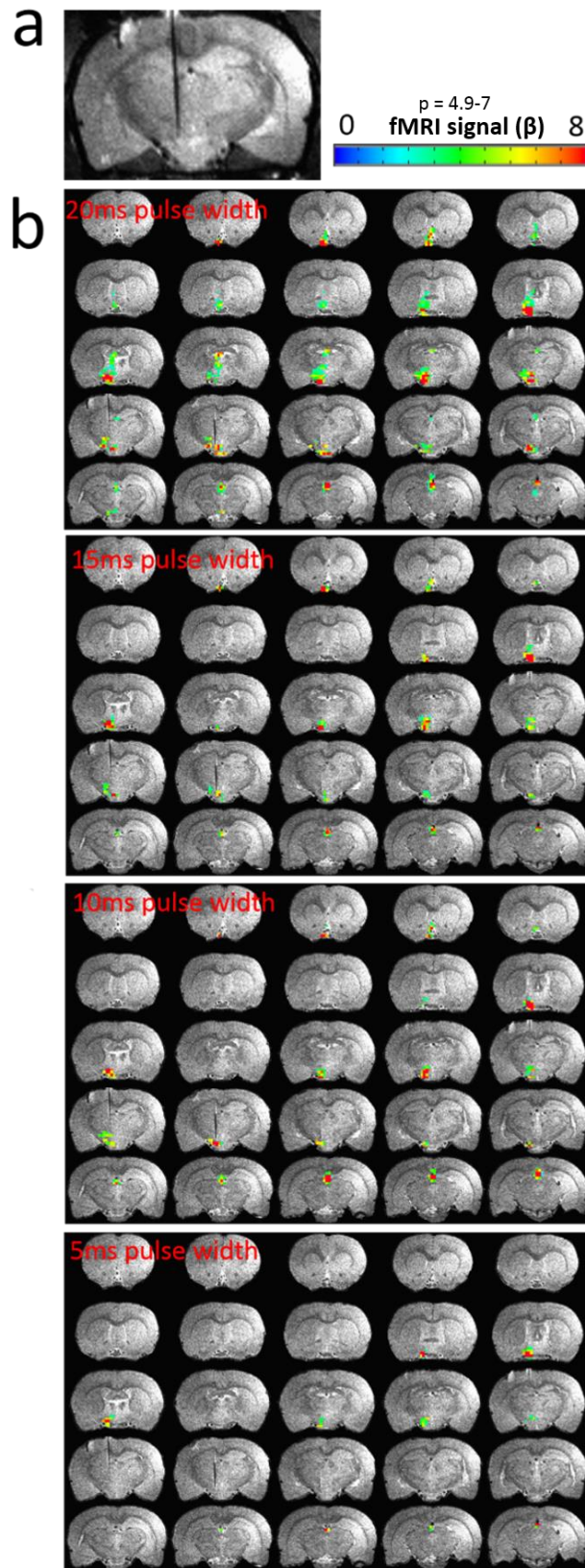


**Supplementary Figure 3.** MRI-based relocation outside of the rat brain and the registration of coordinates. **a** Agarose with manganese was applied to cover the skull (yellow arrow). By lowering the fiber into the agarose, we could calculate the distance between fiber tip (green arrow) and burr hole (red arrow) from the anatomical images. The burr hole is filled with agarose as well. **b** Atlas coordinates (Co1). **c** MRI/DTI Atlas of the Rat Brain (Co2, provided by Dr. G. Allen Johnson). **d** 3D anatomical images of an individual rat.

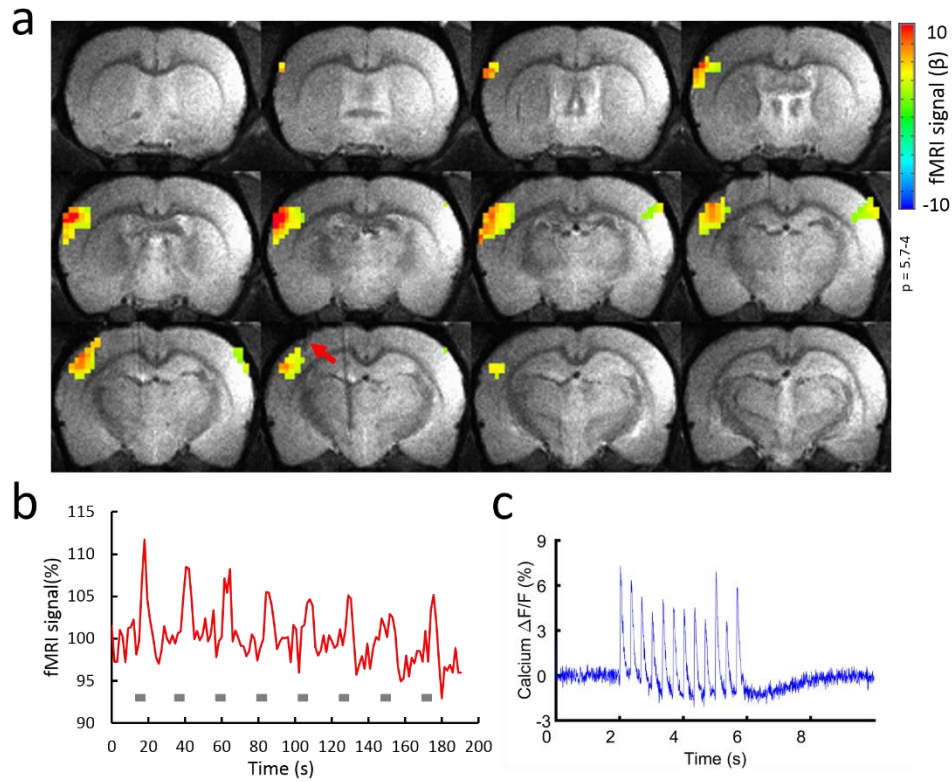
For coordinates registration, agarose has been previously applied above the burr hole of the skull and the fiber tip (previously positioned above the burr hole using the MgRA system under the guidance of the build-in camera inside the MR scanner) can be directly imaged to determine its coordinates in the MRI images (Supplementary Figure 3a). Then, an algorithm was designed to register a four coordinate system for the fiber tip position: atlas coordinate (Co1), MRI/DTI rat brain atlas (Co2, provided by Dr. G. Allen Johnson), MRI coordinate (Co3) and robotic arm coordinate (Co4). In short, the Co1 is first transferred to the Co2 by the algorithm (Supplementary Figure 3b, c). By registering the 2D anatomical images of individual rat (Co3) to the MRI/DTI brain atlas (Co2), the transformation between the Co1 and Co3 is settled (Red arrow in Supplementary Figure 3c). Since the fiber tip position is directly detected in the MRI images above the craniotomy, the related coordinate offset from the fiber tip to the targeted function nuclei can be calculated based on the multiple transformation matrices.



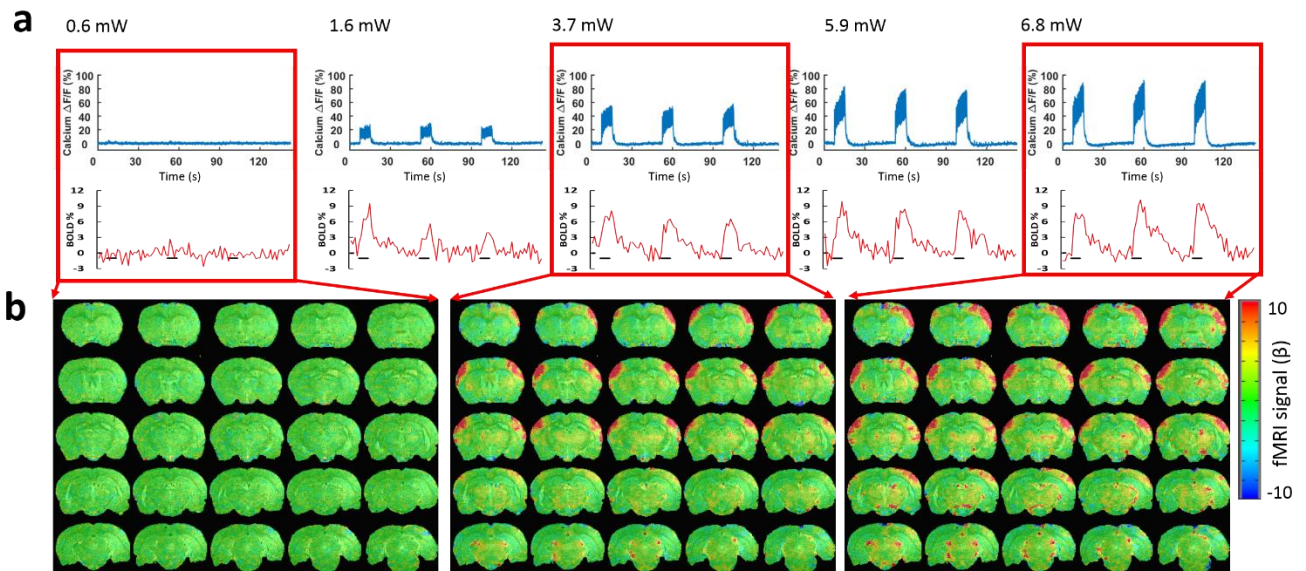
**Supplementary Figure 4.** The time-lapsed anatomical images to illustrate the optical fiber targeting the Lateral Hypothalamus for opto-fMRI studies.



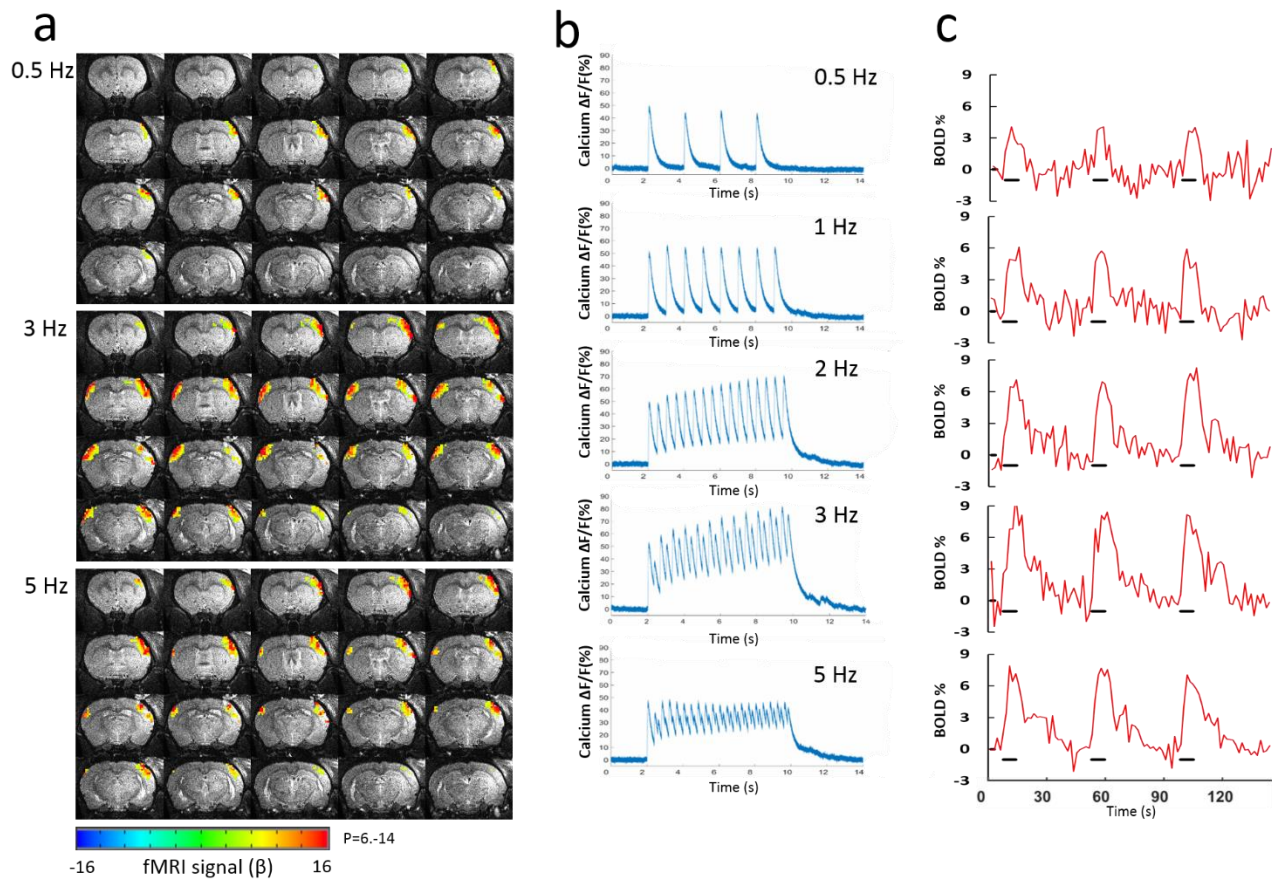
**Supplementary Figure 5.** Whole brain activity maps in response to 15s LH optogenetic stimulation at different pulse widths. **a** Anatomical image showing the position of the optical fiber for delivering light. **b** BOLD activation maps of a representative animal exhibited a pulse width-dependent pattern in response to 20ms, 15ms, 10ms and 5ms pulse widths (5 Hz, laser power of 12.6 mW, 15 s on 45 s off, 12 epochs). GLM-based t-statistics in AFNI is used.



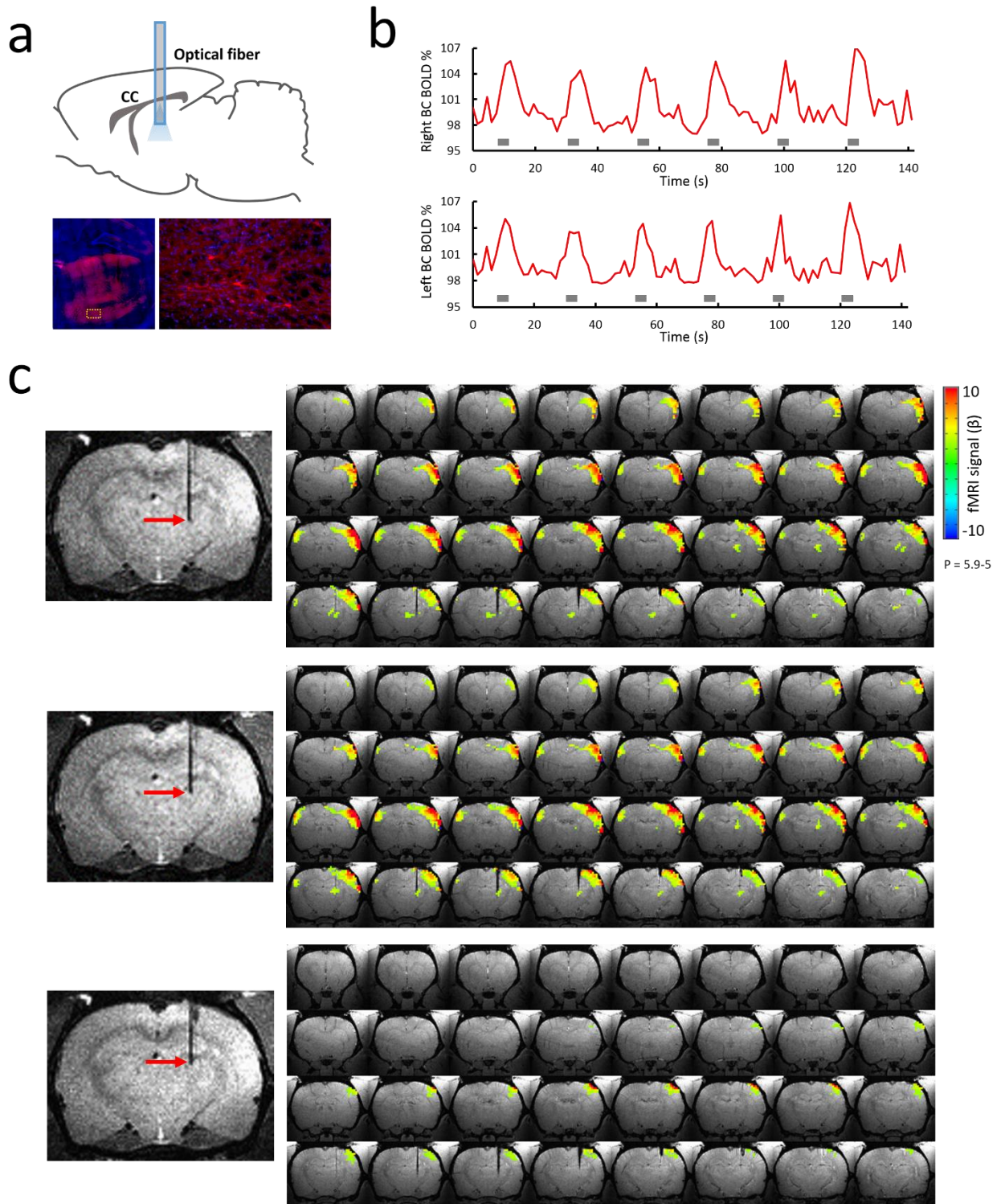
**Supplementary Figure 6.** Sensory-evoked neuronal  $\text{Ca}^{2+}$  recordings with simultaneous BOLD fMRI. **a** Representative color-coded BOLD-fMRI in response to a block design whisker-electrical stimulation. GLM-based t-statistics in AFNI is used. **b** The time course of evoked fMRI signal from BC-S1 ROI (see **a**) in the left hemisphere. **c** Average of simultaneously optical fiber (red arrow in **a**) recorded  $\text{Ca}^{2+}$  signals for one epoch (3 Hz, 4 s, 2 mA).



**Supplementary Figure 7.** Laser power dependent BOLD signals in S1 with simultaneous  $\text{Ca}^{2+}$  recordings (S1BF) upon light exposure in VPM. **a** Representative percentage changes of calcium signal (top) and BOLD responses (lower) for 3 epochs detected at 5 different laser powers. At 0.6 mW, hardly any fMRI and calcium signal was detected. BOLD and calcium signal increased proportionally with increased laser power. **b** Examples of whole brain activity maps at 0.6 mW, 3.7 mW and 6.8 mW.

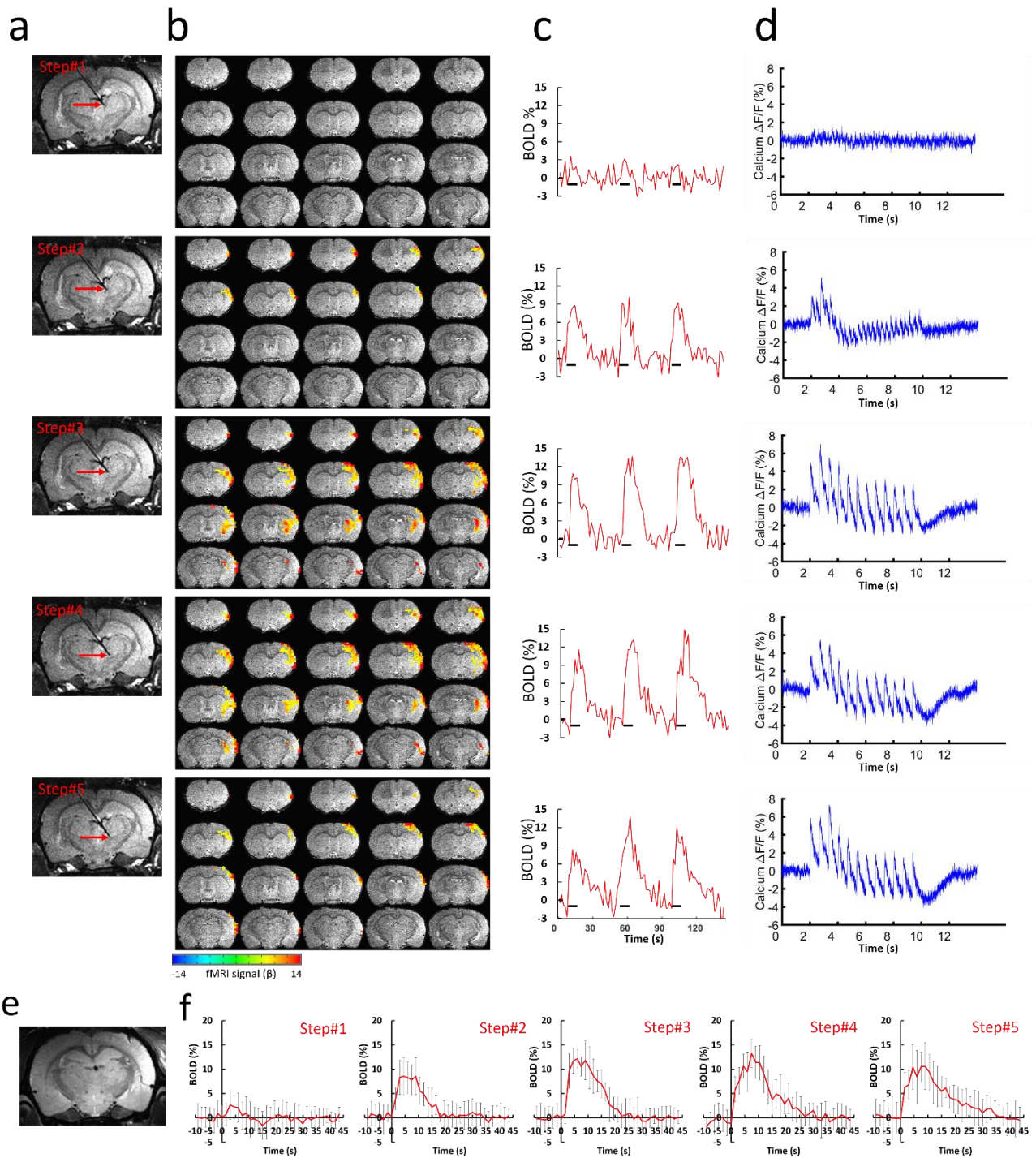


**Supplementary Figure 8.** Frequency dependent BOLD signals in S1 with simultaneous  $\text{Ca}^{2+}$  recordings (S1BF) upon light exposure in the Thalamus. **a** Examples of BOLD maps in response to 0.5 Hz, 3 Hz, 5 Hz. The strongest response was induced by 3 Hz stimulation, instead of 5 Hz. GLM-based t-statistics in AFNI is used. **b** Averaged calcium signal percentage change in one epoch. Evoked calcium spikes with almost full recovery to the baseline in 2 s per spike at 0.5 Hz. From 1 Hz to 3 Hz, the calcium signal was elevated through the 8 s stimulation period, while at 5 Hz, some of the spikes per pulse were even missed and the overall plateau amplitude was not further increased. **c** BOLD signal for 3 epochs upon stimulation (black line) was increased according to the increased frequency, but not at 5 Hz, which is consistent with the calcium signal observation.

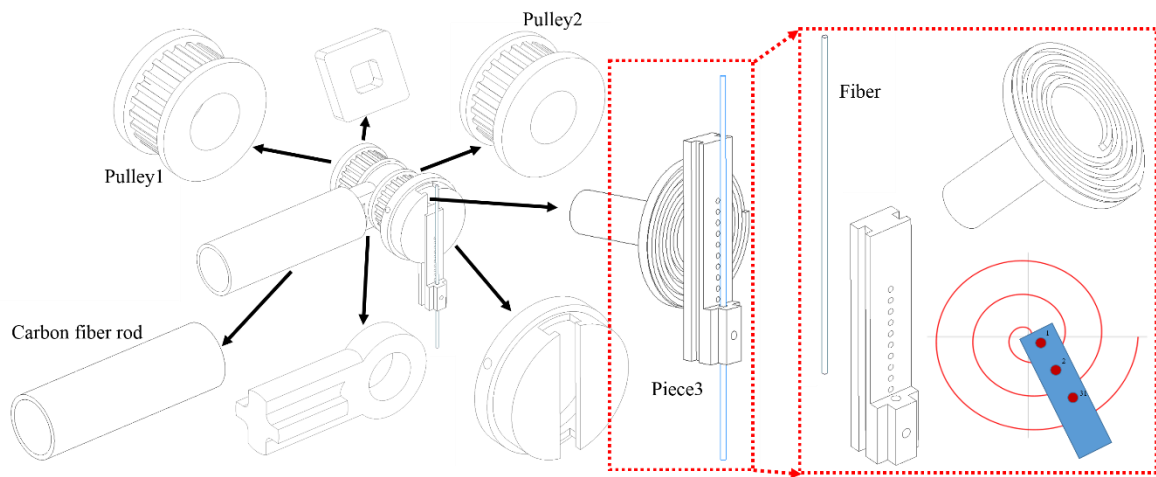


**Supplementary Figure 9.** Optogenetic excitation of thalamic cells drives local and Somatosensory cortical positive BOLD. **a** Top: Sketch showing the point of thalamic injection of AAV5.CAG.ChR2-mCherry and optical stimulation. Lower: histological image of ChR2-mCherry expression in the thalamus (left); higher magnification (right). Red, ChR2-mCherry; blue, 4',6-Diamidin-2-phenylindol (DAPI). **b** Opto-fMRI haemodynamic response (averaged across activated voxels in Somatosensory cortical ROI, see **c**, whole brain top right) in both hemispheres during optical stimuli (5Hz, 4s on 18.5s off, 10 ms pulse width, laser power 5.5 mW). **c** BOLD activation at 3 different locations along the vertical insertion trajectory. GLM-based t-statistics in AFNI is used.

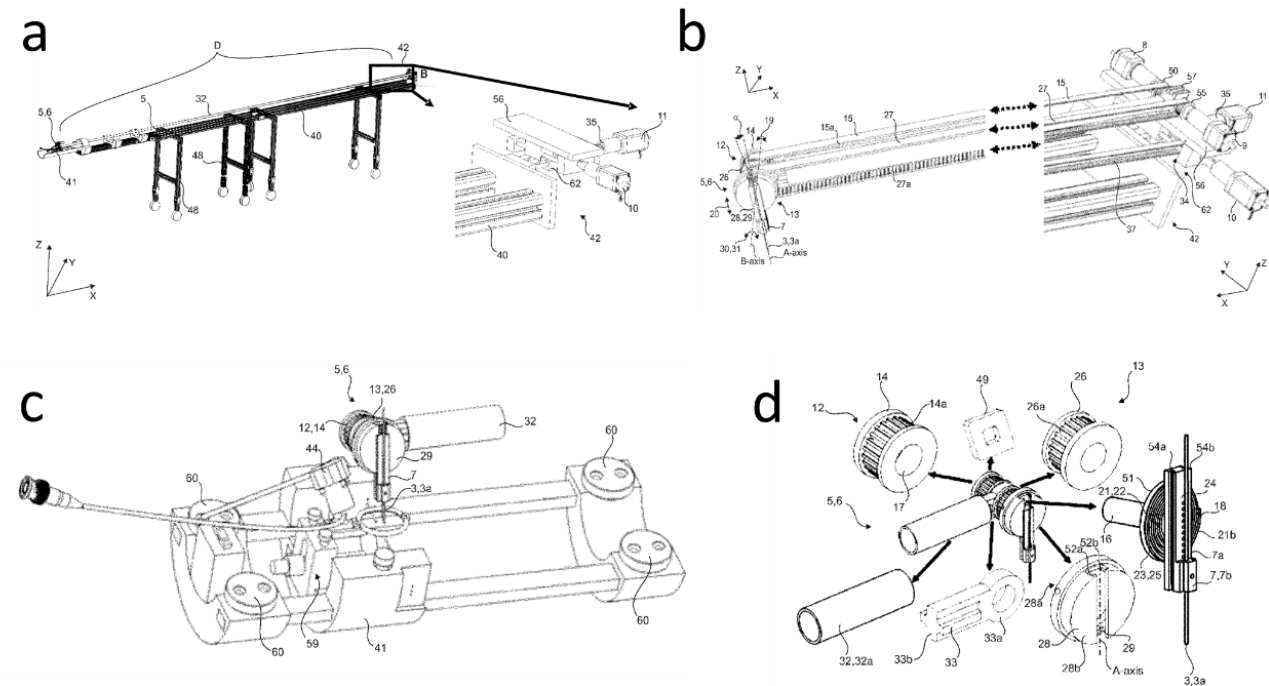




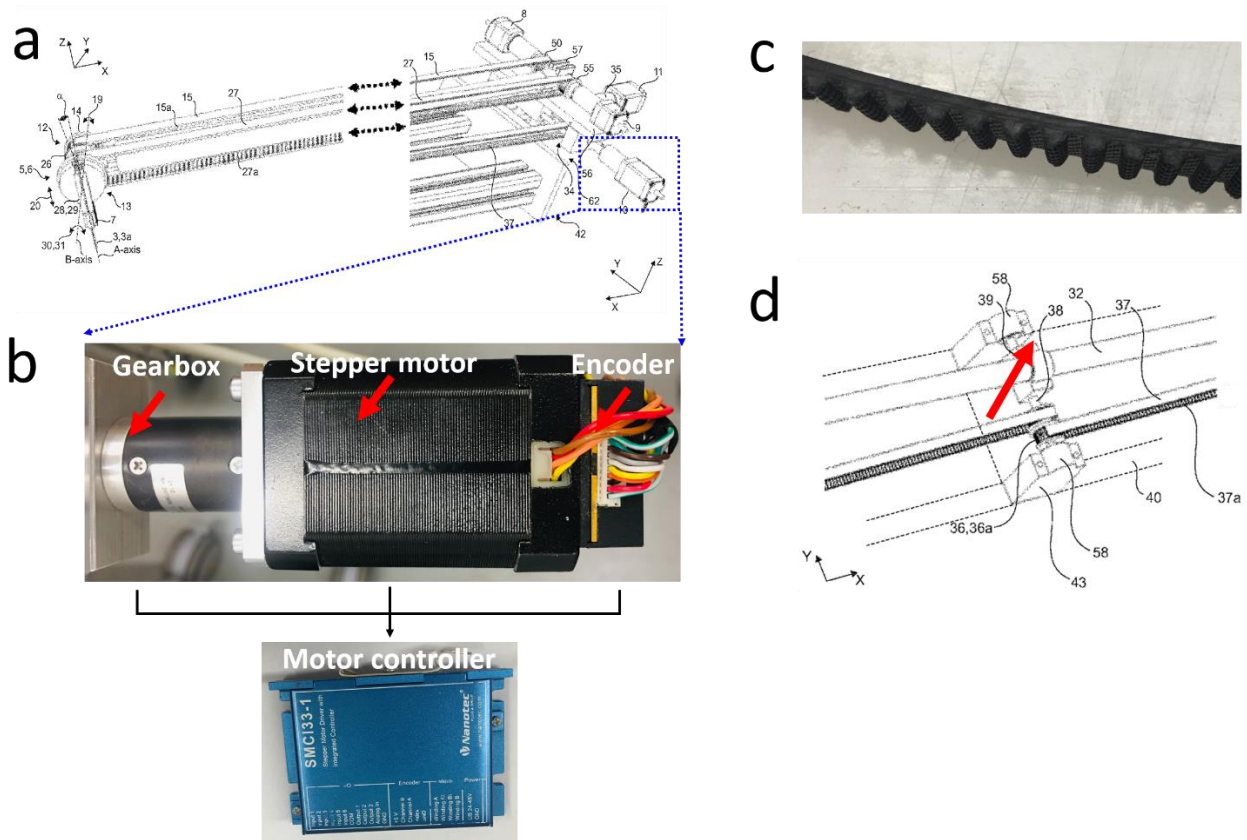
**Supplementary Figure 10.** Region-specific optogenetic activated neuronal  $\text{Ca}^{2+}$  recordings with simultaneous BOLD fMRI. **a** T2-weighted anatomical images illustrate five fiber locations. **b** Different BOLD fMRI in Somatosensory cortex evoked by optogenetic stimuli in different thalamic regions. **c** BOLD signals for 3 epochs (3 Hz, Laser power 4.2 mW, 8 s on 37 s off, 10 epochs) within ipsilateral Somatosensory cortex ROI (see **b** middle panel) corresponding to the different locations. **d** Simultaneously recorded evoked calcium signal through the 8 s stimulation period. **e** Anatomical RARE MR image illustrates the fiber tip location for calcium recording in Barrel cortex. **f** The average BOLD signals of ipsilateral hemisphere at different fiber tip locations. Error bars represent mean $\pm$ SD.



**Supplementary Figure 11.** Detailed design for the head part of the MgRA.



**Supplementary Figure 12.** Detailed design of the MgRA (figures from the approved European patent). **a** The schematic view of the whole MgRA mechanical design including the cross table to mount the stepper motors. **b** The coupling of the stepper motors (back part) to the matching toothed pulley in the head was achieved by a synchronous belt drive in a form-fit manner. **c** Custom-designed rat holder with a built-in MRI compatible camera, surface coil and head part of the MgRA. **d** The components of the head part of the MgRA. For more details see the approved European patent as following link: (<https://patentscope.wipo.int/search/en/detail.jsf?docId=EP215319263&tab=PCTDESCRIPTION&maxRec=1000>).



**Supplementary Figure 13.** Detailed design of the back part of the MgRA. **a** The coupling of the stepper motors (back part) to the matching toothed pulley in the head was achieved by a synchronous belt drive in a form-fit manner. **b** The encoder (NOE2-05-B14, Nanotec, Germany) is used with motor controller (SMCI33-1, Nanotec, Germany) so that the stepper motor (ST4118D1804-B, Nanotec, Germany) can be run in a close-loop mode. **c** Multi-groove belt (optibelt OMEGA 3M, Optibelt, Germany) used to fit into a matching toothed pulley. **d** Closed belts can be cascaded to transfer the motion (red arrow). All schematic figures shown here are from the approved MgRA European patent.

# Mapping the brain-wide network effects by optogenetic activation of the corpus callosum

Yi Chen<sup>1,2</sup>, Filip Sobczak<sup>1,2</sup>, Patricia Pais-Roldán<sup>1,2</sup>, Cornelius Schwarz<sup>3</sup>, Alan P. Koretsky<sup>4</sup>, Xin Yu<sup>1,5\*</sup>

1 Research Group of Translational Neuroimaging and Neural Control, High-field Magnetic Resonance, Max Planck Institute for Biological Cybernetics, Tübingen, Baden-Württemberg, Germany

2 Graduate Training Centre of Neuroscience, University of Tübingen, Tübingen, Baden-Württemberg, Germany

3 Werner Reichardt Center for Integrative Neuroscience, Tübingen, Baden-Württemberg, Germany

4 National Institute of Neurological Disorders and Stroke, Bethesda, Maryland, United States of America

5 Athinoula A. Martinos Center for Biomedical Imaging, Massachusetts General Hospital and Harvard Medical School, Charlestown, Massachusetts, United States of America

## Corresponding author:

Dr. Xin Yu

Email: [xin.yu@tuebingen.mpg.de](mailto:xin.yu@tuebingen.mpg.de), [xyu9@mgh.harvard.edu](mailto:xyu9@mgh.harvard.edu)

Address: Max-Planck-Ring 11, 72076, Tuebingen, Germany

Phone: +497071 601-740

Fax: +49 7071 601-701

## This PDF file includes:

Main Text

Supplementary Information

**ABSTRACT (150 words)**

Optogenetically-driven manipulation of circuit-specific activity enables causality studies, but its global brain-wide effect is rarely reported. Here, we applied simultaneous fMRI and calcium recording with optogenetic activation of the corpus callosum(CC) connecting barrel cortices(BC). Robust positive BOLD was detected in the ipsilateral BC due to antidromic activity, spreading to the ipsilateral motor cortex(MC) and posterior thalamus(PO). In the orthodromic target, positive BOLD was reliably evoked by 2Hz light pulses, whereas 40Hz light pulses led to reduced Calcium-indicative of CC-mediated inhibition. This presumed optogenetic CC-mediated inhibition was further elucidated by pairing light pulse with whisker stimulation at varied inter-stimulus intervals. Whisker-induced positive BOLD and calcium signals were reduced at intervals of 50/100ms. The calcium-amplitude modulation(AM)-based correlation with whole-brain fMRI signal revealed that the inhibitory effects spread to contralateral BC, ipsilateral MC and PO. This work raises the need for fMRI to elucidate the brain-wide network activation in response to optogenetic stimulation.

## INTRODUCTION

The genetic expression of channelrhodopsin (ChR2) has been extensively applied to target specific cell types to ensure the activation of neuronal ensembles of interest (Nagel, Ollig et al. 2002, Boyden, Zhang et al. 2005, Li, Gutierrez et al. 2005, Zhang, Wang et al. 2006). Optogenetic tools have revolutionized the strategy to perturb or manipulate the behavior of animals (Lima and Miesenbock 2005, Nagel, Brauner et al. 2005, Adamantidis, Zhang et al. 2007, Tsai, Zhang et al. 2009). To interpret the linkage of the brain function to specific behavioral readout relies on the assumed circuit-specific manipulation through *in vivo* optogenetic activation (Cardin, Carlen et al. 2010, Carter, Yizhar et al. 2010, Tye and Deisseroth 2012, Kim, Adhikari et al. 2017). Optogenetic activation of numerous brain sites and defined neuronal populations in animals has been very successful to modulate behavior. However, there is a lack of systematic mapping of the result of specific modulation on brain-wide network activity, which may relay and affect the proposed link between function and behavior. Progress in this direction depends on the combined application of methods to explore large scale brain dynamics as well (Inoue, Takada et al. 2015, Bernal-Casas, Lee et al. 2017, Gao, Asano et al. 2019, Sych, Chernysheva et al. 2019). One useful method for this purpose is functional magnetic resonance imaging (fMRI) , which has been successfully combined with optogenetics (Lee, Durand et al. 2010, Ryali, Shih et al. 2016, Yu, He et al. 2016, Albers, Schmid et al. 2018, Grandjean, Corcoba et al. 2019, Just and Faber 2019). We use here a method that adds GCaMP-mediated calcium recordings through an optical fiber for concurrent fMRI and neuronal calcium signal recording (Schulz, Sydekum et al. 2012, Schwalm, Schmid et al. 2017, Albers, Wachsmuth et al. 2018, He, Wang et al. 2018, Wang, He et al. 2018). This multi-modal cross-scale brain dynamic mapping scheme (fMRI, optogenetics and calcium recording) allows elucidating network activity upon circuit-specific optogenetic activation on the specific target level as well as across large brain regions (Schulz, Sydekum et al. 2012, Schmid, Wachsmuth et al. 2016, Albers, Schmid et al. 2018, Albers, Wachsmuth et al. 2018, He, Wang et al. 2018, Wang, He et al. 2018, van Alst, Wachsmuth et al. 2019).

Corpus callosum (CC), the major neural fiber bundles connecting the two hemispheres, plays a critical role to mediate the interhemispheric cortico-cortical connections (Sperry 1961, Gazzaniga 2005, Karolis, Corbetta et al. 2019). Despite the highly-correlated structural anomalies of the CC with a wide range of disorders, e.g., schizophrenia (Innocenti, Ansermet et al. 2003, Pomarol-Clotet, Canales-Rodriguez et al. 2010), autism (Egaas, Courchesne et al. 1995, Anderson, Druzgal et al. 2011), epilepsy (Spencer, Spencer et al. 1988, van Eijsden, Otte et al. 2011) and mental retardation (Schaefer and Bodensteiner 1999, van Schooneveld, Jennekens-Schinkel et al. 2011), CC-mediated neural mechanisms are primarily studied in loss-of-function models, such as split-brain/callosotomy or partial callosal lesion (Gazzaniga 2000, Gazzaniga 2005, Schulte, Muller et al. 2010). To directly investigate the functional roles of callosal projections on regulating the interhemispheric excitatory-inhibitory balance, both *in vitro* and *in vivo* studies have applied micro-stimulation on one hemisphere or the callosal

fiber bundles (Kawaguchi 1992, Kumar and Huguenard 2001, Hoffmeyer, Enager et al. 2007, Karayannis, Huerta-Ocampo et al. 2007), or performed bilateral motor or sensory tasks in both human (Schnitzler, Kessler et al. 1996, Ogawa, Lee et al. 2000, Ni, Gunraj et al. 2009, Bocci, Caleo et al. 2011) and animal models (Ogawa, Lee et al. 2000, Shuler, Krupa et al. 2001, Berwick, Redgrave et al. 2004, Wiest, Bentley et al. 2005, Nemoto, Hoshi et al. 2012). Since the callosal fibers are reciprocally projecting to two hemispheres, bilateral, ortho- vs. antidromically evoked neural activity has been difficult to disentangle. With optogenetic tools, the callosal projection neurons can be specifically (primarily) labeled with ChR2 from one hemisphere, enabling the unidirectional modulation of callosal activity (Petreanu, Huber et al. 2007, Palmer, Schulz et al. 2013, Iordanova, Vazquez et al. 2018). The optogenetically driven callosal activity has been particularly helpful to disentangle interhemispheric inhibitory effects, e.g., in the auditory cortex (Rock and Apicella 2015), prefrontal cortex (Lee, Gee et al. 2014) or hindlimb somatosensory cortex (Palmer, Schulz et al. 2012). The goal of the present studies was to widen the view beyond of target-specific excitatory-inhibitory regulation by using multi-modal fMRI platform to characterize the global neural network activity upon optogenetic callosal activation.

In the present study, we implemented the multi-modal fMRI platform with optogenetics to map the CC-mediated inhibition on the brain-wide network dynamics in three consecutive steps. First, we identified the antidromic vs. orthodromic effect of CC-specific optogenetic stimulation. Optogenetic stimulation of callosal fibers connecting the barrel cortex (BC) to the other hemisphere, revealed robust antidromic activation in the ipsilateral BC. In the orthodromic direction, both fMRI and neuronal calcium signals in the contralateral BC indicated strong depression of calcium signals with 40Hz light pulses. Second, we specified the temporal characteristics of this presumptive CC-mediated inhibition on the thalamocortical activation to the BC. The optogenetic CC light pulses were paired with the whisker stimulation electrical pulses at varying intervals from 0 ms to 200 ms in a randomized stimulation scheme. Significant inhibitory effects at 50 ms and 100 ms interval were detected by both fMRI and neural calcium recordings of the right BC activated by whisker stimulation, but little difference was observed in the antidromically evoked fMRI signal in the ipsilateral BC. Thirdly, to further examine the brain-wide activity regulation upon paired optogenetic and whisker stimulation, the concurrent evoked-calcium signals in the contralateral BC was real-time detected at varying conditions and correlated with whole-brain fMRI signals. Besides the contralateral BC, the homologous ventral part of the ipsilateral BC, the motor cortex and posterior thalamus (PO) from the same side of the contralateral BC were detected in the correlation maps, showing amplitude modulation by CC-mediated inhibition at varied time intervals. This study not only specifies the optogenetically driven CC-mediated regulation of the local excitation/inhibition balance but also depicts the power of multi-modal fMRI to characterize the brain-wide network activity associated with circuit-specific optogenetic activations *in vivo*. It highlights a vital aspect of the brain-wide activity for circuit-specific causality studies with optogenetic tools.

## **Methods**



**Animal procedures.** The study was performed in accordance with the German Animal Welfare Act (TierSchG) and Animal Welfare Laboratory Animal Ordinance (TierSchVersV). This is in full compliance with the guidelines of the EU Directive on the protection of animals used for scientific purposes (2010/63/EU). The study was reviewed by the ethics commission (§15 TierSchG) and approved by the state authority (Regierungspräsidium, Tübingen, Baden-Württemberg, Germany). A 12-12 hour on/off lighting cycle was maintained to assure undisturbed circadian rhythm. The food and water were obtainable ad libitum. A total of 24 (17 for fMRI and 7 for electrophysiology) male Sprague–Dawley rats were used in this study.

**Viral injection.** Intracerebral viral injection was performed in 4-week-old rats to express the viral vectors containing the light-sensitive protein channelrhodopsin-2 (ChR2, for optogenetics) and/or the calcium-sensitive protein (GCaMP, for calcium recording) in neurons. The construct AAV5.Syn.GCaMP6f.WPRE.SV40 was used to express GCaMP in the left BC and the constructs AAV5.CaMKII.hChR2(H134R)-mCherry.WPRE.hGH was used to express ChR2 in the right BC. The stereotaxic coordinates of the injections were 2.5 mm posterior to Bregma, 5 mm bilateral to the midline, 0.8-1.4 mm below the cortical surface. Rats were anesthetized with 1.5-2% isoflurane via nose cone and placed on a stereotaxic frame, an incision was made on the scalp and the skull was exposed. Craniotomies were performed with a pneumatic drill so as to cause minimal damage to cortical tissue. A volume of 0.6-0.9  $\mu$ L and 0.6  $\mu$ L, for optogenetics and calcium signal recording, respectively, was injected using a 10  $\mu$ L syringe and 35-gauge needle. The injection rate was controlled by an infusion pump (Pump 11 Elite, Harvard Apparatus, USA). After injection, the needle was left in place for approximately 5 min before being slowly withdrawn. The craniotomies were sealed with bone wax and the skin around the wound was sutured. Rats were subcutaneously injected with antibiotic and painkiller for 3 consecutive days to prevent bacterial infections and relieve postoperative pain.

**Immunohistochemistry.** To verify the phenotype of the transfected cells, opsin localization and optical fiber placement, perfused rat brains were fixed overnight in 4% paraformaldehyde and then equilibrated in 15% and 30% sucrose in 0.1 M PBS at 4°C. 30  $\mu$ m-thick coronal sections were cut on a cryotome (CM3050S, Leica, Germany). Free-floating sections were washed in PBS, mounted on microscope slides, and incubated with DAPI (VectaShield, Vector Laboratories, USA) for 30 mins at room temperature. Wide-field fluorescent images were acquired using a microscope (Zeiss, Germany) for assessment of GCaMP and ChR2 expression in BC. Digital images were minimally processed using ImageJ to enhance brightness and contrast for visualization purposes.

**Optical setup for calcium recordings.** A laser was used as excitation light source (OBIS 488LS, Coherent, Germany) with a heat sink to enable laser operation throughout the entire specified temperature range from 10°C to 40°C. The light passed through a continuously variable neutral density filter (NDC-50C-2M-B, Thorlabs, Germany) and was reflected on a dichroic beam splitter (F48-487, AHF analysentechnik AG, Germany). The beam

was collected into an AR coated achromatic lens (AC254-030-A, Thorlabs, Germany) fixed on a threaded flexure stage (HCS013, Thorlabs, Germany) mounted on an extension platform (AMA009/M, Thorlabs, Germany) of a fiber launch system (MAX350D/M, Thorlabs, Germany). The laser beam was projected into the fiber and propagated to its tip. The fluorescence emitted by neurons was collected through the fiber tip, propagated back and collimated by the achromatic lens, passed through the dichroic beam splitter and filtered by a band-pass filter (ET525/50M, Chroma, USA) and focused by an AR coated achromatic lens (AC254-030-A, Thorlabs, Germany). A silicon photomultiplier module (MiniSM 10035, SensL, Germany) was applied to detect the emitted fluorescence. The entire optical system was enclosed in a light isolator box. The photomultiplier output was amplified (gain = 100) by a voltage amplifier (DLPVA-100-BLN-S, Femto, Germany), digitized and detected by BIOPAC system (MP150 System, BIOPAC Systems, USA).

**Animal preparation and fiber optic implantation for fMRI.** Anesthesia was first induced in the animal with 5% isoflurane in the chamber. The anesthetized rat was intubated using a tracheal tube and a mechanical ventilator (SAR-830, CWE, USA) was used to ventilate animals throughout the whole experiment. Femoral arterial and venous catheterization was performed with polyethylene tubing for blood sampling, drug administration, and constant blood pressure measurements. After the surgery, isoflurane was switched off, and a bolus of the anesthetic alpha-chloralose (80 mg/kg) was infused intravenously. A mixture of alpha-chloralose (26.5 mg/kg/h) and pancuronium (2 mg/kg/h) was constantly infused to maintain the anesthesia/keep the animal anesthetized and reduce motion artifacts.

Before transferring the animal to the MRI scanner, two craniotomies were performed: one for fixed fiber implantation to record calcium signals from BC, and the other one for dynamic insertion of the optical fiber to stimulate the CC using optogenetics (dynamic insertion was achieved by using a remote positioning tool (Chen, Pais-Roldan et al. 2019)). The animal was placed on a stereotaxic frame, the scalp was opened and two ~1.5 mm diameter burr holes were drilled on the skull. The dura was carefully removed and an optical fiber with 200  $\mu\text{m}$  core diameter (FT200EMT, Thorlabs, Germany) was inserted into the BC, at coordinates: 2.75-3.3 mm posterior to Bregma, 5.0 mm lateral to the midline, 1.2-1.4 mm below the cortical surface. An adhesive gel was used to secure the calcium recording fiber to the skull. The craniotomy for optogenetics on CC in the other hemisphere, at coordinates: 2.75-3.3 mm posterior to Bregma, 1.8-2.4 mm lateral to the midline, was covered by agarose gel for the robotic arm-driven fiber insertion inside the MRI scanner. The eyes of the rats were covered by black light proof tapes to prevent stimulation of the visual system during the optogenetic fMRI, which may occur in cases with imperfect coverage or under the strong power of light pulses through tissue.

**Functional MRI acquisition.** All images were acquired with a 14.1 T/26 cm horizontal bore magnet interfaced to an Avance III console and equipped with a 12 cm gradient set capable of providing 100 G/cm over a time of 150

$\mu$ s. A transceiver single-loop surface coil with an inner diameter of 22 mm was placed directly over the rat head to acquire anatomical and fMRI images. Magnetic field homogeneity was optimized first by global shimming for anatomical images and followed by FASTMAP shimming protocol for the EPI sequence. Functional images were acquired with a 3D gradient-echo EPI sequence with the following parameters: Echo Time 11.5 ms, repetition time 1.5 s, FOV 1.92 cm  $\times$  1.92 cm  $\times$  1.92 cm, matrix size 48  $\times$  48  $\times$  48, spatial resolution 0.4 mm  $\times$  0.4 mm  $\times$  0.4 mm. For anatomical reference, the RARE sequence was applied to acquire 48 coronal slices with the same geometry as that of the fMRI images. The paradigm for each trial consisted of 360 dummy scans to reach steady-state, 10 pre-stimulation scans, 5 scans during stimulation (stimulation period 8 s), 35 post-stimulation scans with total 13 epochs and 15 epochs for refined stimulus design (See **Stimulation protocols**).

For fMRI and electrophysiology studies, needle electrodes were placed on whisker pads of the rats, and electric pulses (333  $\mu$ s duration at 1.5 mA repeated at 3 Hz for 4 seconds) were first used as stimulation to serve as a positive control for the evoked BOLD signal or local field potential/calcium signal. Once that reliable fMRI signals and calcium signals were observed in response to electrical stimulation, optical stimulation was performed. For optogenetic stimulation, square pulses of blue light (473 nm) were delivered using a laser (MBL-III, CNI, China) connected to the 200  $\mu$ m core optical fiber (FT200EMT, Thorlabs, Germany) and controlled by Master 9 (Master-9, A.M.P.I., Israel) to deliver blue light pulses at 1-40 Hz, 1-20 ms pulse width with 2-8 s duration. The light intensity was tested before each experiment and was calibrated with a power meter (PM20A, Thorlabs, Germany) to emit 0.6 mW to 40 mW from the tip of the optical fiber for CC activation.

**Stimulation protocols.** A 2 Hz, 8 s optogenetic stimulus train (O train; 16 pulses to the corpus callosum) was delivered preceding a conditioning stimulus train (W train; same pulse parameters were used, 0.75-1.5 mA) while varying the time interval between stimuli (0, 10, 25, 50, 100 and 200 ms), or without a W train, in a single trial. These stimulation conditions were automatically executed using a laser (MBL-III, CNI, China) and a stimulator (A365 Stimulus Isolator, WPI, USA) triggered by a combination program provided by pulse generator (Master-9, A.M.P.I., Israel), which were precisely synchronized with the start time of the image acquisition sequence in each trial. Each trial consisted of the first fixed whisker stimuli block (W) and 12 blocks randomized for 6 different conditions, W, O, WO, W50O, W100O, W200O, in total 13 min and 15 s for each trial. For refined inter-stimulus intervals design, first fixed whisker stimuli block (W) and 14 blocks randomized for 7 different conditions were used: W, OW, O10W, O25W, O50W, O100W, and O200W, in total 15 min 15 s for each trial. The tables below show the number of continuous trials acquired in this study, as well as light power for optogenetic stimulation.

Table 1. The number of trials acquired for 6 conditions.

	Rat#1	Rat #2	Rat #3	Rat #4	Rat #5	Rat #6
<b>Trials</b>	6	4	4	4	6	5

<b>Acquiring Time</b>	79m 30s	53m	53m	53m	79m 30s	66m 15s
-----------------------	---------	-----	-----	-----	---------	---------

Table 2. The number of trials acquired with refined stimulus design.

	<b>Rat#7</b>	<b>Rat #8</b>	<b>Rat #9</b>	<b>Rat #10 (LFP)</b>
<b>Trials</b>	9	12	5	7
<b>Acquiring Time</b>	137m 15s	183m	76m 15s	106m 45s

Table 3. Light power for optogenetic stimulation.

	<b>L6</b>	<b>L6.5</b>	<b>L7</b>	<b>L7.5</b>	<b>L8</b>	<b>L8.5</b>	<b>L9</b>	<b>L9.5</b>	<b>L9.9</b>	<b>L10</b>
<b>Light power (mW)</b>	2.6	5.4	9.2	13.2	17.6	23.7	29.2	35.3	39.9	>40

**Simultaneous calcium recording with electrophysiology.** The anesthetic and surgical preparation procedures were similar to the fMRI experiments. For antidromic activity recording experiments in **Fig. 1** and **Fig. S2-5**, tungsten microelectrode (UEWSDDSMCN1M, FHC, USA) was implanted in the right BC to record the LFP from the callosal projection neurons. For orthodromic activity in **Fig.2** and **Fig. S7-10**, the same kind of tungsten microelectrode was attached to the fiber optic closely, implanted in the left BC, then secured to the skull by an adhesive gel. To calculate the coordinates of optical fiber implantation for CC activation, a FLASH anatomical MRI image was acquired to confirm the virus injection one day before the experiment. The LFP was recorded and amplified through the EEG module of the BIOPAC system (gain factor, 5000, band-pass filter, 0.02-100 Hz, sampling rate, 5,000/s). In parallel, the GCaMP6f-mediated fluorescent signal and blood pressure were digitized and recorded with BIOPAC (MP150 System, BIOPAC Systems, USA) at a sampling rate of 5 kHz. The experiment design and equipment used afterward were similar to the fMRI experiments.

**Data analysis.** Acquired data were analyzed using Functional NeuroImages software (AFNI, NIH, USA) and custom-written Matlab (MATLAB, MathWorks, USA) programs for calcium signals. The fiber optical neuronal calcium signals were low-pass filtered at 100 Hz using zero-phase shift digital filtering (filtfilt function in MATLAB). The relative percentage change of fluorescence ( $\Delta F/F$ ) was defined as  $(F-F_0)/F_0$ , where  $F_0$  is the baseline, i.e., the average fluorescent signal in a 2 s pre-stimulation window. For **Fig. 2d**, the spike value is defined by the maximal value for the difference in  $\Delta F/F$  in a time window 0.3 s after the stimulus, as shown from 40 Hz in **Fig. 2c**, while the baseline drift is the average calcium signal from 0.3–8 s after the spike recovered to baseline for 40 Hz stimulation. For **Fig. 3e**, the first epoch for each trial (fixed W condition) was excluded in the data analysis and the calcium signal was averaged for each condition from all the acquired trials for each animal. Each condition was then normalized by the maximum positive deflection of calcium signal alone conditions. For **Fig. 3f, h, i**, the

amplitude peak of the neuronal fluorescent signal in response to 8 s whisker stimulus was calculated as the maximal difference in  $\Delta F/F$  in a time window 300 ms after stimulus, then normalized to the whisker only (W) condition (100%). The unnormalized amplitude for the difference in  $\Delta F/F$  for each epoch was used to generate the calcium signal-based regressor (**Fig. S14**) for fMRI correlation map in **Fig. 4**.

For evoked fMRI analysis, EPI images were first aligned to anatomical images acquired in the same orientation with the same geometry. The anatomical MRI images were registered to a template across animals, as well as EPI datasets. The baseline signal of EPI images was normalized to 100 for statistical analysis of the multiple trials of EPI time courses. The time courses of the BOLD signal were extracted from regions of interest, e.g., barrel cortex, motor cortex, and posterior thalamus, which were segmented on the anatomical images based on the brain atlas and activation or correlation values. The BOLD amplitude for each condition was defined as the average value for the volumes within the 0-10.5 s following the onset of stimulation (when stimulation duration was 8 s). The hemodynamic response function (HRF) used was the default of the block function of the linear program 3dDeconvolve in AFNI. BLOCK (L, 1) computes a convolution of a square wave of duration L and makes a peak amplitude of block response = 1, with  $g(t) = t^4 e^{-t} / [4^4 e^{-4}]$  (peak value=1). In this case, each beta weight represents the peak height of the corresponding BLOCK curve for that class, i.e. the beta weight is the magnitude of the response to the entire stimulus block, as shown in **Fig. 1, 3** and **Fig. S1**. The HRF model is defined as follows:

$$HRF(t) = \int_0^{\min(t, L)} g(t-s) ds$$

For correlation analysis, a calcium signal amplitude modulated regressor (AM2) based AFNI BLOCK (L, 1) function was used (**Fig. S14**). The regressor for amplitude modulated response model is as follows:

$$r_{AM2}(t) = \sum_{k=1}^K h(t - \tau_k) \cdot (a_k - \bar{a})$$

Where  $a_k$  = value of  $k^{th}$  auxiliary behavioral information value (ABI), i.e., calcium amplitude value for the difference in  $\Delta F/F$  for each epoch, and  $\bar{a}$  is the average calcium amplitude value for all the epochs for the individual animal. The statistics and  $\beta$  for AM2 regressor make activation map of voxels whose BOLD response vary proportionally to ABI, i.e., the changes in calcium signals for each epoch.

## RESULTS

### Antidromic activation by callosal optogenetic stimulation.

By injecting the AAV-ChR2 viral vectors into the barrel cortex (BC) of rats, ChR2 can be expressed in callosal projection neurons (CPNs), in particular through their axonal fiber bundles projecting to the contralateral BC (**Fig.**

**1a**) (Petreanu, Huber et al. 2007, Xin Yu 2013). Based on our previous work (Chen, Pais-Roldan et al. 2019), an MRI-guided robotic arm was used to provide high flexibility to insert the optical fiber and sufficient targeting accuracy on the ~200  $\mu\text{m}$  callosal fiber bundle for multi-modal fMRI. The most salient BOLD fMRI signal evoked by CC optogenetic stimulation was detected at the ipsilateral BC housing the labeled CPN ( $n = 8$  animals, **Fig. 1b, c**, 5 Hz light pulses). The antidromically evoked hemodynamic responses to 5 Hz stimulation were significantly stronger than the responses to 2 Hz (**Fig. 1d**). In addition, antidromic BOLD and local field potential (LFP) signal were evoked by systematically varying laser power, light pulse width, frequency and duration of the optogenetic stimulation (**Fig. 1e, Fig. S1 and S2**). The fMRI analysis revealed widespread brain activation in the ipsilateral hemisphere, which likely originates from antidromic CPN activity spread by multi-synaptic pathways to the motor cortex and posterior thalamus (**Fig. 1f**). These widespread ipsilateral effects were readily seen with 5Hz stimulation paradigm but could not be evoked using lower stimulus frequencies.

Next, we examined the temporal characteristics of the antidromic activity. In general, CC-mediated antidromic LFP responses in BC to different pulse widths and frequencies were similar to the responses observed when BC was directly activated (**Fig. S3 and S4**). Likewise, the whole-brain BOLD signal showed time courses and distributions as reported earlier with direct BC stimulation (Yu, Chung et al. 2012, Yu, He et al. 2016). We were concerned that the stimulation light could have activated CPN directly in the BC. To test this concern, we recorded the LFPs evoked by optogenetic CC and direct BC stimulation in the same rat (**Fig. 1g, h**), and found that the latency of the response was systematically higher for CC as compared to BC stimulation (negative peak latency: BC:  $8.13 \pm 1.89$  ms, CC:  $11.27 \pm 0.78$  ms; positive peak latency: BC:  $17.00 \pm 4.65$  ms, CC:  $21.07 \pm 2.60$  ms;  $n = 6$  animals, paired t test,  $*p = 0.002$ ,  $**p = 0.009$ ) (**Fig. 1i**). Otherwise the time course of the LFP response was similar, which showed, firstly that CC stimulation is likely stimulating the CC axons as intended, and secondly that BC is activated in a very similar way by CPNs as with direct stimulation. In support of this conclusion, we found that optogenetically activating callosal fibers from the other hemisphere (opposite to the virus injection site) readily showed latency differences (**Fig. S5**), as expected from the axonal conduction delays of the transmission of the electrical impulses (Simmons and Pearlman 1983, Caminiti, Carducci et al. 2013).

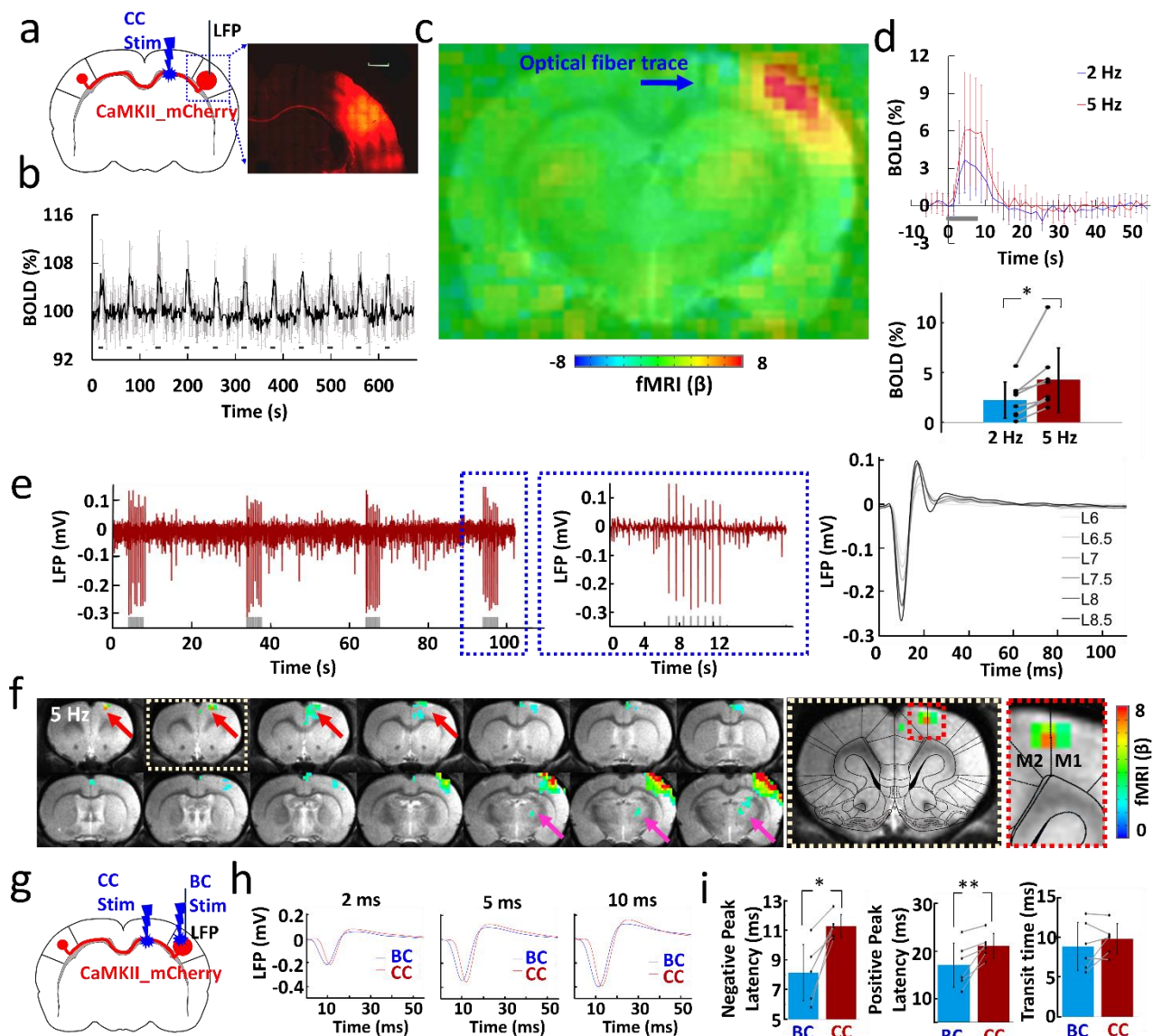


**Fig.1.** Antidromic activation upon corpus callosum optogenetic stimulation. **a, Left:** Schematic of experimental design. **Right:** Representative wide-field fluorescence image illustrating the robust expression of ChR2-mCherry at the injection site (right BC) and along the CC. Medial is to the left. Red, AAV5.CaMKII.ChR2-mCherry. Scale bar, 1 mm. **b,** Average time courses of fMRI signal changes in right BC ( $n = 8$  animals) upon optogenetic stimulation. Error bars represent mean $\pm$ SD. **c,** Averaged fMRI map showing the strong antidromic activation in BC in the right hemisphere with fiber optic trace (blue arrow) during optogenetic stimulation of CC from 8 rats of block design: 8 s on/ 52 s off, 11 epochs, 10 ms light pulse, 5 Hz. **d, Top:** Averaged BOLD signals upon different stimulation frequencies (2 Hz in blue, 5 Hz in red). Error bars represent mean $\pm$ SD. **Lower:** Mean amplitudes of the BOLD signals (0-10.5 s) for 2 Hz and 5 Hz ( $n=8$ , paired t test,  $*p=0.006$ ). Error bars represent mean $\pm$ SD. **e, Left:** The representative local field potential (LFP) for antidromic activation (gray lines, light pulses). **Right:** Laser power dependent LFPs (pulse width, 10 ms). **f,** Representative BOLD map showing the activity in the projected motor cortex (red arrows) and posterior thalamus (magenta arrow) from the antidromic activity in the BC. Broken boxes showed the enlarged view of projected motor cortex (GLM-based t-statistics in AFNI is used.  $P$  (corrected)=0.0319). **g,** Schematic of experimental design. **h,** The representative LFP for direct BC light stimulation (blue) and antidromic activation (red) recorded with light pulse durations of 2, 5 and 10 ms. **i,** The

different peak latency and transit time for the LFP induced by CC and BC light stimulation (n = 6 animals, paired t test, \*p = 0.002, \*\*p = 0.009, pulse width, 10 ms). Error bars represent mean±SD.

### **Orthodromic activation by callosal optogenetic stimulation.**

Compared to antidromically evoked activity, the BOLD signal in the contralateral hemisphere evoked by orthodromic stimulation was smaller, and the stimulus-response relationship was different. For instance, quite different from the antidromic situation, the BOLD signal observed with 2 Hz optogenetic CC stimulation was stronger than that with 5 Hz (**Fig. S6**). To investigate the CC-mediated corticocortical interaction in the contralateral hemisphere, we injected the Syn-GCaMP6f and CaMKII-ChR2-mCherry into the left and right BC, respectively, and recorded both calcium and LFP signal upon optogenetic CC stimulation (**Fig. 2a, b**). Here we focused on layer 5 (**Fig. 2b**), because it is the main target lamina of corpus callosum projections (Suarez, Fenlon et al. 2014, Rock and Apicella 2015), as well as the main output layer of the barrel cortex (Fox 2008). **Fig. 2c** shows the frequency-dependent orthodromic calcium signals from one representative rat. As mentioned before evoked calcium transients appeared in strict frequency-dependent fashion. A strong transient was detected following each light pulse at 2 Hz, while at higher frequencies, only the first pulse triggered a full-fledged calcium response (**Fig. 2c**). The subsequent pulse responses were depressed or missing entirely and gave way to a slow decrement in fluorescence (**Fig. 2c**). The decrement of Ca<sup>2+</sup> signal was constantly present throughout the entire stimulus interval (see gray bar 40 Hz stimulation in **Fig. 2c**), and slowly relaxed back to baseline only after the end of stimulation. Simultaneous LFP and calcium recordings in a representative rat shared the same pattern, strengthening the notion of a strong suppression of responses at higher stimulus frequencies (**Fig. S7**), and offering an explanation for the likewise decreased orthodromic BOLD signals at 5 Hz (**Fig. S6**). The calcium baseline drift for 40 Hz was reproduced in animals and was quantified in **Fig. 2d**, suggesting a highly robust corticocortical inhibition effect as previously reported by electrophysiological recording (Butovas and Schwarz 2003, Butovas, Hormuzdi et al. 2006, Lee, Gee et al. 2014). The evoked LFP and calcium signals dependencies on the laser power, light pulse width and duration provide strong evidence for reliable detection of the orthodromic activity (**Fig. S8-10**). It is noteworthy that the CC-mediated orthodromic activity shows different response patterns for both LFP/calcium and fMRI signals from the antidromic activity, indicating a distinct impact on the local excitation-inhibition balance through the CC-mediated inputs.



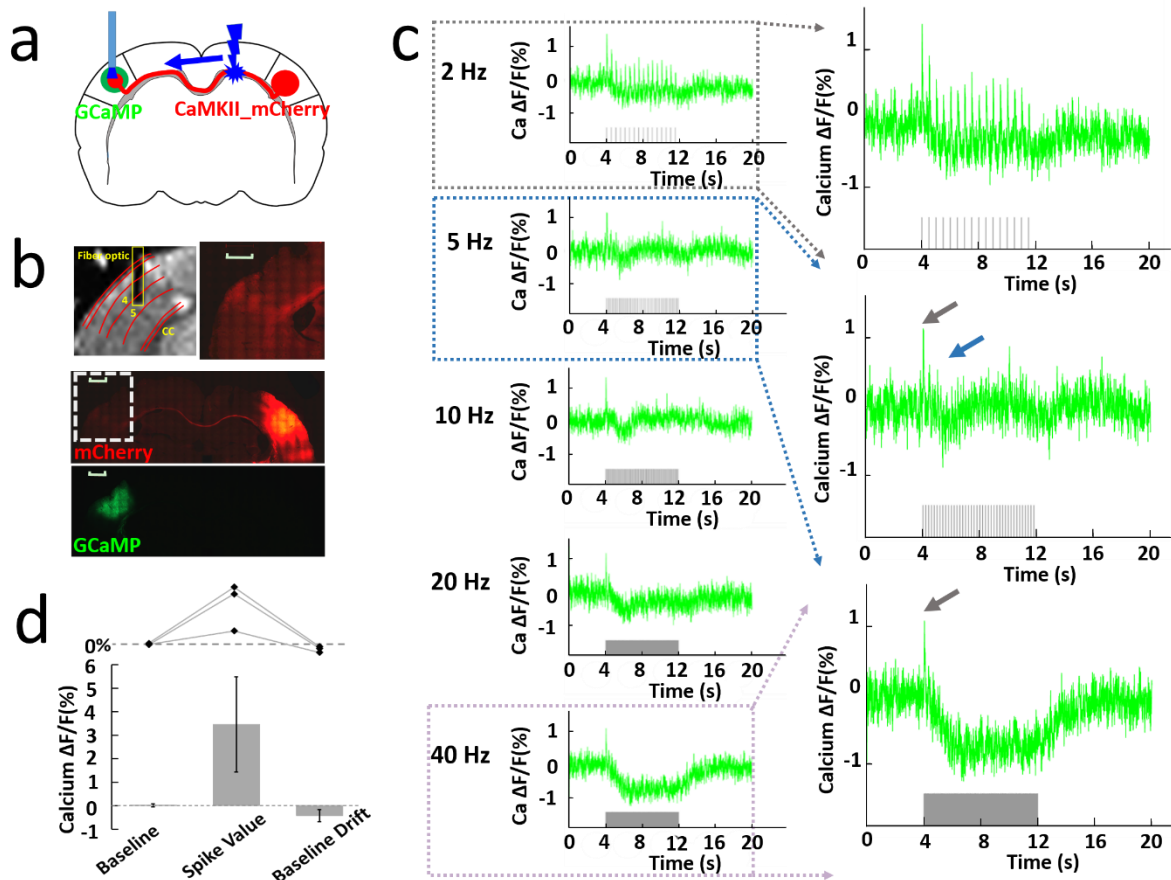


**Fig.2.** Orthodromic activation upon corpus callosum optogenetic stimulation. **a**, Schematic of experimental design. **b**, *Top left*: Representative RARE anatomical image used to identify the optical fiber location for calcium signal recording in the layer V of barrel cortex. *Top right*: Enlarged immunostaining image illustrating the ChR2-mCherry expression in the left hemisphere (opposite to the injection site). *Middle*: Representative wide-field fluorescence image illustrating robust ChR2-mCherry at the injection site (right BC) and along the axonal fibers to the other hemisphere. Red, AAV5.CaMKII.ChR2-mCherry. *Bottom*: The immunostaining image illustrating robust GCaMP6f expression (green) in the left barrel cortex. Scale bar, 1 mm. **c**, *Left*: Representative calcium signal changes upon 8 s of orthodromic activation responses to 2, 5, 10, 20 and 40 Hz stimulation. *Right*: Enlarged calcium signal changes responses to 2, 5 and 40 Hz stimulation. **d**, The analysis of calcium baseline, spike value and baseline drift from 3 animals. Error bars represent mean  $\pm$  SD.

### The CC-mediated inhibitory effects on the sensory-evoked cortical activity

Next, we investigated the effect of CC-mediated suppression on sensory-evoked cortical activity. The optogenetic light pulse train ('O', 2 Hz, 16 pulses in 8 s) for CC optogenetic stimulation was delivered at time intervals of 0, 50, 100 and 200ms after stimulating the primary afferents in the whisker pad with a microstimulation pulse train ('W', 2 Hz, 16 pulses). In total 6 conditions (W, O, OW, O50W, O100W and O200W, OxW means optogenetic pulse leads the whisker stimulation pulse for "x" ms) were delivered in trials of randomized order (**Fig. 3a**) using the multi-model fMRI platform (**Fig. 3b**). Typical raw calcium signals and stimulation design are shown in **Fig. 3c** with a W condition leading the other randomized 12 epochs (6 conditions repeated twice in a randomized order).

We found a strong suppression of BOLD in the orthodromic direction with latencies of 50 and 100 ms (**Fig. 3d, g**). The suppression was partially recovered at the O200W condition. This phenomenon was absent on the antidromic side (**Fig. 3g**). A similar picture emerged with averaged calcium signals recorded in layer 5 of the contralateral BC (**Fig. 3e**).  $\text{Ca}^{2+}$  signals and BOLD were highly correlated (**Fig. 3g, e**), showing reduced calcium percentage changes at O50W and O100W conditions across animals (**Fig. 3f**). Normalizing both signals to the whisker-only (W) condition (**Fig. S11**), we find the mean signal changes of BOLD from 100% (W) to 107.3%, 59.2%, 56.8% and 100.4%, while the calcium signal changed from 100% (W) to 127.8%, 45.2%, 59.5% and 107.1% at conditions of OW, O50W, O100W, and O200W, respectively (**Fig. 3h**). To investigate the temporal features of the interaction on a more precise scale, we refined the stimulus intervals for whisker stimulation by adding 10 and 25 ms conditions (W, OW, O10W, O25W, O50W, O100W, and O200W) in another group of rats (**Fig. 3i** and **Fig. S12**). Again similar patterns emerged as seen before (**Fig. 3i** and **Fig. S12**). For O10W, no significant difference was observed in comparison to the OW condition, but the calcium responses at O25W were significantly lower than the OW condition (**Fig. S12**). As reported from *in vitro* CC electrical stimulation studies by Kawaguchi et al. (Kawaguchi 1992), CC stimulation leads to two inhibitory postsynaptic potential (IPSP) peaks (the earlier peak at ~30 ms, and the later peak at ~180 ms), which could underlie the inhibitory effects at O25W and the later recovery at O200W to different extents. Furthermore, the simultaneous LFP and calcium recording confirmed the time-interval specific inhibitory effects by direct optogenetic CC stimulation to modulate the sensory-evoked cortical activity pattern in the BC (**Fig. S13**). These results are consistent with results using whisker, forepaw, and visual stimulation in rodents and human studies (Schnitzler, Kessler et al. 1996, Ogawa, Lee et al. 2000, Shuler, Krupa et al. 2001, Berwick, Redgrave et al. 2004, Wiest, Bentley et al. 2005, Ni, Gunraj et al. 2009, Bocci, Caleo et al. 2011, Nemoto, Hoshi et al. 2012).

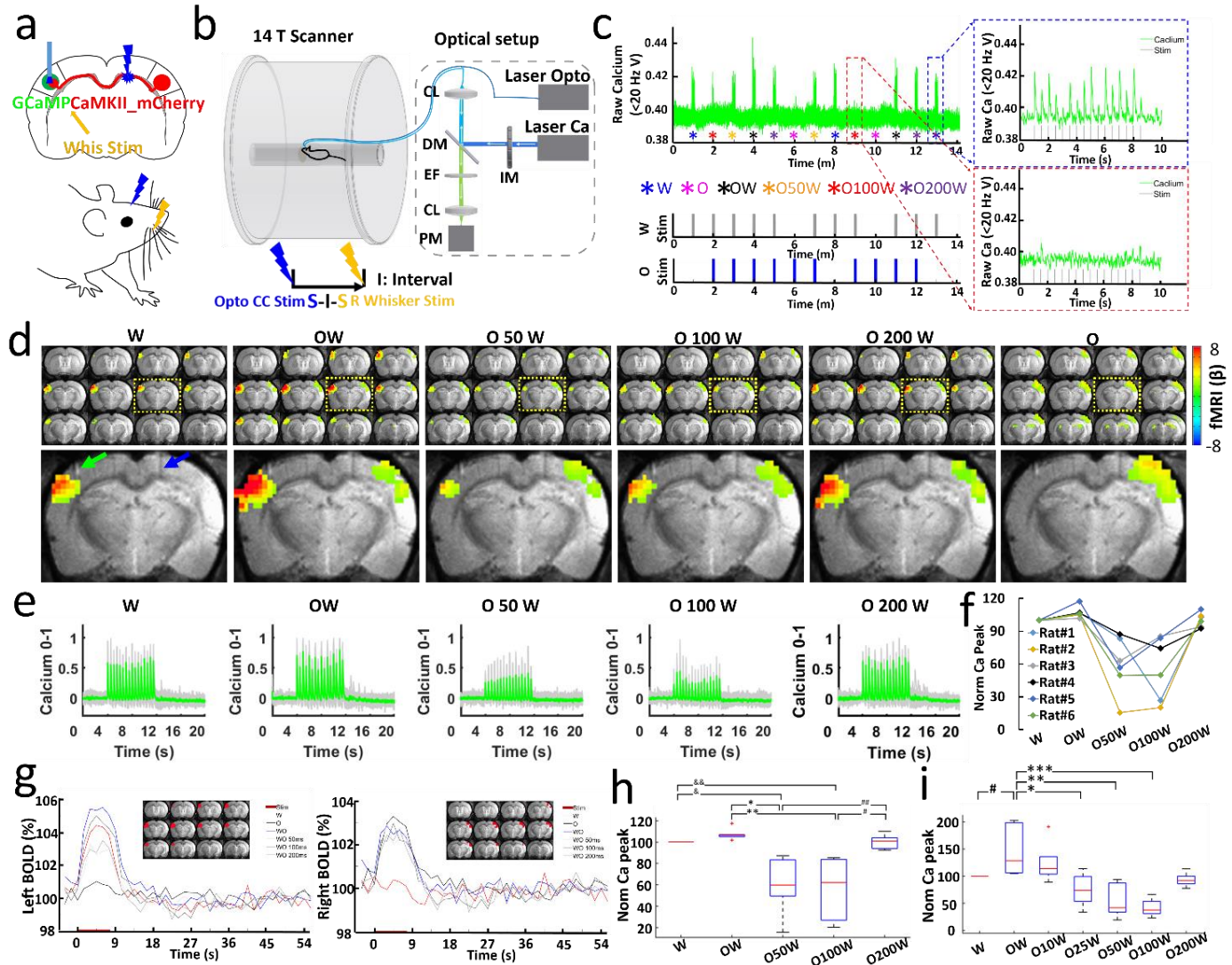


**Fig. 3.** Simultaneous measurement of BOLD and calcium signals during CC optogenetic stimulation and electrical whisker stimulation with varying time intervals. **a**, Stimulation scheme. There are 6 conditions, whisker stimuli only (W), CC stimuli only (O), CC stimuli and whisker stimuli together (OW), CC stimuli and 50 ms, 100ms, 200 ms delayed whisker stimuli (O50W, O100W, O200W). **b**, Schematic drawing of the experimental setup to conduct optogenetic fMRI with simultaneous fiber-optic calcium recording. CL: Coupling Lens, DM: Dichroic Mirror, EF: Emission Filter, PM: Photomultiplier, IM: Intensity Modulation. **c**, Typical calcium signals for condition W (blue dash box) and O100W (red dash box) from a representative rat. **d**, *Top*: Averaged fMRI map of brain-wide activity for 6 conditions across 6 rats (GLM-based t-statistics in AFNI is used.  $p$  (corrected)  $< 0.01$ ) of block design: 8 s on/ 52 s off, 13 epochs, 20 ms light pulse, 2 Hz, 5–39 mw. *Bottom*: Enlarged brain slice showing the differences of BOLD mapping in BC in both hemispheres with fiber optic trace for optogenetic stimulation (blue arrow) and calcium recording fiber (green arrow). **e**, Averaged normalized calcium signal in left BC, grey lines showing the individual normalized calcium signal from 6 rats (Trials # = 29, details see Methods, table 1). **f**, Normalized calcium signal for an individual rat as a function of conditions: W, OW, O50W, O100W, O200W. **g**, *Left*: Averaged BOLD changes in the ROI (red region on anatomical images) in the left BC induced by whisker stimulation. *Right*: averaged BOLD changes in the ROI (red region on anatomical images) in the right BC induced by CC stimulation. **h**, Averaged normalized calcium signal changes across 6 rats modulated by stimulus time intervals (ANOVA,  $p < 0.01$ ). **i**, Averaged normalized calcium signal changes across 4 rats modulated by stimulus time intervals (ANOVA,  $p < 0.03$ ).

## Global network mapping based on the optogenetically-driven CC-mediated inhibitory effects

The 3D fMRI data with concurrent calcium signal acquired at different conditions with CC and whisker stimulation allowed analyzing the global effect of the optogenetically-driven CC-mediated inhibition. To this end, the calcium signal amplitude modulation (AM) factor was applied to the ideal function produced by the general linear model (GLM), which was correlated with the 3D fMRI time course (**Fig. S14**) (Cox 1996, Wang, He et al. 2018). As shown in Fig S14, the calcium-AM regressor is derived from the stimulation-driven ideal function, of which the GLM analysis leads to a AM-specific correlation with the whole brain fMRI signal. Thus, the calcium-based AM-correlation with the entire brain generated a map of global brain dynamic changes related to specific CC-mediated inhibition effect. The strongest correlation was found in the left BC (**Fig 4**). A positive correlation was further observed in the ipsilateral motor cortex and posterior thalamus (PO), which are projection targets of the BC, as well as the ventral right BC (**Fig. 4a, b, c**). We next extracted the time courses from the highlighted ROIs to examine the changes of the fMRI signals at different conditions. The averaged time courses from the right BC ROI reflected the patterns seen in the orthodromically affected BC before. In these conditions (O50W and O100W), the BOLD signals were reduced with respect to the other conditions (**Fig. 4d**). Similar patterns of BOLD responses were detected in the MC (**Fig. 4e**) as well as the PO (**Fig. 4f**) directly connected to the left BC. It is noteworthy that the positively correlated right BC area was not overlapping with cortical areas housing the CPNs (**Fig. 3**). In summary, these results demonstrate that the global network is modulated with the CC-specific evoked activity in BC. The specificity of CPN precludes the possibility that MC and PO might have integrated the callosal and sensory input independently of BC.

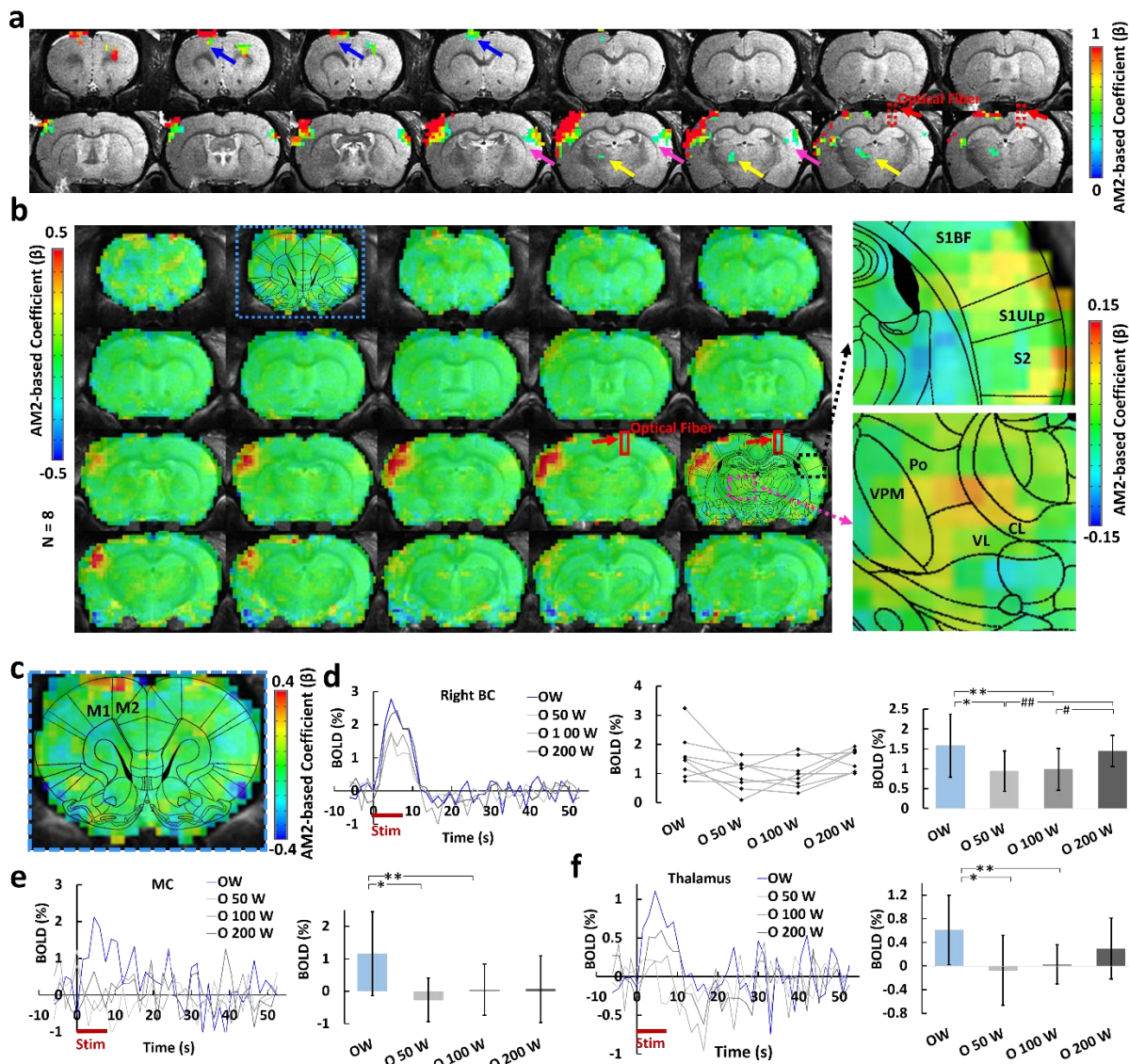


**Fig. 4.** Calcium AM-based whole brain BOLD correlation analysis. **a**, one representative animal map overlaid on the anatomical image with a statistical threshold ( $p$  (corrected)  $< 0.05$ , cluster size  $> 15$  voxels, MC, blue arrows, BC, magenta arrows, PO, yellow arrows, optical fiber trace, red arrows). **b**, Group-averaged correlation maps show the spatial distribution of the positive correlation located at left BC, MC, as well as the PO by overlying with the brain atlas (red square, optical fiber traces, right panel: the enlarged images of the correlation map overlaid on the brain atlas). **c**, Enlarged correlation map shows the positive correlation at the MC. **d**, *Left*: Averaged time courses from the right BC at different conditions ( $n = 8$  rats). *middle*: Mean amplitudes of the BOLD signals (0-10.5 s) for individual rats. *Right*: Averaged amplitudes of the BOLD signals (0-10.5 s, mean $\pm$ SD, ANOVA,  $*p = 0.027$ ,  $**p = 0.004$ ,  $\#p = 0.030$ ,  $###p = 0.003$ ). **e**, *Left*: averaged time courses from the MC ( $n = 8$  rats). *Right*: Averaged amplitudes of the BOLD signals (0-10.5 s, mean $\pm$ SD, ANOVA,  $*p = 0.005$ ,  $**p = 0.01$ ). **f**, *Left*: Averaged time courses from the PO ( $n = 8$  rats). *Right*: Averaged amplitudes of the BOLD signal (0-10.5 s, mean $\pm$ SD, ANOVA,  $*p = 0.009$ ,  $**p = 0.012$ ). W: whisker stimulation only, OW: simultaneous optical and whisker stimulation, O[x]W optical stimulation followed by [x] ms-delayed whisker stimulation.

## DISCUSSION

We have performed simultaneous BOLD-fMRI and calcium recording in combination with callosal-circuit specific optogenetic stimulation to map the brain-wide network activation. The robust BOLD signal due to the antidromic activity was detected in the ipsilateral BC, which also led to fMRI detection in the ipsilateral MC and PO region with the higher frequency stimulus. In contrast, the positive BOLD signal through the CC-orthodromic activity was only reliably observed at the lower frequency optogenetic stimulus. With the 40Hz light pulses, the calcium baseline suppression was detected and interpreted to be due to the CC-mediated cortico-cortical inhibitory effect. To further test this CC-mediated inhibition was further paired with the whisker stimulation paradigm at varying inter-stimulus intervals from 0 ms to 200 ms, showing significant suppression at the O50W and O100W conditions in the left BC by the concurrent fMRI and calcium recording. By extracting the event-dependent calcium peak amplitudes at varied conditions as a regressor, an amplitude modulation (AM)-based correlation map revealed the brain-wide inhibitory effects spreading through the ventral border of the right BC and the left MC and PO. Thus, the multi-modal fMRI platform provides a thorough brain-wide network activation maps for the CC-specific optogenetic stimulation.

The observation of strong antidromic propagation by callosal optogenetic stimulation and related synaptic spread of activity presents a caveat for the conclusion of circuit specificity for *in vivo* optogenetic studies. In particular, when neuronal projection terminals labeled with ChR-2 from neurons located at specific functional nuclei are targeted, possible spreading network activity from the antidromically activated brain sites need to be considered. In our experiments, BOLD signals were detected in both MC and PO projected from the antidromically activated BC (at 5Hz light pulses), indicating a (for the experimental purpose unintended) wide-spread optogenetic activation pattern in the brain-wide network (**Fig 1e**). This spread is likely due to synaptic propagation via activated local or regional axon collaterals of CPNs (Wilson 1987, White and Czeiger 1991, Cauller, Clancy et al. 1998, Mitchell and Macklis 2005, Fame, MacDonald et al. 2011). For the present spread into motor and sensorimotor structures, deep layer CPN with long-range projections into sensorimotor brain areas are likely involved (Veinante and Deschenes 2003). In addition, multi-synaptic pathways, involving either cortico-cortical or cortico-thalamic projections may have contributed to the spread brain-wide activation (Kleinfeld and Deschenes 2011, Gambino, Pages et al. 2014). In conclusion, it is mandatory to consider brain-wide activation patterns, even in case of application of highly circuit-specific optogenetic activation schemes.

Certainly, the optogenetic callosal fiber activation also elicits the specific unidirectional callosal orthodromic activity as well, similar to earlier reports (Kawaguchi 1992, Hoffmeyer, Enager et al. 2007, Karayannis, Huerta-Ocampo et al. 2007). In addition, the optogenetic activation of the callosal projection terminals from brain slices leads to better characterization of the excitatory and inhibitory circuit regulation by callosal inputs (Petreanu, Huber et al. 2007, Palmer, Schulz et al. 2012, Lee, Gee et al. 2014, Rock and Apicella 2015, Petrus, Saar et al. 2019). Our observations further support the non-linear neurovascular coupling events with the optical intrinsic signal

measurements and laser-doppler flowmetry upon the optogenetic or electrical CC stimulation (Hoffmeyer, Enager et al. 2007, Iordanova, Vazquez et al. 2018). In our study, the fact that orthodromic BOLD signals were readily observed with low-frequency stimulation (2 Hz), but were strongly reduced at the higher frequency (5Hz), reveals a critical non-linear manner of the hemodynamic responses driven by the CC-mediated neuronal activation (**Fig. 1f, 2c**, and **Fig. S6**). We show here that peripheral whisker stimulation is well suited to study the suppressive effects of orthodromically conveyed activity specific to the callous, which is not possible using *in vivo* bilateral stimulation paradigms in rodents (Ogawa, Lee et al. 2000, Shuler, Krupa et al. 2001, Berwick, Redgrave et al. 2004, Wiest, Bentley et al. 2005, Nemoto, Hoshi et al. 2012) or bilateral motor or visual tasks in humans (Schnitzler, Kessler et al. 1996, Ni, Gunraj et al. 2009, Bocci, Caleo et al. 2011) where other pathways may be involved. In particular, CC-induced orthodromic activity of L5 pyramidal neurons evoked a calcium transient followed by marked depression of calcium signals responding to light pulses on CC (**Fig. 2c,d**) (consistent with the optogenetic results in brain slices (Lee, Gee et al. 2014)). Electrophysiology in brain slices has elucidated that CC-mediated glutamatergic excitatory postsynaptic potentials are followed by early GABA<sub>A</sub>- and late GABA<sub>B</sub>-mediated inhibitory postsynaptic potentials lasting for several hundred milliseconds (Kawaguchi 1992, Kumar and Huguenard 2001, Karayannis, Huerta-Ocampo et al. 2007, Palmer, Schulz et al. 2012), strongly suggesting that the depression seen here is partly due to synaptic inhibition. Also, while pairing with 2 Hz whisker stimulation, a time course of the depressive effect around 50-100 ms interval fit the previous finding that local intracortical activation is characterized by activation of long-lasting synaptic GABAergic inhibition (Butovas and Schwarz 2003, Butovas, Hormuzdi et al. 2006, Cardin, Carlen et al. 2009, Logothetis, Augath et al. 2010, Moore, Carlen et al. 2010, Palmer, Schulz et al. 2013). In particular, besides the robust inhibition detected in the paired O50W and O100W conditions, a refined temporal scale at the O25W condition further demonstrates the CC-mediated inhibitory effect (**Fig. S12**), which can be potentially caused by the GABA<sub>A</sub>-mediated early IPSP peak elicited by the direct electrical CC stimulation (Kawaguchi 1992). The fact that antidromic activity is not susceptible for the paired optogenetic and whisker stimulation (surely due to weaker ipsilateral whisker-evoked activity, but also likely due to the relative strength of antidromic activation), supports the notion that the depression of whisker-evoked activity is due mainly to local (contralateral) interaction of CC-evoked and whisker-evoked activity, rather than to possible CC activity evoked by indirect activation of additional CPNs via antidromic activation.

The whole-brain fMRI with concurrent calcium recording allows accessing brain-wide network effects of CC-mediated inhibition (**Fig. 4a, b**). In particular, the application of the AM-based GLM allows separating the stimulus-driven responses from the AM factor, which creates specific correlation maps to the CC-mediated inhibitory effects. The calcium amplitude-modulation (AM)-based correlation map highlighted three brain regions: the ventral part of right BC, the left MC, and PO. The ventral right BC was likely activated by reciprocal callosal connections, the majority of which, as argued above, may have been quenched by the strong antidromic effect via labeled CPNs. In the injection experiments, however, the ventral BC was regularly spared and did not receive virus, and therefore

may have been less affected by overriding antidromic activity. Outside BC on the orthodromic side the AM-dependent correlation was detected as well in the right MC and PO. The CC-mediated inhibitory effect on the spatially distinct MC could be caused by the long-range S1-MC projection for sensorimotor integration (Ferezou, Haiss et al. 2007, Matyas, Sreenivasan et al. 2010, Kleinfeld and Deschenes 2011, Chen, Carta et al. 2013, Feldmeyer, Brecht et al. 2013). The direct BOLD activation in the MC was detected by whisker stimulation through the sensorimotor connection (Yu, Qian et al. 2014), which was also shown in the antidromic activity-based spreading activation patterns (**Fig 1e**). The CC-mediated inhibitory effect on the PO is likely via corticothalamic projections originating from BC layer 5b neurons (Groh, Bokor et al. 2014, Mease, Sumser et al. 2016, Mease, Sumser et al. 2016, Sumser, Mease et al. 2017). This finding points at a potential participation of the callosal inputs in the regulation of a wider network of a reciprocal thalamocortical network which mediates BC signals from the other hemisphere for whisking related processing (Petreanu, Mao et al. 2009, Theyel, Llano et al. 2010, Feldmeyer, Brecht et al. 2013, Gambino, Pages et al. 2014, Manita, Suzuki et al. 2015, Mease, Metz et al. 2016, Sumser, Mease et al. 2017). Therefore, besides the antidromically evoked network activation pattern, the orthodromic CC-mediated inhibition generates a brain-wide activity pattern of its own.

In summary, by taking advantage of optogenetics to activate unidirectional callosal fiber, calcium indicators (GCaMP6f) to track specific L5 pyramidal neuronal activity, and simultaneous whole-brain fMRI mapping, this work bridges the scales from the cellular to the whole brain network level for CC-mediated activity. We present a multi-modal fMRI platform to map and analyze the CC-regulated excitation/inhibition balance across multiple scales, which should be useful to decipher brain network dysfunction induced from CC abnormalities. Brain-wide network activation from callosal-circuit optogenetic stimulation underscores the caution to interpret circuit-specific regulatory mechanisms underlying behavioral or functional outcomes with optogenetics in animals.

### **Author Contributions**

X.Y. designed and supervised the research, Y.C. and X.Y. performed animal experiments, Y.C. acquired data, Y.C. analyzed data, A.K., C.S., F.S. and P.P-R. provided conceptual and technical support, X.Y., Y.C., A.K. and C.S. wrote the manuscript.

**Data availability.** Excel files are included for each quantitative plot included in the main figures. All other data generated during this study are available from the corresponding author upon reasonable request.

**Code availability.** The Analysis of Functional NeuroImages software (AFNI, NIH, USA) and Matlab (MATLAB, MathWorks, USA) were used to process the fMRI and simultaneously acquired calcium signals, respectively. The relevant source codes can be downloaded through <https://afni.nimh.nih.gov/afni/>. The related image processing codes are available from the corresponding author upon reasonable request.



**Competing interests.** The authors declare no competing interests.

## ACKNOWLEDGEMENTS

The financial support of the NIH grant (1RF1NS113278), Max-Planck-Society, DFG ([YU 215/3-1](#)), BMBF (01GQ1702), the intramural research program of NINDS (A. Koretsky) and the China Scholarship Council (Ph.D. fellowship to Y. Chen) are gratefully acknowledged. We thank Dr. N. Avdievitch and Ms. H. Schulz for technical support, Dr. P. Douay, Mrs. R. König, Dr. E. Weiler, Ms. S. Fischer and Mrs. M. Pitscheider for animal support, the AFNI team for the software support, the Genetically-Encoded Neuronal Indicator and Effector Program and the Janelia Farm Research Campus for kindly providing viral plasmids.

## REFERENCES

- Adamantidis, A. R., F. Zhang, A. M. Aravanis, K. Deisseroth and L. de Lecea (2007). "Neural substrates of awakening probed with optogenetic control of hypocretin neurons." *Nature* **450**(7168): 420-424.
- Albers, F., F. Schmid, L. Wachsmuth and C. Faber (2018). "Line scanning fMRI reveals earlier onset of optogenetically evoked BOLD response in rat somatosensory cortex as compared to sensory stimulation." *Neuroimage* **164**: 144-154.
- Albers, F., L. Wachsmuth, T. M. van Alst and C. Faber (2018). "Multimodal Functional Neuroimaging by Simultaneous BOLD fMRI and Fiber-Optic Calcium Recordings and Optogenetic Control." *Mol Imaging Biol* **20**(2): 171-182.
- Anderson, J. S., T. J. Druzgal, A. Froehlich, M. B. DuBray, N. Lange, A. L. Alexander, T. Abildskov, J. A. Nielsen, A. N. Cariello, J. R. Cooperrider, E. D. Bigler and J. E. Lainhart (2011). "Decreased interhemispheric functional connectivity in autism." *Cereb Cortex* **21**(5): 1134-1146.
- Bernal-Casas, D., H. J. Lee, A. J. Weitz and J. H. Lee (2017). "Studying Brain Circuit Function with Dynamic Causal Modeling for Optogenetic fMRI." *Neuron* **93**(3): 522-532 e525.
- Berwick, J., P. Redgrave, M. Jones, N. Hewson-Stoate, J. Martindale, D. Johnston and J. E. Mayhew (2004). "Integration of neural responses originating from different regions of the cortical somatosensory map." *Brain Res* **1030**(2): 284-293.
- Bocci, T., M. Caleo, E. Giorli, D. Barloscio, L. Maffei, S. Rossi and F. Sartucci (2011). "Transcallosal inhibition dampens neural responses to high contrast stimuli in human visual cortex." *Neuroscience* **187**: 43-51.
- Boyden, E. S., F. Zhang, E. Bamberg, G. Nagel and K. Deisseroth (2005). "Millisecond-timescale, genetically targeted optical control of neural activity." *Nat Neurosci* **8**(9): 1263-1268.
- Butovas, S., S. G. Hormuzdi, H. Monyer and C. Schwarz (2006). "Effects of electrically coupled inhibitory networks on local neuronal responses to intracortical microstimulation." *J Neurophysiol* **96**(3): 1227-1236.
- Butovas, S. and C. Schwarz (2003). "Spatiotemporal effects of microstimulation in rat neocortex: a parametric study using multielectrode recordings." *J Neurophysiol* **90**(5): 3024-3039.
- Caminiti, R., F. Carducci, C. Piervincenzi, A. Battaglia-Mayer, G. Confalone, F. Visco-Comandini, P. Pantano and G. M. Innocenti (2013). "Diameter, length, speed, and conduction delay of callosal axons in macaque monkeys and humans: comparing data from histology and magnetic resonance imaging diffusion tractography." *J Neurosci* **33**(36): 14501-14511.
- Cardin, J. A., M. Carlen, K. Meletis, U. Knoblich, F. Zhang, K. Deisseroth, L. H. Tsai and C. I. Moore (2009). "Driving fast-spiking cells induces gamma rhythm and controls sensory responses." *Nature* **459**(7247): 663-667.

Cardin, J. A., M. Carlen, K. Meletis, U. Knoblich, F. Zhang, K. Deisseroth, L. H. Tsai and C. I. Moore (2010). "Targeted optogenetic stimulation and recording of neurons in vivo using cell-type-specific expression of Channelrhodopsin-2." *Nat Protoc* **5**(2): 247-254.

Carter, M. E., O. Yizhar, S. Chikahisa, H. Nguyen, A. Adamantidis, S. Nishino, K. Deisseroth and L. de Lecea (2010). "Tuning arousal with optogenetic modulation of locus coeruleus neurons." *Nat Neurosci* **13**(12): 1526-1533.

Cauler, L. J., B. Clancy and B. W. Connors (1998). "Backward cortical projections to primary somatosensory cortex in rats extend long horizontal axons in layer I." *Journal of Comparative Neurology* **390**(2): 297-310.

Chen, J. L., S. Carta, J. Soldado-Magraner, B. L. Schneider and F. Helmchen (2013). "Behaviour-dependent recruitment of long-range projection neurons in somatosensory cortex." *Nature* **499**(7458): 336-340.

Chen, Y., P. Pais-Roldan, X. M. Chen, M. H. Frosz and X. Yu (2019). "MRI-guided robotic arm drives optogenetic fMRI with concurrent Ca<sup>2+</sup> recording." *Nature Communications* **10**.

Cox, R. W. (1996). "AFNI: software for analysis and visualization of functional magnetic resonance neuroimages." *Comput Biomed Res* **29**(3): 162-173.

Egaas, B., E. Courchesne and O. Saitoh (1995). "Reduced size of corpus callosum in autism." *Arch Neurol* **52**(8): 794-801.

Fame, R. M., J. L. MacDonald and J. D. Macklis (2011). "Development, specification, and diversity of callosal projection neurons." *Trends Neurosci* **34**(1): 41-50.

Feldmeyer, D., M. Brecht, F. Helmchen, C. C. Petersen, J. F. Poulet, J. F. Staiger, H. J. Luhmann and C. Schwarz (2013). "Barrel cortex function." *Prog Neurobiol* **103**: 3-27.

Ferezou, I., F. Haiss, L. J. Gentet, R. Aronoff, B. Weber and C. C. Petersen (2007). "Spatiotemporal dynamics of cortical sensorimotor integration in behaving mice." *Neuron* **56**(5): 907-923.

Fox, K. (2008). "Barrel Cortex." *Barrel Cortex*: 1-+.

Gambino, F., S. Pages, V. Kehayas, D. Baptista, R. Tatti, A. Carleton and A. Holtmaat (2014). "Sensory-evoked LTP driven by dendritic plateau potentials in vivo." *Nature* **515**(7525): 116-+.

Gao, R., S. M. Asano, S. Upadhyayula, I. Pisarev, D. E. Milkie, T. L. Liu, V. Singh, A. Graves, G. H. Huynh, Y. Zhao, J. Bogovic, J. Colonell, C. M. Ott, C. Zugates, S. Tappan, A. Rodriguez, K. R. Mosaliganti, S. H. Sheu, H. A. Pasolli, S. Pang, C. S. Xu, S. G. Megason, H. Hess, J. Lippincott-Schwartz, A. Hantman, G. M. Rubin, T. Kirchhausen, S. Saalfeld, Y. Aso, E. S. Boyden and E. Betzig (2019). "Cortical column and whole-brain imaging with molecular contrast and nanoscale resolution." *Science* **363**(6424).

Gazzaniga, M. S. (2000). "Cerebral specialization and interhemispheric communication: does the corpus callosum enable the human condition?" *Brain* **123** ( Pt 7): 1293-1326.

Gazzaniga, M. S. (2005). "Forty-five years of split-brain research and still going strong." *Nat Rev Neurosci* **6**(8): 653-659.

Grandjean, J., A. Corcoba, M. C. Kahn, A. L. Upton, E. S. Deneris, E. Seifritz, F. Helmchen, E. O. Mann, M. Rudin and B. J. Saab (2019). "A brain-wide functional map of the serotonergic responses to acute stress and fluoxetine." *Nat Commun* **10**(1): 350.

Groh, A., H. Bokor, R. A. Mease, V. M. Plattner, B. Hangya, A. Stroh, M. Deschenes and L. Acsady (2014). "Convergence of cortical and sensory driver inputs on single thalamocortical cells." *Cereb Cortex* **24**(12): 3167-3179.

He, Y., M. Wang, X. Chen, R. Pohmann, J. R. Polimeni, K. Scheffler, B. R. Rosen, D. Kleinfeld and X. Yu (2018). "Ultra-Slow Single-Vessel BOLD and CBV-Based fMRI Spatiotemporal Dynamics and Their Correlation with Neuronal Intracellular Calcium Signals." *Neuron* **97**(4): 925-939 e925.

Hoffmeyer, H. W., P. Enager, K. J. Thomsen and M. J. Lauritzen (2007). "Nonlinear neurovascular coupling in rat sensory cortex by activation of transcallosal fibers." *J Cereb Blood Flow Metab* **27**(3): 575-587.

Innocenti, G. M., F. Ansermet and J. Parnas (2003). "Schizophrenia, neurodevelopment and corpus callosum." *Mol Psychiatry* **8**(3): 261-274.

Inoue, K. I., M. Takada and M. Matsumoto (2015). "Neuronal and behavioural modulations by pathway-selective optogenetic stimulation of the primate oculomotor system." *Nat Commun* **6**: 8378.

Iordanova, B., A. Vazquez, T. D. Kozai, M. Fukuda and S. G. Kim (2018). "Optogenetic investigation of the variable neurovascular coupling along the interhemispheric circuits." J Cereb Blood Flow Metab **38**(4): 627-640.

Just, N. and C. Faber (2019). "Probing activation-induced neurochemical changes using optogenetics combined with functional magnetic resonance spectroscopy: a feasibility study in the rat primary somatosensory cortex." J Neurochem **150**(4): 402-419.

Karayannis, T., I. Huerta-Ocampo and M. Capogna (2007). "GABAergic and pyramidal neurons of deep cortical layers directly receive and differently integrate callosal input." Cereb Cortex **17**(5): 1213-1226.

Karolis, V. R., M. Corbetta and M. Thiebaut de Schotten (2019). "The architecture of functional lateralisation and its relationship to callosal connectivity in the human brain." Nat Commun **10**(1): 1417.

Kawaguchi, Y. (1992). "Receptor subtypes involved in callosally-induced postsynaptic potentials in rat frontal agranular cortex in vitro." Exp Brain Res **88**(1): 33-40.

Kim, C. K., A. Adhikari and K. Deisseroth (2017). "Integration of optogenetics with complementary methodologies in systems neuroscience." Nat Rev Neurosci **18**(4): 222-235.

Kleinfeld, D. and M. Deschenes (2011). "Neuronal Basis for Object Location in the Vibrissa Scanning Sensorimotor System." Neuron **72**(3): 455-468.

Kumar, S. S. and J. R. Huguenard (2001). "Properties of excitatory synaptic connections mediated by the corpus callosum in the developing rat neocortex." J Neurophysiol **86**(6): 2973-2985.

Lee, A. T., S. M. Gee, D. Vogt, T. Patel, J. L. Rubenstein and V. S. Sohal (2014). "Pyramidal neurons in prefrontal cortex receive subtype-specific forms of excitation and inhibition." Neuron **81**(1): 61-68.

Lee, J. H., R. Durand, V. Gradinaru, F. Zhang, I. Goshen, D. S. Kim, L. E. Fenno, C. Ramakrishnan and K. Deisseroth (2010). "Global and local fMRI signals driven by neurons defined optogenetically by type and wiring." Nature **465**(7299): 788-792.

Li, X., D. V. Gutierrez, M. G. Hanson, J. Han, M. D. Mark, H. Chiel, P. Hegemann, L. T. Landmesser and S. Herlitze (2005). "Fast noninvasive activation and inhibition of neural and network activity by vertebrate rhodopsin and green algae channelrhodopsin." Proc Natl Acad Sci U S A **102**(49): 17816-17821.

Lima, S. Q. and G. Miesenbock (2005). "Remote control of behavior through genetically targeted photostimulation of neurons." Cell **121**(1): 141-152.

Logothetis, N. K., M. Augath, Y. Murayama, A. Rauch, F. Sultan, J. Goense, A. Oeltermann and H. Merkle (2010). "The effects of electrical microstimulation on cortical signal propagation." Nat Neurosci **13**(10): 1283-1291.

Manita, S., T. Suzuki, C. Homma, T. Matsumoto, M. Odagawa, K. Yamada, K. Ota, C. Matsubara, A. Inutsuka, M. Sato, M. Ohkura, A. Yamanaka, Y. Yanagawa, J. Nakai, Y. Hayashi, M. E. Larkum and M. Murayama (2015). "A Top-Down Cortical Circuit for Accurate Sensory Perception." Neuron **86**(5): 1304-1316.

Matyas, F., V. Sreenivasan, F. Marbach, C. Wacongne, B. Barse, C. Mateo, R. Aronoff and C. C. Petersen (2010). "Motor control by sensory cortex." Science **330**(6008): 1240-1243.

Mease, R. A., M. Metz and A. Groh (2016). "Cortical Sensory Responses Are Enhanced by the Higher-Order Thalamus." Cell Rep **14**(2): 208-215.

Mease, R. A., A. Sumser, B. Sakmann and A. Groh (2016). "Cortical Dependence of Whisker Responses in Posterior Medial Thalamus In Vivo." Cereb Cortex **26**(8): 3534-3543.

Mease, R. A., A. Sumser, B. Sakmann and A. Groh (2016). "Corticothalamic Spike Transfer via the L5B-POm Pathway in vivo." Cereb Cortex **26**(8): 3461-3475.

Mitchell, B. D. and J. D. Macklis (2005). "Large-scale maintenance of dual projections by callosal and frontal cortical projection neurons in adult mice." Journal of Comparative Neurology **482**(1): 17-32.

Moore, C. I., M. Carlen, U. Knoblich and J. A. Cardin (2010). "Neocortical interneurons: from diversity, strength." Cell **142**(2): 189-193.

Nagel, G., M. Brauner, J. F. Liewald, N. Adeishvili, E. Bamberg and A. Gottschalk (2005). "Light activation of channelrhodopsin-2 in excitable cells of *Caenorhabditis elegans* triggers rapid behavioral responses." Curr Biol **15**(24): 2279-2284.

Nagel, G., D. Ollig, M. Fuhrmann, S. Kateriya, A. M. Musti, E. Bamberg and P. Hegemann (2002). "Channelrhodopsin-1: a light-gated proton channel in green algae." *Science* **296**(5577): 2395-2398.

Nemoto, M., Y. Hoshi, C. Sato, Y. Iguchi, I. Hashimoto, E. Kohno, T. Hirano and S. Terakawa (2012). "Diversity of neural-hemodynamic relationships associated with differences in cortical processing during bilateral somatosensory activation in rats." *Neuroimage* **59**(4): 3325-3338.

Ni, Z., C. Gunraj, A. J. Nelson, I. J. Yeh, G. Castillo, T. Hoque and R. Chen (2009). "Two phases of interhemispheric inhibition between motor related cortical areas and the primary motor cortex in human." *Cereb Cortex* **19**(7): 1654-1665.

Ogawa, S., T. M. Lee, R. Stepnoski, W. Chen, X. H. Zhu and K. Ugurbil (2000). "An approach to probe some neural systems interaction by functional MRI at neural time scale down to milliseconds." *Proc Natl Acad Sci U S A* **97**(20): 11026-11031.

Palmer, L. M., J. M. Schulz and M. E. Larkum (2013). "Layer-specific regulation of cortical neurons by interhemispheric inhibition." *Commun Integr Biol* **6**(3): e23545.

Palmer, L. M., J. M. Schulz, S. C. Murphy, D. Ledergerber, M. Murayama and M. E. Larkum (2012). "The cellular basis of GABA(B)-mediated interhemispheric inhibition." *Science* **335**(6071): 989-993.

Peteanu, L., D. Huber, A. Sobczyk and K. Svoboda (2007). "Channelrhodopsin-2-assisted circuit mapping of long-range callosal projections." *Nat Neurosci* **10**(5): 663-668.

Peteanu, L., T. Mao, S. M. Sternson and K. Svoboda (2009). "The subcellular organization of neocortical excitatory connections." *Nature* **457**(7233): 1142-1145.

Petrus, E., G. Saar, Z. Ma, S. Dodd, J. T. R. Isaac and A. P. Koretsky (2019). "Interhemispheric plasticity is mediated by maximal potentiation of callosal inputs." *Proc Natl Acad Sci U S A* **116**(13): 6391-6396.

Pomarol-Clotet, E., E. J. Canales-Rodriguez, R. Salvador, S. Sarro, J. J. Gomar, F. Vila, J. Ortiz-Gil, Y. Iturria-Medina, A. Capdevila and P. J. McKenna (2010). "Medial prefrontal cortex pathology in schizophrenia as revealed by convergent findings from multimodal imaging." *Mol Psychiatry* **15**(8): 823-830.

Rock, C. and A. J. Apicella (2015). "Callosal projections drive neuronal-specific responses in the mouse auditory cortex." *J Neurosci* **35**(17): 6703-6713.

Ryali, S., Y. Y. Shih, T. Chen, J. Kochalka, D. Albaugh, Z. Fang, K. Supekar, J. H. Lee and V. Menon (2016). "Combining optogenetic stimulation and fMRI to validate a multivariate dynamical systems model for estimating causal brain interactions." *Neuroimage* **132**: 398-405.

Schaefer, G. B. and J. B. Bodensteiner (1999). "Developmental anomalies of the brain in mental retardation." *International Review of Psychiatry* **11**(1): 47-55.

Schmid, F., L. Wachsmuth, M. Schwalm, P. H. Prouvot, E. R. Jubal, C. Fois, G. Pramanik, C. Zimmer, C. Faber and A. Stroh (2016). "Assessing sensory versus optogenetic network activation by combining (o)fMRI with optical Ca<sup>2+</sup> recordings." *J Cereb Blood Flow Metab* **36**(11): 1885-1900.

Schnitzler, A., K. R. Kessler and R. Benecke (1996). "Transcallosally mediated inhibition of interneurons within human primary motor cortex." *Exp Brain Res* **112**(3): 381-391.

Schulte, T., E. M. Muller and E. M. Oehring (2010). "Contribution of callosal connections to the interhemispheric integration of visuomotor and cognitive processes." *Neuropsychol Rev* **20**(2): 174-190.

Schulz, K., E. Sydekum, R. Krueppel, C. J. Engelbrecht, F. Schlegel, A. Schroter, M. Rudin and F. Helmchen (2012). "Simultaneous BOLD fMRI and fiber-optic calcium recording in rat neocortex." *Nat Methods* **9**(6): 597-602.

Schwalm, M., F. Schmid, L. Wachsmuth, H. Backhaus, A. Kronfeld, F. Aedo Jury, P. H. Prouvot, C. Fois, F. Albers, T. van Alst, C. Faber and A. Stroh (2017). "Cortex-wide BOLD fMRI activity reflects locally-recorded slow oscillation-associated calcium waves." *Elife* **6**.

Shuler, M. G., D. J. Krupa and M. A. Nicolelis (2001). "Bilateral integration of whisker information in the primary somatosensory cortex of rats." *J Neurosci* **21**(14): 5251-5261.

Simmons, P. A. and A. L. Pearlman (1983). "Receptive-field properties of transcallosal visual cortical neurons in the normal and reeler mouse." *J Neurophysiol* **50**(4): 838-848.

Spencer, S. S., D. D. Spencer, P. D. Williamson, K. Sass, R. A. Novelly and R. H. Mattson (1988). "Corpus Callosotomy for Epilepsy .1. Seizure Effects." *Neurology* **38**(1): 19-24.

Sperry, R. W. (1961). "Cerebral Organization and Behavior: The split brain behaves in many respects like two separate brains, providing new research possibilities." *Science* **133**(3466): 1749-1757.

Suarez, R., L. R. Fenlon, R. Marek, L. Avitan, P. Sah, G. J. Goodhill and L. J. Richards (2014). "Balanced interhemispheric cortical activity is required for correct targeting of the corpus callosum." *Neuron* **82**(6): 1289-1298.

Sumser, A., R. A. Mease, B. Sakmann and A. Groh (2017). "Organization and somatotopy of corticothalamic projections from L5B in mouse barrel cortex." *Proc Natl Acad Sci U S A* **114**(33): 8853-8858.

Sych, Y., M. Chernysheva, L. T. Sumanovski and F. Helmchen (2019). "High-density multi-fiber photometry for studying large-scale brain circuit dynamics." *Nat Methods* **16**(6): 553-560.

Theyel, B. B., D. A. Llano and S. M. Sherman (2010). "The corticothalamocortical circuit drives higher-order cortex in the mouse." *Nat Neurosci* **13**(1): 84-88.

Tsai, H. C., F. Zhang, A. Adamantidis, G. D. Stuber, A. Bonci, L. de Lecea and K. Deisseroth (2009). "Phasic firing in dopaminergic neurons is sufficient for behavioral conditioning." *Science* **324**(5930): 1080-1084.

Tye, K. M. and K. Deisseroth (2012). "Optogenetic investigation of neural circuits underlying brain disease in animal models." *Nat Rev Neurosci* **13**(4): 251-266.

van Alst, T. M., L. Wachsmuth, M. Datunashvili, F. Albers, N. Just, T. Budde and C. Faber (2019). "Anesthesia differentially modulates neuronal and vascular contributions to the BOLD signal." *Neuroimage* **195**: 89-103.

van Eijsden, P., W. M. Otte, W. S. van der Hel, O. van Nieuwenhuizen, R. M. Dijkhuizen, R. A. de Graaf and K. P. Braun (2011). "In vivo diffusion tensor imaging and ex vivo histologic characterization of white matter pathology in a post-status epilepticus model of temporal lobe epilepsy." *Epilepsia* **52**(4): 841-845.

van Schooneveld, M. M., A. Jennekens-Schinkel, P. C. van Rijen, K. P. Braun and O. van Nieuwenhuizen (2011). "Hemispherectomy: a basis for mental development in children with epilepsy." *Epileptic Disord* **13**(1): 47-55.

Veinante, P. and M. Deschenes (2003). "Single-cell study of motor cortex projections to the barrel field in rats." *Journal of Comparative Neurology* **464**(1): 98-103.

Wang, M., Y. He, T. J. Sejnowski and X. Yu (2018). "Brain-state dependent astrocytic Ca(2+) signals are coupled to both positive and negative BOLD-fMRI signals." *Proc Natl Acad Sci U S A* **115**(7): E1647-E1656.

White, E. L. and D. Czeiger (1991). "Synapses Made by Axons of Callosal Projection Neurons in Mouse Somatosensory Cortex - Emphasis on Intrinsic Connections." *Journal of Comparative Neurology* **303**(2): 233-244.

Wiest, M. C., N. Bentley and M. A. Nicolelis (2005). "Heterogeneous integration of bilateral whisker signals by neurons in primary somatosensory cortex of awake rats." *J Neurophysiol* **93**(5): 2966-2973.

Wilson, C. J. (1987). "Morphology and Synaptic Connections of Crossed Corticostriatal Neurons in the Rat." *Journal of Comparative Neurology* **263**(4): 567-580.

Xin Yu, S. D., and Alan P. Koretsky (2013). "Targeting Projection Fibers for Optogenetics and fMRI." *Proc. Intl. Soc. Mag. Reson. Med.* **21**.

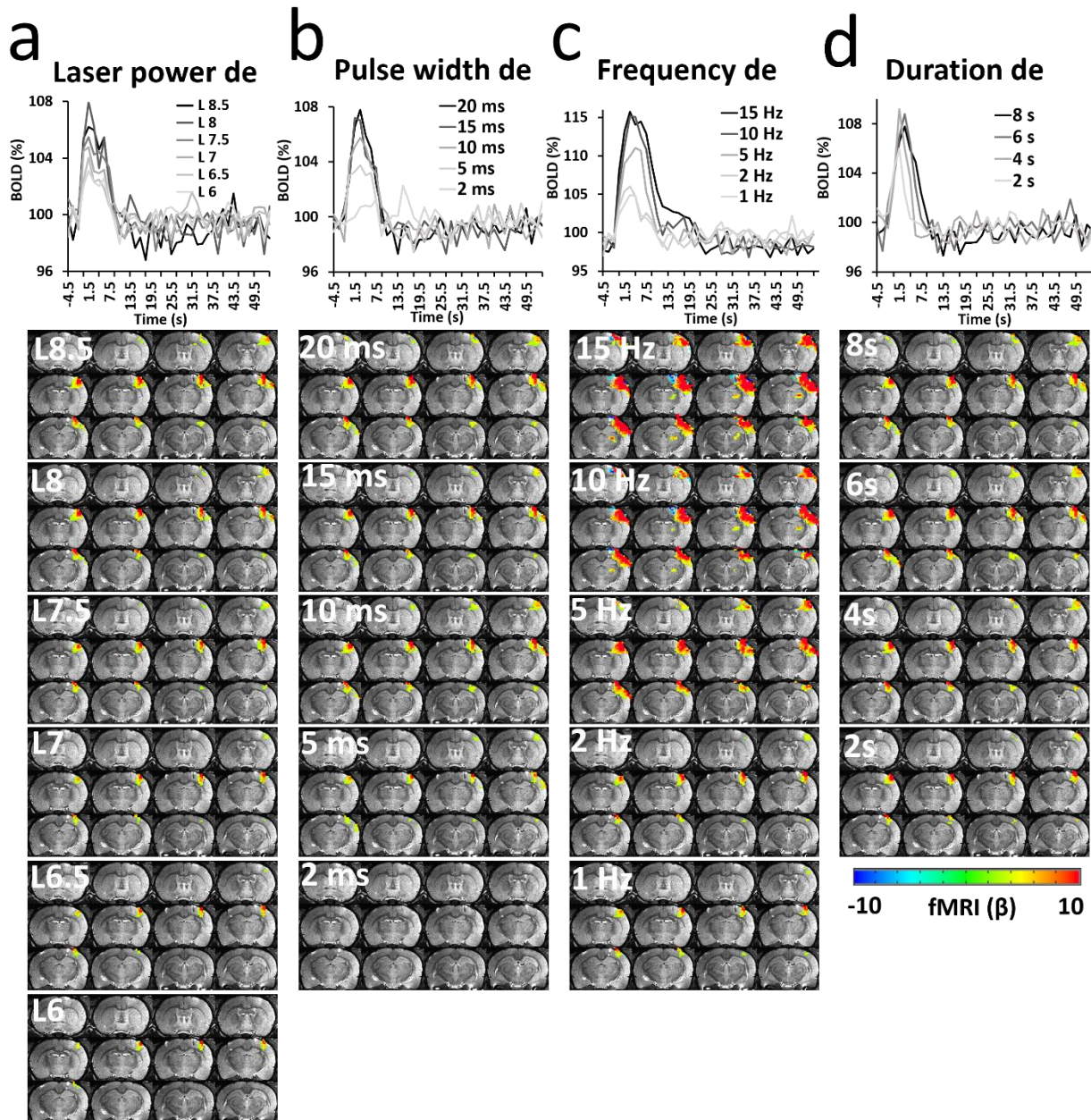
Yu, X., S. Chung, D. Y. Chen, S. Wang, S. J. Dodd, J. R. Walters, J. T. Isaac and A. P. Koretsky (2012). "Thalamocortical inputs show post-critical-period plasticity." *Neuron* **74**(4): 731-742.

Yu, X., Y. He, M. Wang, H. Merkle, S. J. Dodd, A. C. Silva and A. P. Koretsky (2016). "Sensory and optogenetically driven single-vessel fMRI." *Nat Methods* **13**(4): 337-340.

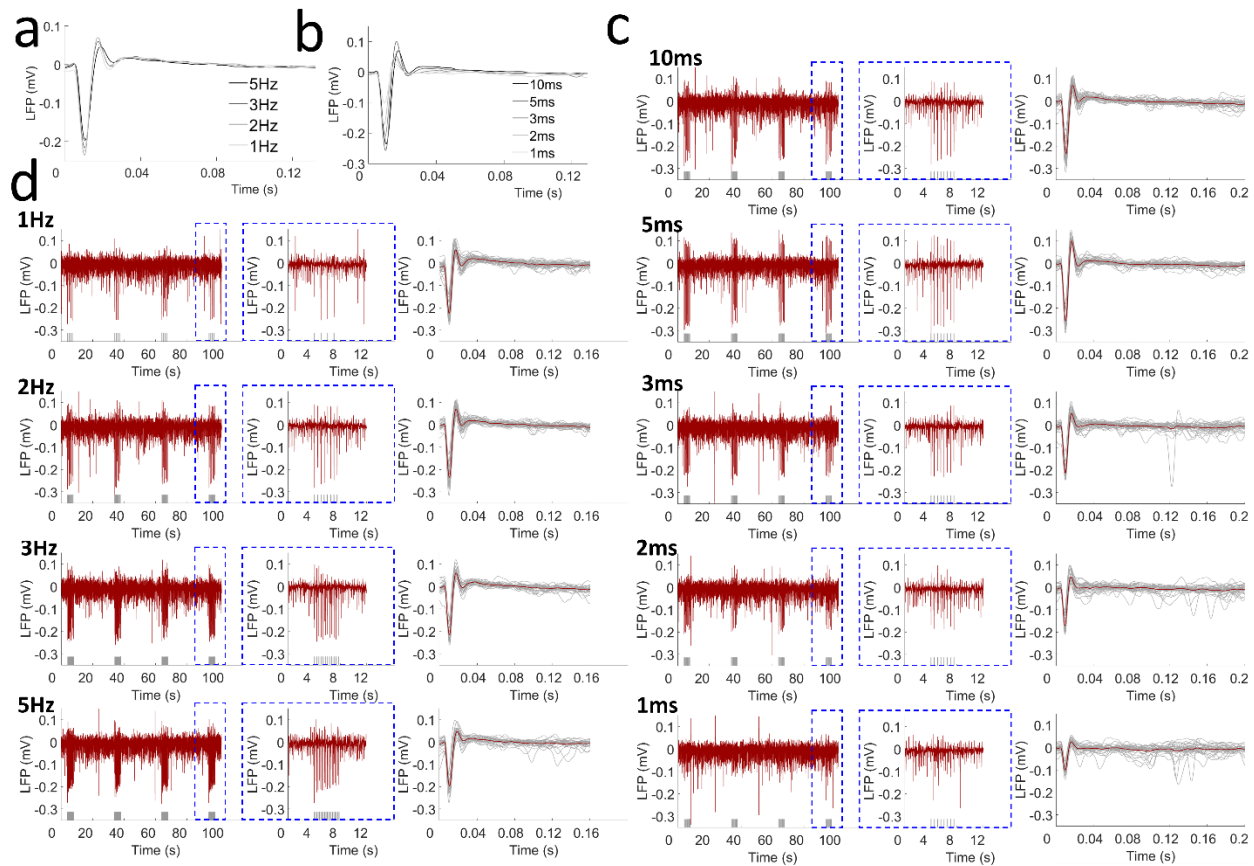
Yu, X., C. Qian, D. Y. Chen, S. J. Dodd and A. P. Koretsky (2014). "Deciphering laminar-specific neural inputs with line-scanning fMRI." *Nat Methods* **11**(1): 55-58.

Zhang, F., L. P. Wang, E. S. Boyden and K. Deisseroth (2006). "Channelrhodopsin-2 and optical control of excitable cells." *Nat Methods* **3**(10): 785-792.

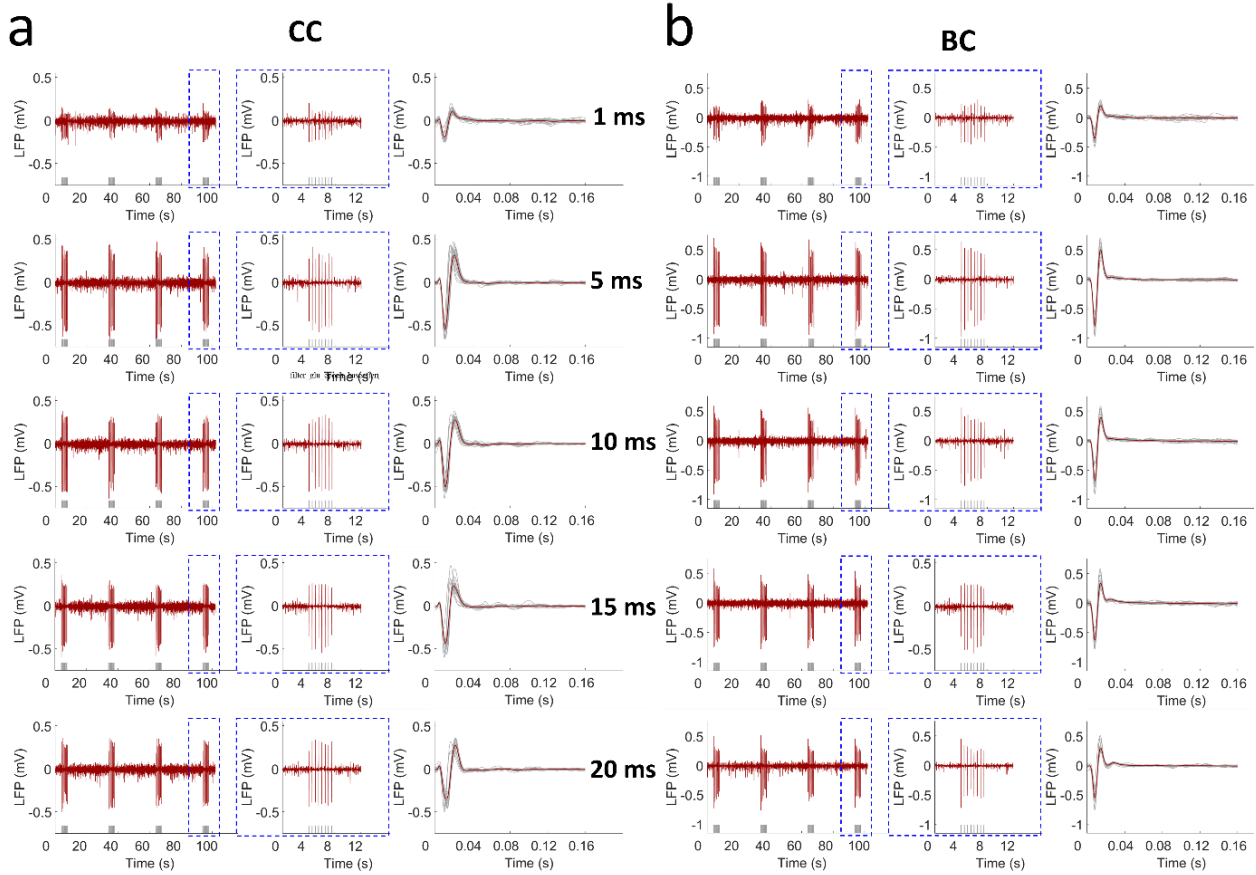
## Supplementary information



**Supplementary Figure 1.** Representative functional maps and time courses of the fMRI signal (average of 13 epochs, 60 s per epoch) upon CC light activation with (a) laser power dependency (2 Hz, 8 s, 20 ms pulse width), (b) pulse width dependency (2, 5, 10, 15 and 20 ms pulse width, 2 Hz, 8 s, L 8), (c) frequency dependency (1, 2, 5, 10 and 15 Hz, 8 s, L 8, 20 ms pulse width) and (d) duration dependency (2, 4, 6 and 8 s, 2 Hz, 20 ms pulse width, L 8). It is noteworthy that exposure to light with high frequency (10 and 15 Hz) at high power (35 mW) led to heating effects, inducing artifacts close to the fiber tip (c), as well as very strong antidromic activity. GLM-based t-statistics in AFNI is used,  $p$  (corrected)  $< 0.005$ .

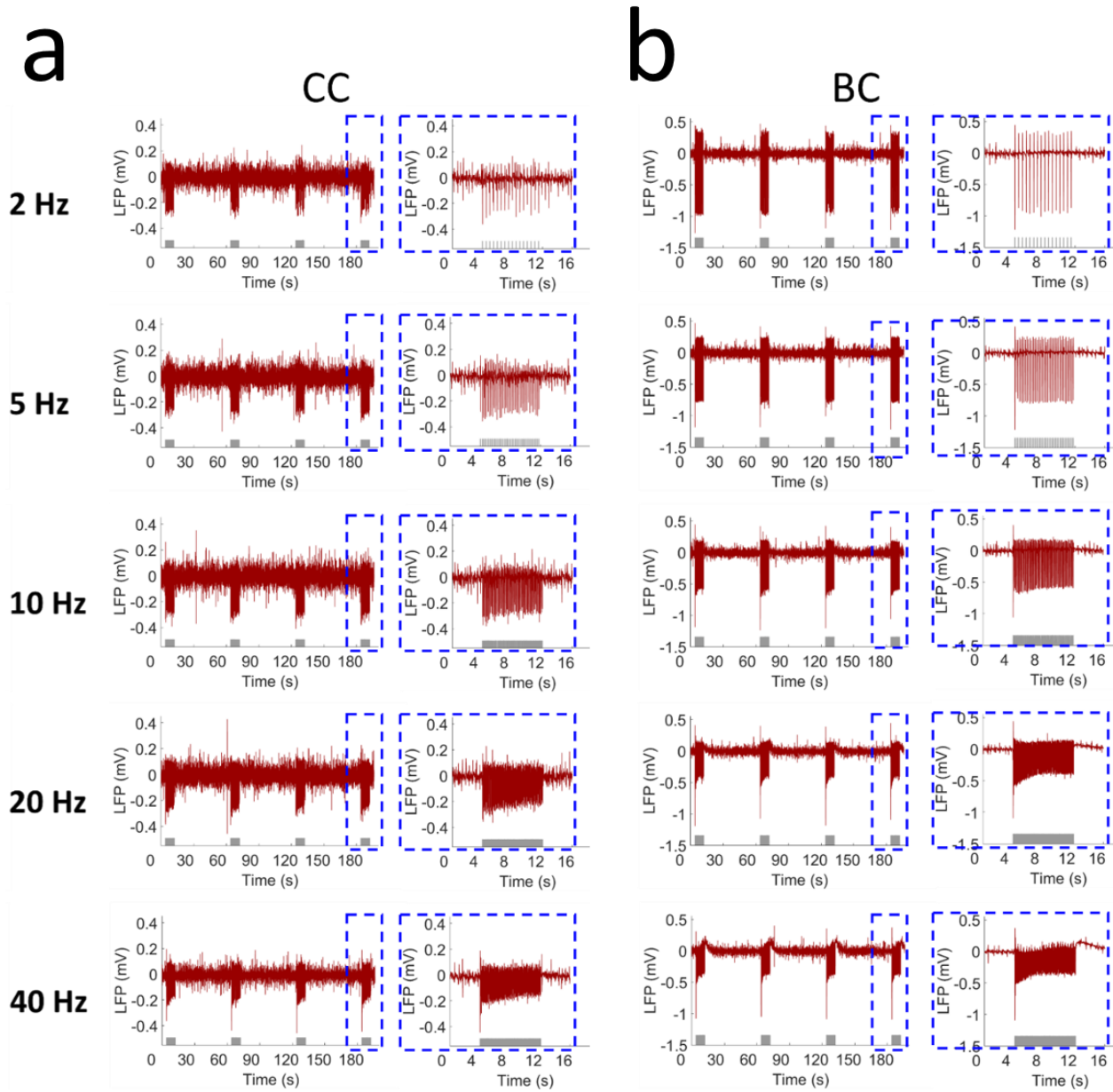


**Supplementary Figure 2.** The light-driven antidromic LFP with frequency and pulse width dependency of a representative rat. **(a)** Averaged LFP driven by light pulses at different frequencies (1, 2, 3 and 5 Hz; 10 ms pulse width, L 7.5, 4 s stimulation 26 s rest, 16 epochs). **(b)** Averaged LFP driven by light pulses at different pulse widths (1, 2, 3, 5 and 10 ms pulse width; 2 Hz, L 7.5, 4 s stimulation 26 s rest, 16 epochs). **(c)** The raw LFP trace by optogenetic stimulation (*left*, 4 epochs), the enlarged representative LFP for one epoch (*middle*) and the averaged LFP from one trial (red line). The grey lines show all the LFP from this trial (*right*) upon different stimulation frequencies. **(d)** The raw LFP trace during optogenetic stimulation (*left*, 4 epochs), the enlarged representative LFP for one epoch (*middle*) and the averaged LFP from one trial (red line). The grey lines show all the LFP from this trial (*right*) upon different stimulation light pulse widths. Grey lines beneath the LFP indicate the stimulation.

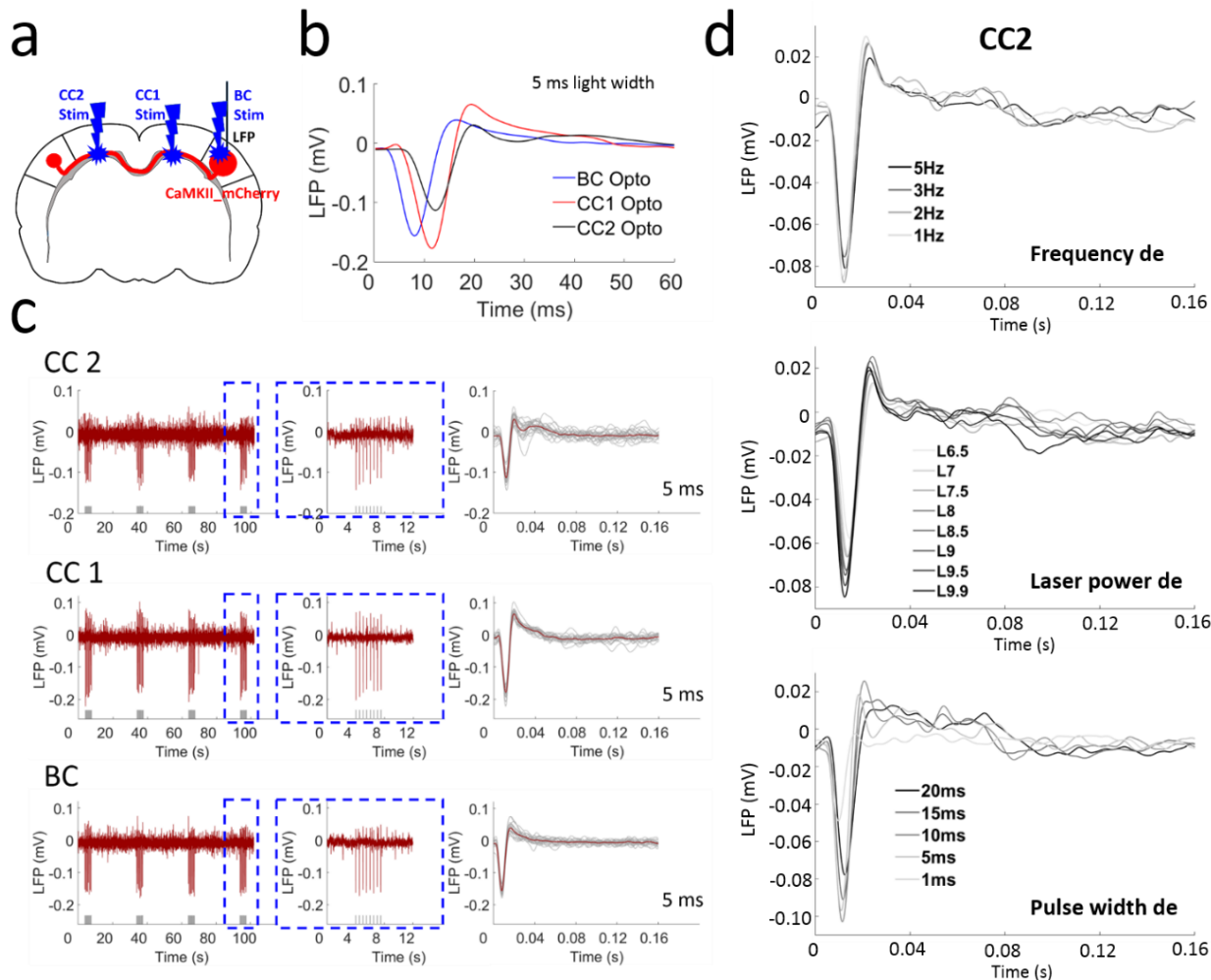


**Supplementary Figure 3.** Light-driven LFP for antidromic activity from CC (**a**) stimulation and BC (**b**) direct stimulation showing similar pattern with pulse width dependency of a representative rat. Every panel in **a** and **b** shows the raw LFP trace observed upon optogenetic stimulation (*left*, 4 epochs), the enlarged representative LFP for one epoch (*middle*) from the dashed blue box and the averaged LFP from one trial (red line). The grey lines show all the LFP from this trial (*right*). Grey lines beneath the LFP indicate the stimulation.

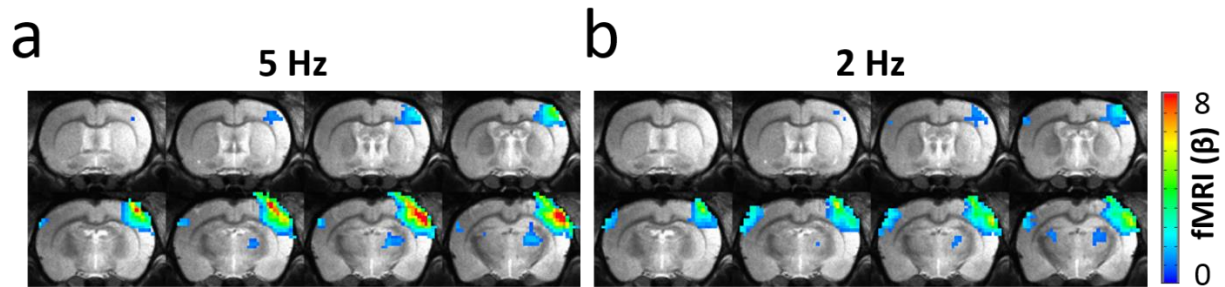




**Supplementary Figure 4.** Light-driven LFP for antidromic activity from CC stimulation (**a**) and BC direct stimulation (**b**) showing similar pattern with frequency dependency of a representative rat. Every panel in **a** and **b** shows the raw LFP trace by optogenetic stimulation (*left*, 4 epochs), the enlarged representative LFP for one epoch (*right*) from the dashed blue box. Grey lines beneath the LFP indicate the stimulation.

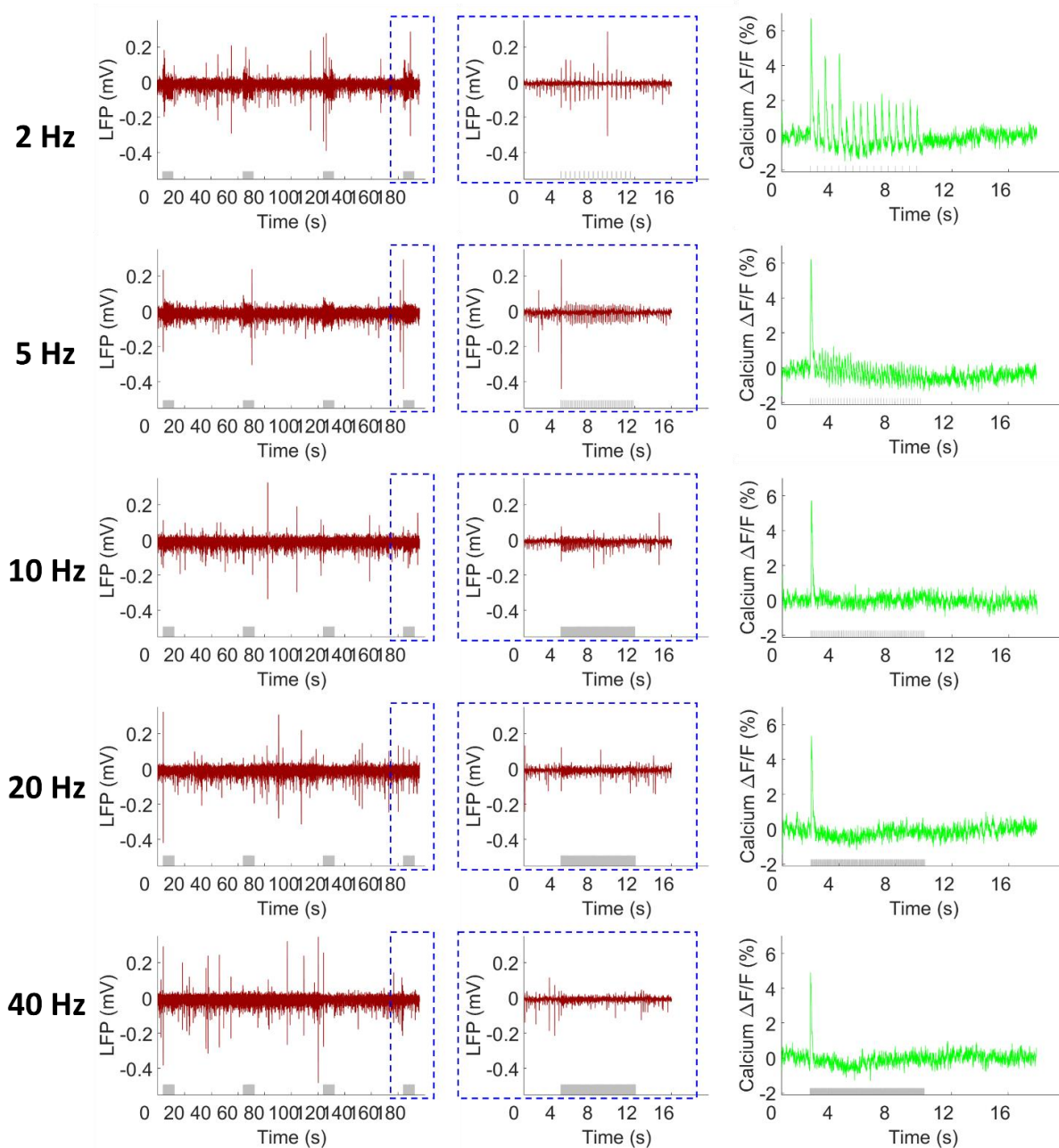


**Supplementary Figure 5.** Light-driven LFP for antidromic activity from CC stimulation in both hemispheres and BC direct stimulation. **(a)** The schematic plan for the experiment design. **(b)** Averaged LFP from the CC2 stimulation in the hemisphere opposite to the virus injection site (blue line), CC1 stimulation in the same hemisphere (red line) and BC direct stimulation (black line) shown different temporal features. **(c)** The raw LFP trace by optogenetic stimulation (*left*, 4 epochs), the enlarged representative LFP for one epoch (*middle*) from the dashed blue box and the averaged LFP from one trial (red line). The grey lines show all the LFP from this trial (*right*). **(d)** Averaged LFP upon optogenetic stimulation of CC2 with frequency (*upper panel*), laser power (*middle panel*) and pulse width (*lower panel*) dependency showing reliably detected antidromic activity.



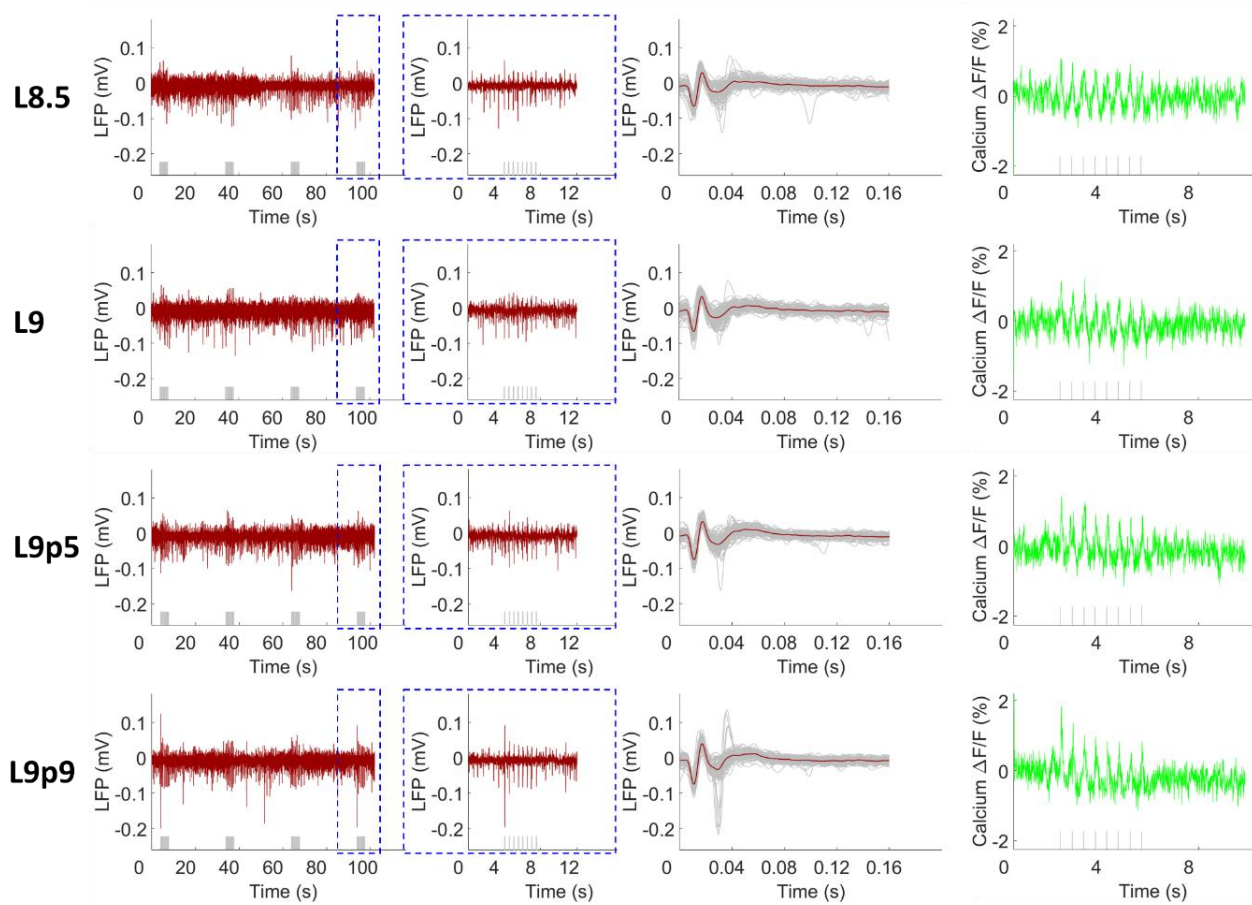
**Supplementary Figure 6.** Light-driven functional maps demonstrating opposite relationships for antidromic and orthodromic activities in the BC to 5 Hz (**a**) and 2 Hz (**b**). The antidromic activity in the right hemisphere and the orthodromic activity in the left hemisphere responses to 5 Hz was stronger and weaker, respectively, compared to 2 Hz. GLM-based t-statistics in AFNI is used.  $p$  (corrected)  $< 0.01$ .

## Frequency dependency



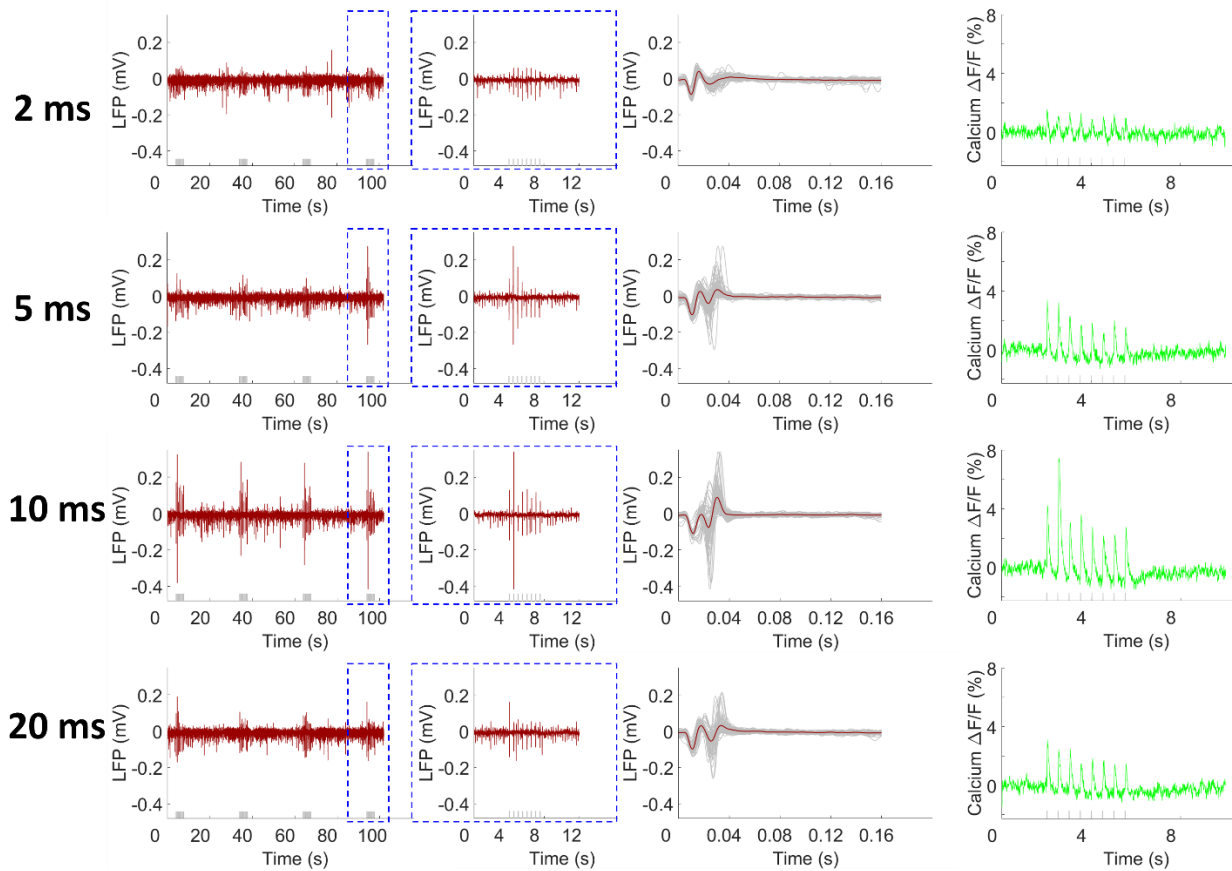
**Supplementary Figure 7.** The frequency dependency of simultaneous LFP (red) and calcium response signals (green). Every panel shows the raw LFP trace elicited by optogenetic stimulation (*left*, 4 epochs), the enlarged representative LFP for one epoch from the dashed blue box (*middle*) and averaged calcium signal (8 s stimulation 52 s rest, 15 epochs, L9, pulse width 10 ms). Grey lines beneath the LFP and calcium signals indicate the stimulation.

## Laser power dependency



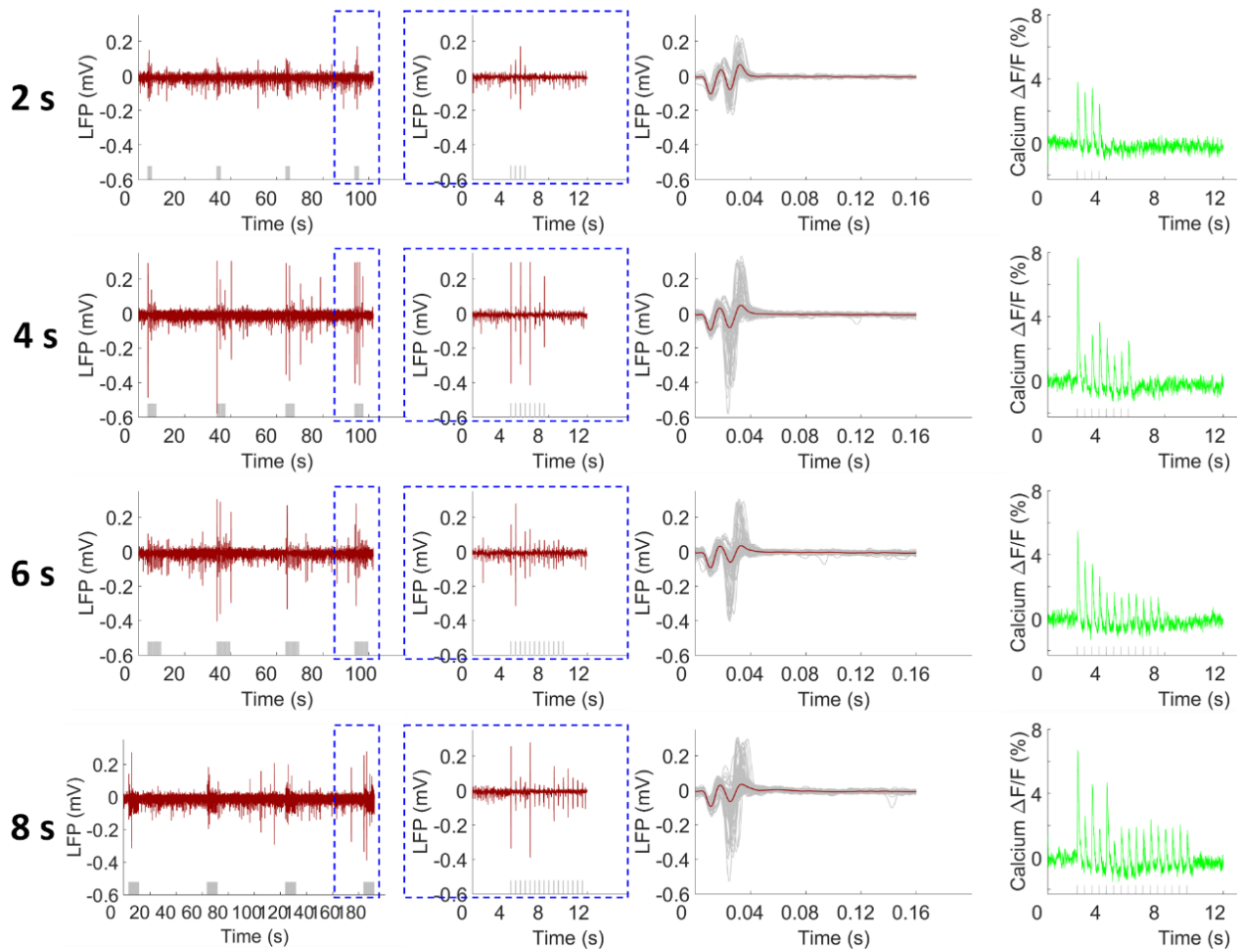
**Supplementary Figure 8.** The laser power dependency of simultaneous LFP (red) and calcium signals (green) showing that both amplitudes increased as a function of the laser power. Every panel shows the raw LFP trace elicited by optogenetic stimulation (*left*, 4 epochs), the enlarged representative LFP for one epoch from the dashed blue box (*middle*), the averaged LFP from one trial (red line). Grey lines showing all the LFP from this trial (*right*) and the averaged calcium signal (4 s stimulation 26 s rest, 11 epochs, L9, pulse width 10 ms). Grey lines beneath the LFP and calcium signals indicate the stimulation.

## Laser pulse width dependency

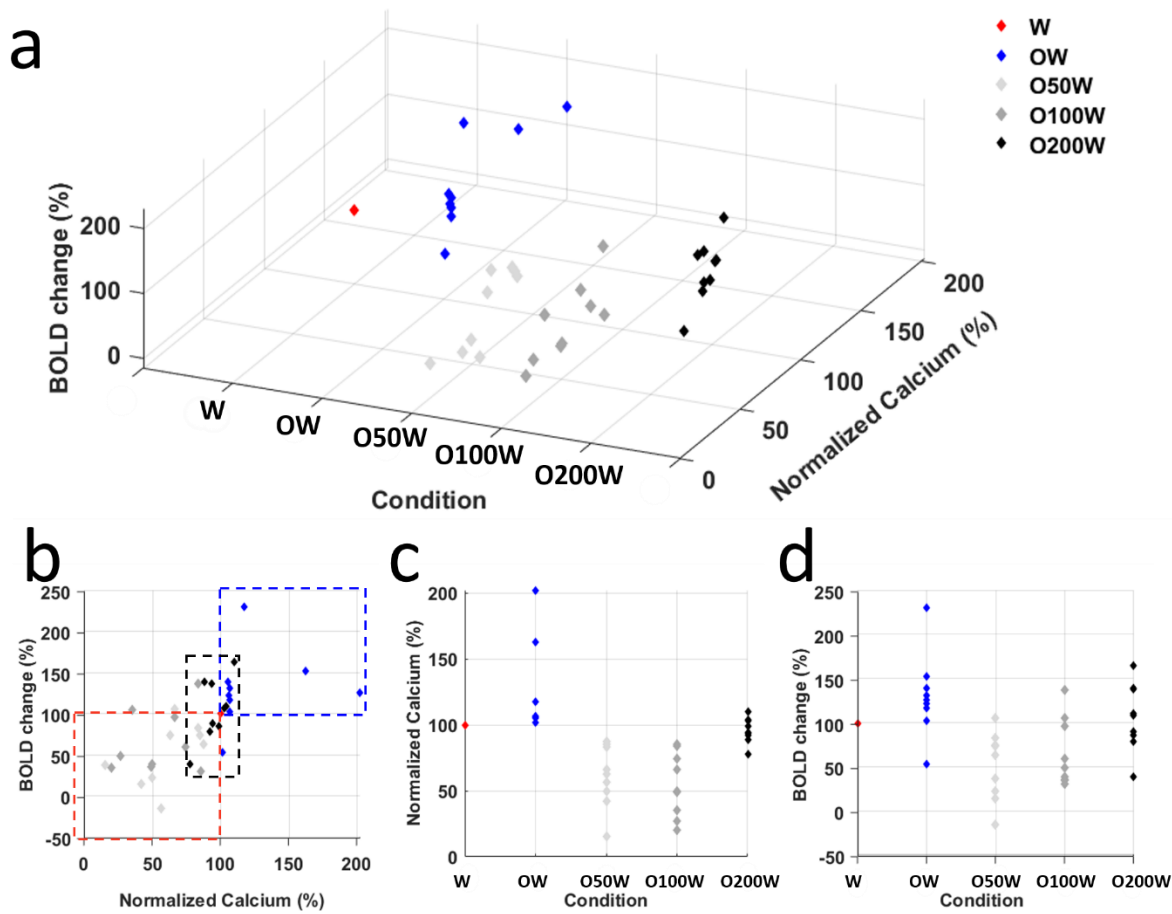


**Supplementary Figure 9.** The laser pulse width dependency of simultaneous LFP (red) and calcium signals (green). Calcium signals increased and the LFP pattern demonstrated stronger depolarization according to the increased pulse width at 2 ms, 5 ms and 10 ms. In contrast, for the 20 ms pulse width stimulation, there was decreased calcium signal and weaker depolarization of LFP. Every panel shows the raw LFP trace elicited by optogenetic stimulation (*left*, 4 epochs), the enlarged representative LFP for one epoch from the dashed blue box (*middle*), the averaged LFP from one trial (red line, with the grey lines showing all the LFP from this trial) (*right*) and the averaged calcium signal (2 Hz, 4 s stimulation 26 s rest, 11 epochs, L9). Grey lines beneath the LFP and calcium signals indicate the stimulation.

## Duration dependency

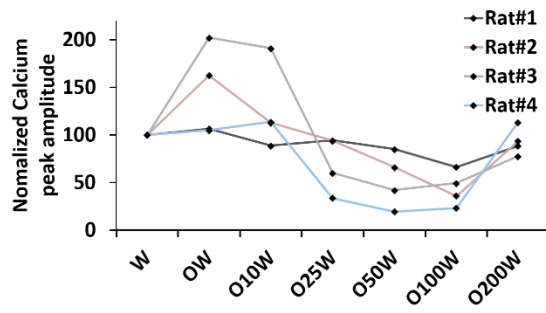
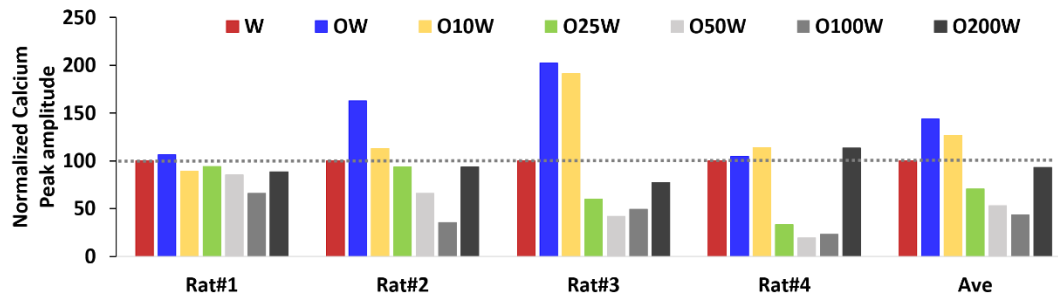


**Supplementary Figure 10.** The duration dependency of simultaneous LFP (red) and calcium signals (green). Every panel shows the raw LFP trace elicited by optogenetic stimulation (*left*, 4 epochs), the enlarged representative LFP for one epoch from the dashed blue box (*middle*), the averaged LFP from one trial (red line, with the grey lines showing all the LFP from this trial) (*right*) and the averaged calcium signal (2 Hz, 11 epochs, L9, pulse width 10 ms). Grey lines beneath the LFP and calcium signals indicate the stimulation.

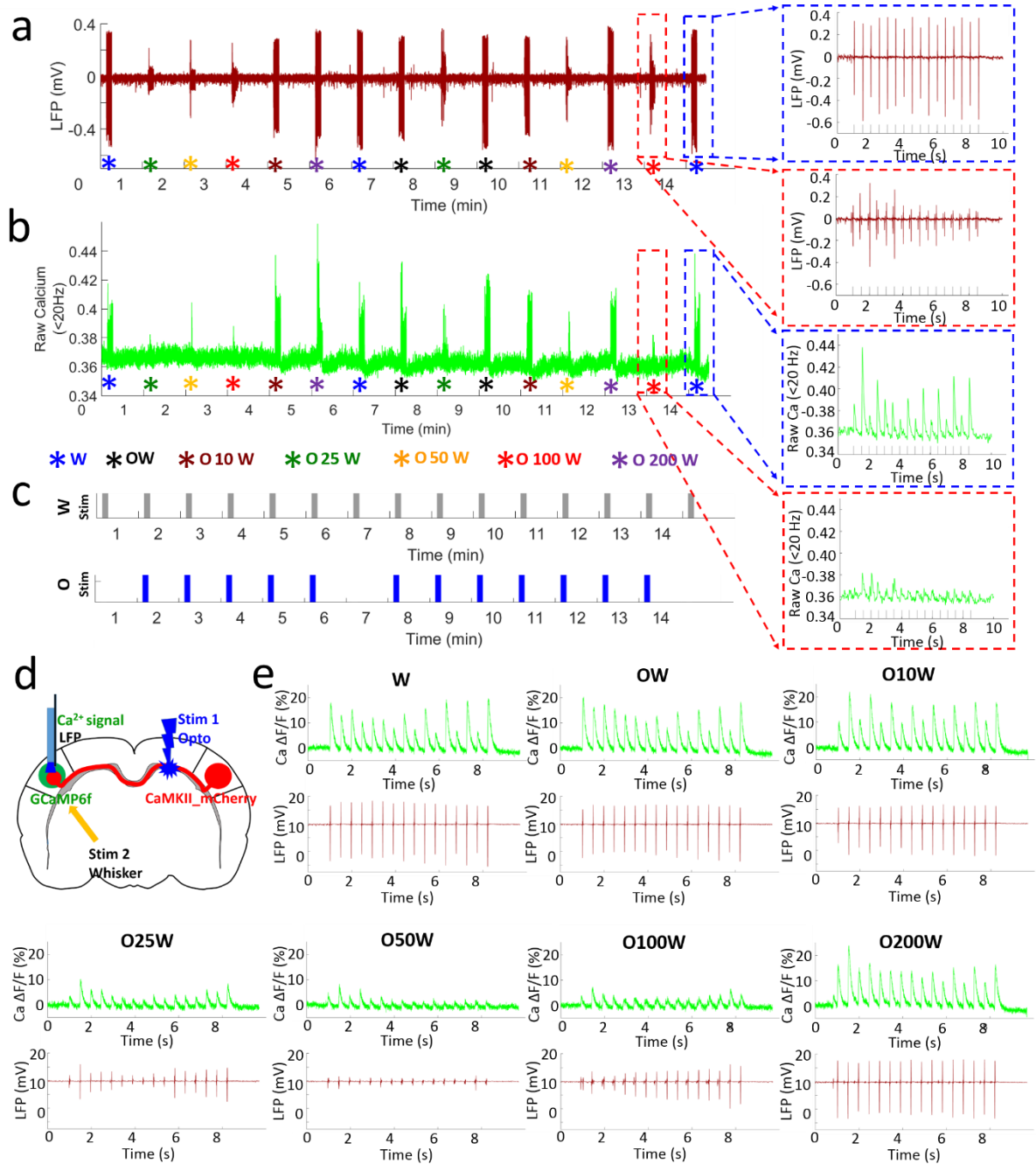


**Supplementary Figure 11.** The scatter plots of the evoked BOLD and calcium signals for 5 stimulation conditions (W, OW, O50W, O100W and O200W) in 9 animals. **(a)** 3D plot of the BOLD changes (Z axis), calcium changes (Y axis) and stimulation conditions (X axis). Both BOLD and calcium signals are normalized to condition W. **(b)** View from the correlation of BOLD changes with calcium signals. The central red diamond is the baseline to which the data were normalized. Blue diamonds represent the condition OW, most of them distributed in the dashed blue box, showing increased neuronal activities. Light grey diamonds and dark grey diamonds represent the condition O50W and O100W, respectively, most of them located in the dashed red box, showing suppressed neuronal activities. **(c)** Normalized calcium signals as a function of condition. **(d)** Normalized BOLD changes as a function of condition. W: whisker stimulation only, OW: simultaneous optical and whisker stimulation, O[x]W optical stimulation followed by [x] ms-delayed whisker stimulation.



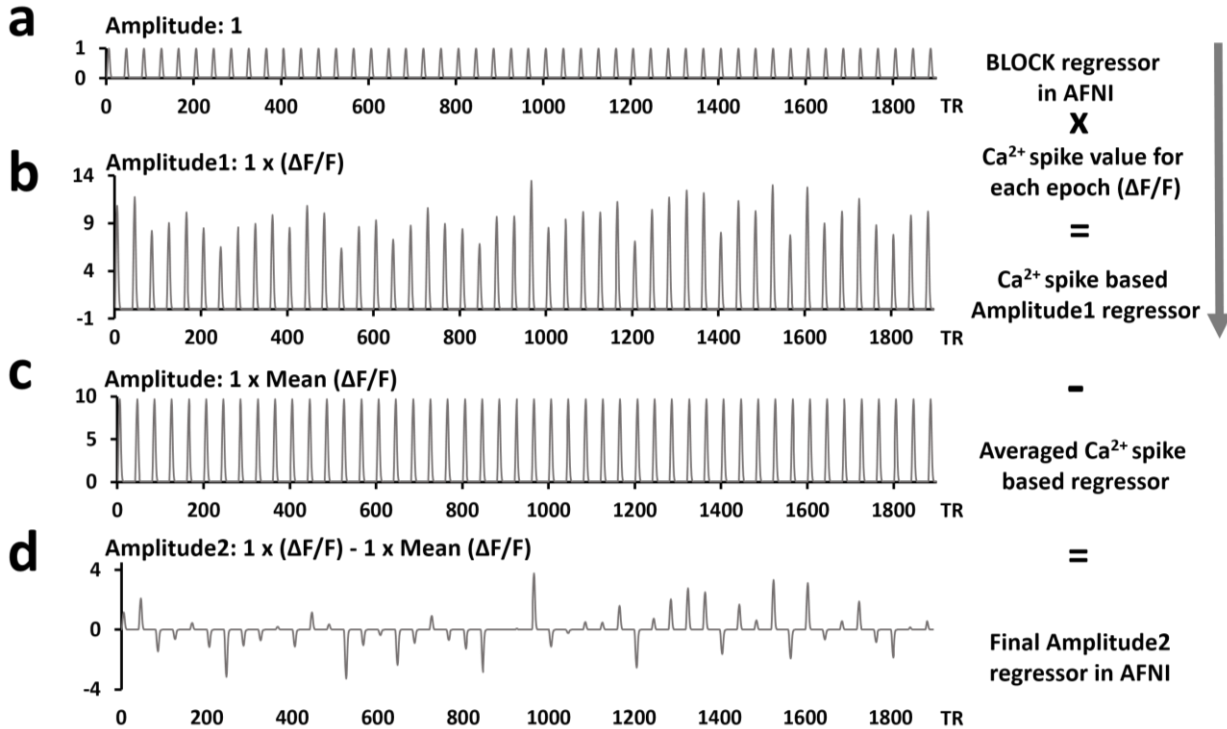
**a****b**

**Supplementary Figure 12.** The effect of conditioning stimuli in the sensory evoked calcium signals in the left hemisphere for 7 refined conditions (W, OW, O10W, O25W, O50W, O100W and O200W). **(a)** The scatter plot of the calcium signals normalized to condition W from 4 rats. **(b)** The individual pattern changes of calcium signals from 4 animals, as well as the averaged calcium signal change pattern for all the 7 conditions.



**Supplementary Figure 13.** Typical LFP (red) and calcium signals (green) of one trial from a representative rat. **(a)** Different amplitudes of LFP and **(b)** calcium signal changes showing the different neuronal activity upon seven randomized stimulation conditions. **(c)**. Simplified diagram representing the typical calcium signals and LFP for condition W (blue dash boxes in **a** and **b**, upper graph in **c**) and O100W (red dash boxes in **a** and **b**, lower graph in **c**) in one epoch. **(d)** Schematic of the experimental design. **(e)** Averaged calcium signals and LFP in left barrel cortex, further confirming the spatial and temporal features of sensory-evoked cortical activity pattern shaped by callosal inputs. W: whisker stimulation only, OW: simultaneous optical and whisker stimulation, O[x]W optical stimulation followed by [x] ms-delayed whisker stimulation.

Data analyzing flow diagram for a representative rat:  
 48 epochs (12 epoch each trail x 4 trials)  
 1920 TR (40 TR each epoch x 48 epochs).



**Supplementary Figure 14.** The flow diagram to generate the calcium signal-based regressor for the fMRI correlation map. (a) version 1 of the regressor, generated with the parameter BLOCK (L, 1), which generates a convolution of a square wave of duration L with the stimulation train and makes a peak amplitude of block response = 1. (b) the variable calcium amplitude of each epoch from a representative rat is used to generate the AM1 (amplitude modulated 1) regressor in 3dDeconvolve command in AFNI. (c) the averaged calcium amplitude of all the epochs is used to generate the regressor of no interest. (d) by computing 'b - c', the differences from the mean calcium amplitude can be detected. This new vector constitutes the final regressor AM2. 'AM2' allows to detect voxels that activate but do not change proportionally to the amplitude factor, as well as provides a direct measure of the proportionality of the activation in response to changes in the input amplitude factors (from the description of 3dDeconvolve program in AFNI).

ARTICLE

<https://doi.org/10.1038/s41467-019-12850-x>

OPEN

# Mapping optogenetically-driven single-vessel fMRI with concurrent neuronal calcium recordings in the rat hippocampus

Xuming **Chen**<sup>1,2,3</sup>, Filip **Sobczak**<sup>1,4</sup>, Yi **Chen**<sup>1,4</sup>, Chunqi **Qian**<sup>5,6</sup>, Zuneng **Lu**<sup>3</sup>, Cenk **Ayata**<sup>7,8</sup>, Nikos **Logothetis**<sup>1,9</sup> & Xin **Yu**<sup>1,10\*</sup>

Extensive in vivo imaging studies investigate the hippocampal neural network function, mainly focusing on the dorsal CA1 region given its optical accessibility. Multi-modality fMRI with simultaneous hippocampal electrophysiological recording reveal broad cortical correlation patterns, but the detailed spatial hippocampal functional map remains lacking given the limited fMRI resolution. In particular, hemodynamic responses linked to specific neural activity are unclear at the single-vessel level across hippocampal vasculature, which hinders the deciphering of the hippocampal malfunction in animal models and the translation to critical neurovascular coupling(NVC) patterns for human fMRI. We simultaneously acquired optogenetically-driven neuronal Ca<sup>2+</sup> signals with single-vessel blood-oxygen-level-dependent(BOLD) and cerebral-blood-volume(CBV)-fMRI from individual venules and arterioles. Distinct spatiotemporal patterns of hippocampal hemodynamic responses were correlated to optogenetically evoked and spreading depression-like calcium events. The calcium event-related single-vessel hemodynamic modeling revealed significantly reduced NVC efficiency upon spreading depression-like(SDL) events, providing a direct measure of the NVC function at various hippocampal states.

<sup>1</sup>Max Planck Institute for Biological Cybernetics, 72076 Tuebingen, Germany. <sup>2</sup>University of Tubingen, 72076 Tubingen, Germany. <sup>3</sup>Department of Neurology, Institution of Neuropsychiatry Research, Renmin Hospital of Wuhan University, Wuhan, China. <sup>4</sup>Graduate Training Centre of Neuroscience, International Max Planck Research School, University of Tuebingen, 72074 Tuebingen, Germany. <sup>5</sup>Laboratory of Functional and Molecular Imaging, NINDS, NIH, Bethesda, MD, USA. <sup>6</sup>Department of Radiology, Michigan State University, East Lansing, MI, USA. <sup>7</sup>Department of Radiology, Massachusetts General Hospital, Charlestown, MA, USA. <sup>8</sup>Department of Neurology, Massachusetts General Hospital, Boston, MA, USA. <sup>9</sup>Imaging Science and Biomedical Engineering, University of Manchester, Manchester M13 9PT, UK. <sup>10</sup>Athinoula A. Martinos Center for Biomedical Imaging, Charlestown, MA, USA.  
\*email: [xin.yu@tuebingen.mpg.de](mailto:xin.yu@tuebingen.mpg.de); [xyu9@mg.harvard.edu](mailto:xyu9@mg.harvard.edu)

Over the past few decades the combination of behavioral and psychophysical studies with anatomical, pharmacological, and functional magnetic resonance imaging (fMRI), permitting whole-brain mapping of brain networks, has expanded our understanding of brain function and occasionally dysfunction. The blood oxygen level-dependent (BOLD) fMRI<sup>1–4</sup>, in particular, is now used as a standard tool for demarcating brain states, and potentially, dynamic transitions from one state to another<sup>5–9</sup>. Nonetheless, fathoming into the true and eventually detailed neural mechanisms underlying the BOLD positive and negative responses, more so at the level of cortical microcircuits and deep brain nuclei, is currently still extremely difficult if not impossible. Conventional fMRI yields surrogate signals such as continuous blood flow, volume, and oxygenation changes<sup>1–4,10,11</sup>. These indirect functional mapping schemes cannot differentiate between function-specific processing and neuromodulation, between bottom-up and top-down signals, occasionally confusing even excitation and inhibition, depending on the circuit-dependent direct or indirect nature of local neural activity<sup>5,12–15</sup>. The origin of such problems is not only due to the weak spatial specificity of the fMRI signal to its neural source but also to the very fact that the exact relationship between the metabolic/hemodynamic responses and the underlying neural activity patterns remains mostly elusive. Using high-resolution fMRI methods to map the animal brain, BOLD and cerebral blood volume (CBV) fMRI signals can be detected from individual arteriole and venule voxels from deep cortical layers<sup>16–18</sup>. Beyond the *in vivo* penetrating depth of conventional optical imaging, single-vessel fMRI methods have enabled direct measurement of vessel-specific hemodynamic responses with fMRI in a large spatial scale to interpret better the neurovascular coupling (NVC) contribution to the fMRI signal acquired in deep brain regions.

Simultaneous fMRI and electrophysiological recordings offered the first insights into the NVC underlying the cortical fMRI signal in both task-related and resting-state conditions<sup>19,20</sup>. Lately, genetically encoded Ca<sup>2+</sup> indicators, for example, GCaMP, mediating Ca<sup>2+</sup> imaging from neurons or astrocytes have also been combined with optical hemodynamic imaging or fMRI, demonstrating various NVC patterns across multiple scales at different cortical states<sup>21–28</sup>. Besides the multi-modal correlation analysis of cortical dynamic signals, the highly varied global correlation of the fMRI signal to the concurrent hippocampal ripple activity has also demonstrated region-specific cortical NVC patterns<sup>29</sup>. In contrast to extensive cortical NVC studies to interpret the fMRI signal acquired in the cortex, the linkage between subcortical NVC events to the fMRI signal, for example, in the hippocampus, has not been well elucidated. Not only has the 3D location of the hippocampus in the brain restricted its accessibility to conventional optical imaging methods but also the mesoscale hippocampal vasculature has been seldom specified for hemodynamic mapping with fMRI. Previous *in vivo* hippocampal functional imaging studies applied micro-lens/micro-prism through the cortical tissue or removed the cortex above the hippocampus<sup>30–33</sup>. The optical fiber has been used to target the hippocampus for the measurement of Ca<sup>2+</sup> from individual cell types or for fast dynamic recordings<sup>34–38</sup>. Using long-wavelength light pulses for deeper tissue penetration, three-photon microscopy has further expanded the optical penetration depth for NVC imaging of dorsal hippocampal CA1 regions in mice with a much less invasive surgical procedure in the mouse brain<sup>39–41</sup>. Nevertheless, it remains challenging to detect subcortical NVC events in animals with larger brains, such as rats and non-human primates, using multi-photon microscopic imaging methods. Although rodent hippocampal vasculature has been well described in histological studies by Coyle<sup>42,43</sup> in the mid 1970s, no

multi-modality neuroimaging studies have been performed to decipher the detailed vessel-specific hemodynamic responses throughout the hippocampal vasculature with fMRI and concurrent neuronal activity measurement in the hippocampus.

Here, we developed a multi-modal fMRI platform, aiming to specify the properties of NVC across the rat hippocampus. The experiments were performed in a high magnetic field scanner (14.1 T), with customized radiofrequency (RF) coils, and the balanced steady-state free precession (bSSFP) method that permits the acquisition of the fMRI signal from individual cortical penetrating arterioles and venules<sup>22</sup>, thereby expanding the line-scanning-based method for real-time single-vessel fMRI mapping<sup>18,44,45</sup>. This high spatial resolution vessel-specific fMRI mapping method allowed to directly measure mesoscale hemodynamic responses of the hippocampal vasculature. In particular, we applied the single-vessel fMRI to map the BOLD and CBV-weighted fMRI signal from interleaved arterioles and venules in the rat hippocampus, of which detailed vascular hemodynamic responses were imaged with a high spatiotemporal resolution. This has not been accomplished by other existing non-invasive global functional neuroimaging methods. This work provides direct evidence to show the deep brain large-scale hemodynamic vascular mapping with single-vessel fMRI beyond the penetration depth of conventional optical imaging methods. Using implanted optical fibers, optogenetically evoked neuronal Ca<sup>2+</sup> and the spreading depression-like Ca<sup>2+</sup> (SDL-Ca<sup>2+</sup>) events were detected with simultaneous single-vessel BOLD fMRI, demonstrating distinct spatiotemporal features of vascular hemodynamic responses. The varying NVC efficiency (NVCe) can be estimated by directly modeling single-vessel fMRI responses to concurrent Ca<sup>2+</sup> events across the hippocampal vasculature. The simultaneous single-vessel hippocampal fMRI and Ca<sup>2+</sup> recording not only provides a multi-modal platform for specifying the multi-scale NVC in the hippocampus but also sheds light on future pathological hippocampal NVC studies in disease animal models with stroke, epilepsy, and Alzheimer's disease.

## Results

### Multi-modal hippocampal fMRI and local field potential.

To study the hippocampal NVC with the multi-modal fMRI platform (Fig. 1a), we co-expressed channelrhodopsin-2 (ChR2) and the genetically encoded Ca<sup>2+</sup> sensor, GCaMP6f, in the rat hippocampus using adeno-associated viral (AAV) vectors (AAV5.Syn.GCaMP6f.WPRE.SV40; AAV5.CAG.hChR2-mCherry.WPRE.SV40). Figure 1b shows neurons labeled with either ChR2-mcherry or GCaMP6f in both barrel cortex (BC) and hippocampus for optogenetic fMRI with concurrent Ca<sup>2+</sup> signal recording. First, optogenetically evoked local field potential (LFP) and GCaMP-mediated Ca<sup>2+</sup> signals were simultaneously detected in the hippocampus of rats at varied light pulse widths, power levels, and frequencies (Fig. 1c, d, Supplementary Fig. 1). It is noteworthy that the optical light pulse introduced large artifacts for the GCaMP-mediated Ca<sup>2+</sup> fluorescent signal detection. Given the specific temporal feature of optogenetically evoked Ca<sup>2+</sup> transients, artifacts detected by the fast-sampling silicon photomultiplier (SiPM) can be distinguished easily from Ca<sup>2+</sup> transients given its short light pulse duration. Figure 1d, e shows the peak fluorescent Ca<sup>2+</sup> signal at ~50–60 ms after the onset of the optogenetic light pulses with various widths from 1 to 20 ms, which is consistent with previous observations in the cortex<sup>21</sup>. This result demonstrates the feasibility of hippocampal optical fiber Ca<sup>2+</sup> recordings with optogenetic stimulation.

Next, we aimed to verify the multi-modal fMRI platform in combination with both optogenetic stimulation and simultaneous Ca<sup>2+</sup> recordings. Figure 1f demonstrates the optogenetically activated BOLD fMRI signals at the BC and the hippocampus

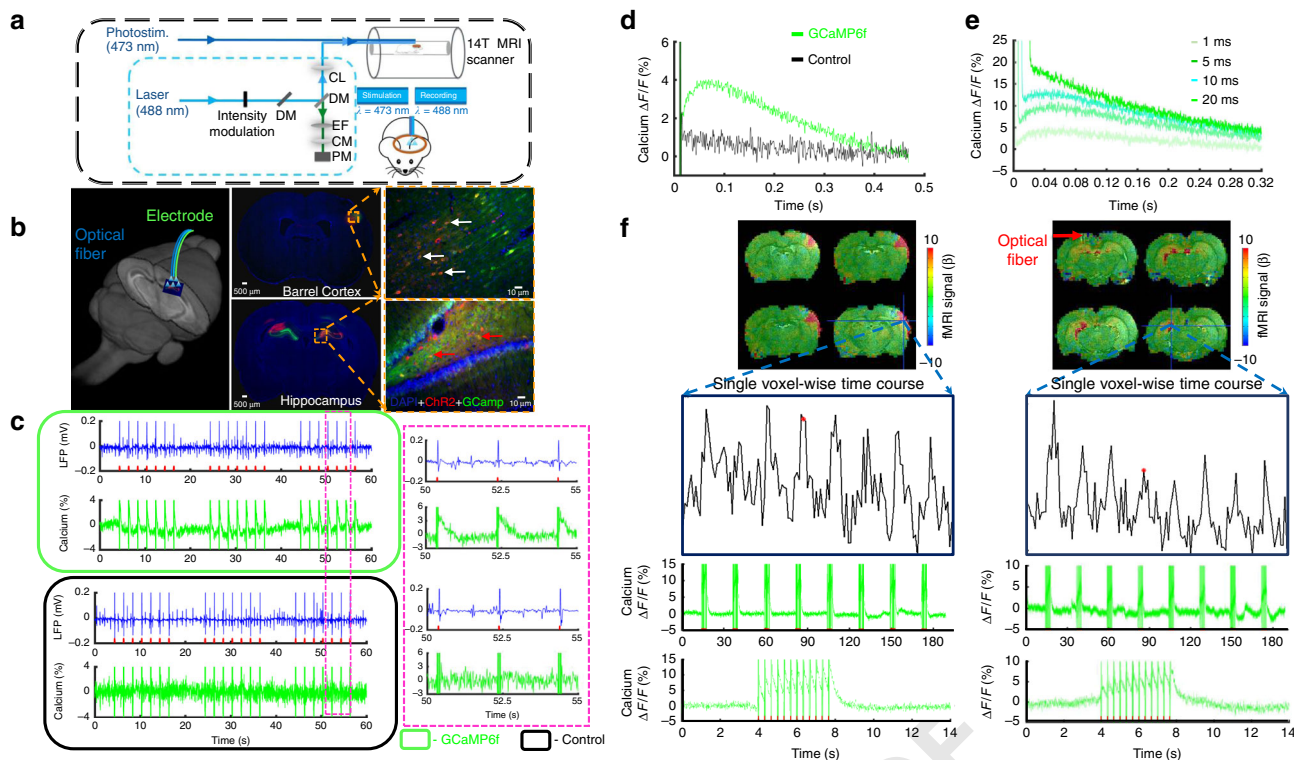


**Fig. 1** Optogenetically evoked  $\text{Ca}^{2+}$  recording with LFP or fMRI. **a** Schematic drawing for the light path of optogenetic activation and calcium recordings in the multi-modal fMRI platform (PM, photomultiplier; EF, emission filter; DM, dichroic mirror; CL, coupling lens). **b** Schematic drawing of optical fibers implantation to target the rat hippocampus in a 3D view (left). Channelrhodopsin (ChR2, red) and GcaMP6f (green) were co-expressed in the barrel cortex (BC, upper, white arrows) and hippocampus (lower, red arrows) with enlarged images (dashed box, right). **c** Simultaneous LFP (blue) and neuronal  $\text{Ca}^{2+}$  (green) traces in the hippocampus following optical stimulation (10 ms light pulse, 1 Hz, 7 s, 4 mW; upper: GCaMP6f expression; lower: control, right panel, enlarged view). **d** Averaged traces of optogenetically evoked  $\text{Ca}^{2+}$  spikes in the hippocampus (green: GCaMP6f expression; black: control). **e** Averaged traces of optogenetically evoked  $\text{Ca}^{2+}$  spikes with different widths of the light pulse (1, 5, 10, and 20 ms). **f** A representative color-coded BOLD fMRI map from the BC (left) and hippocampus (optical fiber insertion trace: red arrow), together with associated fMRI time courses (lower, top) and concurrent neuronal  $\text{Ca}^{2+}$  signals (lower, middle) in the block-design paradigm (illumination: 10 ms light pulse, 3 Hz, 4 s, 5 mW, zoomed views are averaged evoked  $\text{Ca}^{2+}$  signals from one epoch)

with the 3D echo planar imaging fMRI (EPI-fMRI) method<sup>46,47</sup>. Both evoked BOLD fMRI signals from activated brain voxels and concurrent  $\text{Ca}^{2+}$  transients from nearby neurons can be detected using the block-design optogenetic stimulation paradigm. These multi-modal NVC events were acquired across spatial scales from the sub-millimeter scale neuronal ensembles surrounding the fiber tip to the macroscopic vascular hemodynamic response detected by fMRI. It is important to note that direct light pulse exposure on the naive rat hippocampus did not cause detectable positive BOLD fMRI signal through hippocampal vasculature due to the local blood flow regulation, that is, cerebral blood flow changes, as previously reported by ultrasound Doppler signal measurement<sup>48</sup>. The high power light pulse (>25 mW from 200  $\mu\text{m}$  fiber tip) caused the focal negative fMRI signal near the fiber tip due to heating-induced susceptibility changes (frequency offset) (Supplementary Fig. 2)<sup>49</sup>. In contrast, the optogenetic stimulation of rats with Chr2 expression in the hippocampus evoked the strongest signals at the choroid plexus located at the dorsal wall of the lateral ventricle across multiple slices, containing draining veins from the hippocampus in a sub-centimeter scale away from the optical fiber tip (Fig. 1f). Although these results indicate that the direct effect of light exposure on the flow regulation contributes less to the measurable BOLD signal, the widely spread hemodynamic responses in hippocampal vasculature upon optogenetic stimulation remain poorly characterized with EPI-fMRI given the limited spatial resolution. These results also led to implementing the high-resolution single-

vessel fMRI method into the multi-modal fMRI platform for hippocampal NVC mapping.

**Optogenetic hippocampal fMRI with Chr2 variant (C1V1).** It should be noted that in order to reduce the spectral wavelength overlap of GCaMP-based fluorescent signal excitation and optogenetic light pulse stimulation at 473 nm, we additionally applied the Chr2 variant (C1V1) to switch the optogenetic light pulse to 590 nm. Supplementary Figure 3 demonstrates similar dynamic patterns of the concurrent LFP or fMRI signal and fiber optic  $\text{Ca}^{2+}$  signal upon C1V1-mediated optogenetic activation in the rat hippocampus. These results further verify the feasibility of detecting optogenetically driven BOLD and intracellular neuronal  $\text{Ca}^{2+}$  signals in the hippocampus with the multi-modal fMRI platform.

**Optogenetic single-vessel hippocampal BOLD and CBV fMRI.** As shown with the magnetic resonance angiography (MRA) imaging in Fig. 2a, the hippocampal vasculature is aligned in parallel branches supplying blood to the saddle-shaped structure of the hippocampus<sup>50</sup> (Fig. 2a, Supplementary Movie 1). To visualize individual vessels, we applied a 2D multiple gradient echo (MGE) slice transecting the parallel hippocampal vascular branches with 40° angle to the midline (Fig. 2a). Similar to previous single-vessel MRI studies in the cortex<sup>18,22</sup>, the 2D MGE images were acquired at different time of echo (TE) to distinguish

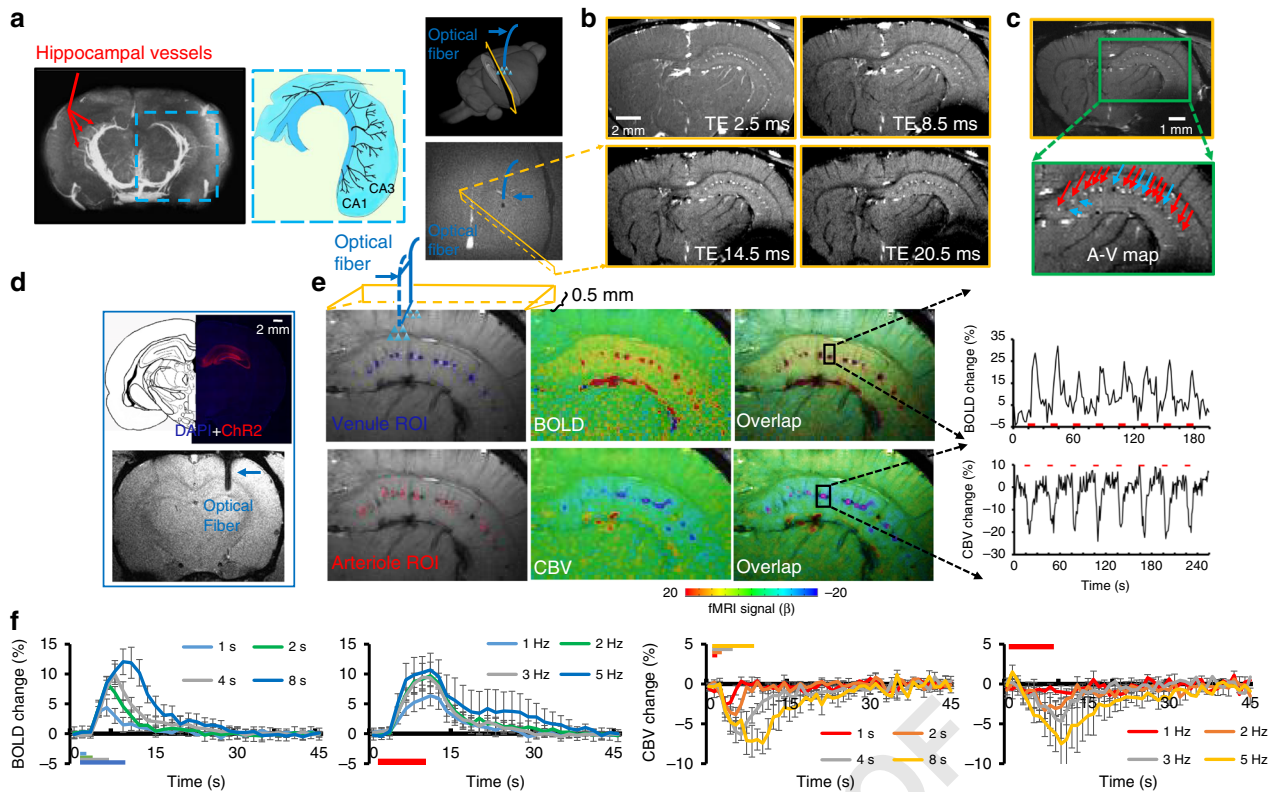


**Fig. 2** Single-vessel hippocampal BOLD and CBV-w fMRI. **a** The magnetic resonance angiography (MRA) image shows major vascular branches penetrating the rat hippocampus (middle image is the schematic drawing of the hippocampal transverse plane of vessels aligned in parallel [modified from Peter Coyle (1976)]). The 3D view of the 2D slice alignment to cover the transverse hippocampal structure (lower image is the horizontal view to show the 2D slice with 40° to the midline to cross the penetrating vessels, dark hole: the fiber optic tip). **b** Representative images of 2D MGE slices from the hippocampus at different TEs. **c** A-V map derived from images in **b**. Arterioles and venules appear as bright and dark dots, respectively (zoomed view of hippocampal arterioles (bright dots, red arrows) and venules (dark dots, blue arrows)). **d** A histological section shows Chr2 expressed in the hippocampus (upper). The T2\*-weighted (T2\*-W) image shows the optical fiber inserted into the hippocampus (lower, blue arrow). **e** Venule (blue)/arteriole (red) ROIs on A-V maps (left). Evoked BOLD (upper) and CBV-weighted (lower) fMRI maps on the same 2D slice (center) and overlap (active voxels are in purple in overlap images). Time courses of the evoked BOLD and CBV-weighted fMRI with the block-design paradigm from a representative venule (upper) and arteriole (lower) ROI (illumination: 10 ms light pulse, 3 Hz, 4 s, 5 mW). **f** Averaged BOLD (upper) and CBV-weighted (lower) fMRI responses from different stimulation durations (1, 2, 4, and 8 s) and frequencies (1, 2, 3, and 5 Hz) ( $n = 4$ , mean  $\pm$  SEM)

individual arteriole and venule voxels from the surrounding parenchyma voxels enriched with capillaries. At shorter TE, due to in-flow effects from vessels at the short time of repetition (TR), all vessel voxels appear brighter than the surrounding voxels based on the T1-weighted MR contrast; however, at the longer TE, the fast T2\* decay of the deoxygenated blood leads to darker signal intensity in venule voxels only (Fig. 2b, Supplementary Movie 2)<sup>18</sup>. Thus, by integrating the MGE images acquired at different TEs, we could distinguish individual hippocampal arterioles (bright dots) and venules (dark dots) from the anatomical single-vessel 2D map (arteriole-venule (A-V) map), showing the interleaved arterioles and venules in the hippocampus (Fig. 2c).

One essential improvement of this work is to apply the single-vessel bSSFP-fMRI to detect the optogenetically evoked fMRI signal in the rat hippocampus, demonstrating the deep brain single-vessel hemodynamic mapping with fMRI beyond the penetration depth of conventional optical imaging methods. Following the BOLD fMRI experiment, the CBV-weighted single-vessel fMRI was performed after the intravenous MION (iron oxide particle) injection. Figure 2d shows the optical fiber targeting the hippocampal CA1 region expressing ChR2. Upon optogenetic activation, peak BOLD signals were primarily overlapping with venule voxels, showing positive BOLD signals from individual venules. Peak CBV-weighted signals were located

at arteriole voxels, showing negative CBV-weighted signals from individual arterioles in the hippocampus (Fig. 2e, Supplementary Movie 3). Besides the CBV-weighted single-vessel fMRI maps, we also calculated the CBV percentage change (%) map based on BOLD fMRI time courses acquired before the injection of MION particles<sup>51</sup>, showing positive %CBV changes from individual arterioles (Supplementary Fig. 4). Figure 2f shows vessel-specific mean hemodynamic BOLD and CBV-weighted responses upon the optogenetic stimulation at varying durations and frequencies of light pulses, demonstrating highly robust optogenetically driven single-vessel fMRI signals in the hippocampus. It is also noteworthy that the strong BOLD signal from the draining veins through the lateral ventricle can be distinguished from the hippocampal vasculature, showing a spatially more refined hemodynamic mapping than the EPI-fMRI mapping in Fig. 1f.

**Optogenetic single-vessel fMRI with concurrent Ca<sup>2+</sup> recording.** We performed a simultaneous bSSFP-based single-vessel optogenetic fMRI and optical fiber Ca<sup>2+</sup> recording. Both optical fibers were inserted to target the CA1 region, and the 2D bSSFP slice was chosen to be 500  $\mu$ m away from the optical fiber along the caudal-ventral axis (Fig. 3a), which avoided the potential focal vascular blood flow regulation by direct light exposure<sup>48</sup>. Upon optogenetic activation, both BOLD and CBV-weighted

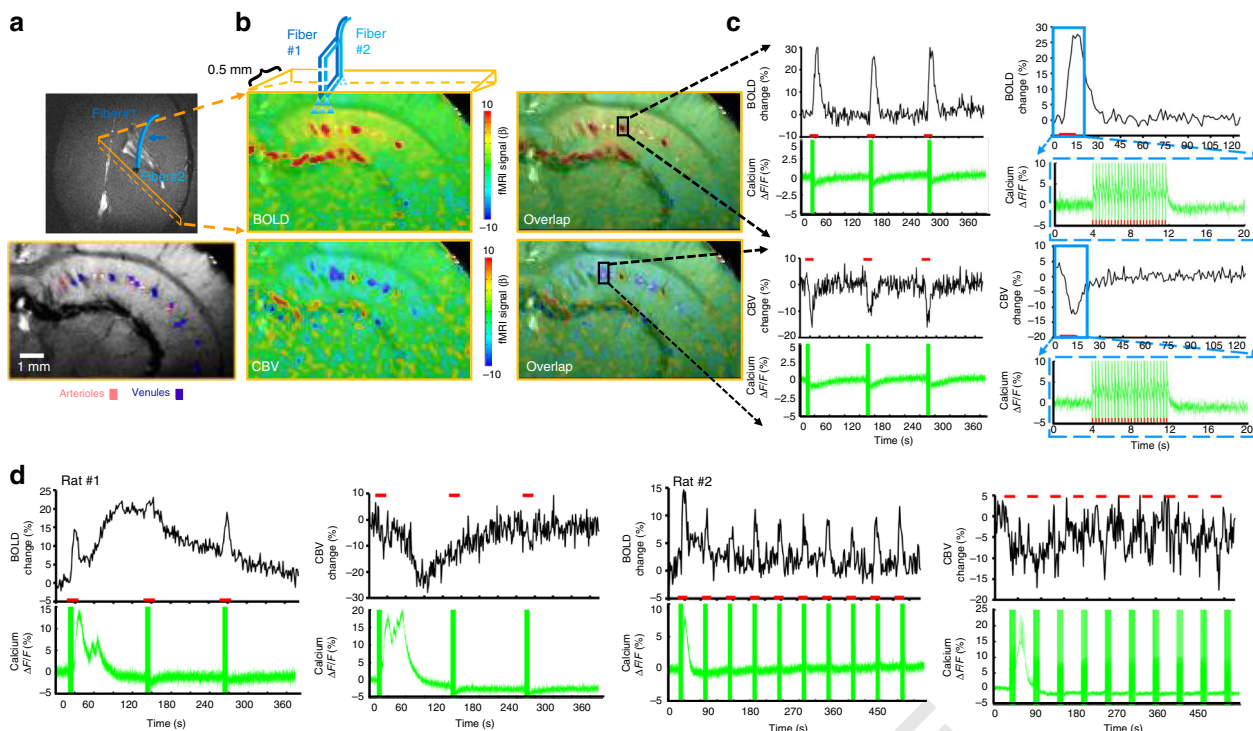


**Fig. 3** Concurrent fMRI and  $\text{Ca}^{2+}$  recording in the hippocampus. **a** Schematic drawing of the hippocampal single-vessel fMRI with two optical fibers (blue arrow) for optogenetic stimulation and  $\text{Ca}^{2+}$  recordings. A representative A-V map shows individual arterioles (bright dots, red markers) and venules (dark dots, purple markers) on the same 2D slice. **b** Evoked BOLD (upper) and CBV-weighted (lower) fMRI maps and overlapping maps on the A-V map. **c** Time courses of evoked BOLD and CBV-weighted fMRI signal from a single venule (upper) or arteriole (lower) ROI with the concurrent neuronal  $\text{Ca}^{2+}$  signal (illumination: 10 ms light pulse, 3 Hz, 8 s, 5 mW). Averaged time course of the fMRI signal and the evoked  $\text{Ca}^{2+}$  spike train. **d** A representative time course of single-vessel BOLD and CBV-weighted fMRI signal changes with concurrent hippocampus SDL- $\text{Ca}^{2+}$  responses (illumination: 10 ms light pulse, 3 Hz, 8 s, 5 mW (left); 10 ms light pulse, 3 Hz, 8 s, 5 mW)

fMRI signals were detected from individual hippocampal venules and arterioles with concurrent  $\text{Ca}^{2+}$  transients following each light pulse (Fig. 3a–c), showing highly correlated NVC events in the hippocampus. Similar to the previous experiment, averaged time courses of evoked BOLD and CBV-weighted signals showed robust responses with altered amplitudes and durations from individual venules and arterioles at varying durations (1, 2, 4, and 8 s) and light pulse frequencies (1, 2, 3, and 5 Hz), which were detected simultaneously with evoked neuronal  $\text{Ca}^{2+}$  transients in the hippocampus (Supplementary Fig. 5). These results demonstrate the feasibility of multi-modal imaging of NVC events in the hippocampus, linking the evoked  $\text{Ca}^{2+}$  transients from CA1 neuronal ensembles to the widely spread vessel-specific hemodynamic responses in the sub-centimeter scale hippocampal vasculature.

In contrast to the trains of  $\text{Ca}^{2+}$  transients evoked by low-frequency light pulses, the evoked  $\text{Ca}^{2+}$  signal did not return to baseline between light pulses at a higher frequency, showing an accumulative  $\text{Ca}^{2+}$  plateau response corresponding to the high-amplitude fMRI signal detected in hippocampal vessels (Fig. 3c, Supplementary Fig. 5). Interestingly, we also observed a large-scale hippocampal  $\text{Ca}^{2+}$  transient, that is, the SDL- $\text{Ca}^{2+}$  transient, at inter-stimulus intervals following optogenetic stimulation with 3 or 5 Hz light pulses at 8 s stimulation-on duration (Fig. 3d). The SDL- $\text{Ca}^{2+}$  transients coincided with the spreading positive BOLD and negative CBV-weighted signals during inter-stimulus intervals in the hippocampus (Fig. 3d).

As previously reported<sup>52,53</sup>, the high-frequency optogenetic activation (>10 Hz) in the hippocampus leads to seizure-like events in animals. The simultaneous LFP and fiber optic  $\text{Ca}^{2+}$  recordings also detected epileptic events as a train of strong LFP

deflections and concurrent  $\text{Ca}^{2+}$  transients. These epileptic events were often accompanied by a large amplitude SDL- $\text{Ca}^{2+}$  event in the hippocampus (Fig. 4a), which was previously reported in the cortex of both animal and human brains<sup>54,55</sup>, but not with concurrent fMRI. Interestingly, the epileptic  $\text{Ca}^{2+}$  transients could be elicited concurrently with SDL- $\text{Ca}^{2+}$  during inter-stimulus intervals even with 3 and 5 Hz light pulse stimulation, followed by the spreading positive BOLD signal from individual vessels in the hippocampus (Fig. 4b). Occasionally, after spontaneous high-amplitude  $\text{Ca}^{2+}$  events, evoked single-vessel BOLD signals were diminished in the following 5–6 min and then gradually recovered with reduced amplitude, indicating the conventional depression pattern (Fig. 4b, trial #3). We have systematically analyzed occurrence rates of the SDL and SLD with seizure (SDL + seizure) events across multiple trials recorded from rats, showing that the occurrence rate is dependent on the optogenetic light pulse frequency and stimulation duration (Fig. 4c). When the light pulse stimulation duration is longer than 8 s, the occurrence rate of the SDL events ( $36.2 \pm 5.5\%$ ) was significantly higher than that ( $12.5 \pm 3.8\%$ ,  $p = 0.001$ ) of the 4 s stimulation-on duration (Fig. 4c). These results demonstrate that the multi-modal fMRI platform can detect both optogenetically evoked and spontaneous SDL- $\text{Ca}^{2+}$  transients with specifically coupled fMRI signals, presenting a unique scheme to investigate the NVCe to varied hippocampal activities.

**Vessel-specific NCE at different forms of  $\text{Ca}^{2+}$  spikes.** Different from the random incidence of epileptic events (Fig. 4c,  $\leq 4$  s,  $2 \pm 1.1\%$ ,  $\geq 8$  s,  $3.5 \pm 1.2\%$ ), SDL- $\text{Ca}^{2+}$  events were often detected after the first epoch of 8 s optogenetic stimulation across multiple trials of several animals ( $\geq 50\%$  induction rate, Fig. 4c, 8 s, 5 Hz, and



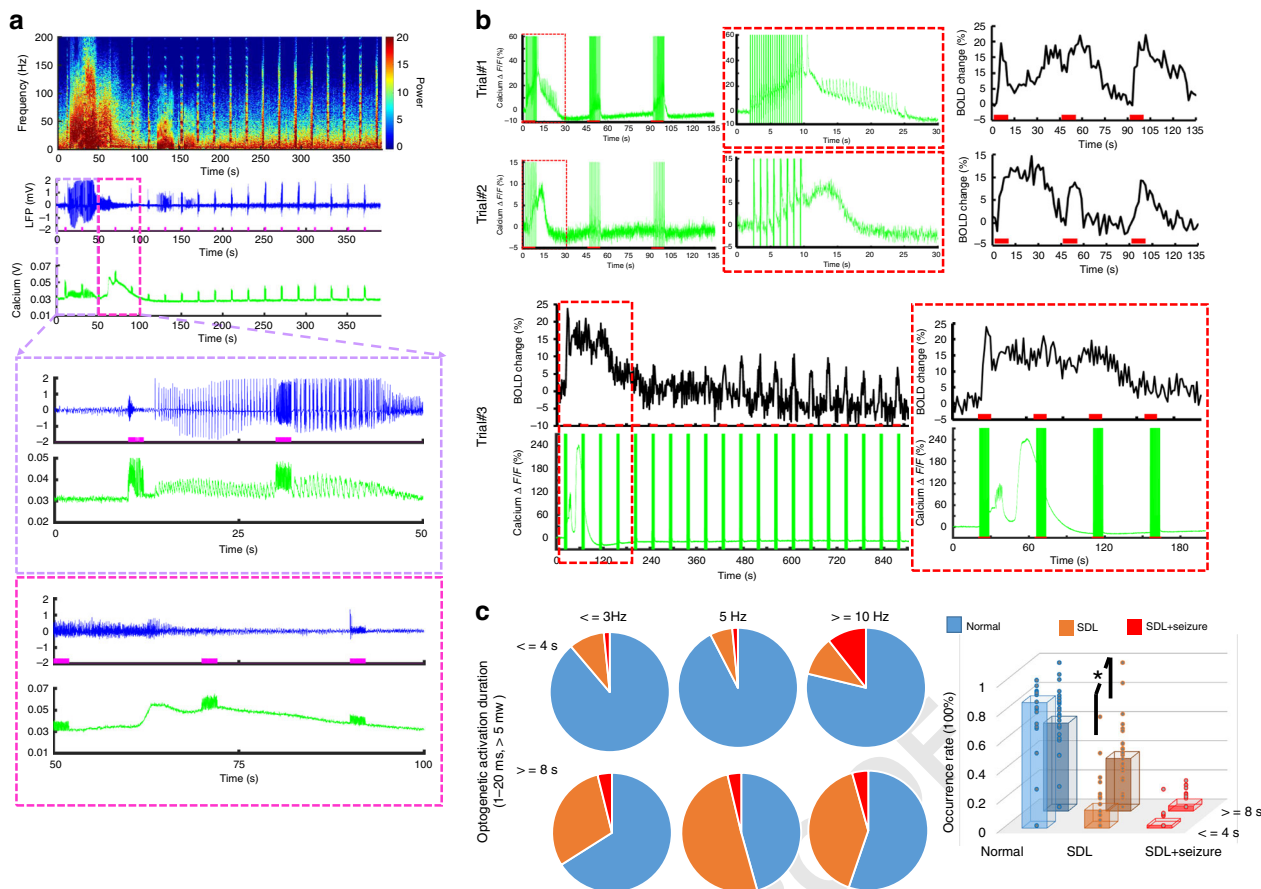


**Fig. 4** SDL and seizure-based  $\text{Ca}^{2+}$  recordings with LFP or fMRI. **a** Representative traces of SD and seizure spikes in the hippocampus: power spectra of LFP (top), LFP trace (middle), and  $\text{Ca}^{2+}$  signal (bottom). Zoomed views of the area are outlined in the upper panel (purple/pink box) (illumination: 10 ms light pulse, 50 Hz, 2 s, 5.5 mW). **b** Representative trials (3 rats) of neuronal  $\text{Ca}^{2+}$  signal (green) with simultaneous single-vessel BOLD fMRI signal (black) (upper: 10 ms light pulse, 1 Hz, SDL and 3 Hz, SLD + seizure  $\text{Ca}^{2+}$  events, 8 s, 6 mW; lower: 20 ms light pulse, 5 Hz, 8 s, 5.5 mW). Zoomed views of the area are outlined in the red box. **c** Quantification of the occurrence percentage of normal, SDL and SDL + seizure  $\text{Ca}^{2+}$  events as a function of optogenetic light pulse frequency ( $\leq 3$  Hz, 5 Hz,  $\geq 10$  Hz) and stimulation duration ( $\leq 4$  s, 382 trials,  $\geq 8$  Hz, 448 trials,  $n = 28$  rats). Induction rate of SDL- $\text{Ca}^{2+}$  events in trials with 8 s stimulation duration is significantly higher than that of trials with 4 s stimulation ( $*p = 0.001$ ,  $n = 28$  rats, mean  $\pm$  SEM)

$\geq 10$  Hz conditions). It enabled to statistically compare the spatiotemporal hemodynamic response pattern and the NVCe between the SDL and the optogenetically evoked  $\text{Ca}^{2+}$  transients in the hippocampal vasculature. The bSSFP-fMRI method was used to characterize the distinct spatiotemporal hemodynamic patterns of the single-vessel fMRI signal coupled to either optogenetically evoked or SDL- $\text{Ca}^{2+}$  events in the hippocampus. The single-vessel hippocampal A-V map can be used to specify the relative position of individual vessels with respect to the optical fiber tip (Fig. 5a). First, BOLD fMRI signals from individual venules were extracted to show the temporal dynamics corresponding to different  $\text{Ca}^{2+}$  events. In contrast to the evoked BOLD signals that co-occurred instantaneously across different hippocampal penetrating venules upon the optogenetic stimulation, the SDL- $\text{Ca}^{2+}$ -coupled BOLD signals presented a propagation delay from individual venules as a function of distance to the optical fiber. Figure 5b shows the early onset and time to peak (TTP) from the venule closest to the optical fiber ( $V_0$ ), and the delayed onset time and TTP from hippocampal venules aligned further away from the optical fiber ( $V_{-1,-2}$ ,  $V_{1,2}$ ). BOLD signal propagation velocity was estimated by measuring TTP or the half-peak onset time ( $t_{1/2}$ ) across different hippocampal venules ( $v_{\text{TTP}} = 4.58 \pm 0.47$  mm/min;  $v_{t_{1/2}} = 5.94 \pm 1.31$  mm/min) (Fig. 5c), which fell into the top-end SD propagation speed range (1–6 mm/s) detected in the cortex<sup>54–56</sup>. In addition, time-lapsed

fMRI maps show slowly spreading BOLD signals from individual venules through the sub-centimeter scale hippocampal vasculature corresponding to SDL- $\text{Ca}^{2+}$  events, which are different from the optogenetic activation pattern specific to evoked  $\text{Ca}^{2+}$  events (Fig. 5d, Supplementary Movie 4). Also noteworthy is the fact that although peak BOLD amplitudes were similar between the two different forms of  $\text{Ca}^{2+}$  events, the evoked  $\text{Ca}^{2+}$  transient amplitude was significantly lower than that of the SDL- $\text{Ca}^{2+}$  event across different trials from the same animal and among different animals (Fig. 5e). These results suggested that varied NVc events are coupled to the optogenetically evoked and SDL- $\text{Ca}^{2+}$  signal, and can be directly measured with the multi-modal single-vessel fMRI method in the hippocampus from the same experimental trials.

Concurrent single-vessel fMRI and  $\text{Ca}^{2+}$  signals can be used to estimate the efficiency of the vessel-specific NVc according to the different forms of neuronal activity. In contrast to the conventional general linear model (GLM) that fits the fMRI signal with the ideal time course, describing the hemodynamic function derived from the stimulation paradigm, we analyzed the concurrent  $\text{Ca}^{2+}$  signal amplitude and applied an amplitude modulated (AM) response model to calculate  $\beta$ -coefficients, as estimates of the NVc to the optogenetically evoked and SDL- $\text{Ca}^{2+}$  events (Supplementary Fig. 6, see Methods section for details)<sup>21</sup>. Figure 5f demonstrates NVc  $\beta$  maps of the two forms

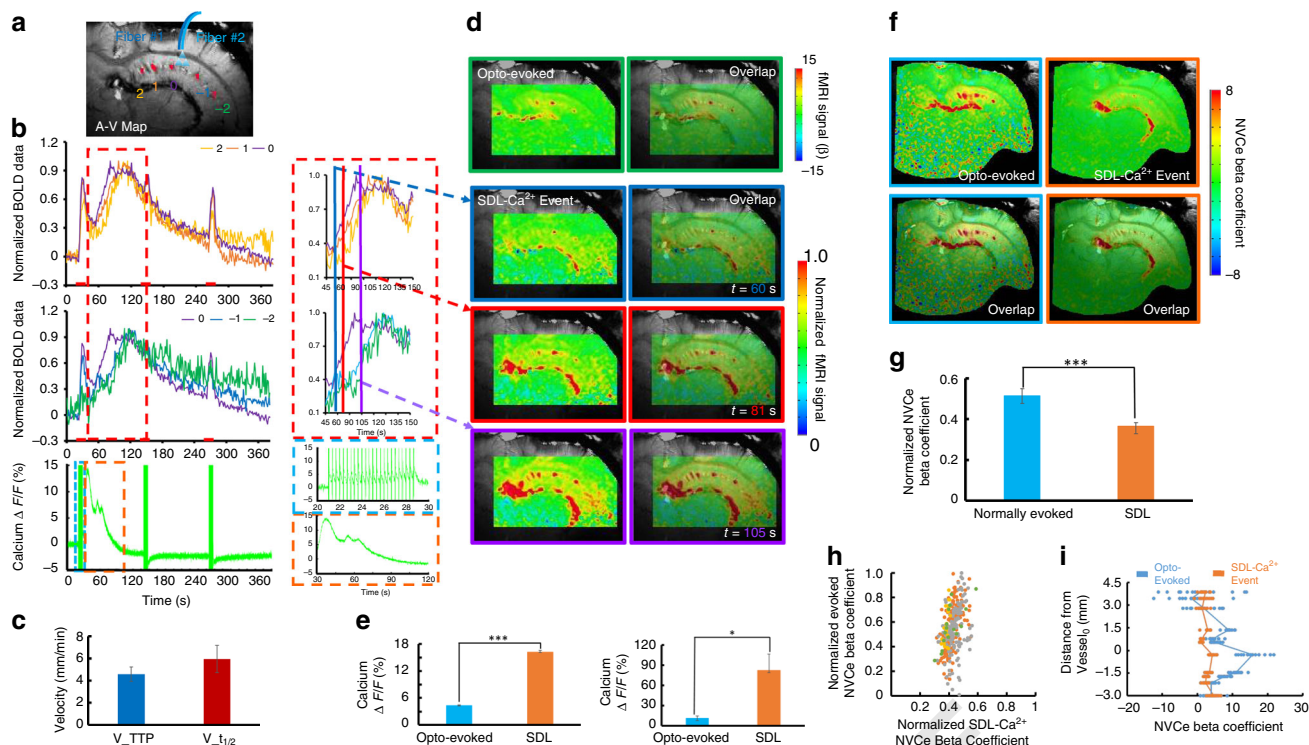


**Fig. 5**  $\text{Ca}^{2+}$ -based NVCe mapping. **a** Numbered venules on the A–V map. Venule 0 (purple) is the one closest to the optical fiber tip, venules 1, 2 and –2 are vessels with different directions in the hippocampal structure. **b** Time courses of normalized single-vessel BOLD fMRI signal from individual venules, as shown in Fig. 4a, are plotted (top) with the concurrent neuronal  $\text{Ca}^{2+}$  signal (bottom). Insets are the magnified figures of the dashed box in the left to highlight the SDL- $\text{Ca}^{2+}$  events and coupled single-vessel BOLD responses (illumination: 10 ms light pulse, 3 Hz, 8 s, 5 mW). **c** Velocity of SDL- $\text{Ca}^{2+}$  events spreading between different hippocampal venules with different time to peak (TTP) and  $t_{1/2}$  (18 vessels from 3 rats, mean  $\pm$  SEM). **d** Representative color-coded BOLD fMRI map (optogenetically evoked) from the hippocampus (upper). Time-lapsed function maps and semi-transparent overlapping images on the A–V map at 60 s (blue box), 81 s (red box), and 105 s (purple box) during the trial. **e** Amplitude of optogenetically evoked  $\text{Ca}^{2+}$  signals is significantly lower than that of SDL- $\text{Ca}^{2+}$  spikes in the hippocampus (left:  $*p = 6.22e - 11$ , 10 trials from a representative rat; right:  $*p = 0.028$ ,  $n = 4$  rats). **f** NVCe coefficient map for both optogenetically evoked and SDL- $\text{Ca}^{2+}$  events. **g** Z-score normalized NVC coefficients of optogenetically evoked events are significantly higher than those of SDL- $\text{Ca}^{2+}$  events ( $n = 4$  rats,  $*p = 0.003$ ). **h** Scatter plot of z-score normalized coefficients from optogenetically evoked vs. SDL- $\text{Ca}^{2+}$  events from each trial in four representative rats. **i** Z-score normalized NVCe coefficients from individual vessels were plotted as a function of vessel distance for both optogenetically evoked and SDL- $\text{Ca}^{2+}$  events in a representative rat

of  $\text{Ca}^{2+}$  events, showing peak NVCe  $\beta$  values on individual hippocampal venules. Mean vessel-specific NVCe  $\beta$  values of optogenetically evoked  $\text{Ca}^{2+}$  events were significantly higher than those of SDL- $\text{Ca}^{2+}$  events (Fig. 5g). To better quantify the spatial distribution of the NVCe across hippocampal vasculature, we plotted  $\beta$ -coefficients from individual venules as a function of the relative distance to  $V_0$  (Fig. 5i). Despite the fact that the SDL- $\text{Ca}^{2+}$  events were elicited in the hippocampal structure close to  $V_0$ , the NVCe  $\beta$  values were found to be similar and evenly distributed across the hippocampal vasculature, whereas NVCe  $\beta$  values of optogenetically evoked  $\text{Ca}^{2+}$  events showed a distance-dependent distribution (Fig. 5h, i, scatter plot of NVCe  $\beta$  values from all hippocampal vessels through multiple trials of four animals). These results demonstrate altered NVCe linking to normal and SDL hippocampal activity detected by the multi-modal fMRI platform.

**Discussion**

Here, we developed a multi-modal fMRI platform to investigate detailed, spatiotemporally resolved NVC events in rat hippocampus. By implementing simultaneous optogenetic single-vessel fMRI and optical fiber  $\text{Ca}^{2+}$  recordings, distinct hemodynamic spatiotemporal patterns across the sub-centimeter hippocampal vasculature could be directly characterized based on concurrent neuronal  $\text{Ca}^{2+}$  signals, for example, optogenetically evoked or

SDL- $\text{Ca}^{2+}$  events, for the first time. We believe that this method provides a unique multi-modal/cross-scale mapping scheme for the study of neurovascular activity in the hippocampus in both normal and pathological conditions.

Despite extensive imaging studies on hippocampal neural activity, the actual information flow from neuronal activity to the hippocampal neurovascular system, the modulation of which provides the vast majority of fMRI signals, has seldom been taken into account in investigations attempting to relate behavior to the function or dysfunction of this structure<sup>30,33,57</sup>. One major barrier is our ability to access large-scale hippocampal vascular dynamics in vivo with minimally invasive procedures, preserving NVC function. Three critical features needed to be solved for existing neuroimaging methods: large field of view (FOV), high resolution to detect the vessel-specific hemodynamic signal with sufficient signal-to-noise ratio (SNR), and accessibility to deep brain nuclei. Although wide-field two-photon or the newly developed three-photon microscopy has significantly enlarged the FOV and the penetration depth for in vivo brain optical imaging with cellular resolution<sup>39–41,58</sup>, it remains challenging to acquire vascular hemodynamic signaling through the sub-centimeter hippocampal structure in rats and higher mammals.

The fMRI signal directly represents vascular hemodynamic responses to indicate large-scale brain function. Our work and other animal fMRI studies have demonstrated the optogenetically

evoked hippocampal BOLD signal in the context of whole-brain functional mapping<sup>52,59</sup>. By improving the spatial resolution of the fMRI image, it is possible to detect fMRI signals from individual penetrating vessels through the cortex<sup>17,18,60,61</sup>. The real power of single-vessel fMRI can be further released when targeting large deep brain regions beyond the penetration depth of conventional optical methods. To achieve sufficient SNR, the bSSFP-based single-vessel fMRI method was applied with an implanted surface RF coil<sup>22</sup>. The RF coil implantation could be merged with the optical fiber targeting the hippocampus during the surgical procedure. The RF coil implanted to the skull substantially increased  $B1$  field sensitivity and prevented additional signal loss due to the extra space occupied for fiber fixation between the surface coil and the brain, which can be readily implemented by MRI users with 7 to 11.7 T scanners. This optimized multi-modal fMRI platform employed optogenetic single-vessel fMRI mapping to detect venule-specific BOLD and arteriole-specific CBV-weighted signals from individual vessels aligned in parallel through the hippocampal structure (Fig. 2), which have been previously described only by histological studies<sup>42,43</sup>. We delivered optical fiber-mediated optogenetic stimulation using light pulses with varied frequencies and power levels to specify BOLD and CBV-weighted fMRI signals from individual hippocampal vessels (Supplementary Fig. 4), as well as evoked LFP spikes and  $\text{Ca}^{2+}$  transients (Supplementary Fig. 1), representing highly correlated NVC features in the hippocampus. Single-vessel fMRI provides a unique mapping scheme to identify large-spread hemodynamic response patterns in the hippocampal vasculature.

Optogenetic light exposure may contribute directly to hemodynamic responses in the hippocampus. As reported by Christie et al.<sup>48</sup>, direct light exposure can directly regulate blood flow through arteriole dilation following the reduced  $\text{Ca}^{2+}$  signal from smooth muscle cells, similar to NVC events but independent of neuroglial activity. Our work and a previous optogenetic fMRI study<sup>49</sup> on naive animals mainly detect the susceptibility-based non-physiological MRI signal changes sensitive to the light-induced heating effect, which can shadow the MRI signal relevant to blood flow changes as detected by ultrasound Doppler measurement. In addition, the direct heating effect through light illumination can alter the spiking activity in the animal brain<sup>62</sup>. To avoid the confounding effects of light exposure-induced blood flow regulation, we have aligned the single-vessel 2D slice at least 500  $\mu\text{m}$  away from the optical fiber tip. Also, both two-photon and single-vessel fMRI studies have shown that the spatial scale of the hemodynamic coherence in the arteriole network is  $<2$  mm spatial scale in the cortex<sup>22,58</sup>. The spatial distribution of light exposure-induced flow regulation can be controlled using light pulses with low frequency and power, which could further reduce direct light-exposure contribution to the sub-centimeter scale hippocampal vascular hemodynamic responses and heating-induced neuronal activity modulation.

Using GCaMP6f, optogenetically evoked hippocampal neuronal  $\text{Ca}^{2+}$  transients showed similar temporal dynamics to cortical  $\text{Ca}^{2+}$  transients detected by the optical fiber in anesthetized rats upon sensory stimulation<sup>21</sup>. This temporal feature makes it possible to distinguish individual  $\text{Ca}^{2+}$  transients from light pulse-induced artifacts, which has been previously reported in the Opto-fMRI with  $\text{Ca}^{2+}$  dye (OGB-1) sensing-based optical fiber measurements<sup>28</sup>. To reduce the spectral signal cross-talk, we applied a red-shifted ChR2 variant (C1V1) to alter the optogenetic light pulse up to 590 nm (Supplementary Fig. 3). Although the artifacts can be significantly reduced, the remaining light pulse signals detected by the photomultiplier can be caused by imperfect filtering of the dichroic filter. It is noteworthy that the optogenetic light pulses were delivered at 1–5 mW from the

200  $\mu\text{m}$  optical fiber tip, which is significantly higher than the power used for GCaMP fluorescent excitation (5–10  $\mu\text{W}$ )<sup>21</sup>. Since the optical excitation was delivered at a low power level for continuous  $\text{Ca}^{2+}$  signal recording, its effect on optogenetic activation is negligible.

To better validate hippocampal  $\text{Ca}^{2+}$  transients free of optogenetic light pulse artifacts, we also observed individual  $\text{Ca}^{2+}$  transients coinciding with interictal LFP spikes during seizure induction following high-frequency optogenetic activation (Fig. 4). These interictal spikes paired with the train of spontaneous  $\text{Ca}^{2+}$  transients have also been observed in the mouse cortex with an optogenetically induced seizure<sup>63</sup>. Also, we observed robust SDL- $\text{Ca}^{2+}$  events during inter-stimulus intervals in the hippocampus following 8 s ( $\geq 5$  Hz) optogenetic stimulation (Fig. 4). These SDL- $\text{Ca}^{2+}$  events were recently reported to follow trains of interictal spikes during the optogenetically induced seizure<sup>63</sup> in the mouse cortex, which could be reliably detected in the hippocampus following optogenetic stimulation with fMRI. In our study, the number of seizure events detected by calcium recordings is much smaller than that of the SDL events, which might be due to the lack of sensitivity of calcium recording to detect interictal spikes through the 8-m optical fiber. The multi-modal fMRI mapping scheme allows us to specify unique NVC patterns according to different formats of hippocampal activity.

The hippocampal CA1 region has been considered as a key component in the framework of epilepsy induction and treatment<sup>53,57,64</sup>. Previous hippocampal Opto-fMRI studies have also shown the seizure behavior in animals following high-frequency light exposure, demonstrating broad hippocampal BOLD fMRI spatial patterns and global hemodynamic effects concurrent with epileptic events<sup>52,65</sup>, which are different from the evoked hippocampal activity with Opto-fMRI<sup>59,66</sup>. Epileptic events observed in the cortex are usually accompanied by cortical spreading depression<sup>54,55,63</sup>, which is typically studied with fMRI by direct KCl topical treatment or focal ischemia in animal brains<sup>67</sup>. In the hippocampus, we detected robust SDL- $\text{Ca}^{2+}$  events independent of epileptic activity in inter-stimulus intervals when 3–5 Hz optogenetic light pulses were used (Fig. 3d, Supplementary Fig. 5B), which have dominated the random incidence of epileptic events using similar stimulation paradigm in the hippocampus. The optogenetically induced cortical spreading depression has been reported in the mouse cortex without seizure induction<sup>68</sup>. These SDL- $\text{Ca}^{2+}$  events link to specific spatiotemporal patterns of hippocampal vascular hemodynamic responses. Intermediate characteristics of SDL- $\text{Ca}^{2+}$ -specific NVC events can be quantitatively examined to bridge the normal condition to the typical spreading depression, as well as hippocampal epileptic events despite their scarce occurrence in normal animals.

Coupled to SDL- $\text{Ca}^{2+}$  events, the BOLD signal propagation through individual hippocampal vessels has a 4–6 mm/min velocity in a  $\sim 6$ –8 mm spatial scale (Fig. 5c). This speed falls to the relatively top-end propagation speed range of cortical SD detected from the neuronal network<sup>54–56,68,69</sup>. This observation might be because of intrinsic architectural differences between the cortex and the hippocampus; the latter is highly susceptible to SD and may sustain faster SD propagation speed<sup>70,71</sup>. Kunkler et al.<sup>72</sup> have observed  $\text{Ca}^{2+}$  waves occurring in neurons ( $\sim 6$  mm/min) and astrocytes ( $\sim 4$  mm/min) during SD initiation and propagation in hippocampal organ cultures. Meanwhile, in contrast to astrocytic  $\text{Ca}^{2+}$  waves propagation speed of (2–3.3 mm/min) related to cortical SD in both rat and mouse neocortex<sup>69,73,74</sup>, Heuser et al.<sup>75</sup> also reported a 6–8 mm/min propagation speed of SD  $\text{Ca}^{2+}$  waves from both neurons and astrocytes in the hippocampal CA1 region. Interestingly, unique, spontaneous astrocytic  $\text{Ca}^{2+}$  waves, which have been reported to propagate at  $\sim 4$  mm/min in the hippocampus, do not show the long-term spreading

Q9

depression features<sup>76</sup>. It is noteworthy that the neuronal  $\text{Ca}^{2+}$  signal was only acquired through the single optical fiber inserted into the hippocampus with limited coverage of neuronal activation in comparison to the large-scale hippocampal vascular dynamic mapping with single-vessel fMRI. To better characterize neuron–glial–vascular interaction at various brain states in the hippocampus, we will apply the multiple fiber insertion with single-vessel fMRI to image transgenic mice expressing GCaMP specifically in astrocytes<sup>77</sup>, as well as the right-shifted calcium indicator in neurons<sup>78</sup>, with a multi-slice single-vessel fMRI method to cover the three-dimensional hippocampal structure.

Besides the similarity of the propagation speed of SDL- $\text{Ca}^{2+}$ -specific hemodynamic responses to SD events reported in the hippocampus, the baseline  $\text{Ca}^{2+}$  signal was reduced following the SDL- $\text{Ca}^{2+}$  event for 5–6 min (Fig. 3d). Nevertheless, we only detected the correlated BOLD signal increase and CBV-weighted signal decrease (due to vasodilation), but no clear sign of vasoconstriction-based fMRI signal change was detected. Also, suppressed fMRI signals recovered in 3–6 min in most of the SDL- $\text{Ca}^{2+}$  events (except for one dramatic case showing a long-term depression over 10 min, which was shown in Fig. 4b). Interestingly, although no clear vasoconstriction-based fMRI signal was detected following the SDL- $\text{Ca}^{2+}$  event, significantly reduced NVCe was detected when comparing to the optogenetically evoked  $\text{Ca}^{2+}$  transients (Fig. 5). Consistent with impaired NVC during cortical SD<sup>54,79</sup>, we provide a multi-modal fMRI platform to directly measure altered NVCe directly linked to concurrent SDL- $\text{Ca}^{2+}$  events in the hippocampus.

In summary, we have developed a multi-modal fMRI platform to acquire concurrent neuronal  $\text{Ca}^{2+}$  and single-vessel fMRI signal in a subcortical brain region, for example, the hippocampus. This method allows for detecting hemodynamic fMRI responses from individual vessels through the sub-centimeter hippocampal vasculature. In particular, when neuronal activation is elicited in the hippocampus, large-scale vascular hemodynamic responses can be represented based on the estimated NVCe. This multi-modal fMRI platform will possibly be used to specify distinct NVC events through the hippocampal structure in animal models at various disease states.

## Methods

**Animal preparation and instrument setup.** All surgical and experimental procedures reported in this paper were approved by local authorities (Regierungsspraesidium, Tübingen Referat 35, Veterinärwesen, Leiter Dr. Maas) and were in full compliance with guidelines of the European Community (EUVD 86/609/EEC) for the care and use of laboratory animals. Experimental animals were rodents, specifically Sprague–Dawley male rats, ~3 to 4 weeks old, or ~90 g, provided by Charles River Laboratories in Germany. The rats were housed in transparent Plexiglass cages (381 × 513 × 256 mm<sup>3</sup>) under conditions of well-controlled humidity and temperature. A 12–12 h on/off lighting cycle was maintained to assure an undisturbed circadian rhythm. Food and water were obtainable ad libitum. A total of 37 male Sprague–Dawley rats were used at 2–3 months of age. Five rats were imaged under 14 T at the Max Planck Institute (both BOLD and CBV-weighted fMRI data with A–V maps were acquired from four of five rats). In 12 rats, optogenetically driven neuronal calcium signals were concurrently recorded with BOLD/CBV-weighted signals (in 4 of these 12 rats optogenetically evoked responses and SDL- $\text{Ca}^{2+}$  calcium events were acquired). Twenty rats were used for concurrent optogenetically driven electrophysiological and neuronal calcium recordings. For the SDL and seizure induction rate calculation, 4 of the 32 rats were not included due to a failed calcium signal detection from hippocampal neurons. If the optical fiber insertion caused severe micro-bleeding in the hippocampus, which led to poor calcium recording and optogenetic activation, the data acquired from that rat was not included in the statistical analysis.

**Viral injection.** After 1 week habitation, rats were injected with the non-replicating AAV vectors into BC and hippocampus (AAV5.Syn.GCaMP6f.WPRE.SV40: Addgene100837-AAV5; AAV5.CAG.hChR2 (H134R)-mCherry.WPRE.SV40: Addgene100054-AAV5; AAV9-CaMKIIa-C1V1 (t/t)-TS-EYFP: Addgene35499-AAV9). Viral vectors were procured from the University of Pennsylvania Vector Core. The injection process was carried out under isoflurane anesthesia with an induction concentration of 5.0% and a maintenance concentration of 1.5–2.0% in

an oxygen-enhanced gas (30% oxygen). Following their stabilization, the rats were secured in a stereotaxic apparatus (Model 900, David Kopf Instruments). Eyes of the rats were protected with an ophthalmic ointment (Puralube), and the level of anesthesia was regularly checked by testing toe and tail pinch reflexes. With a midline incision, one small craniotomy (1–2 mm) was performed above the region of interest by using a dissecting microscope (Leica) and a pneumatic drill (Ideal Micro Drill, Harvard Apparatus). A 10  $\mu\text{L}$  syringe (NanoFil, World Precision Instruments Inc.) with a 35 gauge beveled metal needle (World Precision Instruments Inc.) were placed in the stereotaxic frame and slowly lowered towards target sites (BC: caudal, 2.5 mm, lateral, 5.0 mm, and ventral, 1.5–0.9 mm; hippocampus: caudal, 4.2 mm, lateral, 2.8 mm, and ventral, 2.75–2.65 mm, respectively, from bregma). The flow rate of the virus injection was controlled by an infusion pump (Pump11 Elite, Harvard Apparatus) at a speed of 0.1  $\mu\text{L}/\text{min}$ . The total injection volume was around 0.2–0.6  $\mu\text{L}$  (ChR2)/0.6–1  $\mu\text{L}$  (GCaMP6f). After the injection, the syringe needle was kept in place for an additional 10 min before being slowly withdrawn. The hole was sealed by bone wax (W31G, Ethicon), and the incision was sutured. Ketoprofen (5 mg/kg, q.d. (one a day)) was subcutaneously injected to relieve postoperative pain for 3 days after surgery. fMRI experiments were performed 4–8 weeks after the injection to ensure the expression of the AAV viral vectors.

**Optical fiber/electrode preparation and implantation.** Optical stimulation and electrophysiological recordings were performed with a 2 m (bench experiment) or 8 m (fMRI experiment) optical fiber (FT200-EMT, NA = 0.39, 200  $\mu\text{m}$ , Thorlabs). The coating of both ends of the optical fiber was stripped off. One end was glued into an FC/PC connector (Thorlabs), and the other end was carefully polished by using polishing sand papers with appropriately selected grit size (LF1P/3P/5P, Thorlabs). Optical quality of the polishing interface was confirmed by using a fiber inspection microscope (FS200, Thorlabs). For simultaneous  $\text{Ca}^{2+}$  recording and fMRI, two fibers (one for optical stimulation, the other for  $\text{Ca}^{2+}$  recording) were closely glued (454, Loctite) together. For simultaneous  $\text{Ca}^{2+}$  and electrophysiological recording, a Tungsten electrode (1 M $\Omega$ , ~100  $\mu\text{m}$ , FHC) was closely glued to the optical fiber tips. The dura was carefully removed, the optical fibers with the electrode were slowly inserted into either the BC or the hippocampus. The reference and ground were placed on the screws, which were fixed above the cerebellum. After implantation, the fibers with the electrode were glued to the skull for acute terminal experiments.

**Animal preparation for fMRI.** The experiments were described in the previous studies<sup>18,45,61</sup>. Briefly, after induction of anesthesia, animals were endotracheally intubated with a mechanical ventilator (SAR-830, CWE). Plastic catheters (PE50, INSTECH) were carefully implanted into the right femoral artery/vein of rats to administer drugs and monitor arterial blood gases. After catheterization, the rats were secured into a stereotaxic apparatus. One small craniotomy (1–2 mm) was performed just above the regions of the virus injection and the dura was carefully removed. Two optical fibers were slowly inserted into the virus expression regions in the hippocampus, and the fibers together with a custom-made coil were fixed above the skull by using super glue (454, Loctite). Around 30 min for fixation, after the injection of a bolus of  $\alpha$ -chloralose (60 mg/kg, intravenously (i.v.)), the rats were transferred into the MR scanner (14T, Bruker). Maintenance anesthesia was switched from isoflurane to continuous infusion of  $\alpha$ -chloralose (infusion rate: 26.5 mg/kg/h). Throughout the whole experiment, the rectal temperature of the rat was monitored and maintained at around 37 °C by using a feedback heating system. All relevant physiological parameters were continuously monitored, including rectal temperature, arterial blood pressure (Biopac 150, Biopac Systems Inc.), pressure of the tidal ventilation (SAR-830, CWE), and end-tidal  $\text{CO}_2$  (capnometer, Novamatrix). Arterial blood gas was measured regularly to guide physiological status adjustments by changing the respiratory volume or administering the sodium bicarbonate (8.4%, Braun) to maintain normal pH levels. For  $\alpha$ -chloralose anesthetized animals, a muscle relaxant (pancuronium bromide, 1 mg/kg/h) was intravenously injected to minimize motion artifacts. Dextran-coated iron oxide (15 mg of Fe/kg, BioPAL, MA, i.v.) was additionally injected for obtaining high SNR CBV-weighted signal.

**Optogenetic-driven  $\text{Ca}^{2+}$  with electrophysiological recording.** Around 4–8 weeks after virus injection, LFP signal and  $\text{Ca}^{2+}$  signal were simultaneously recorded in a terminal experiment. Virus injection coordinates were first confirmed by a FLASH (fast low angle shot) anatomical MRI image before surgery. Anesthetics and surgical preparation procedures were similar to those of the fMRI experiments. After insertion, the LFP signal was amplified using a BioPac EEG100C module (gain factor, 5000, bandpass filter, 0.02–100 Hz, sampling rate, 5000/s). The GCaMP6f-mediated  $\text{Ca}^{2+}$  signal was recorded by the analog input module of the BioPac 150 system. For electrical stimulation, electrodes were placed into rat whisker pads and later delivered electrical pulse sequences (1.0–2.0 mA, 330  $\mu\text{s}$  duration repeated at 1–5 Hz) by using a high voltage stimulator (A360LA, WPI). Stimulation was controlled by the Master-9 AMPI system (Jerusalem, Israel) based on the stimulus paradigm, and triggering pulses were recorded by the analog input module of the BioPac 150 system (sampling rate, 5000/s). For optical stimulation, light pulses were delivered through the 473 nm laser (CNI, China). An

analog module was applied to trigger the light pulse to give the optical stimulation with different pulse durations (1, 2, 4, and 8 s). Light intensity from the fiber tip was measured by using fiber optical power meters (PM20A, Thorlabs), which were controlled from 1 to 36 mW (light power higher than 40 mW was beyond the measurement range).

**Perfusion, section, and microscope.** In all terminal experiments, after completion of the data acquisition, rats were euthanized under deep anesthesia with isoflurane (5%). They were subsequently transcatheterially perfused with 0.1 M ice-cold phosphate-buffered saline (PBS, Gibco) and 4% paraformaldehyde (PFA). Brains were carefully removed from the skulls and placed into 4% PFA for post fixation (4 °C, overnight). Then, they were cryoprotected in 30% sucrose in PBS at 4 °C for 2–3 days before being flash frozen in OCT on dry ice and finally stored at –80 °C. Brain slices were sectioned in 30 μm thickness using a cryostat (CM1860, Leica). Brain slices were mounted on glass slides (Super-frost, Fisherbrand) and covered with coverslips. A mounting medium with DAPI (4',6-diamidino-2-phenylindole; VectaShield, Vector) was used to protect the fluorescence signal and to stain nuclei. Wide-field images were acquired to assess the expression of ChR2/GCaMP in the BC and the hippocampus with a microscope (Zeiss). The images were minimally processed by ImageJ to enhance the brightness for visualization purposes.

**The optical setup for optical fiber Ca<sup>2+</sup> recordings.** The light path was built based on a previous report (Fig. 1a)<sup>21,22</sup>. The light source comes from a 488 nm laser (MBL-III, CNI). Light beams were first reflected through a dichroic mirror (F48–487, reflection 471–491 nm, >94%, transmission 500–1200 nm, >93%, AHF). Then, by using an objective lens fixed on the fiber launch (MBT613D/M, Thorlabs), the light beam was focused on the optical fiber (FT200-EMT, NA = 0.39, 200 μm, Thorlabs). The laser intensity was measured at the optical fiber tip (5 μW for neuronal calcium recording) by an optical power meter (PM20A, Thorlabs). The same optical fiber guided the emitted fluorescent signal back to the light path. The light beam was successively passed through a dichroic mirror and an optical filter (F37–516, 500–550 nm bandpass, AHF). By using a tube lens (AC254–030–A1-ML, Thorlabs), the GCaMP6-mediated fluorescent signal was coupled to a Peltier-cooled SiPM with a transimpedance preamplifier (MiniSM-10035–X08, SensL). Before being recorded by the analog input module of the Biopac 150 system, the signal from the photomultiplier was amplified by a voltage amplifier (DHPVA-100, Femto).

**MRI and fMRI procedures.** All images were obtained by using a 14T/26 cm horizontal-bore magnet (Magnex Scientific) interfaced through the Bruker Avance III (Bruker). The scanner has a 12 cm Magnet gradient set with a strength of 100 Gauss per cm (G/cm), and a 150 μs rise time (Resonance Research Inc.). Home-made surface transceiver RF coils with an internal diameter of 7.5 and 21 mm, respectively, were used for fMRI image acquisition.

**Echo planar imaging fMRI.** EPI image acquisition was preceded by FASTMAP shimming (i.e., measuring B<sub>0</sub> field plots along projections instead of mapping whole imaging planes). By adjustments of echo spacing, symmetry, and setting up the B<sub>0</sub> compensation, it considerably increases the speed and performance. By using the custom-made single surface coil, parameters of the 3D gradient echo sequence were as below: volume TR = 1.5 s; TE = 14 ms; bandwidth: 170 kHz; flip angle: 12°; matrix: 64 × 64 × 16; in-plane resolution: 300 × 300 μm<sup>2</sup>; slice thickness: 500 μm. The paradigm consisted of 360 dummy scans enabling the emergence of reaching the steady state, 10 pre-stimulation scans, 3 scans during stimulation, and 12 post-stimulation scans with 8 epochs for each run or 5 scans during stimulation and 25 post-stimulation scans for 10 epochs. For anatomical images, the RARE (rapid imaging with refocused echoes) sequence was implemented to acquire images with the same geometry of the fMRI images.

**Balanced steady-state free precession fMRI.** The bSSFP-fMRI method was applied to acquire evoked fMRI signals using the following parameters: TR: 11.7 ms; TE: 5.85 ms; matrix: 128 × 128; FOV: 12.8 × 12.8 mm<sup>2</sup>; in-plane resolution: 100 × 100 μm<sup>2</sup>; flip angle: 22° (BOLD); TR: 10.4 ms; TE: 5.2 ms; matrix: 96 × 96; FOV: 12.8 × 12.8 mm<sup>2</sup>; in-plane resolution: 130 × 130 μm<sup>2</sup>; flip angle: 17° (CBV); slice thickness: 500 μm. The paradigm consisted of 300 dummy scans to reach the steady state, 25 pre-stimulation scans, 1 scan during stimulation, and 14 post-stimulation scans with a total of 8 epochs for each run, 1 scan during stimulation, and 29 post-stimulation scans with a total of 10 epochs for each run, and 1 scan during stimulation and 79 post-stimulation scans with a total of 3 epochs for each run. CBV-weighted fMRI signals were acquired after intravenous injection of dextran-coated iron oxide (BioPAL, MA, i.v.).

**Single-vessel MGE Imaging.** For the detection of the individual arterioles and venules in rat hippocampus, a 2D MGE sequence was applied with the following parameters: TR: 50 ms; TE: 2.5, 5.5, 11.5, 14.5, 17.5, 17.5, 20.5, 23.5 ms; flip angle: 58°; matrix: 256 × 192; in-plane resolution: 67 × 67 μm<sup>2</sup>; slice thickness: 500 μm. The MGE images were averaged from the 2nd echo to the 5th/6th echo to get the A–V map (Fig. 2c).

**Data analysis and statistics.** Preprocessing and analysis of functional imaging data were carried out by using the software package, Analysis of Functional NeuroImages (AFNI) (NIH, Bethesda, MD). Evoked calcium signals were processed in Matlab (MATLAB, MathWorks, USA).

For calcium data analysis, neuronal calcium signals were low-pass filtered (100 Hz) by zero-phase shift digital filtering. The relative percentage change of the calcium fluorescence ( $\Delta F/F$ ) was defined as  $(F - F_0)/F_0$ , where  $F_0$  is the baseline fluorescent signal.

For the EPI-fMRI analysis, EPI images were aligned to anatomical datasets, which were registered to template images across the trials. Baselines of EPI images were normalized to 100 for multiple trials of block-design statistical analysis of EPI time courses.

For bSSFP-fMRI analysis, the tag-based registration method was used to register the single-vessel functional map with the A–V map. We normalized time courses of bSSFP-fMRI signals from SDL-Ca<sup>2+</sup> events by scaling the maximum to 1 (Fig. 5b). GLM analysis was applied to estimate evoked and SDL-Ca<sup>2+</sup> NVCe  $\beta$ -coefficients.  $\beta$  Estimates were used to indicate the amplitude of the BOLD and CBV-weighted responses in  $\beta$  maps. For the CBV percentage (%) map, the %CBV was estimated based on the equation: %CBV =  $\ln(S_{Fe-base}/S_{stim})/\ln(S_{Fe-pre}/S_{Fe-base})$ . The  $S_{Fe-base}$  is the baseline level fMRI signal after iron oxide particle injection, and  $S_{Fe-pre}$  is the baseline level fMRI signal before iron oxide particle injection<sup>51</sup>.

For the analysis of fMRI signals recorded simultaneously with hippocampal SDL-Ca<sup>2+</sup> transients, an AM response model based on an AFNI script was implemented to perform GLM analysis.

The AM response model is given by:

$$r_{AM1}(t) = \sum_{k=1}^K h(t - \tau_k) \alpha_k,$$

where  $\alpha_k$  is the value of  $k$ th amplitude of hippocampal SDL Ca<sup>2+</sup> transient.  $h(t)$  is the hemodynamic response function based on the  $y$  variate function implemented by the AFNI BLOCK function:

$$h(t) = \int_0^{\min(t,L)} s^4 e^{-s} / [4^4 e^{-4}] ds,$$

where  $L$  is the duration of the response. A varied duration ( $L$ ) was applied to test the goodness of fit for the general linear model with  $t$  statistics reported in Supplementary Fig. 6. Both NVCe  $\beta$ -coefficients were estimated simultaneously, using GLM analysis implemented in the AFNI 3dDeconvolve function. The response regressors are shown in the equation:

$$Y(t) = \beta_1 h(t) + \beta_2 r_{AM1}(t) + \epsilon,$$

where  $\beta_1$  is the optogenetically evoked coefficient and  $\beta_2$  is the SDL-Ca<sup>2+</sup> coefficient.  $\epsilon$  is the error term. Polynomial terms regressing the baseline drift are not shown. The calculated  $\beta$ -coefficient was represented in a voxel-wise manner, as a  $\beta$  map, which can be overlapped on the A–V map of the 2D hippocampal slice in Fig. 5f or Supplementary Fig. 6D.

Evoked NVCe  $\beta$ -coefficients and SDL-Ca<sup>2+</sup> NVCe  $\beta$ -coefficients were normalized within each trial to have zero mean and unit variance. Coefficients were scaled to the range 0–1 using the minimal and maximal values (Fig. 5g, h). Student's  $t$  test (two-tailed) was performed for group analysis, to compare the calcium  $\Delta F/F$  (Fig. 5e) or the normalized NVCe  $\beta$ -coefficient (Fig. 5g) between optogenetically evoked responses and SDL-Ca<sup>2+</sup> events in calcium and fMRI data. Also, one-way analysis of variance was performed to examine the goodness of fit for the hemodynamic function with varied duration. Data with error bars were displayed as means  $\pm$  SEM.  $P$  values <0.05 were considered statistically significant. No blinding and randomization design was needed in this work.

**Reporting summary.** Further information on research design is available in the Nature Research Reporting Summary linked to this article.

## Data availability

Raw data can be provided upon email request to the corresponding author. Excel files are included for each quantitative plot included in main figures. Source data underlying Figs. 2f, 4c, 5c, e, g–i are provided as a Source Data file. The data presented in the figures and other summary level data are contained within the Supplementary Files. Further information on research design is available in the Nature Research Reporting Summary linked to this article.

## Code availability

AFNI software (NIH, USA) and Matlab (MATLAB, MathWorks, USA) were used to process fMRI and simultaneously acquired calcium signals, respectively. Relevant source codes can be downloaded through <https://afni.nimh.nih.gov/afni/>. Related image processing codes can be provided upon direct email request to the corresponding author.

Received: 11 April 2019; Accepted: 1 October 2019;  
Published online: xx xxx 2019

## References

- Ogawa, S. et al. Intrinsic signal changes accompanying sensory stimulation: functional brain mapping with magnetic resonance imaging. *Proc. Natl. Acad. Sci. USA* **89**, 5951–5955 (1992).
- Kwong, K. K. et al. Dynamic magnetic resonance imaging of human brain activity during primary sensory stimulation. *Proc. Natl. Acad. Sci. USA* **89**, 5675–5679 (1992).
- Bandettini, P. A., Wong, E. C., Hinks, R. S., Tikofsky, R. S. & Hyde, J. S. Time course EPI of human brain function during task activation. *Magn. Reson. Med.* **25**, 390–397 (1992).
- Kim, S. G. & Ogawa, S. Biophysical and physiological origins of blood oxygenation level-dependent fMRI signals. *J. Cereb. Blood Flow Metab.* **32**, 1188–1206 (2012).
- Logothetis, N. K. What we can do and what we cannot do with fMRI. *Nature* **453**, 869–878 (2008).
- Fox, M. D. & Raichle, M. E. Spontaneous fluctuations in brain activity observed with functional magnetic resonance imaging. *Nat. Rev. Neurosci.* **8**, 700–711 (2007).
- Biswal, B., Yetkin, F. Z., Haughton, V. M. & Hyde, J. S. Functional connectivity in the motor cortex of resting human brain using echo-planar MRI. *Magn. Reson. Med.* **34**, 537–541 (1995).
- Chang, C. et al. Tracking brain arousal fluctuations with fMRI. *Proc. Natl. Acad. Sci. USA* **113**, 4518–4523 (2016).
- Drew, P. J., Duyn, J. H., Golanov, E. & Kleinfeld, D. Finding coherence in spontaneous oscillations. *Nat. Neurosci.* **11**, 991–993 (2008).
- Belliveau, J. W. et al. Functional mapping of the human visual cortex by magnetic resonance imaging. *Science* **254**, 716–719 (1991).
- Detre, J. A., Leigh, J. S., Williams, D. S. & Koretsky, A. P. Perfusion imaging. *Magn. Reson. Med.* **23**, 37–45 (1992).
- Lauritzen, M. On the neural basis of fMRI signals. *Clin. Neurophysiol.* **119**, 729–730 (2008).
- Devor, A. et al. Suppressed neuronal activity and concurrent arteriolar vasoconstriction may explain negative blood oxygenation level-dependent signal. *J. Neurosci.* **27**, 4452–4459 (2007).
- Chaigneau, E. et al. The relationship between blood flow and neuronal activity in the rodent olfactory bulb. *J. Neurosci.* **27**, 6452–6460 (2007).
- Anenberg, E., Chan, A. W., Xie, Y., LeDue, J. M. & Murphy, T. H. Optogenetic stimulation of GABA neurons can decrease local neuronal activity while increasing cortical blood flow. *J. Cereb. Blood Flow Metab.* **35**, 1579–1586 (2015).
- Yu, X. et al. Direct imaging of macrovascular and microvascular contributions to BOLD fMRI in layers IV–V of the rat whisker-barrel cortex. *Neuroimage* **59**, 1451–1460 (2012).
- Moon, C. H., Fukuda, M. & Kim, S. G. Spatiotemporal characteristics and vascular sources of neural-specific and -nonspecific fMRI signals at submillimeter columnar resolution. *Neuroimage* **64**, 91–103 (2013).
- Yu, X. et al. Sensory and optogenetically driven single-vessel fMRI. *Nat. Methods* **13**, 337–340 (2016).
- Logothetis, N. K., Pauls, J., Augath, M., Trinath, T. & Oeltermann, A. Neurophysiological investigation of the basis of the fMRI signal. *Nature* **412**, 150–157 (2001).
- Scholvinck, M. L., Maier, A., Ye, F. Q., Duyn, J. H. & Leopold, D. A. Neural basis of global resting-state fMRI activity. *Proc. Natl. Acad. Sci. USA* **107**, 10238–10243 (2010).
- Wang, M., He, Y., Sejnowski, T. J. & Yu, X. Brain-state dependent astrocytic Ca(2+) signals are coupled to both positive and negative BOLD-fMRI signals. *Proc. Natl. Acad. Sci. USA* **115**, E1647–E1656 (2018).
- He, Y. et al. Ultra-slow single-vessel BOLD and CBV-based fMRI spatiotemporal dynamics and their correlation with neuronal intracellular calcium signals. *Neuron* **97**, 925–939 (2018). e925.
- Lind, B. L. et al. Fast Ca(2+) responses in astrocyte end-foot and neurovascular coupling in mice. *Glia* **66**, 348–358 (2018).
- Otsu, Y. et al. Calcium dynamics in astrocyte processes during neurovascular coupling. *Nat. Neurosci.* **18**, 210–218 (2015).
- Ma, Y. et al. Resting-state hemodynamics are spatiotemporally coupled to synchronized and symmetric neural activity in excitatory neurons. *Proc. Natl. Acad. Sci. USA* **113**, E8463–E8471 (2016).
- Albers, F., Wachsmuth, L., van Alst, T. M. & Faber, C. Multimodal functional neuroimaging by simultaneous BOLD fMRI and fiber-optic calcium recordings and optogenetic control. *Mol. Imaging Biol.* **20**, 171–182 (2018).
- Schwalm, M. et al. Cortex-wide BOLD fMRI activity reflects locally-recorded slow oscillation-associated calcium waves. *Elife* **6**, <https://doi.org/10.7554/eLife.27602> (2017).
- Schmid, F. et al. Assessing sensory versus optogenetic network activation by combining (o)fMRI with optical Ca<sup>2+</sup> recordings. *J. Cereb. Blood Flow Metab.* **36**, 1885–1900 (2016).
- Logothetis, N. K. et al. Hippocampal-cortical interaction during periods of subcortical silence. *Nature* **491**, 547–553 (2012).
- Dombeck, D. A., Harvey, C. D., Tian, L., Looger, L. L. & Tank, D. W. Functional imaging of hippocampal place cells at cellular resolution during virtual navigation. *Nat. Neurosci.* **13**, 1433–1440 (2010).
- Low, R. J., Gu, Y. & Tank, D. W. Cellular resolution optical access to brain regions in fissures: imaging medial prefrontal cortex and grid cells in entorhinal cortex. *Proc. Natl. Acad. Sci. USA* **111**, 18739–18744 (2014).
- Attardo, A., Fitzgerald, J. E. & Schnitzer, M. J. Impermanence of dendritic spines in live adult CA1 hippocampus. *Nature* **523**, 592–596 (2015).
- Lovett-Barron, M. et al. Dendritic inhibition in the hippocampus supports fear learning. *Science* **343**, 857–863 (2014).
- Sawinski, J. et al. Visually evoked activity in cortical cells imaged in freely moving animals. *Proc. Natl. Acad. Sci. USA* **106**, 19557–19562 (2009).
- Hirano, M., Yamashita, Y. & Miyakawa, A. In vivo visualization of hippocampal cells and dynamics of Ca<sup>2+</sup> concentration during anoxia: feasibility of a fiber-optic plate microscope system for in vivo experiments. *Brain Res.* **732**, 61–68 (1996).
- Doronina-Amiltonova, L. V. et al. Implantable fiber-optic interface for parallel multisite long-term optical dynamic brain interrogation in freely moving mice. *Sci. Rep.* **3**, 3265 (2013).
- Kudo, Y. et al. A single optical fiber fluorometric device for measurement of intracellular Ca<sup>2+</sup> concentration: its application to hippocampal neurons in vitro and in vivo. *Neuroscience* **50**, 619–625 (1992).
- Miyamoto, D. & Murayama, M. The fiber-optic imaging and manipulation of neural activity during animal behavior. *Neurosci. Res.* **103**, 1–9 (2016).
- Kobat, D., Horton, N. G. & Xu, C. In vivo two-photon microscopy to 1.6-mm depth in mouse cortex. *J. Biomed. Opt.* **16**, 106014 (2011).
- Wang, T. et al. Three-photon imaging of mouse brain structure and function through the intact skull. *Nat. Methods* **15**, 789–792 (2018).
- Ouzounov, D. G. et al. In vivo three-photon imaging of activity of GCaMP6-labeled neurons deep in intact mouse brain. *Nat. Methods* **14**, 388–390 (2017).
- Coyle, P. Vascular patterns of the rat hippocampal formation. *Exp. Neurol.* **52**, 447–458 (1976).
- Coyle, P. Spatial features of the rat hippocampal vascular system. *Exp. Neurol.* **58**, 549–561 (1978).
- Silva, A. C. & Koretsky, A. P. Laminar specificity of functional MRI onset times during somatosensory stimulation in rat. *Proc. Natl. Acad. Sci. USA* **99**, 15182–15187 (2002).
- Yu, X., Qian, C., Chen, D. Y., Dodd, S. J. & Koretsky, A. P. Deciphering laminar-specific neural inputs with line-scanning fMRI. *Nat. Methods* **11**, 55–58 (2014).
- Turner, R., Le Bihan, D., Moonen, C. T., Despres, D. & Frank, J. Echo-planar time course MRI of cat brain oxygenation changes. *Magn. Reson. Med.* **22**, 159–166 (1991).
- Mansfield, P. Multi-planar image-formation using NMR spin echoes. *J. Phys. C* **10**, L55–L58 (1977).
- Christie, I. N. et al. fMRI response to blue light delivery in the naive brain: implications for combined optogenetic fMRI studies. *Neuroimage* **66**, 634–641 (2013).
- Dorr, A., Sled, J. G. & Kabani, N. Three-dimensional cerebral vasculature of the CBA mouse brain: a magnetic resonance imaging and micro computed tomography study. *Neuroimage* **35**, 1409–1423 (2007).
- Shih, Y. Y., Wey, H. Y., De La Garza, B. H. & Duong, T. Q. Striatal and cortical BOLD, blood flow, blood volume, oxygen consumption, and glucose consumption changes in noxious forepaw electrical stimulation. *J. Cereb. Blood Flow Metab.* **31**, 832–841 (2011).
- Rungta, R. L., Osmanski, B. F., Boido, D., Tanter, M. & Charkak, S. Light controls cerebral blood flow in naive animals. *Nat. Commun.* **8**, 14191 (2017).
- Weitz, A. J. et al. Optogenetic fMRI reveals distinct, frequency-dependent networks recruited by dorsal and intermediate hippocampus stimulations. *Neuroimage* **107**, 229–241 (2015).
- Osawa, S. et al. Optogenetically induced seizure and the longitudinal hippocampal network dynamics. *PLoS ONE* **8**, e60928 (2013).
- Ayata, C. & Lauritzen, M. Spreading depression, spreading depolarizations, and the cerebral vasculature. *Physiol. Rev.* **95**, 953–993 (2015).
- Fabricius, M. et al. Association of seizures with cortical spreading depression and peri-infarct depolarisations in the acutely injured human brain. *Clin. Neurophysiol.* **119**, 1973–1984 (2008).
- Fabricius, M. et al. Cortical spreading depression and peri-infarct depolarization in acutely injured human cerebral cortex. *Brain* **129**, 778–790 (2006).
- Muldoon, S. F. et al. GABAergic inhibition shapes interictal dynamics in awake epileptic mice. *Brain* **138**, 2875–2890 (2015).
- Mateo, C., Knutsen, P. M., Tsai, P. S., Shih, A. Y. & Kleinfeld, D. Entrainment of arteriole vasomotor fluctuations by neural activity is a basis of blood-

- oxygenation-level-dependent “resting-state” connectivity. *Neuron* **96**, 936–948 (2017). e933.
59. Chan, R. W. et al. Low-frequency hippocampal–cortical activity drives brain-wide resting-state functional MRI connectivity. *Proc. Natl. Acad. Sci. USA* **114**, E6972–E6981 (2017).
60. Poplawsky, A. J. et al. Dominance of layer-specific microvessel dilation in contrast-enhanced high-resolution fMRI: comparison between hemodynamic spread and vascular architecture with CLARITY. *Neuroimage* <https://doi.org/10.1016/j.neuroimage.2017.08.046> (2017).
61. Xue, F. S., Wang, Q., Liao, X., Yuan, Y. J. & Xiong, J. Can a model of graded difficulty in Laerdal SimMan exactly compare performances of direct and indirect laryngoscopes? *Eur. J. Anaesthesiol.* **29**, 53–54 (2012); author reply 54–55.
62. Owen, S. F., Liu, M. H. & Kreitzer, A. C. Thermal constraints on in vivo optogenetic manipulations. *Nat. Neurosci.* **22**, 1061–1065 (2019).
63. Khoshkhoo, S., Vogt, D. & Sohal, V. S. Dynamic, cell-type-specific roles for GABAergic interneurons in a mouse model of optogenetically inducible seizures. *Neuron* **93**, 291–298 (2017).
64. Bernard, C. et al. Acquired dendritic channelopathy in temporal lobe epilepsy. *Science* **305**, 532–535 (2004).
65. Duffy, B. A., Choy, M., Chuapeco, M. R., Madsen, M. & Lee, J. H. MRI compatible optrodes for simultaneous LFP and optogenetic fMRI investigation of seizure-like afterdischarges. *Neuroimage* **123**, 173–184 (2015).
66. Takata, N. et al. Optogenetic activation of CA1 pyramidal neurons at the dorsal and ventral hippocampus evokes distinct brain-wide responses revealed by mouse fMRI. *PLoS ONE* **10**, e0121417 (2015).
67. Kao, Y. C. et al. Dynamic perfusion and diffusion MRI of cortical spreading depolarization in photothrombotic ischemia. *Neurobiol. Dis.* **71**, 131–139 (2014).
68. Chung, D. Y. et al. Determinants of optogenetic cortical spreading depolarizations. *Cereb. Cortex* <https://doi.org/10.1093/cercor/bhy021> (2018).
69. Enger, R. et al. Dynamics of ionic shifts in cortical spreading depression. *Cereb. Cortex* **25**, 4469–4476 (2015).
70. Dani, J. W., Chernjavsky, A. & Smith, S. J. Neuronal activity triggers calcium waves in hippocampal astrocyte networks. *Neuron* **8**, 429–440 (1992).
71. Nedergaard, M., Cooper, A. J. & Goldman, S. A. Gap junctions are required for the propagation of spreading depression. *J. Neurobiol.* **28**, 433–444 (1995).
72. Kunkler, P. E. & Kraig, R. P. Calcium waves precede electrophysiological changes of spreading depression in hippocampal organ cultures. *J. Neurosci.* **18**, 3416–3425 (1998).
73. Peters, O., Schipke, C. G., Hashimoto, Y. & Kettenmann, H. Different mechanisms promote astrocyte  $\text{Ca}^{2+}$  waves and spreading depression in the mouse neocortex. *J. Neurosci.* **23**, 9888–9896 (2003).
74. Chuquet, J., Hollender, L. & Nimchinsky, E. A. High-resolution in vivo imaging of the neurovascular unit during spreading depression. *J. Neurosci.* **27**, 4036–4044 (2007).
75. Heuser, K. et al.  $\text{Ca}^{2+}$  signals in astrocytes facilitate spread of epileptiform activity. *Cereb. Cortex* **28**, 4036–4048 (2018).
76. Kuga, N., Sasaki, T., Takahara, Y., Matsuki, N. & Ikegaya, Y. Large-scale calcium waves traveling through astrocytic networks in vivo. *J. Neurosci.* **31**, 2607–2614 (2011).
77. Srinivasan, R. et al. New transgenic mouse lines for selectively targeting astrocytes and studying calcium signals in astrocyte processes in situ and in vivo. *Neuron* **92**, 1181–1195 (2016).
78. Dana, H. et al. Sensitive red protein calcium indicators for imaging neural activity. *Elife* **5**, <https://doi.org/10.7554/eLife.12727> (2016).
79. Dreier, J. P. The role of spreading depression, spreading depolarization and spreading ischemia in neurological disease. *Nat. Med.* **17**, 439–447 (2011).

## Acknowledgements

This research was supported by NIH Brain Initiative funding (RF1NS113278-01), German Research Foundation (DFG) SPP-1655 and Yu215/3-1, BMBF 01GQ1702, internal funding from Max Planck Society, and the Ph.D. support from the Chinese Scholarship Council (for X.C., Y.C.). We thank Dr. R. Pohmann and Dr. K. Buckenmaier for technical support; Dr. E. Weiler, Dr. P. Douay, Mrs. R. König, Ms. S. Fischer, and Ms. H. Schulz for animal/lab maintenance and support; the AFNI team for software support.

## Author contributions

X.Y., N.K., and X.C. designed the research; X.C. and X.Y. performed animal experiments; X.C. and F.S. performed data analysis; Y. C., C.Q., C.A., and Z.L. provided technical support; X.Y., N.K., C.A., and X.C. wrote the paper.

## Competing interests

The authors declare no competing interests.

## Additional information

**Supplementary information** is available for this paper at <https://doi.org/10.1038/s41467-019-12850-x>.

**Correspondence** and requests for materials should be addressed to X.Y.

**Peer review information** *Nature Communications* thanks Cornelius Faber, Yen-Yu Ian Shih and the other, anonymous, reviewer(s) for their contribution to the peer review of this work.

**Reprints and permission information** is available at <http://www.nature.com/reprints>

**Publisher's note** Springer Nature remains neutral with regard to jurisdictional claims in published maps and institutional affiliations.



**Open Access** This article is licensed under a Creative Commons Attribution 4.0 International License, which permits use, sharing, adaptation, distribution and reproduction in any medium or format, as long as you give appropriate credit to the original author(s) and the source, provide a link to the Creative Commons license, and indicate if changes were made. The images or other third party material in this article are included in the article's Creative Commons license, unless indicated otherwise in a credit line to the material. If material is not included in the article's Creative Commons license and your intended use is not permitted by statutory regulation or exceeds the permitted use, you will need to obtain permission directly from the copyright holder. To view a copy of this license, visit <http://creativecommons.org/licenses/by/4.0/>.

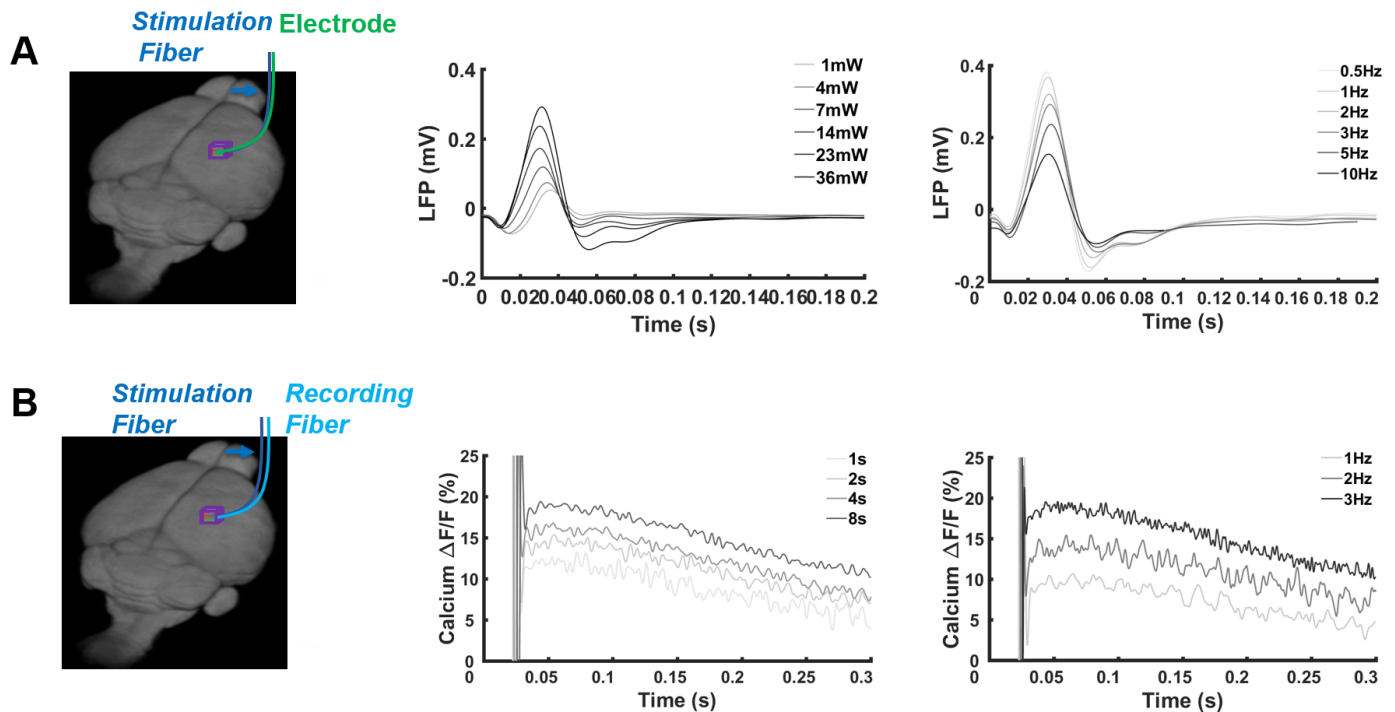
© The Author(s) 2019

# Supplementary information

**Mapping optogenetically-driven single-vessel fMRI with concurrent neuronal calcium recordings in the rat hippocampus**

Chen et al.

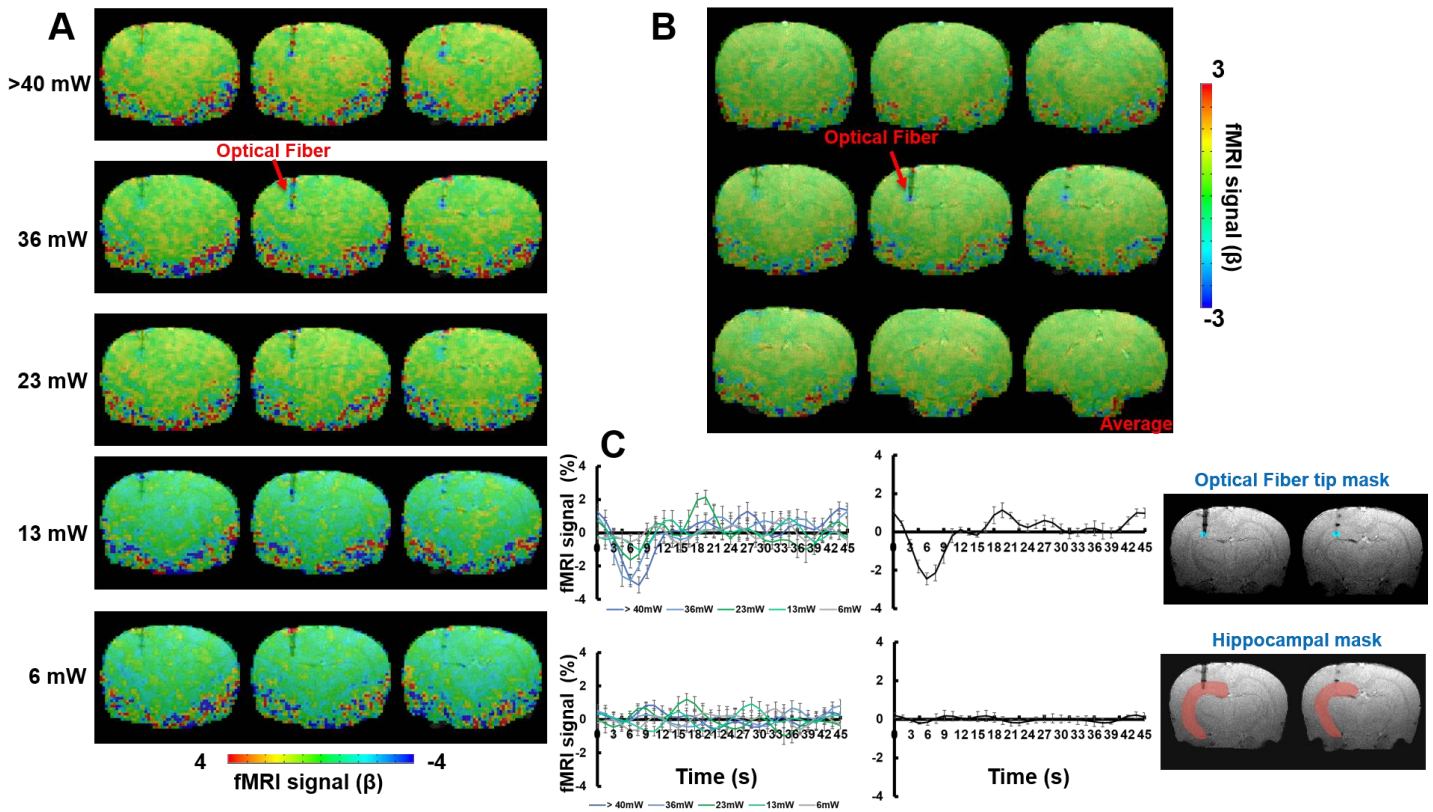




**Supplementary Figure 1. Optogenetically evoked LFP and GCamp6f-mediated  $\text{Ca}^{2+}$  recording in the hippocampus.**

**A.** Optogenetically evoked LFP traces with 10 ms light pulse stimulation at different powers (1-36 mW) averaged from trails with 3 Hz light pulse stimulation paradigm and frequencies (0.5-10 Hz) averaged from trails with 14 mW power of the light pulse (4 s on with 16 s off repeated for 20 times).

**B.** Optogenetically evoked neuronal  $\text{Ca}^{2+}$  traces with 10 ms light pulse stimulation at different stimulation on durations (1, 2, 4, 8 s) and frequencies (1-3 Hz) from experimental trails with each epoch in 20 s (1-4s on) and 45 s (8s on) repeated for 20 times.

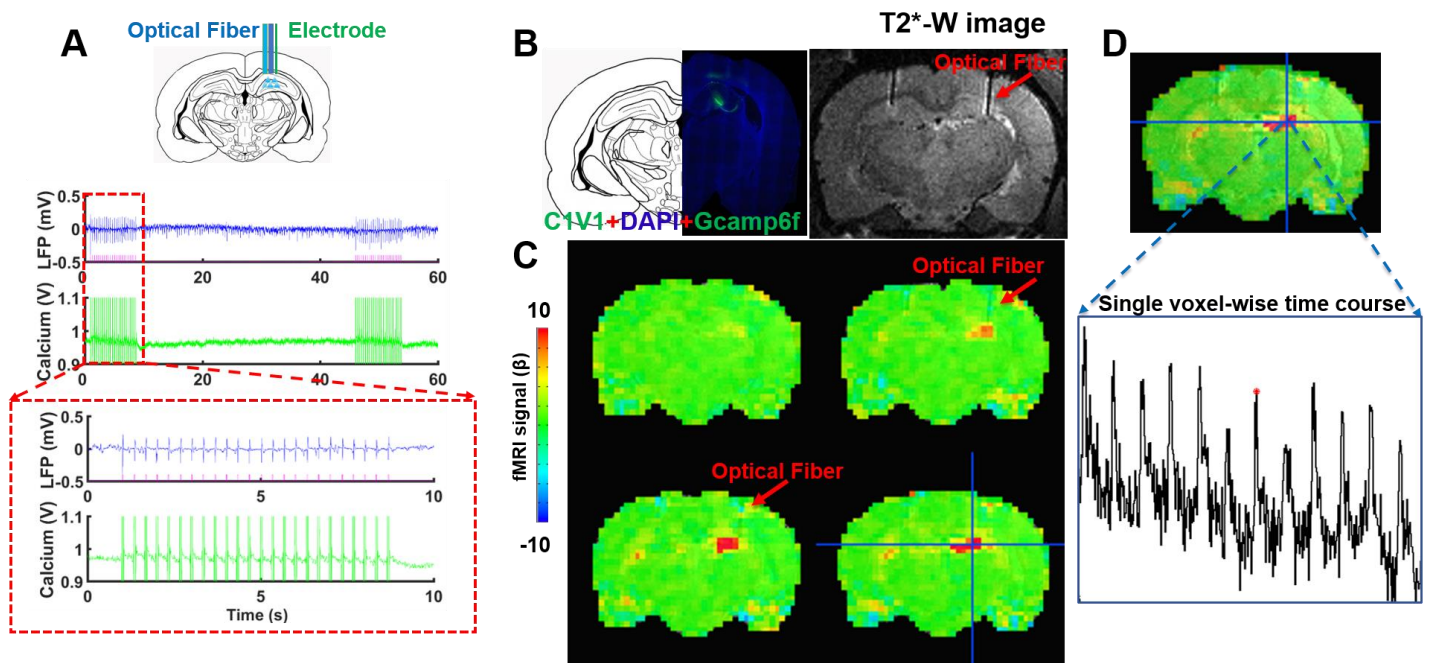


**Supplementary Figure 2. Blue light-evoked B0 offset-induced MRI signal changes close to the fiber tip in the naive rat hippocampus.**

**A.** Representative color-coded EPI-fMRI maps at different powers (6->40 mW) (illumination: 10 ms light pulse, 10 Hz, 8 s).

**B.** Averaged color-coded EPI-fMRI map from different powers (13, 23, 36, >40 mW) (illumination: 10 ms light pulse, 10 Hz, 8 s).

**C.** Averaged EPI-fMRI time courses from optical fiber tip (upper) and hippocampus (lower) at different stimulation powers (6->40 mW), averaged EPI-fMRI time courses from all the different powers (23, 36, >40 mW) (middle), and ROIs in blue contour (optic fiber tip) and red contour (hippocampus) of the MRI images (right).



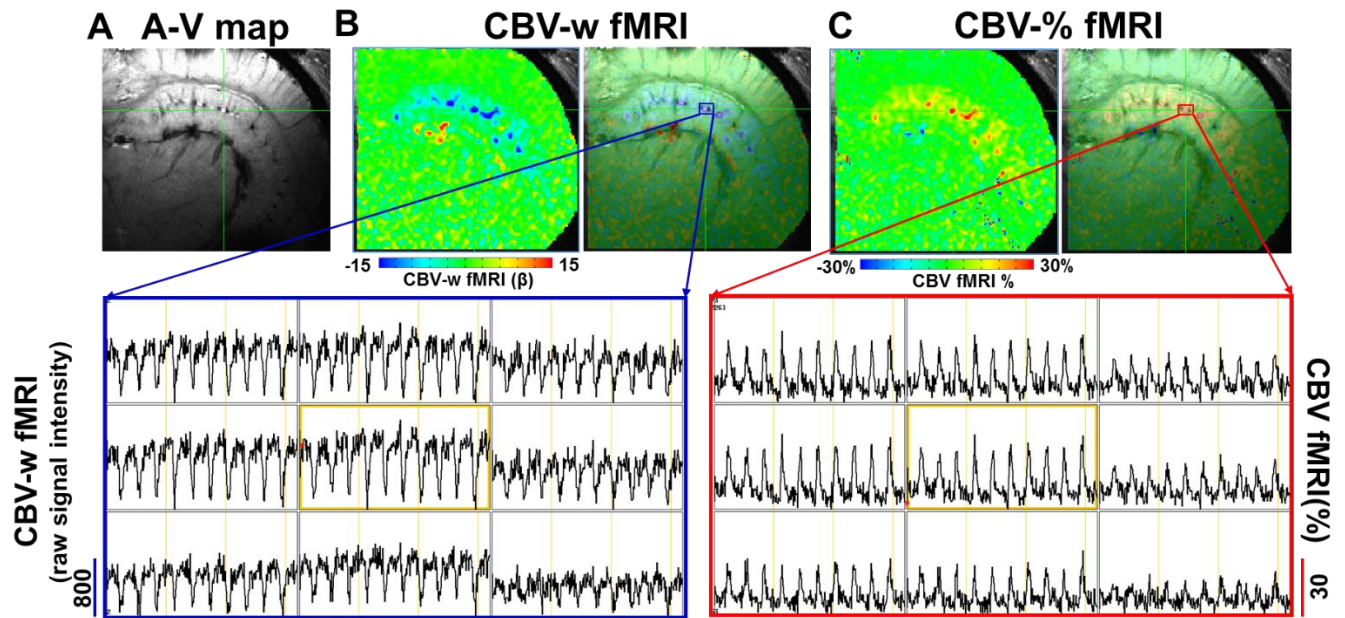
**Supplementary Figure 3. Simultaneous C1V1-evoked GCaMP6f-mediated Ca<sup>2+</sup> recording with LFP or EPI-fMRI in the hippocampus.**

**A.** Simultaneous LFP (blue) and Ca<sup>2+</sup> signal (green) traces from neurons expressing C1V1 in the hippocampus with optogenetic stimulation (illumination: 10 ms light pulse, 3 Hz, 8 s, 5 mW, 590 nm) with enlarged view outlined in the red box.

**B.** Immunohistological staining of C1V1 and Gcamp6f co-expressed in the hippocampus (left), and the T2\*-weighted (T2\*-W) image shows the optical fiber (red arrow) inserted into the hippocampus.

**C.** A representative color-coded BOLD-fMRI map shows the optogenetically activated hippocampus through C1V1 (illumination: 10 ms light pulse, 3 Hz, 8 s, 5 mW, 590 nm).

**D.** The BOLD-fMRI time course from a single voxel in hippocampus is plotted in a block-design paradigm (12 epochs).

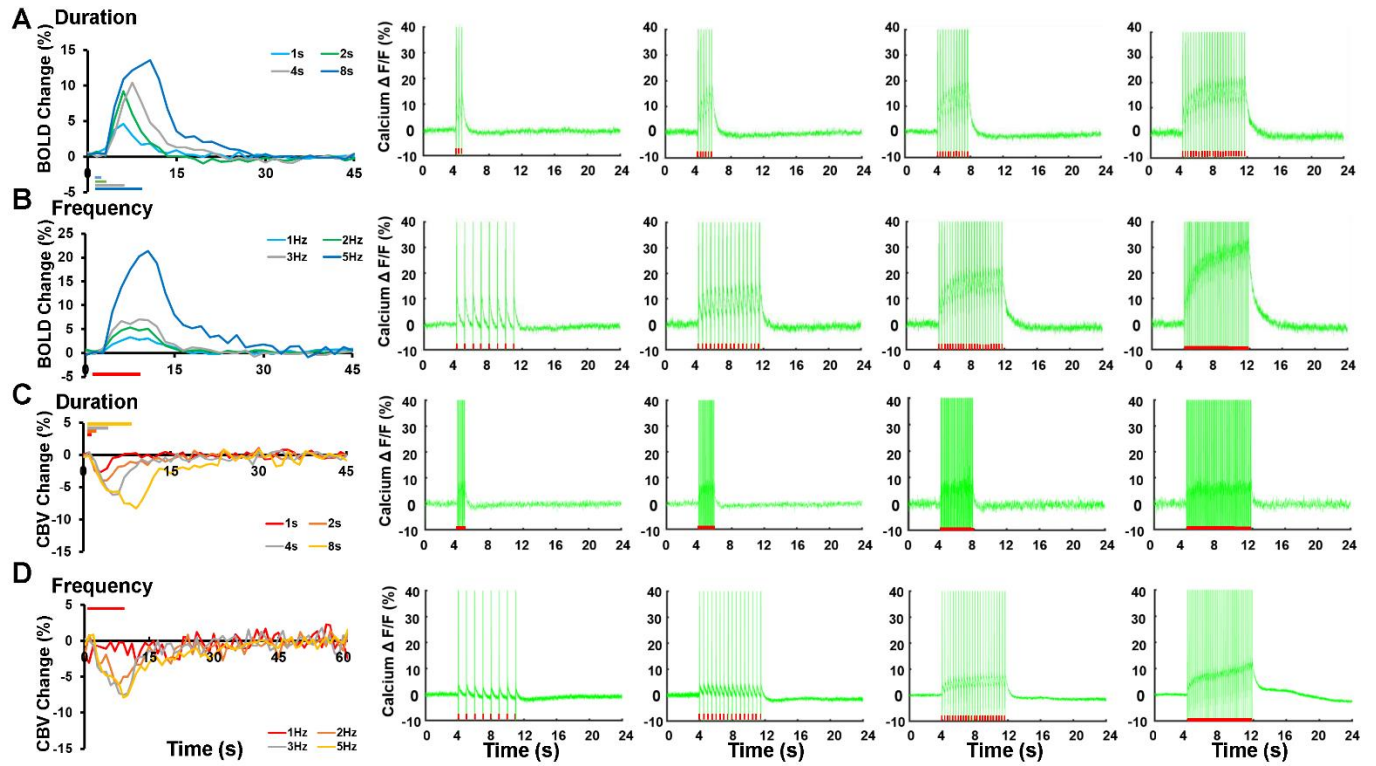


**Supplementary Figure 4. The Optogenetically driven hippocampal single-vessel CBV % map.**

**A.** Representative 2D A-V map of the hippocampal vasculature.

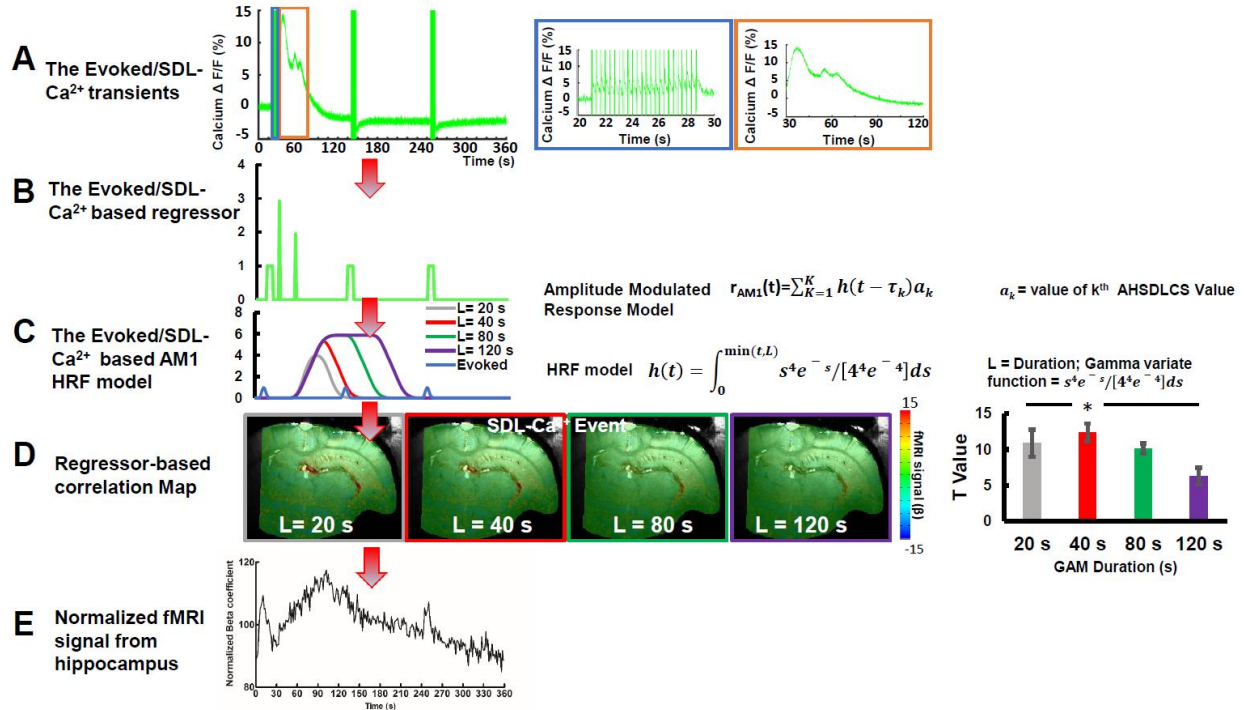
**B.** The CBV-weighted fMRI map shows the T2\*-weighted signal changes from the individual hippocampal arterioles (bright dots). The time courses of the CBV-w signal from arterioles voxels (3x3 windows, blue box) show the negative signal changes per epoch of the stimulation paradigm.

**C.** The CBV % fMRI map shows the percent CBV signal changes from the individual hippocampal arterioles (bright dots). The time courses of the CBV % signal from arterioles voxels (3x3 windows, red box) show the positive signal changes per epoch of the stimulation paradigm.



**Supplementary Figure 5. Simultaneous single-vessel BOLD/CBV fMRI and  $\text{Ca}^{2+}$  recordings in the hippocampus with different optogenetic stimulation paradigms.**

- A.** Stimulation duration-dependent BOLD-fMRI with concurrent  $\text{Ca}^{2+}$  recordings (1, 2, 4, 8 s).
- B.** Stimulation frequency-dependent BOLD-fMRI with concurrent  $\text{Ca}^{2+}$  recordings (1, 2, 3, 5 Hz).
- C.** Stimulation duration-dependent CBV-fMRI with concurrent  $\text{Ca}^{2+}$  recordings (1, 2, 4, 8 s).
- D.** Stimulation frequency-dependent CBV-fMRI with concurrent  $\text{Ca}^{2+}$  recordings (1, 2, 3, 5 Hz).



**Supplementary Figure 6. The flow diagram to calculate the SDL-Ca<sup>2+</sup> signal-based single-vessel BOLD fMRI correlation map.**

**A.** Neuronal Ca<sup>2+</sup> signals and single-vessel BOLD fMRI signals were acquired simultaneously during SDL-Ca<sup>2+</sup> events. A representative time course of the neuronal Ca<sup>2+</sup> signal shows the optogenetically evoked Ca<sup>2+</sup> signal and the SDL-Ca<sup>2+</sup> signal with enlarged views of these two events (blue and orange box).

**B.** Peak timing and amplitudes of the optogenetically evoked and SDL-Ca<sup>2+</sup> events were used to create the regressors for the single-vessel BOLD fMRI correlation.

**C.** Amplitude modulated BOLD response models are generated base on the Evoked/SDL-Ca<sup>2+</sup>-based regressors. The ideal functions (HRF models) of the representative time course of Evoked/SDL-Ca<sup>2+</sup> signal are represented with varied duration (L).

**D.** Voxel-wise correlation maps of the single-vessel BOLD fMRI signal with the simultaneously acquired neuronal Ca<sup>2+</sup> signal with the HRF models at varied duration (L), showing t statistic values at L=40 s (ANOVA, one way, F=4.93, p=0.013, n=5).

**E.** A representative time course of the single-vessel BOLD fMRI signal from the hippocampus shows the positive fMRI signal correlated to the occurrence of the SDL-Ca<sup>2+</sup> signal.